

THE EFFECTS OF TURBULENCE ON THE  
AERODYNAMICS OF LONG-SPAN BRIDGES

A Dissertation

Submitted to the Graduate School  
of the University of Notre Dame  
In Partial Fulfillment of the Requirements  
for the Degree of

Doctor of Philosophy

by

Frederick Louis Haan, Jr., B.S.E., M.S.M.E.

---

Ahsan Kareem, Director

---

Albin A. Szewczyk, Director

Department of Aerospace and Mechanical Engineering

Notre Dame, Indiana

April 2000

© Copyright by  
Frederick L. Haan, Jr.  
2000  
All rights reserved

THE EFFECTS OF TURBULENCE ON THE  
AERODYNAMICS OF LONG-SPAN BRIDGES

Abstract

by

Frederick L. Haan, Jr.

Atmospheric flows are turbulent. Experimental analysis of wind-induced vibration problems must address this issue by either matching turbulence characteristics completely or by acknowledging uncertainty in conclusions as a result of imperfect simulations. Because the former is for all practical purposes currently impossible, the latter must be understood as fully as possible.

This experimental study of the effects of turbulence on long-span bridge aerodynamics examined the anatomy of turbulence effects on the self-excited forces responsible for flutter and investigated the spanwise correlation of the overall aerodynamic lift and moment. A forced-vibration technique was used with a model of rectangular cross section instrumented with 64 pressure transducers. Spanwise coherence measurements were made on both stationary and oscillating models in a series of smooth and turbulent flows.

Unsteady pressure distributions were examined to observe turbulence-induced changes in the self-excited forces. This allowed a clearer understanding of turbulence

effects than was possible by observing only integrated quantities such as flutter derivatives. For the cross section studied, turbulence stabilized the self-excited forces. Regions of maximum pressure amplitudes were observed to shift toward the leading edge with increasing turbulence intensity—similar to the behavior observed in pressure distributions on stationary bodies. This upstream shifting was responsible for the bulk of the changes in the overall stability characteristics.

Spanwise correlation was quantified for both total aerodynamic forces and for self-excited and buffeting components separately. Self-excited forces showed essentially unity coherence for the entire spanwise separation range studied (2.4B). This supports the assumption common in analytical estimates of fully correlated self-excited forces. It does not, however, support the hypothesis that the stabilizing effect of turbulence observed in full aeroelastic tests is due to a turbulence-induced decrease in the spanwise coherence of the self-excited forces. In the future, greater spanwise separations need to be tested for full understanding of this behavior. Spanwise correlation of the buffeting force components showed exceptional similarity between stationary and oscillating model tests.

This work is dedicated to my wife Julie. No one else fully knows what went into this effort. No one else put more into it. No one else can better share with me the joy of the accomplishment.

## TABLE OF CONTENTS

LIST OF FIGURES .....	vi
NOMENCLATURE.....	xix
ACKNOWLEDGEMENTS .....	xxii
CHAPTER 1. INTRODUCTION.....	1
1.1 Turbulence and Flow-Induced Vibration .....	1
1.2 Flutter of Bluff Bodies/Bridges .....	3
1.3 Aerodynamic Analysis Applied to Bridge Design Problems .....	10
1.4 Motivation for Study of Turbulence Effects .....	22
1.5 Outline for the rest of the dissertation.....	34
CHAPTER 2. APPROACH AND BACKGROUND .....	36
2.1 The Current Approach.....	36
2.2 Background of Bluff-Body Aerodynamics.....	42
CHAPTER 3. EXPERIMENTAL SETUP.....	53
3.1 The Atmospheric Wind Tunnel.....	53
3.2 Model .....	54
3.3 Motion Driving Equipment .....	57
3.4 Data Acquisition Equipment .....	61
3.5 Pressure Measurements .....	63
3.6 Velocity Measurements .....	64
CHAPTER 4. VELOCITY MEASUREMENTS .....	66
4.1 Summary of Incident Turbulent Flows.....	66
4.2 Velocity Profiles.....	67
4.3 Spectral Measurements .....	77
4.4 Correlation Measurements .....	80
CHAPTER 5. PRESSURE FIELDS ON STATIONARY MODEL.....	86
5.1 Summary of Pressure Analysis Methods.....	86
5.2 Preliminary Tests.....	86
5.3 Statistical Distributions of Pressure .....	91
5.4 Pressure Spectra .....	97

CHAPTER 6. PRESSURE FIELDS ON OSCILLATING MODELS—SECTION RESULTS.....	106
6.1 Summary of Pressure Measurement Experiments.....	106
6.2 Force and Pressure Spectra.....	107
6.3 Streamwise Distributions of Amplitude and Phase.....	140
6.4 Flutter Derivatives.....	154
6.5 Aerodynamic Admittance Functions.....	157
6.6 Statistical Distributions of Pressure.....	166
CHAPTER 7. SPANWISE COHERENCE AND CORRELATION RESULTS.....	178
7.1 Summary of Measurements of Spanwise Behavior.....	178
7.2 Spanwise Correlation and Coherence of Forces—Stationary Model.....	178
7.3 Streamwise Position Dependence of Spanwise Pressure Correlation—Stationary Model.....	185
7.4 Spanwise Correlation and Coherence of Forces—Oscillating Model.....	190
7.5 Streamwise Position Dependence of Spanwise Pressure Correlation—Oscillating Model.....	208
CHAPTER 8. DISCUSSION OF PRESSURE RESULTS.....	219
8.1 Discussion of Sectional Forces.....	219
8.1.1 Pressure Amplitude and Phase Behavior.....	220
8.1.2 Flutter Derivatives.....	226
8.1.3 Buffeting Forces on Oscillating Models.....	233
8.2 Discussion of Spanwise Behavior.....	234
8.2.1 Comparison of Stationary and Oscillating Model Results.....	234
8.2.2 Comparison of Velocity and Pressure Correlation.....	243
8.2.3 Reduced Velocity Dependence.....	246
CHAPTER 9. CONCLUSIONS AND RECOMMENDATIONS.....	251
9.1 Conclusions.....	251
9.2 Recommendations for Future Work.....	254
APPENDIX A. PRESSURE MEASUREMENT PROCEDURES.....	257
A.1 Pressure Transducers.....	257
A.2 Static Pressure Calibration.....	259
A.3 Dynamic Pressure Calibration.....	262
A.3.1 Pressure Tubing Dynamical Response.....	262
A.3.2 Acceleration Response of Air Mass in Tubing.....	265
A.3.3 Electrical Noise Issues.....	273
APPENDIX B. VELOCITY MEASUREMENT PROCEDURES.....	275
B.1 Description of Hardware.....	275
B.2 Description of Calibration and Measurement Procedures.....	276

APPENDIX C. DIGITAL SIGNAL PROCESSING TECHNIQUES.....	279
C.1 Statistical Estimates .....	279
C.2 Spectral Estimates .....	280
C.3 Correlation Estimates .....	284
C.4 Coherence Estimates .....	287
APPENDIX D. UNCERTAINTY ANALYSIS .....	289
D.1 Voltage Measurement Uncertainty.....	290
D.2 Calibration Uncertainty .....	292
D.3 Uncertainty Propagation into Derived Quantities .....	295
REFERENCES.....	301

## LIST OF FIGURES

1-1	Schematic illustration of vortex structures forming from shear layers separating from the leading and trailing edges of a rectangular cross section.....	6
1-2	Model of the cross section of a streamlined bridge deck with two degrees of freedom—one for heaving and one for torsion. ....	7
1-3	Plot of $A_2^*$ for two bridge deck sections and an airfoil illustrating how cross section shape can affect aerodynamic damping through this coefficient (Data from Scanlan & Tomko, 1971). ....	14
1-4	First and second mode shapes of the Great Belt East Bridge (Denmark) in the swaying, bending, and twisting directions (from Larsen & Jacobsen, 1992).....	16
1-5	Flutter derivative $A_2^*$ from the simulated trussed deck section model of Scanlan & Lin (1978). The section model is shown in the inset. ....	24
1-6	Flutter derivative $A_2^*$ of the Golden Gate deck section in flows generated by the neutral and low-pass modes of Huston’s (1986) active turbulence generation mechanism.....	26
1-7	Flutter derivative $A_2^*$ for the Great Belt East Bridge deck section taken from the taut-strip model test results of Larose et al. (1993). The deck model’s cross section is shown in the inset.....	27
1-8	RMS response of a full bridge model of the Lions’ Gate Bridge in both smooth and turbulent flow. The critical flutter velocity predicted from section model test results is also shown (from Scanlan & Wardlaw, 1978). ....	28
2-1	Illustration of the definitions of pressure amplitude, $C_p^*(x)$ , and pressure phase, $\psi(x)$ , with respect to the body oscillation. ....	40
2-2	Schematic illustration of flow separation and the resulting pressure field around a bluff body with rectangular cross section. ....	43
2-3	Streamwise distribution of mean pressure coefficient for smooth and turbulent flows about a blunt flat plate with “infinite” afterbody (from Li & Melbourne, 1995).....	48
2-4	Streamwise distribution of rms pressure coefficient for turbulent flows about a blunt flat plate with “infinite” afterbody. ....	48
2-5	Reattachment length versus longitudinal turbulence intensity for a blunt flat plate. ....	50

3-1	Top view schematic diagram of the atmospheric wind tunnel (dimensions are to scale).....	54
3-2	Diagram showing the layout of pressure taps on the surface of the model. ....	55
3-3	Photograph of the upper surface of the model. Through the upper surface, the pressure taps, pressure transducers, and all associated wiring is visible.....	56
3-4	Diagram of pressure model cross section showing streamwise placement of pressure taps. ....	57
3-5	Schematic diagram of mechanisms for pitching and plunging the section model.	59
3-6	Picture of pressure model mounted on its motion driving mechanisms in the atmospheric wind tunnel. ....	59
3-7	Torsional oscillation amplitude versus reduced velocity. ....	61
3-8	Schematic diagram of the data acquisition system including the 72-channel sample and hold equipment and the PC-based data acquisition card.....	62
3-9	Top view schematic diagram of the traverse mechanism for hot film probes set up for horizontal traverses in the wind tunnel.....	65
4-1	Vertical profiles of mean longitudinal velocity in smooth flow at various lateral distances from the center of the tunnel.....	70
4-2	Vertical profiles of longitudinal turbulence intensity in smooth flow at various lateral distances from the center of the tunnel.....	71
4-3	Spanwise profile of mean longitudinal velocity for smooth flow .....	71
4-4	Spanwise profile of mean longitudinal velocity for turbulent flows with turbulence intensity of 6%.....	72
4-5	Spanwise profile of mean longitudinal velocity for turbulent flows with turbulence intensity of 12%.....	72
4-6	Spanwise profile of mean flow angle for smooth flow .....	73
4-7	Spanwise profiles of mean flow angle for turbulent flows with turbulence intensity of 6%.....	73
4-8	Spanwise profiles of mean flow angle for turbulent flows with turbulence intensity of 12%.....	74
4-9	Spanwise profile of turbulence intensity for smooth flow .....	74
4-10	Spanwise profiles of longitudinal turbulence intensity for all turbulent flows.....	75
4-11	Spanwise profiles of vertical turbulence intensity for all turbulent flows.....	75
4-12	Spanwise profiles of longitudinal integral scale for each turbulent flow.....	76
4-13	Spanwise profiles of vertical integral scale for each turbulent flow .....	76
4-14	Power spectral density plots of the $u$ velocity component for the Case 6 flows.....	78
4-15	Power spectral density plots of the $u$ velocity component for the Case 12 flows.....	78
4-16	Power spectral density plots of the $w$ velocity component for the Case 6 flows.....	79
4-17	Power spectral density plots of the $w$ velocity component for the Case 12 flows.....	79

4-18	Streamwise correlation coefficients for $u$ -components of flows with 6% turbulence intensity. ....	81
4-19	Streamwise correlation coefficients for $u$ -components of flows with 12% turbulence intensity. ....	82
4-20	Streamwise correlation coefficients for $w$ -components of flows with 6% turbulence intensity. ....	82
4-21	Streamwise correlation coefficients for $w$ -components of flows with 12% turbulence intensity. ....	83
4-22	Spanwise correlation coefficients with exponential curve fits for $u$ -components of flows with 6% turbulence intensity. ....	83
4-23	Spanwise correlation coefficients with exponential curve fits for $u$ -components of flows with 12% turbulence intensity. ....	84
4-24	Spanwise correlation coefficients with exponential curve fits for $w$ -components of flows with 6% turbulence intensity. ....	84
4-25	Spanwise correlation coefficients with exponential curve fits for $w$ -components of flows with 12% turbulence intensity. ....	85
5-1	Spanwise distributions of mean pressure coefficients at two streamwise locations, $x/B = 0.11$ and $x/B = 0.79$ .....	88
5-2	Spanwise distributions of RMS pressure coefficients at two streamwise locations, $x/B = 0.11$ and $x/B = 0.79$ .....	89
5-3	Streamwise distribution of RMS pressures for upper and lower surfaces at the model centerline measured to set the reference angle of attack. ....	90
5-4	Streamwise distributions of RMS pressure fluctuations compared with data from the literature. ....	91
5-5	Mean pressure distributions for a stationary model in all flow cases. ....	95
5-6	RMS pressure distributions for a stationary model in all flow cases. ....	95
5-7	Peak pressure distribution for a stationary model in all flow cases. ....	96
5-8	Skewness coefficient distribution for a stationary model in all flow cases. ....	96
5-9	Kurtosis coefficient distribution for a stationary model in all flow cases. ....	97
5-10	Power spectral densities for pressure signals on a stationary body in smooth flow. ....	101
5-11	Power spectral densities for pressure signals on a stationary body in Case 6a flow. ....	102
5-12	Power spectral densities for pressure signals on a stationary body in Case 6b flow. ....	103
5-13	Power spectral densities for pressure signals on a stationary body in Case 12a flow. ....	104
5-14	Power spectral densities for pressure signals on a stationary body in Case 12b flow. ....	105
6-1	Lift force spectra in smooth flow for both stationary and $U_r = 3.1$ tests (stationary results shaded). ....	114

6-2	Lift force spectra in smooth flow for both stationary and $U_r = 8$ tests (stationary results shaded).....	114
6-3	Lift force spectra in smooth flow for both stationary and $U_r = 20$ tests (stationary results shaded).....	115
6-4	Moment spectra in smooth flow for both stationary and $U_r = 3.1$ tests (stationary results shaded).....	115
6-5	Moment spectra in smooth flow for both stationary and $U_r = 8$ tests (stationary results shaded).....	116
6-6	Moment spectra in smooth flow for both stationary and $U_r = 20$ tests (stationary results shaded).....	116
6-7	Lift force spectra for $I_u = 6\%$ for both stationary and $U_r = 3.1$ tests (stationary results shaded).....	117
6-8	Lift force spectra for $I_u = 12\%$ for both stationary and $U_r = 3.1$ tests (stationary results shaded).....	117
6-9	Moment spectra for $I_u = 6\%$ for both stationary and $U_r = 3.1$ tests (stationary results shaded).....	118
6-10	Moment spectra for $I_u = 12\%$ for both stationary and $U_r = 3.1$ tests (stationary results shaded).....	118
6-11	Lift force spectra for $I_u = 6\%$ for both stationary and $U_r = 8$ tests (stationary results shaded).....	119
6-12	Lift force spectra for $I_u = 12\%$ for both stationary and $U_r = 8$ tests (stationary results shaded).....	119
6-13	Moment spectra for $I_u = 6\%$ for both stationary and $U_r = 8$ tests (stationary results shaded).....	120
6-14	Moment spectra for $I_u = 12\%$ for both stationary and $U_r = 8$ tests (stationary results shaded).....	120
6-15	Lift force spectra for $I_u = 6\%$ for both stationary and $U_r = 20$ tests (stationary results shaded).....	121
6-16	Lift force spectra for $I_u = 12\%$ for both stationary and $U_r = 20$ tests (stationary results shaded).....	121
6-17	Moment spectra for $I_u = 6\%$ for both stationary and $U_r = 20$ tests (stationary results shaded).....	122
6-18	Moment spectra for $I_u = 12\%$ for both stationary and $U_r = 20$ tests (stationary results shaded).....	122
6-19	RMS lift coefficient versus reduced velocity. Stationary model results are presented on the far right.....	123
6-20	RMS moment coefficient versus reduced velocity. Stationary model results are presented on the far right.....	123
6-21	Relative differences between RMS lift coefficient for stationary (S) and the buffeting lift component (B) of the oscillating model tests.....	124

6-22	Relative differences between RMS moment coefficient for stationary (S) and the buffeting moment component (B) of the oscillating model tests. ....	124
6-23	Power spectral density functions for pressure signals in smooth flow for both stationary and $U_r = 3.1$ tests (stationary results shaded).....	125
6-24	Power spectral density functions for pressure signals in Case 6a flow for both stationary and $U_r = 3.1$ tests (stationary results shaded).....	126
6-25	Power spectral density functions for pressure signals in Case 6b flow for both stationary and $U_r = 3.1$ tests (stationary results shaded).....	127
6-26	Power spectral density functions for pressure signals in Case 12a flow for both stationary and $U_r = 3.1$ tests (stationary results shaded).....	128
6-27	Power spectral density functions for pressure signals in Case 12b flow for both stationary and $U_r = 3.1$ tests (stationary results shaded).....	129
6-28	Power spectral density functions for pressure signals in smooth flow for both stationary and $U_r = 8$ tests (stationary results shaded).....	130
6-29	Power spectral density functions for pressure signals in Case 6a flow for both stationary and $U_r = 8$ tests (stationary results shaded).....	131
6-30	Power spectral density functions for pressure signals in Case 6b flow for both stationary and $U_r = 8$ tests (stationary results shaded).....	132
6-31	Power spectral density functions for pressure signals in Case 12a flow for both stationary and $U_r = 8$ tests (stationary results shaded).....	133
6-32	Power spectral density functions for pressure signals in Case 12b flow for both stationary and $U_r = 8$ tests (stationary results shaded).....	134
6-33	Power spectral density functions for pressure signals in smooth flow for both stationary and $U_r = 20$ tests (stationary results shaded).....	135
6-34	Power spectral density functions for pressure signals in Case 6a flow for both stationary and $U_r = 20$ tests (stationary results shaded).....	136
6-35	Power spectral density functions for pressure signals in Case 6b flow for both stationary and $U_r = 20$ tests (stationary results shaded).....	137
6-36	Power spectral density functions for pressure signals in Case 12a flow for both stationary and $U_r = 20$ tests (stationary results shaded).....	138
6-37	Power spectral density functions for pressure signals in Case 12b flow for both stationary and $U_r = 20$ tests (stationary results shaded).....	139
6-38	Example power spectral density functions for pressure signals at $x = 0.012B$ for stationary and oscillating model tests.....	141
6-39	Pressure amplitude distributions for a reduced velocity of 3.1. ....	143
6-40	Pressure amplitude distributions for a reduced velocity of 8. ....	144
6-41	Pressure amplitude distributions for a reduced velocity of 20. ....	144
6-42	Pressure amplitude distributions at a reduced velocity of 3.1 in Case 6 flows (error bars represent 95% confidence intervals).....	145
6-43	Pressure amplitude distributions at a reduced velocity of 3.1 in Case 12 flows (error bars represent 95% confidence intervals).....	145

6-44	Pressure amplitude distributions at a reduced velocity of 8 in Case 6 flows (error bars represent 95% confidence intervals).....	146
6-45	Pressure amplitude distributions at a reduced velocity of 8 in Case 12 flows (error bars represent 95% confidence intervals).....	146
6-46	Pressure amplitude distributions at a reduced velocity of 20 in Case 6 flows (error bars represent 95% confidence intervals).....	147
6-47	Pressure amplitude distributions at a reduced velocity of 20 in Case 12 flows (error bars represent 95% confidence intervals).....	147
6-48	Pressure phase distributions in smooth flow and small-scale turbulent flows at a reduced velocity of 3.1. ....	149
6-49	Pressure phase distributions in smooth flow and small-scale turbulent flows at a reduced velocity of 8. ....	150
6-50	Pressure phase distributions in smooth flow and small-scale turbulent flows at a reduced velocity of 20. ....	150
6-51	Pressure phase distributions for $U_r = 3.1$ and $I_u = 6%$ showing the effect of changing scales (error bars represent 95% confidence intervals).....	151
6-52	Pressure phase distributions for $U_r = 3.1$ and $I_u = 12%$ showing the effect of changing scales (error bars represent 95% confidence intervals).....	151
6-53	Pressure phase distributions for $U_r = 8$ and $I_u = 6%$ showing the effect of changing scales (error bars represent 95% confidence intervals).....	152
6-54	Pressure phase distributions for $U_r = 8$ and $I_u = 12%$ showing the effect of changing scales (error bars represent 95% confidence intervals).....	152
6-55	Pressure phase distributions for $U_r = 20$ and $I_u = 6%$ showing the effect of changing scales (error bars represent 95% confidence intervals).....	153
6-56	Pressure phase distributions for $U_r = 20$ and $I_u = 12%$ showing the effect of changing scales (error bars represent 95% confidence intervals).....	153
6-57	Flutter derivative $A_2^*$ in smooth and turbulent flow. ....	155
6-58	Flutter derivative $A_3^*$ for smooth and turbulent flow. ....	156
6-59	Flutter derivative $H_2^*$ in smooth and turbulent flow.....	156
6-60	Flutter derivative $H_3^*$ in smooth and turbulent flow.....	157
6-61	Lift admittance functions for $I_u = 6%$ for both stationary and $U_r = 3.1$ tests (stationary results shaded). ....	160
6-62	Lift admittance functions for $I_u = 12%$ for both stationary and $U_r = 3.1$ tests (stationary results shaded). ....	160
6-63	Moment admittance functions for $I_u = 6%$ for both stationary and $U_r = 3.1$ tests (stationary results shaded). ....	161
6-64	Moment admittance functions for $I_u = 12%$ for both stationary and $U_r = 3.1$ tests (stationary results shaded). ....	161
6-65	Lift admittance functions for $I_u = 6%$ for both stationary and $U_r = 8$ tests (stationary results shaded). ....	162

6-66	Lift admittance functions for $I_u = 12\%$ for both stationary and $U_r = 8$ tests (stationary results shaded).....	162
6-67	Moment admittance functions for $I_u = 6\%$ for both stationary and $U_r = 8$ tests (stationary results shaded).....	163
6-68	Moment admittance functions for $I_u = 12\%$ for both stationary and $U_r = 8$ tests (stationary results shaded).....	163
6-69	Lift admittance functions for $I_u = 6\%$ for both stationary and $U_r = 20$ tests (stationary results shaded).....	164
6-70	Lift admittance functions for $I_u = 12\%$ for both stationary and $U_r = 20$ tests (stationary results shaded).....	164
6-71	Moment admittance functions for $I_u = 6\%$ for both stationary and $U_r = 20$ tests (stationary results shaded).....	165
6-72	Moment admittance functions for $I_u = 12\%$ for both stationary and $U_r = 20$ tests (stationary results shaded).....	165
6-73	RMS pressure distributions for model oscillating at $U_r = 3.1$ in each flow case.....	169
6-74	Stationary model RMS pressure values (Stat) and oscillating model RMS values with peak content subtracted (B) for small-scale turbulence at $U_r = 3.1$ .....	169
6-75	Stationary model RMS pressure values (Stat) and oscillating model RMS values with peak content subtracted (B) for large-scale turbulence at $U_r = 3.1$ .....	170
6-76	RMS pressure distributions for model oscillating at $U_r = 8$ in each flow case.....	170
6-77	Stationary model RMS pressure values (Stat) and oscillating model RMS values with peak content subtracted (B) for small-scale turbulence at $U_r = 8$ .....	171
6-78	Stationary model RMS pressure values (Stat) and oscillating model RMS values with peak content subtracted (B) for large-scale turbulence at $U_r = 8$ .....	171
6-79	RMS pressure distributions for model oscillating at $U_r = 20$ in each flow case.....	172
6-80	Stationary model RMS pressure values (Stat) and oscillating model RMS values with peak content subtracted (B) for small-scale turbulence at $U_r = 20$ .....	172
6-81	Stationary model RMS pressure values (Stat) and oscillating model RMS values with peak content subtracted (B) for large-scale turbulence at $U_r = 20$ .....	173
6-82	Peak pressure distributions for model oscillating at $U_r = 3.1$ in each flow case.....	173
6-83	Peak pressure distributions for model oscillating at $U_r = 8$ in each flow case.....	174
6-84	Peak pressure distributions for model oscillating at $U_r = 20$ in each flow case.....	174
6-85	Skewness coefficient distributions for model oscillating at $U_r = 3.1$ in each flow case.....	175

6-86	Skewness coefficient distributions for model oscillating at $U_r = 8$ in each flow case. ....	175
6-87	Skewness coefficient distributions for model oscillating at $U_r = 20$ in each flow case. ....	176
6-88	Kurtosis coefficient distributions for model oscillating at $U_r = 3.1$ in each flow case. ....	176
6-89	Kurtosis coefficient distributions for model oscillating at $U_r = 8$ in each flow case. ....	177
6-90	Kurtosis coefficient distributions for model oscillating at $U_r = 20$ in each flow case. ....	177
7-1	Cross correlation and coherence were calculated between lift functions at two different spanwise locations as shown in the diagram above. ....	179
7-2	Maximum cross correlation coefficient values for lift on a stationary model. ....	182
7-3	Maximum cross correlation coefficient values for moment on a stationary model. ....	182
7-4	Coherence functions for lift on a stationary model in the Case 6 turbulent flows at several different spanwise separations ('+' Case 6a; 'o' Case 6b). ....	183
7-5	Coherence functions for moment on a stationary model in the Case 6 turbulent flows at several different spanwise separations ('+' Case 6a; 'o' Case 6b). ....	184
7-6	Coherence functions for lift on a stationary model in the Case 12 turbulent flows at several different spanwise separations ('+' Case 12a; 'o' Case 12b). ....	184
7-7	Coherence functions for moment on a stationary model in the Case 12 turbulent flows at several different spanwise separations ('+' Case 12a; 'o' Case 12b). ....	185
7-8	Cross correlations were calculated between individual pressure signals at each streamwise location for various spanwise separations as shown in the diagram above. ....	187
7-9	Pressure correlation functions for pressure taps 1-4 on a stationary model ('+' Case 6a; '-' Case 6b; 'x' Case 12a; '—' Case 12b'). ....	188
7-10	Pressure correlation functions for pressure taps 5-8 on a stationary model ('+' Case 6a; '-' Case 6b; 'x' Case 12a; '—' Case 12b'). ....	188
7-11	Pressure correlation functions for pressure taps 9-12 on a stationary model ('+' Case 6a; '-' Case 6b; 'x' Case 12a; '—' Case 12b'). ....	189
7-12	Pressure correlation functions for pressure taps 13-16 on a stationary model ('+' Case 6a; '-' Case 6b; 'x' Case 12a; '—' Case 12b'). ....	189
7-13	Spanwise correlation scales as a function of streamwise position for the stationary model in each of the four turbulent flows. ....	190
7-14	Cross correlation coefficient for lift for $U_r=3.1$ in smooth and turbulent flows. ....	195

7-15	Cross correlation coefficient for lift for $U_r=8$ in smooth and turbulent flows.....	196
7-16	Cross correlation coefficient for lift for $U_r=20$ in smooth and turbulent flows.....	196
7-17	Spanwise lift correlation scale as a function of reduced velocity.....	197
7-18	Cross correlation coefficient for moment for $U_r=3.1$ in smooth and turbulent flows.....	197
7-19	Cross correlation coefficient for moment for $U_r=8$ in smooth and turbulent flows.....	198
7-20	Cross correlation coefficient for moment for $U_r=20$ in smooth and turbulent flows.....	198
7-21	Spanwise moment correlation scale as a function of reduced velocity.....	199
7-22	Coherence of lift at $U_r=3.1$ in Case 6 flows for various spanwise separations ('+' Case 6a stationary; '-' Case 6a oscillating; 'o' Case 6b stationary; '—' Case 6b oscillating).....	199
7-23	Coherence of lift at $U_r=8$ in Case 6 flows for various spanwise separations ('+' Case 6a stationary; '-' Case 6a oscillating; 'o' Case 6b stationary; '—' Case 6b oscillating).....	200
7-24	Coherence of lift at $U_r=20$ in Case 6 flows for various spanwise separations ('+' Case 6a stationary; '-' Case 6a oscillating; 'o' Case 6b stationary; '—' Case 6b oscillating).....	200
7-25	Coherence of lift at $U_r=3.1$ in Case 12 flows for various spanwise separations ('+' Case 12a stationary; '-' Case 12a oscillating; 'o' Case 12b stationary; '—' Case 12b oscillating).....	201
7-26	Coherence of lift at $U_r=8$ in Case 12 flows for various spanwise separations ('+' Case 12a stationary; '-' Case 12a oscillating; 'o' Case 12b stationary; '—' Case 12b oscillating).....	201
7-27	Coherence of lift at $U_r=20$ in Case 12 flows for various spanwise separations ('+' Case 12a stationary; '-' Case 12a oscillating; 'o' Case 12b stationary; '—' Case 12b oscillating).....	202
7-28	Coherence of moment at $U_r=3.1$ in Case 6 flows for various spanwise separations ('+' Case 6a stationary; '-' Case 6a oscillating; 'o' Case 6b stationary; '—' Case 6b oscillating).....	202
7-29	Coherence of moment at $U_r=8$ in Case 6 flows for various spanwise separations ('+' Case 6a stationary; '-' Case 6a oscillating; 'o' Case 6b stationary; '—' Case 6b oscillating).....	203
7-30	Coherence of moment at $U_r=20$ in Case 6 flows for various spanwise separations ('+' Case 6a stationary; '-' Case 6a oscillating; 'o' Case 6b stationary; '—' Case 6b oscillating).....	203
7-31	Coherence of moment at $U_r=3.1$ in Case 12 flows for various spanwise separations ('+' Case 12a stationary; '-' Case 12a oscillating; 'o' Case 12b stationary; '—' Case 12b oscillating).....	204
7-32	Coherence of moment at $U_r=8$ in Case 12 flows for various spanwise separations ('+' Case 12a stationary; '-' Case 12a oscillating; 'o' Case 12b stationary; '—' Case 12b oscillating).....	204

7-33	Coherence of moment at $U_r=20$ in Case 12 flows for various spanwise separations ('+' Case 12a stationary; '- -' Case 12a oscillating; 'o' Case 12b stationary; '—' Case 12b oscillating).....	205
7-34	Coherence of lift at $f_m$ for $U_r=3.1$ in smooth and turbulent flows.....	205
7-35	Coherence of lift at $f_m$ for $U_r=8$ in smooth and turbulent flows.....	206
7-36	Coherence of lift at $f_m$ for $U_r=20$ in smooth and turbulent flows.....	206
7-37	Coherence of moment at $f_m$ for $U_r=3.1$ in smooth and turbulent flows.....	207
7-38	Coherence of moment at $f_m$ for $U_r=8$ in smooth and turbulent flows.....	207
7-39	Coherence of moment at $f_m$ for $U_r=20$ in smooth and turbulent flows.....	208
7-40	Pressure correlation functions for pressure taps 1-4 at $U_r=3.1$ ('o' smooth flow; '+' Case 6a; '- -' Case 6b; 'x' Case 12a; '—' Case 12b').....	211
7-41	Pressure correlation functions for pressure taps 5-8 at $U_r=3.1$ ('o' smooth flow; '+' Case 6a; '- -' Case 6b; 'x' Case 12a; '—' Case 12b').....	211
7-42	Pressure correlation functions for pressure taps 9-12 at $U_r=3.1$ ('o' smooth flow; '+' Case 6a; '- -' Case 6b; 'x' Case 12a; '—' Case 12b').....	212
7-43	Pressure correlation functions for pressure taps 13-16 at $U_r=3.1$ ('o' smooth flow; '+' Case 6a; '- -' Case 6b; 'x' Case 12a; '—' Case 12b').....	212
7-44	Spanwise pressure correlation scale, $L_{py}$ , as a function of streamwise position for each turbulent flow case at $U_r = 3.1$ .....	213
7-45	Pressure correlation functions for pressure taps 1-4 at $U_r=8$ ('o' smooth flow; '+' Case 6a; '- -' Case 6b; 'x' Case 12a; '—' Case 12b').....	213
7-46	Pressure correlation functions for pressure taps 5-8 at $U_r=8$ ('o' smooth flow; '+' Case 6a; '- -' Case 6b; 'x' Case 12a; '—' Case 12b').....	214
7-47	Pressure correlation functions for pressure taps 9-12 at $U_r=8$ ('o' smooth flow; '+' Case 6a; '- -' Case 6b; 'x' Case 12a; '—' Case 12b').....	214
7-48	Pressure correlation functions for pressure taps 13-16 at $U_r=8$ ('o' smooth flow; '+' Case 6a; '- -' Case 6b; 'x' Case 12a; '—' Case 12b').....	215
7-49	Spanwise pressure correlation scale, $L_{py}$ , as a function of streamwise position for each turbulent flow case at $U_r = 8$ .....	215
7-50	Pressure correlation functions for pressure taps 1-4 at $U_r=20$ ('o' smooth flow; '+' Case 6a; '- -' Case 6b; 'x' Case 12a; '—' Case 12b').....	216
7-51	Pressure correlation functions for pressure taps 5-8 at $U_r=20$ ('o' smooth flow; '+' Case 6a; '- -' Case 6b; 'x' Case 12a; '—' Case 12b').....	216
7-52	Pressure correlation functions for pressure taps 9-12 at $U_r=20$ ('o' smooth flow; '+' Case 6a; '- -' Case 6b; 'x' Case 12a; '—' Case 12b').....	217
7-53	Pressure correlation functions for pressure taps 13-16 at $U_r=20$ ('o' smooth flow; '+' Case 6a; '- -' Case 6b; 'x' Case 12a; '—' Case 12b').....	217
7-54	Spanwise pressure correlation scale, $L_{py}$ , as a function of streamwise position for each turbulent flow case at $U_r = 20$ .....	218
8-1	Pressure phase distributions for smooth flow and small-scale turbulent flows at a reduced velocity of 20.....	221

8-2	Schematic diagram labeling different regimes in the pressure phase diagrams. These regimes include regions of near-constant phase, rapidly-changing phase, and slowly-changing phase.....	221
8-3	Schematic diagram illustrating the concept of the body motion time scale. ....	224
8-4	Pressure phase distributions for smooth and turbulent flows including phase estimated from both convection and oscillation frequency time scales ( $U_r = 20$ ). .....	224
8-5	Pressure phase distributions for smooth turbulent flows including phase estimated from both convection and oscillation frequency time scales ( $U_r = 3.1$ ). .....	225
8-6	Pressure amplitude and phase distributions for the Case 12 flows at $U_r = 20$ . .....	225
8-7	$A_2^*$ versus reduced velocity for smooth and turbulent flow cases from this study compared with smooth flow values for different $B/D$ ratios (“M96” refers to Matsumoto, 1996). .....	227
8-8	$C_p^*(x)\sin(\psi(x))$ plotted versus streamwise position for various reduced velocities in smooth flow. ....	227
8-9	$C_p^*(x)\sin(\psi(x))$ plotted versus streamwise position for all flow cases at $U_r = 8$ . .....	229
8-10	Comparison of pressure phase values in turbulent flow for the current model with $B/D = 6.67$ with values in smooth flow for a model with a longer afterbody ( $B/D = 12.5$ ). .....	230
8-11	$C_p^*(x)\cos(\psi(x))$ plotted versus streamwise position for all flow cases at $U_r = 20$ . .....	233
8-12	Plots of the total, self-excited, and buffeting components of lift for $U_r = 20$ in Case 6a flow. ....	236
8-13	Cross correlation functions for the total, self-excited, and buffeting components of lift for $U_r = 20$ in Case 12b flow at a separation of $\Delta y = 1.2B$ . ....	237
8-14	Cross correlation coefficients ( $\tau = 0$ ) of stationary model lift (Stat) and of the buffeting components (B) of lift with the model oscillating at $U_r = 3.1$ . .....	239
8-15	Cross correlation coefficients ( $\tau = 0$ ) of stationary model lift (Stat) and of the buffeting components (B) of lift with the model oscillating at $U_r = 8$ . .....	239
8-16	Cross correlation coefficients ( $\tau = 0$ ) of stationary model lift (Stat) and of the buffeting components (B) of lift with the model oscillating at $U_r = 20$ . .....	240
8-17	Cross correlation coefficients ( $\tau = 0$ ) of stationary model moment (Stat) and of the buffeting components (B) of moment with the model oscillating at $U_r = 3.1$ . .....	240
8-18	Cross correlation coefficients ( $\tau = 0$ ) of stationary model moment (Stat) and of the buffeting components (B) of moment with the model oscillating at $U_r = 8$ . .....	241

8-19	Cross correlation coefficients ( $\tau = 0$ ) of stationary model moment (Stat) and of the buffeting components (B) of moment with the model oscillating at $U_r = 20$ .....	241
8-20	Cross correlation coefficients ( $\tau = 0$ ) of the self-excited components (se) of lift with the model oscillating at $U_r = 20$ .....	243
8-21	Spanwise correlation, in Case 6 flows, for both the $w$ component of velocity and the buffeting component of lift for $U_r = 8$ .....	245
8-22	Spanwise correlation, in Case 12 flows, for both the $w$ component of velocity and the buffeting component of lift for $U_r = 8$ .....	245
8-23	Normalized cross correlation coefficients for lift at a spanwise separation of $\Delta y = 1.8B$ .....	250
8-24	Normalized cross correlation coefficients for moment at a spanwise separation of $\Delta y = 1.8B$ .....	250
A-1	Schematic diagram of the connectors used for connecting the plastic tubing to both the pressure taps on the surface of the model and the pressure transducers themselves. ....	259
A-2	Setup for static calibration of pressure transducers. ....	260
A-3	Illustrative example of calibration data set for transducer voltage versus calibration pressure. ....	261
A-4	Shaker and speaker equipment used for dynamic calibration of pressure system. ....	263
A-5	Pressure tubing frequency response function, $H_{tubing}(f)$ , as acquired with the swept-sine function approach. ....	264
A-6	Simplified sketch of a model with a pressure tap and transducer separated by a distance $L$ and undergoing an acceleration $\bar{a}$ . ....	266
A-7	Schematic diagram showing an example placement of a pressure tap and its corresponding transducer with an acceleration vector $\bar{a}$ between them. ....	268
A-8	Plot of pressure amplitude distributions as measured—uncorrected—and as corrected for model acceleration effects. ....	270
A-9	Pressure phase distributions as measured—uncorrected—and as corrected for model acceleration effects. ....	270
A-10	Coherence at a given frequency as a function of the amplitude ratio of coherent to incoherent signals at that frequency. ....	272
B-1	The X-probe calibration rig used to step through different angles of attack for a range of velocities. ....	277
B-2	X-wire calibration surface for the $u$ -component of velocity as a function of $E_1$ and $E_2$ .....	278
B-3	X-wire calibration surface for the $w$ -component of velocity as a function of voltages $E_1$ and $E_2$ .....	278

C-1	Plot of a sample pressure PSD highlighting the bins integrated to calculate the signal's amplitude. ....	283
C-2	Plot of an angle signal and pressure signal to illustrate the calculation of the phase from a cross correlation between them. ....	286
C-3	Cross correlation function for the signals shown in Figure C-1 to illustrate the location of the peak and its associated time lag, $\tau_p$ .....	287

## NOMENCLATURE

### Alphabetical Symbols

$A_i^*$	Flutter derivatives related to unsteady moment
$B$	Streamwise dimension of model, also referred to as “bridge deck width”
$B_x$	Bias error of the quantity, $x$
$b$	Half the bridge deck width
$C_p$	Pressure coefficient
$C_{\bar{p}}$	Mean pressure coefficient
$C_{p'}$	RMS pressure coefficient
$C_{\hat{p}}$	Peak pressure coefficient
$C_p^*$	Amplitude of pressure coefficient
$C_{p_a}^*$	Amplitude of pressure coefficient induced by tubing acceleration
$C_{p_m}^*$	Amplitude of pressure coefficient measured by pressure transducer
$D$	Vertical dimension of model
$\Delta t, dt$	Time step between data acquisition cycles
$E$	Voltage from a straight-wire/straight-film probe
$E_1, E_2$	Pair of voltages from an X-wire/X-film probe
$f_h$	Vertical oscillation frequency of model
$f_\alpha$	Torsional oscillation frequency of model
$F_{\text{flap}}$	Frequency (Hz) associated with the “flapping” of the separated/reattaching shear layer
$F_{\text{shed}}$	Frequency (Hz) corresponding to the shedding of structures from a separation bubble
$G_{xx}$	Power spectral density of variable $x$
$h$	Maximum height of the separation bubble
$h(t)$	Vertical displacement of a bridge deck as a function of time
$H_i^*$	Flutter derivatives related to unsteady lift
$H_{\text{tubing}}(f)$	Frequency response function of pressure tubing
$I_i$	Turbulence intensity for the $i^{\text{th}}$ component of velocity fluctuation
$K$	Reduced frequency
$K_u$	Kurtosis coefficient

$L$	Spanwise dimension of model, also total lift per unit span
$L_{ij}$	The integral scale of the $i^{th}$ -component of velocity fluctuation in the $j^{th}$ -direction.
$L_{Ly}$	Spanwise (the “y” direction) correlation scale of lift, $L$ . Lift, $L$ , can be replaced by moment, $M$ , or pressure, $p$ .
$L_{Ly_s}$	Same as $L_{Ly}$ but values are for stationary model tests.
$M$	Total moment per unit span
$P_{raw}(f)$	Fourier transform of $p_{raw}(t)$
$P_x$	Precision error of the quantity, $x$
$p_{amb}$	Ambient pressure measured by the barometer in the laboratory
$p_{raw}(t)$	Time series of pressure before any correction for tubing dynamics
$p_{static}$	Static pressure
$p_{total}$	Total pressure
$p^*$	Amplitude of pressure fluctuation
$q$	Dynamic pressure
$R$	Gas constant for air
$S_i$	Small-scale spectral density parameter for $i^{th}$ component of velocity
$S_k$	Skewness coefficient
$T$	Ambient temperature measured by thermometer in the laboratory
$U$	Mean velocity in the streamwise direction
$U_r$	Reduced velocity, defined as $U_r = U/f_h B$ or $U_r = U/f_\alpha B$
$U_s$	Separation velocity
$u$	Longitudinal component of velocity fluctuation
$u_x$	Uncertainty of the quantity, $x$
$v$	Lateral component of velocity fluctuation
$w$	Vertical component of velocity fluctuation
$x_{RMS}$	Root mean square value of the quantity $x$
$X_k$	Output of FFT algorithm performed on $x(t)$
$X(f_k)$	Fourier transform of $x(t)$ at discrete frequencies, $f_k$
$x$	Streamwise position
$x_R$	Shear layer reattachment length
$x^*$	Non-dimensional streamwise position

### Greek Symbols

$\alpha(t)$	Bridge deck angle of attack as a function of time
$\alpha_0$	Amplitude of bridge deck angle of attack
$\alpha_G$	Geometric angle of attack—measured with protractor on model surface

$\Delta y$	Spanwise separation distance
$\rho$	Air density
$\psi$	Phase of pressure fluctuation
$\psi_m$	Phase of pressure fluctuation measured by pressure transducer

## ACKNOWLEDGEMENTS

I am sincerely grateful to my advisors, Dr. Ahsan Kareem and Dr. Albin A. Szewczyk, for their guidance during this project. I was fortunate to have advisors with complementary backgrounds. Dr. Kareem's wind engineering and structural dynamics experience and Dr. Szewczyk's fluid mechanics experience combined to form a broad foundation for the work. I thank Dr. Kareem for his high standards, for his honest appraisal of my work, and for much-needed encouragement and timely compliments. I greatly admire his ability to draw from a wide range of fields to address the task at hand, and can only hope to emulate this in my career. I thank Dr. Szewczyk for his support and encouragement, for his patience with the rigors of experimental research, for opening opportunities for me in other projects in addition to my dissertation research, and for his hospitality and kindness to my family and me.

I also thank my committee members Dr. Eric Jumper, Dr. Nicos Makris, and Dr. Xinzhong Chen. The time and effort put into critiquing the material, arranging schedules, and in the case of Dr. Makris, travelling, are much appreciated. Dr. Chen is worthy of special thanks for his helpful critique of my research over the past two years. I have learned a great deal from him, and I thank him for patiently sharing his bridge aerodynamics experience with me.

I thank Joel Preston, Mike Swadener, and Marilyn Walker of the Hessert Center for Aerospace Research for countless hours of help with the designs, the paperwork, the

orders, the construction, and the troubleshooting that go along with experiments and with graduate school.

The support of a family allows people to reach beyond themselves, take risks, and accomplish goals. I am deeply aware of this foundation in my life. In this regard, I thank my wife, Julie, for her seemingly tireless support and for her patience throughout the many ups and downs of this project. I thank my children, Katie and Lucas, for loving me just for being Daddy. I also thank my extended family, both the Haans and the Koemans, for years of encouragement, phone calls, email, cards, visits, and vacations.

My enjoyment of graduate school has been due in no small part to the community I have found here. This includes many great people at the South Bend Christian Reformed Church. For their prayers, their love of me and my family, and their help in so many ways I am truly grateful. In addition to friends from church, this community also includes many fellow graduate students: Randy Heinig, Mike Rea, Xinyu Li, Rob Minnitti, Mike Fabian, Rich Sellar, Chris Sullivan, Mark Ellison, Elgin Anderson, Denis Lynch, Ed Fitzgerald, and John Wojno. I thank them for friendship, for technical help, and for commiseration and diversion.

For the encouragement of many other friends, I am truly grateful. In particular, to Dale Eizenga, for his most remarkable knack for giving me perspective, for his steadfast prayer, and for his enduring friendship, I offer my humble thanks.

I also gratefully acknowledge my sponsors, the Department of Aerospace and Mechanical Engineering, the University of Notre Dame, and the National Science Foundation through grants CMS 95-03779 and CMS 95-22145.

## CHAPTER 1. INTRODUCTION

Atmospheric flows are turbulent. Any study of wind-induced vibration problems must confront this issue either by matching turbulence characteristics completely or by acknowledging uncertainty in conclusions as a result of imperfect simulations. Because the former is for all practical purposes currently impossible, the latter must be understood as fully as possible.

To introduce this study of turbulence effects on bridge aerodynamics, a summary is provided of the importance of turbulence effects on different types of flow-induced vibrations with specific attention to bridges. The scope will then be narrowed to look specifically at flutter studies of long-span bridges. The motivation for the current work is then described in a discussion of the state of current knowledge of the effects of turbulence on long-span bridge flutter. Finally, a brief outline of the rest of the dissertation is provided.

### 1.1 Turbulence and Flow-Induced Vibration

Wind-tunnel testing of bridge decks remains an integral component of long-span bridge design because of the complexity of the flow-structure interactions. Matching atmospheric conditions in a wind tunnel requires matching Reynolds numbers, turbulence intensities, integral scales, spectral characteristics of the velocity fluctuations, shear, anisotropy, etc. With atmospheric conditions producing turbulence scales ranging from

0.5 to 10 times typical bridge deck widths (Simiu & Scanlan, 1986, Tuenissen, 1970; and Counihan, 1975) and full-scale Reynolds numbers as much as three orders of magnitude higher than that of test conditions, only a fraction of the turbulence characteristics can be matched in a wind tunnel experiment. As a result, one must try to understand where matching is a necessity and where it is unnecessary because the essential details of the flow are sufficiently captured. The high cost of simulating every turbulent parameter motivates one to understand the effects of imperfect simulation.

Flow-induced vibration problems that must be understood in this turbulent environment are often classified into three distinct types—buffeting, vortex-induced vibration, and flutter. Turbulent buffeting refers to the random, unsteady pressures that a body experiences due to the random, unsteady velocity fluctuations in a turbulent flow. The reaction of the body is a direct result of unsteadiness in the incident flow. Vortex-induced vibration results from the shedding of large-scale vortices into the wake of a body at a specific frequency which—at certain velocities—coincides to some degree with a natural frequency of the structure. The interaction of the shed vortices with the body is a nonlinear vibration problem resulting in amplitudes potentially large enough to cause damage. Flutter results from an interaction between the elastic behavior of a body and the change in the aerodynamic pressures that this behavior affects. The elastic deformation changes the aerodynamic pressures and vice versa—these pressure forces can be called “motion-induced” or “self-excited” forces. Flutter is the term given the unstable interaction scenario where oscillatory perturbations which would otherwise be attenuated are amplified to damaging proportions.

While each of these phenomena warrants investigation for any potential long-span bridge deck design, the changes in the flutter problem—or more specifically, the changes in the self-excited or “motion-induced” forces—resulting from turbulence in the incident flow were the main focus of this study. Although the self-excited forces were the primary focus, this work covered bridge aerodynamics as a whole. Therefore, measurements of both flutter and buffeting forces were made and both were included in the overall analysis. The next section provides a brief overview of aeroelastic analysis for long-span bridges.

## 1.2 Flutter of Bluff Bodies/Bridges

Aeroelasticity and bluff-body aerodynamics blend together in the study of long-span bridge aerodynamics. Engineering long suspension bridges to be stable in high winds involves the elastic structural dynamics of a large structure, the bluff-body aerodynamics of the bridge deck’s shape, and the interaction of these phenomena—i.e. aeroelasticity. This section briefly summarizes the historical and mathematical foundations of modern analysis of bridge aerodynamics.

Flutter is the unstable interaction of an elastic body with a fluid flow where energy drawn from the flow increases the energy of the body’s oscillations. Under non-flutter conditions, both structural and aerodynamic damping attenuate perturbations to a body’s motion. When a critical flutter condition is reached (commonly just a minimum freestream velocity), the aerodynamic forces that result from the body’s motion interact

with the motion itself so as to cancel the structural damping and actually amplify the oscillations.

Analytical methods of studying flutter were motivated by aircraft flutter problems in the first part of the twentieth century. The early analytical formulations of motion-induced forces provided a theoretical framework for later experimental efforts—including those of bridge decks. The basis of these models was the use of infinitesimal sheets of vorticity to model both the vorticity bound to the airfoil—modeled as a flat plate—and that shed into its wake. Using this approach, several authors have derived the relationship between an oscillating flat plate and the unsteady forces on it. Theodorsen’s 1935 paper is often considered the foundation of flutter theory (for excellent summaries and derivations of flutter theory, see Fung (1993), Dowell et al., 1995, and Bisplinghoff et al., 1996).

With plunging and pitching degrees of freedom represented as  $h$  and  $\alpha$ , respectively, the relationships for unsteady lift,  $L$ , and moment,  $M$ , took the form of linear functions of  $h$ ,  $\alpha$ , and their first and second derivatives:

$$L = f(\alpha, \dot{\alpha}, \ddot{\alpha}, h, \dot{h}, \ddot{h}, C(K)) \quad (1-1)$$

$$M = g(\alpha, \dot{\alpha}, \ddot{\alpha}, h, \dot{h}, \ddot{h}, C(K)) \quad (1-2)$$

where  $C(K)$  is the Theodorsen circulation function and  $K$  is the reduced frequency of the oscillations. Reduced frequency is defined as  $K = \omega B/U$  with  $\omega$  being the frequency of oscillation,  $B$  the deck width, and  $U$  the freestream velocity. This analytical relationship—when used in conjunction with the mechanical properties of the body—can predict the mean flow speed at which flutter will occur. The most common approach to these stability predictions is to study infinitesimal motions assuming that if small motions

are stable, then large ones will be stable as well (for a good introduction, see Bisplinghoff et al., 1996). Since large deformations are undesirable, it is commonly considered sufficient to study small motions and ensure they are stable. Bringing a dynamic analysis such as this to bear on long-span bridge design problems did not occur in earnest until after the infamous collapse of the Tacoma Narrows Bridge in 1940.

Before the Tacoma Narrows failure, long-span bridges were designed with primary consideration given to *static* wind loads. Appropriation of the tools, both analytical and experimental, developed for studying aircraft flutter began seriously only after this particular display of the significance of *dynamic* wind loading. While the images of the steel and concrete of the Tacoma Narrows bridge twisting like a toy in the wind have made its collapse the most famous in history, it was not the first bridge to suffer such a fate. Unfortunately, a number of bridges in the nineteenth century failed due to wind action without due change in subsequent bridge design practice (for examples, see Steinman (1954), Scanlan & Wardlaw (1978)).

Scanlan (1993) provides a summary of the early attempts to study dynamic wind loads on bridge decks. Efforts employing Theodorsen's flutter formulation proved unsatisfactory because the separated flow experienced by many bridge decks made Theodorsen's circulation function—derived for a thin airfoil with fully attached flow—inapplicable. Most bridge decks can be classified as bluff bodies because of the separated flow they experience over significant portions of their surface. Flow separation from a bluff body is illustrated schematically in Figure 1-1. The figure shows shear layers separating from the leading and trailing edges of a rectangular cross section. This highly complex unsteady flow structure involves separated regions where large suction pressures

are generated, shear layers which may or may not reattach, and vortex-like structures that shed from the leading and trailing edges. This flow scenario is further complicated by interactions with body motion. Clearly, a thin-airfoil model and its accompanying analytical tools are inadequate for this scenario.

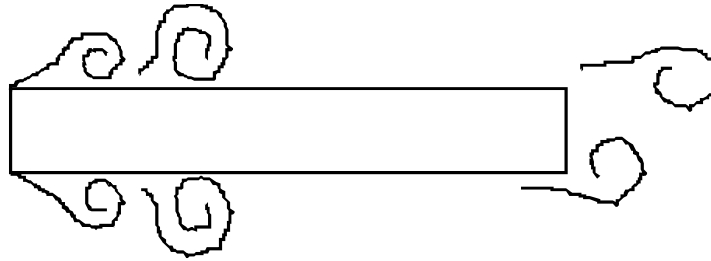


Figure 1-1 Schematic illustration of vortex structures forming from shear layers separating from the leading and trailing edges of a rectangular cross section.

To go beyond the thin airfoil model, Ukeguchi et al. (1966) and Sabzevari & Scanlan (1968) et al. worked to find aerodynamic, motion-related coefficients for sinusoidal motions of bridge decks in smooth flow. The contribution of Scanlan & Tomko (1971), however, has become one of the most widely-used formulations for modern bridge flutter analysis. With thin-airfoil theory as a basis, it is an analytical framework that requires the use of empirical aerodynamic data to describe the complex lift and moment generation mechanisms of separated flows over bodies. What follows here is a brief overview of this formulation.

Assuming a section of a body—such as that shown in Figure 1-2—to have two main degrees of freedom (DOF), call them heaving (or vertical) and torsional displacements  $h$  and  $\alpha$ , respectively, one can write a linear system of equations:

$$\ddot{h} + 2\zeta_h \omega_h \dot{h} + \omega_h^2 h = \frac{1}{m} L(t) \quad (1-3)$$

$$\ddot{\alpha} + 2\zeta_\alpha \omega_\alpha \dot{\alpha} + \omega_\alpha^2 \alpha = \frac{1}{I} M(t) \quad (1-4)$$

where  $\zeta_h$  and  $\zeta_\alpha$  are the damping ratios for the vertical and torsional degrees of freedom, respectively,  $\omega_\alpha$  and  $\omega_h$  are the natural frequencies for the vertical and torsional degrees of freedom, respectively,  $m$  is the mass per unit span of the bridge deck,  $I$  is the mass moment of inertia per unit span of the bridge deck, and  $L(t)$  and  $M(t)$  are the time-varying lift and moment per unit span on the bridge deck, respectively. Dots represent derivatives with respect to time.

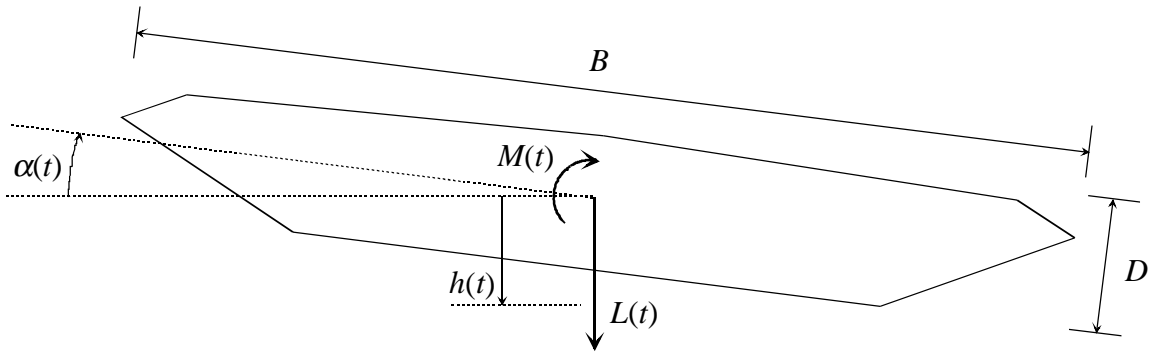


Figure 1-2 Model of the cross section of a streamlined bridge deck with two degrees of freedom—one for heaving and one for torsion.

The time-dependent forces, lift and moment, in equations (1-3) and (1-4) are typically separated into self-excited and buffeting components as follows:

$$L(t) = L_{se}(t) + L_b(t) \quad (1-5)$$

$$M(t) = M_{se}(t) + M_b(t) \quad (1-6)$$

where the subscript “*se*” refers to self-excited and the subscript “*b*” refers to buffeting. The self-excited components are those forces that result from the motion of the body itself and require no other outside forcing. The buffeting components are the unsteady forces resulting from the natural unsteadiness of a turbulent flow and are independent of the body motion. For linear fluid-structure interaction problems, the buffeting forces can be ignored during examinations of motion stability.

To express the time-varying, self-excited lift and moment, Scanlan & Tomko (1971) used expressions similar to the following form (note the similarity to the generic forms of equations (1-1) and (1-2)):

$$L_{se}(t) = q2b \left[ kH_1^*(k) \frac{\dot{h}}{U} + kH_2^*(k) \frac{b\dot{\alpha}}{U} + k^2 H_3^*(k) \alpha + k^2 H_4^*(k) \frac{h}{b} \right] \quad (1-7)$$

$$M_{se}(t) = q2b^2 \left[ kA_1^*(k) \frac{\dot{h}}{U} + kA_2^*(k) \frac{b\dot{\alpha}}{U} + k^2 A_3^*(k) \alpha + k^2 A_4^*(k) \frac{h}{b} \right] \quad (1-8)$$

where  $q = \frac{1}{2} \rho U^2$  is the dynamic pressure,  $U$  is the mean wind velocity,  $b = B/2$  is half the bridge deck width,  $k$  is the reduced frequency of the bridge motion defined as  $k = \omega b/U$ , and the coefficients  $H_i^*$  and  $A_i^*$  are referred to as “flutter derivatives” or “aerodynamic coefficients.” Note that, similar to the formulation for thin-airfoils, the self-excited or aeroelastic lift and moment are given in terms of the two degrees of freedom, their first derivatives in time, and the reduced frequency. Unlike the thin-airfoil work, the coefficients in this formulation are found experimentally.

The model’s attractiveness lies in the fact that it can be adapted to a host of different bridge deck sections as a generic framework with which to utilize experimental

aerodynamic data. This framework clearly delineates the experiments necessary to test a given bridge design for aeroelastic stability. Although the aerodynamic problem is nonlinear, it can be addressed to a certain extent by these linear analytical techniques for two reasons described by Simiu & Scanlan (1986). First, the structure itself “is usually treatable as linearly elastic and its actions dominate the *form* of the response....” Second, the incipient motion “separates the stable and unstable regimes” and “may be treated as having only small amplitude.” These two assumptions enable the use of these tools in bridge stability calculations.

While equations (1-7) and (1-8) make up an empirical framework for the self-excited forces, another empirically-based framework is often employed for the buffeting forces. Similar to the history of bridge flutter analysis, concepts for bridge buffeting analysis were borrowed from aircraft studies. Like the work of Sears (1941) and Liepmann (1952) for thin airfoils, Davenport (1962) developed an analysis technique for bridge buffeting. Based on Davenport’s general work, expressions for buffeting forces commonly take the following form:

$$L_b(t) = -\frac{1}{2} \rho U^2 2b \left( 2C_L \chi_{L_{bu}} \frac{u(t)}{U} + (C'_L + C_D) \chi_{L_{bw}} \frac{w(t)}{U} \right) \quad (1-9)$$

$$M_b(t) = \frac{1}{2} \rho U^2 (2b)^2 \left( 2C_M \chi_{M_{bu}} \frac{u(t)}{U} + C'_M \chi_{M_{bw}} \frac{w(t)}{U} \right) \quad (1-10)$$

where  $L_b$  and  $M_b$  are the buffeting components of the lift and moment, respectively,  $C_L$ ,  $C_M$ , and  $C_D$ , are the static lift, moment, and drag coefficients, respectively, of the bridge deck (and primes denote derivatives with respect to angle of attack),  $u$  and  $w$  are the turbulent velocity fluctuations in the longitudinal and vertical directions, respectively, and

$\chi_{L_{bu}}$ ,  $\chi_{L_{bw}}$ ,  $\chi_{M_{bu}}$ , and  $\chi_{M_{bw}}$  are aerodynamic frequency response. The effectiveness of turbulent velocity fluctuations at generating aerodynamic force on a bridge deck is quantified using these frequency response functions—for example, the relationship between buffeting lift and  $u$  fluctuations is characterized by  $\chi_{L_{bu}}$ . The functions are dependent on frequency, bridge deck shape, and turbulence parameters. While the thin airfoil counterpart to these functions, the Sears function (Sears, 1941), is derived analytically, these functions are found experimentally (like the flutter derivatives). “Aerodynamic admittance” is the term commonly used for the absolute magnitudes of these functions.

### 1.3 Aerodynamic Analysis Applied to Bridge Design Problems

Designing long-span bridges for aerodynamic stability involves three major steps (among others). The analysis framework described in the previous section is used directly in two of these steps. The steps include section model tests, analytical estimates of full-bridge response, and full aeroelastic model tests. This section describes each of these design stages to provide the background information necessary for understanding the gaps in the current knowledge of turbulence effects presented in the following section. The descriptions here focus mainly on the self-excited forces and flutter analysis.

Section model tests are conducted early in the design process. Section models are rigid, small-span replicas of candidate bridge cross section shapes. Their size allows them to represent even small geometric details of the bridges. Such model tests are relatively inexpensive compared to full-aeroelastic bridge models and allow economical

aerodynamic testing of a large number of potential designs. The two DOF analytical models discussed in section 1.2 are perfectly suited to section model testing.

The most common aerodynamic output of section model tests are the flutter derivatives and the aerodynamic admittance described in section 1.2. Experimental aerodynamic data required for identifying flutter derivatives can be and has been obtained in numerous ways. A wind-tunnel model can be described as “an analog simulator that reveals aerodynamic mechanisms affecting bridge stability and general response. The ‘reading’ of this simulator is done by examining its flutter derivatives” (Jones et al., 1995). Methods of “reading” the flutter derivatives can be divided into two major categories: those that use freely-vibrating models and those that force the model motion. Flutter derivatives are extracted from freely-vibrating models by utilizing system identification techniques to identify the model’s dynamic properties—a combination of it’s mechanical properties and the modifications to them due to the flutter derivatives—from vibration data. Models can also be forced to move in a prescribed motion while the aerodynamic forces are obtained directly through either force or pressure measurements. The flutter derivatives are then identified from the formulations (1-7) and (1-8) knowing the forces and displacements.

References reporting self-excited forces identified from free-vibration experiments include Scanlan & Tomko (1971), Huston (1986), Poulsen et al. (1992), Sarkar et al. (1994), and Bogunović Jakobsen & Hjorth-Hansen (1995). Researchers identifying self-excited forces using forced-vibration techniques include Larose et al. (1993), Li (1995), Matsumoto (1996), Matsumoto et al. (1992, 1995), Falco et al. (1992), and Ukeguchi et al. (1966). Sarkar et al. (1993) compared the results of a number of these

different techniques—free and forced vibration methods—and found results to be consistent with each other. Aerodynamic admittance is often obtained from pressure measurements or force-balance measurements on stationary models (for example, Larose & Mann, 1998).

Physical interpretations such as “aerodynamic damping” or aerodynamic stiffness” are often given to the effects of the self-excited forces. These physical interpretations of the flutter derivatives can make the classifications of the different types of flutter more intuitively clear. Combining the torsional equation of motion, (1-4), with the aeroelastic moment expression, (1-8), one obtains the expressions (1-11) and (1-12) below for the coefficients of  $\dot{\alpha}$  and  $\alpha$ , respectively. Aerodynamic effects combine with the structural contribution to damping in the coefficient of  $\dot{\alpha}$  as shown here:

$$2I\zeta_{\alpha}\omega_{\alpha} - q(2b^2)kA_2^*(k)\frac{b}{U} \quad (1-11)$$

And aerodynamic effects alter the coefficient of  $\alpha$  as shown here:

$$I\omega^2 - q(2b^2)k^2A_3^*(k) \quad (1-12)$$

If one interprets expression (1-11) as the “effective damping” and expression (1-12) as the “effective frequency,” then the terms involving  $A_2^*$  and  $A_3^*$  can be understood as *aerodynamic* contributions to damping and frequency of the structure. The remaining terms of equation (1-8) serve to couple the pitching motion to the plunging motion aerodynamically. Analogous statements can be made about the aerodynamic effects on the plunging motion involving the  $H_i^*$  terms.

Examples of the  $A_2^*$  coefficient for two different bridge decks are given in Figure 1-3. In light of the aerodynamic damping expression of expression (1-11), it is evident

that for the original Tacoma Narrows deck section a value of  $A_2^*$  of sufficient magnitude could reduce or even eliminate the effect of the structural damping thus resulting in an unstable “negative damping” situation. This negative damping results in a flutter mode commonly known as single degree of freedom (SDOF) flutter. The Tacoma Narrows Bridge, with this positive trend of its  $A_2^*$  coefficient, suffered an SDOF torsional flutter condition that resulted in its catastrophic failure. A number of researchers (Scanlan & Wardlaw, 1978; Scanlan et al., 1974; Nakamura, 1988) have hypothesized the physical mechanism of this SDOF torsional flutter being related to the shedding of a large vortex-like structure from the leading edge of the body as it undergoes a change in angle of attack (such as shown in Figure 1-1). The suction on the body caused by this structure causes an abrupt increase in the aerodynamic moment before it asymptotes to its steady state value as the fluid structure convects downstream and away from the body. Since the effect of this moment is to increase the same motion that initiated it, the situation is unstable.

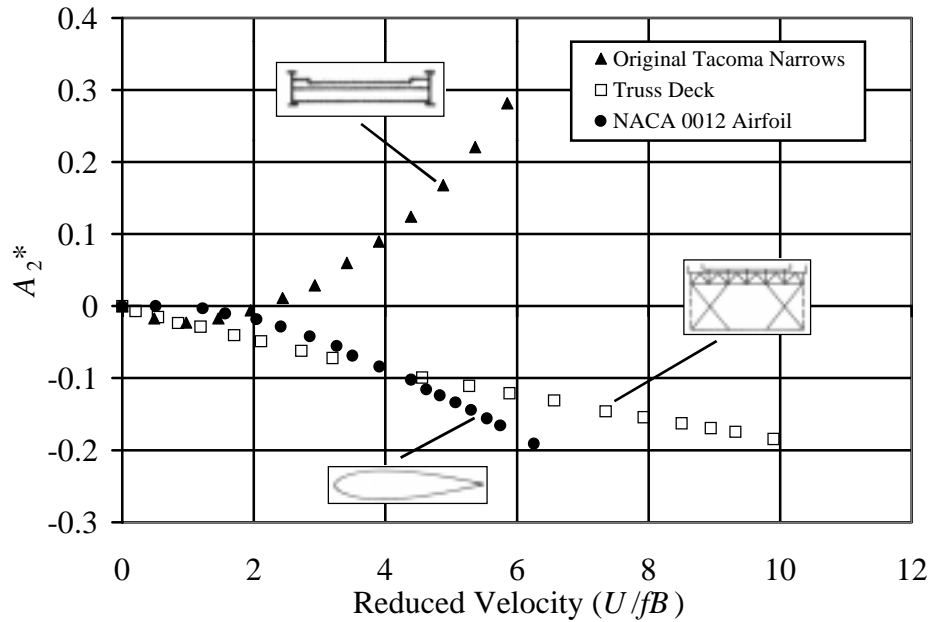


Figure 1-3 Plot of  $A_2^*$  for two bridge deck sections and an airfoil illustrating how cross section shape can affect aerodynamic damping through this coefficient (Data from Scanlan & Tomko, 1971).

Figure 1-3 shows that not all bridge deck sections have positive trends in their  $A_2^*$  values. These sections, like an airfoil, cannot experience flutter in a single mode but only experience flutter when multiple modes couple aerodynamically. In light of the flutter derivative formulation, this coupling occurs through the  $H_2^*$ ,  $H_3^*$ ,  $A_1^*$ , and  $A_4^*$  coefficients. This manifestation of flutter is commonly called “classical” flutter.

While the above physical interpretations of the flutter derivatives are helpful to some extent, they do not provide particularly useful insight into the physical mechanisms of flutter. They provide some measure of how given geometrical changes in cross section affect the aeroelastic stability of a design but do not, in themselves, serve as guides to particular design changes. Rather than identify the flutter derivatives directly, the present

work measured pressure magnitudes and phases across the deck section to determine aeroelastic stability characteristics.

Once section model testing has rendered aerodynamic data from a potential bridge shape, full-bridge response estimates are made by analytically extending the section model data to three dimensions. Estimation of full-bridge response is often based on the approach of Scanlan (1978a, 1978b, 1987). Using structural analysis techniques, the vibration modes of a full bridge are obtained. These modes are calculated neglecting the aerodynamic stiffness effects modeled by the flutter derivatives (assuming that the small ratio of air inertia to structural inertia results in negligible effects on the structural mode shapes). As an example, Figure 1-4 shows the first and second swaying, bending, and twisting modes of the Great Belt East Bridge (Larsen & Jacobsen, 1992). The full-bridge vibration mode shapes are then used to generalize the aerodynamic forces. Scanlan (1987) points out that while the vibration modes most likely to participate in flutter may have been identifiable intuitively for older, more basic, suspension bridge designs, this is not the case for modern cable-stayed bridges having modes “less likely to be ‘pure’ in one single degree of freedom.” This emphasizes the need to have some formal approach to identifying the critical modes of a structure out of the dozens computed from structural analysis.

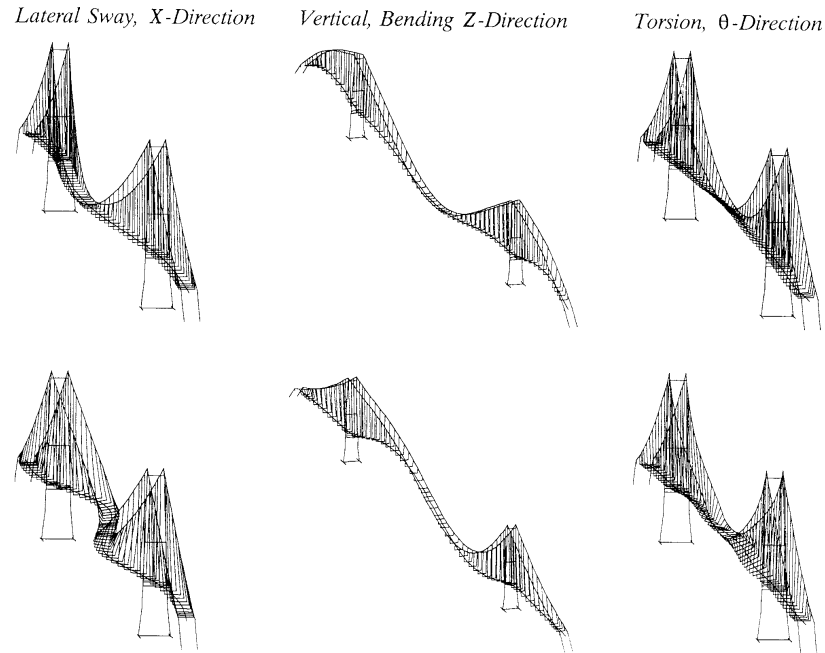


Figure 1-4 First and second mode shapes of the Great Belt East Bridge (Denmark) in the swaying, bending, and twisting directions (from Larsen & Jacobsen, 1992).

Two such formal approaches (based on Scanlan (1987), Scanlan & Jones (1990), and Katsuchi et al. (1999)) are outlined here. The first approach seeks a single mode of the structure which is the dominant flutter mode. Scanlan (1987) has observed that bridge flutter generally involves the dominant action of a single mode. The alternative to this is a “classical” type flutter where the frequencies of multiple bridge modes coalesce into a single flutter mode. While single-mode flutter is the critical condition for the majority of spans in existence today, increasingly longer spans become increasingly more susceptible to coupled flutter. The recently completed Akashi-Kaikyo Bridge with its 1991m main span was the first bridge in the world exhibiting a coupled bending-torsion flutter mode as its critical mode. With even longer spans being planned, a multi-mode, coupled

analysis is essential. A description of a multi-mode, coupled approach will follow the single-mode approach here.

The dimensionless, generalized coordinates of a full bridge are written as:

$$I_i [\ddot{\xi}_i + 2\zeta_i \omega_i \dot{\xi}_i + \omega_i^2 \xi_i] = Q_i(t) \quad (1-13)$$

where  $I_i$  is the generalized inertia and  $\xi_i$  is the dimensionless, generalized coordinate associated with the  $i^{th}$  full-bridge vibration mode, and  $Q_i(t)$  is the generalized force. The displacement of the bridge deck at a spanwise position  $x$  is written as:

$$\alpha(x,t) = \sum_i \xi_i(t) \alpha_i(x) \quad (1-14)$$

$$h(x,t) = \sum_i \xi_i(t) h_i(x) B$$

where  $h_i(x)$  and  $\alpha_i(x)$  are dimensionless components of the full-bridge vibration mode shapes at  $x$  in the vertical and torsional directions, respectively. The generalized force is then defined by:

$$Q_i(t) = \int_{span} (L h_i B + M \alpha_i) dx \quad (1-15)$$

where  $L = L_{se} + L_b$  and  $M = M_{se} + M_b$  are the lift and moment, respectively, per unit span at  $x$ . Note that an actual analysis of full-bridge dynamics would include the swaying component of the deck, sometimes modeled as  $p(x)$  with the drag force  $D$ . For brevity and for continuity with the previously-discussed formulation of the flutter derivatives, this degree of freedom was omitted here.

It is important to observe that the calculation of the generalized force involves the spanwise dependence of lift and moment. In this formulation, it is assumed that the motion-induced forces on a specific spanwise deck location depend only on the shape and

motion of that specific point and the flow immediately upstream of it. This is one aspect of what is commonly called a “strip theory” assumption. Substituting (1-7) and (1-8) into equation (1-15), coupled with the strip theory assumption, results in the following expression for the generalized self-excited forces:

$$\begin{aligned} \frac{Q_{i_{se}}(t)}{qB^3} &= \frac{K}{U} \sum_j \dot{\xi}_j \left( G_{h_j h_i}^{H_1^*} + G_{\alpha_j h_i}^{H_2^*} + G_{h_j \alpha_i}^{A_1^*} + G_{\alpha_j \alpha_i}^{A_2^*} \right) \\ &+ \frac{K^2}{B} \sum_j \xi_j \left( G_{\alpha_j h_i}^{H_3^*} + G_{h_j h_i}^{H_4^*} + G_{\alpha_j \alpha_i}^{A_3^*} + G_{h_j \alpha_i}^{A_4^*} \right) \end{aligned} \quad (1-16)$$

where the  $G$  terms are defined by the following integral which combines the structural and aerodynamic coupling among the various modes:

$$G_{r_m s_n}^{T_p^*} = \int_{span} T_p^*(x) r_m(x) s_n(x) dx \quad (1-17)$$

where  $T_p^* = A_p^*$  or  $H_p^*$  ( $p = 1, 2, 3, 4$ ),  $r, s = h$  or  $\alpha$  and  $m, n = i$  or  $j$ . Since flutter for a single mode is being sought, the cross coupling terms (i.e. those terms for which  $i \neq j$ ) in equation (1-16) can be dropped to simplify the expressions. With this simplification an effective damping expression can be written analogous to that described in equation (1-11). This expression can be written:

$$\bar{\zeta}_i = \frac{\zeta_i \omega_i}{\bar{\omega}_i} - \frac{\rho B^4}{4I_i} \left[ G_{h_i h_i}^{H_1^*}(\bar{K}_i) + G_{h_i \alpha_i}^{H_2^*}(\bar{K}_i) + G_{h_i \alpha_i}^{A_1^*}(\bar{K}_i) + G_{\alpha_i \alpha_i}^{A_2^*}(\bar{K}_i) \right] \quad (1-18)$$

where  $\bar{\zeta}_i$  is the effective damping for mode  $i$ ,  $\bar{K}_i = \frac{B \bar{\omega}_i}{U}$ , and  $\bar{\omega}_i$  is the effective frequency of mode  $i$ . The effective frequency can be written in a form analogous to equation (1-12) as follows:

$$\bar{\omega}_i = \left[ \frac{\omega_i^2}{1 + \frac{\rho B^4}{2I_i} G_{\alpha_i \alpha_i}^{A_3^*}(\bar{k}_i)} \right]^{1/2} \quad (1-19)$$

In many cases,  $\bar{\omega}_i$  is assumed to be equal to  $\omega_i$ . The first term of equation (1-18) is the generalized structural damping of mode  $i$  while the remaining terms are the aerodynamic contribution to the damping. The flutter criterion then is:  $\bar{\zeta}_i \leq 0$ . From an examination of this inequality for each bridge mode over a series of velocities, one can determine the flutter susceptibility of each mode.

As stated, for the longer bridge spans being built and being planned, this single-mode approach is inadequate. A number of researchers have developed multi-mode, coupled analysis techniques for flutter and buffeting analysis (Jain et al., 1995; Miyata et al., 1994; Katsuchi et al., 1999; Chen et al., 2000). The frequency-domain approach of Jain et al. (1996) and Katsuchi et al. (1999) is outlined here, but the advantages of time-domain approaches (such as Chen et al. 2000, 2000a) will be discussed later in this chapter and in subsequent chapters. The first step is to expand equation (1-13) to include all the bridge modes. This requires matrix notation as follows:

$$\hat{\mathbf{I}} \ddot{\mathbf{h}} + \mathbf{A} \dot{\mathbf{h}} + \mathbf{B} \mathbf{h} = \mathbf{Q}_b \quad (1-20)$$

where  $\mathbf{I}$  is an identity matrix,  $\mathbf{h}$  is the generalized coordinate vector, primes denote derivatives with respect to time,  $\mathbf{Q}_b$  is the generalized buffeting force vector. The matrices A and B are expressed as:

$$\mathbf{A}_{ij}(K) = 2\zeta_i K_i \delta_{ij} - \frac{\rho B^4 l K}{2I_i} \left[ G_{h_j h_i}^{H_1^*} + G_{\alpha_j h_i}^{H_2^*} + G_{h_j \alpha_i}^{A_1^*} + G_{\alpha_j \alpha_i}^{A_2^*} \right] \quad (1-21)$$

$$\mathbf{B}_{ij}(K) = K_i^2 \delta_{ij} - \frac{\rho B^4 l K^2}{2I_i} \left[ G_{\alpha_j h_i}^{H_3^*} + G_{h_j h_i}^{H_4^*} + G_{\alpha_j \alpha_i}^{A_3^*} + G_{h_j \alpha_i}^{A_4^*} \right] \quad (1-22)$$

The first terms of the  $\mathbf{A}_{ij}$  and the  $\mathbf{B}_{ij}$  expressions represent structural damping and stiffness, respectively. The remaining terms represent the aerodynamic contributions to damping and frequency and the coupling among the various bridge modes. Equations (1-20) through (1-22) simplify to the single mode formulation for  $i = j$ . Again it should be noted that for the sake of the clarity of these examples, the sway component has been left out of these formulations. Including the drag force and the sway component would add to the number of terms in equations (1-21) and (1-22) but would not change their fundamental character.

Taking a Fourier transform of the above formulation allows equation (1-20) to be written in the frequency domain as:

$$\mathbf{E} \bar{\xi} = \bar{\mathbf{Q}}_b \quad (1-23)$$

where the matrix  $\mathbf{E}$  is a combination of the  $\mathbf{A}$  and  $\mathbf{B}$  matrices of equations (1-21) and (1-22), respectively, and the overbar here denotes the Fourier transform. This formulation of the problem allows consideration of buffeting response including the effects of the aerodynamic contributions to damping and stiffness and the effects of coupling—the latter a necessity for extremely long spans such as Akashi-Kaikyo.

Multi-mode, coupled flutter analysis then consists of solving the following eigenvalue problem:

$$\mathbf{E} \bar{\xi} = 0 \quad (1-24)$$

where the solution is found by identifying the value of  $K$  for which the determinant of  $\mathbf{E}$  vanishes. This involves two equations—one for the real part and one for the imaginary

part—which must be satisfied simultaneously. Since both the critical flow speed and critical flutter frequency are unknown, one solution assumes a value of the reduced frequency,  $K$ , and solves for  $\omega$ . Iteration is required to find values of  $K$  for which the real and imaginary parts of the determinant vanish for the same  $\omega$  (this process is similar to that known as “Theodorsen’s method” for the two DOF case discussed in section 1.2). The critical flutter speed for a given mode is then obtained from the definition of the reduced velocity,  $K = \omega B/U$ . This process is repeated for each of the bridge modes being considered. The critical flutter speed for the overall bridge is obviously, then, the lowest of those obtained for the individual modes. It should be noted that it is not necessarily trivial using this method to track how a bridge’s structural modes/frequencies are being altered as different mean wind speeds,  $U$ , are considered.

Buffeting analysis consists of combining the spectral description of the incident turbulent flow with aerodynamic admittance functions to obtain buffeting forces. An in-depth summary of such analyses will not be provided here, but—as discussed for flutter analysis—it has been found that very long bridge span lengths (such as the 1991m Akashi-Kaikyo Bridge) require multi-mode, coupled analysis techniques to obtain proper buffeting response estimates (Jain et al., 1995; Miyata et al., 1994; Katsuchi et al., 1999; Chen et al., 2000).

The next step in the design of a long-span bridge is an aeroelastic model of the complete bridge. Large wind tunnels are required for such testing. For example, the Boundary Layer Wind Tunnel of the Public Works Research Institute in Tsukuba, Japan—where the Akashi-Kaikyo Bridge was tested—has a test section 41m wide, 4m high, and 30m long (Miyata & Yamaguchi, 1993). Bridge models are designed to match

as closely as possible the first few modes of bending, swaying, and twisting motions. This testing is very expensive, and is only conducted after extensive section model aerodynamic testing and analytical work has brought the design to a near-final state.

The background of aerodynamic testing of long-span bridges provided by this section is the basis for understanding the next section concerning work to improve the state of the art of bridge flutter analysis. Both inconsistencies and experimental work needed to address gaps in current understanding are addressed.

#### 1.4 Motivation for Study of Turbulence Effects

Inconsistencies in past studies and gaps in our understanding of the turbulence effects on long-span bridge stability provided the primary motivation for this project. The inconsistencies manifest themselves in both experimental and numerical simulation results. This section highlights some inconsistencies exhibited in past experimental results and then discusses some gaps in our understanding of turbulence effects—particularly related to spanwise coherence of self-excited forces. The need for physical insights concerning turbulence effects is then presented, and finally, the limitations of the linear approach most often used for bridge analysis is addressed along with the need for nonlinear analysis techniques with corresponding nonlinear experimental data.

Designing a long-span bridge often includes section-model tests to identify stable shapes from candidate bridge decks followed by full, aeroelastic model tests to finalize the design. Section models are used mainly to obtain flutter derivatives for stability estimates while the full, aeroelastic model tests provide further validation of stability

while, hopefully, elucidating full-bridge dynamics. This section presents experimental results from both types of tests that illustrate the gaps in the current understanding of how turbulence affects the motion-induced forces on a bridge deck.

Results from three studies where the flutter derivatives were identified will be presented here. Scanlan & Lin (1978) and Huston (1986) involved section model tests while Larose, Davenport, and King (1993) employed taut-strip models—which, consisting of a long, flexible span pulled taut across a wind tunnel to simulate the fundamental modes of the full bridge, lies somewhere between section models and full, aeroelastic models.

Not many studies have focused explicitly on the effects of turbulence on aeroelastic forces. One of the first to do so was Scanlan & Lin (1978) who used a spring-mounted section model in grid-generated turbulence. Their model simulated a trussed deck section by having holes drilled into the sides of an inverted U-shaped beam.

The results of this study did not reveal a significant difference in the flutter derivatives between smooth and turbulent flow as illustrated in Figure 1-5 for the  $A_2^*$  flutter derivative. Their study concluded, “Results under the two flow conditions do not differ drastically in this instance exhibiting, in fact, similar trends throughout” (Scanlan & Lin, 1978). Each flutter derivative had only slightly and yet consistently greater magnitudes in turbulent flow—from this it follows that the actual lift and moment magnitudes will have greater magnitudes for the turbulent.

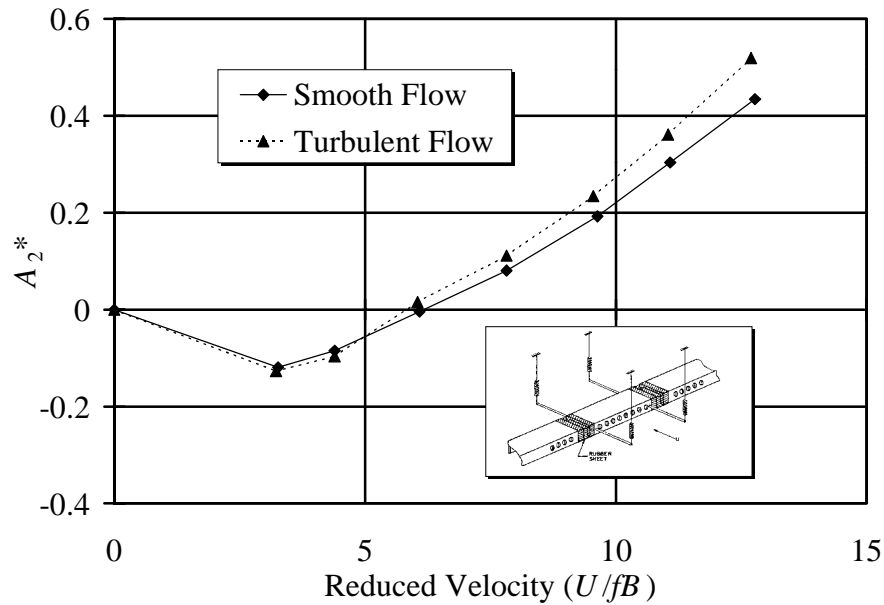


Figure 1-5 Flutter derivative  $A_2^*$  from the simulated trussed deck section model of Scanlan & Lin (1978). The section model is shown in the inset.

Huston (1986) focused specifically on the effects of large incident turbulence length scales on the self-excited forces. Integral scales encountered by a prototype bridge can be several times larger than the bridge deck width, so wind tunnel bridge studies—where the common passive means of turbulence generation produce integral scales that are often the same size or smaller than the deck width—often suffer from scale mismatches.

The approach employed two sets of flapping airfoils—the first set flapped in phase with each other to produce vertical gusting and the other set had adjacent airfoils flapping out of phase with respect to each other to produce horizontal gusting. The two primary flows used in the section-model tests were “neutral,” where the above-mentioned airfoils were held fixed in order to generate a somewhat smooth flow, and “low-pass,”

where a white noise signal, low-pass filtered at 2 Hz, was used to drive both sets of airfoils.

Although Huston employed the term “gusting” over “turbulence” most of the time, it is unclear how closely these gusting flows resemble atmospheric flows. For the neutral mode of operation,  $I_u$  and  $I_w$  were measured to be around 2% while for the low-pass flows, they were 30% and 25%, respectively. Length scales were calculated for the horizontal and vertical velocity fluctuations by finding the frequency associated with the centroids of the respective autospectra. The neutral mode produced horizontal and vertical scales of approximately  $1B$  to  $2.5B$  while the low-pass mode generated vertical scales in the range of  $5B$  to  $12B$  in the horizontal and  $2B$  to  $20B$  in the vertical (the ranges of these values result from the fact that different flow velocities were used in each case). It should be noted, however, that the vertical scale is taken as the *horizontal* correlation of the vertical velocity fluctuation (that is,  $L_{wx}$ ).

Tests on a model of the Golden Gate Bridge deck section, shown in Figure 1-6, yielded the most interesting results. The  $A_2^*$  derivative for this deck showed a significant *destabilizing* change comparing the results in the relatively smooth neutral flow to the results in the large-scale gustiness of the low-pass flow. A positive trend in the  $A_2^*$  values is considered destabilizing because of the resulting negative contribution to damping (as discussed in section 1.2). This result differs with the general conclusion of Scanlan & Lin (1978) but no hypothesis for explaining the difference was or has been offered in the literature.

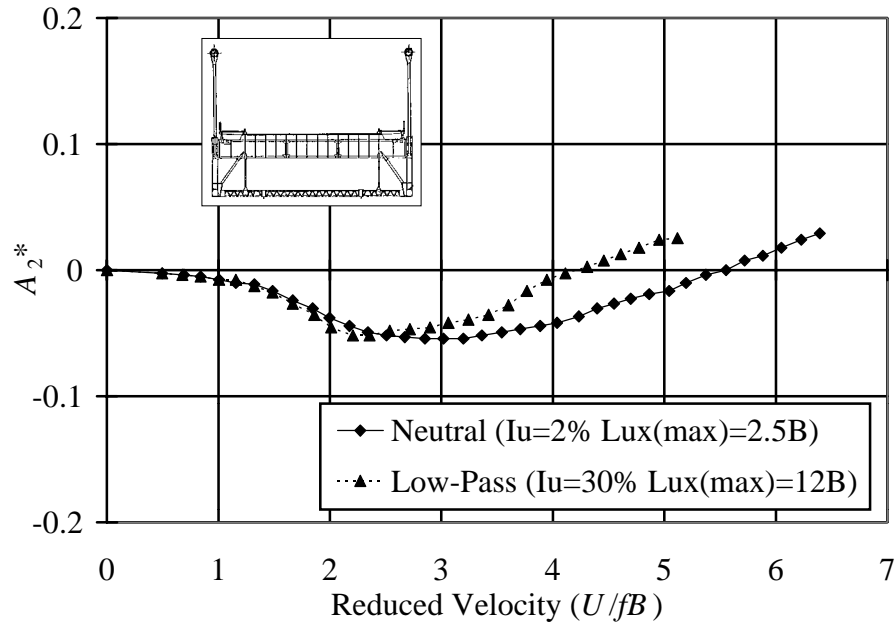


Figure 1-6 Flutter derivative  $A_2^*$  of the Golden Gate deck section in flows generated by the neutral and low-pass modes of Huston's (1986) active turbulence generation mechanism.

The work of Larose, Davenport and King (1993) using a taut-strip model of the Great Belt East Bridge deck section did not focus specifically on the effects of turbulence on self-excited forces, but did show some interesting effects of turbulence on flutter derivatives. This bridge deck, shown with the plot of  $A_2^*$  versus reduced velocity in Figure 1-7, is a closed box girder which behaves more like an airfoil than do trussed girder decks. Values for  $A_2^*$  show similar values for smooth flow and turbulent boundary layer flow while two grid-generated turbulent flows gave significantly different values. In addition, the turbulent boundary layer case showed an increase in the magnitude of the derivatives—especially for the  $A_1^*$  values—while the grid turbulence cases showed a

decrease in magnitude. This differs from the results of Scanlan & Lin (1978) discussed above.

The grid-generated turbulent flows showed decreases in flutter derivative magnitudes for increasing turbulence intensity. However, the fact that the grid 2 flow and the boundary layer flow had similar longitudinal turbulence intensities but significantly different flutter derivatives shows a dependence on parameter(s) other than turbulence intensity. Scales and spanwise coherence were suggested as possible controlling parameters. Understanding these changes from a physical standpoint are difficult when only the flutter derivatives are available.

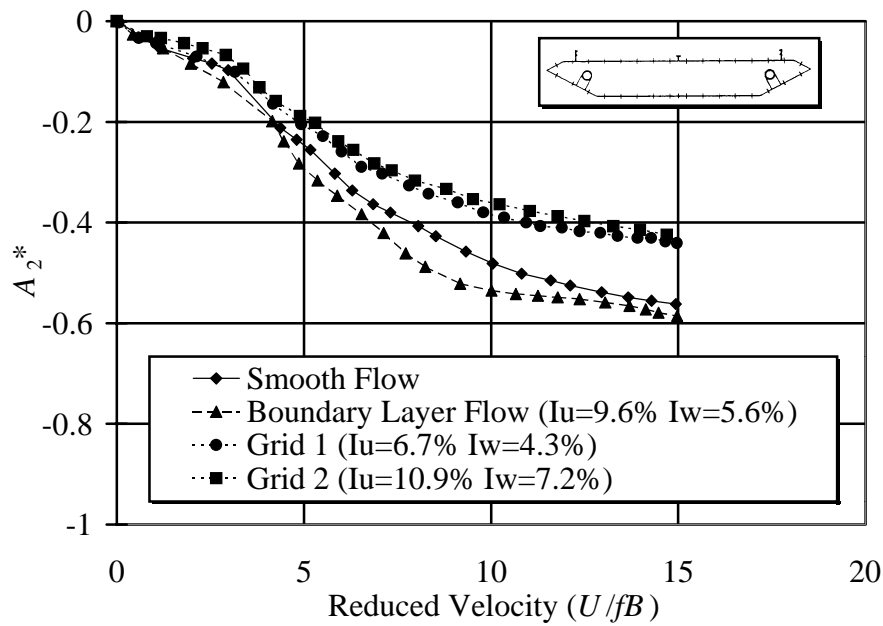


Figure 1-7 Flutter derivative  $A_2^*$  for the Great Belt East Bridge deck section taken from the taut-strip model test results of Larose et al. (1993). The deck model's cross section is shown in the inset.

The difference between smooth and turbulent flow results for full, aeroelastic models of bridges have quite often been illustrated using results from the study of the Lions' Gate Bridge—for example, Irwin & Schuyler (1977). Figure 1-8 (from Scanlan & Wardlaw (1978)) summarizes this work showing the rms response of a single location on the deck of a full, aeroelastic bridge model in both smooth and turbulent flow. A distinct flutter boundary is evident for smooth flow and a gradual rise in response amplitudes without such a distinct flutter boundary is observed for turbulent flow. The figure also shows how well the critical flutter velocity predicted by section model tests of the same deck compared with the full model in smooth flow.

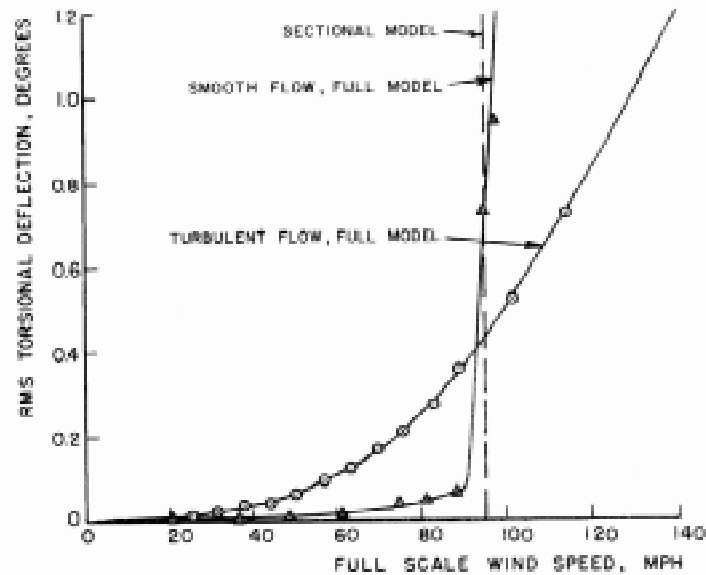


Figure 1-8 RMS response of a full bridge model of the Lions' Gate Bridge in both smooth and turbulent flow. The critical flutter velocity predicted from section model test results is also shown (from Scanlan & Wardlaw, 1978).

Data such as these has led many researchers to conclude that the flutter boundaries found in smooth flow are conservative. The proposed physical explanation for this has

been that turbulent flow reduces the spanwise correlation of the motion-induced forces from their smooth-flow values thus reducing the possibility of unstable motion. Although this hypothesis has been mentioned by a number of researchers, no direct experimental work has addressed this issue. A demonstration of the analytical plausibility of this idea was put forth by Scanlan & Jones (1990) and more rigorously by Scanlan (1997). Scanlan's (1997) approach can be summarized as follows. Consider the single model flutter criterion for a bridge mode for which the twisting motion is dominant. As in section 1.3 using this would be described by comparing the coefficients of  $\dot{\xi}_i$ , the first derivative of the generalized coordinate of mode  $i$ , from equations (1-13) and (1-16) considering only the torsional flutter derivative  $A_2^*$ :

$$\dot{\xi}_i \frac{\rho B^4}{4I_i} \left[ G_{\alpha_i \alpha_i}^{A_2^*(\bar{k}_i)} \right] \geq \frac{\zeta_i \omega_i}{\bar{\omega}_i} \dot{\xi}_i \quad (1-25)$$

where the left hand side of equation (1-25) represents the aerodynamic contribution to damping and the right hand side represents the structural damping. Because the structural frequencies are usually not changed significantly by aerodynamic effects, one can assume that  $\omega_i = \bar{\omega}_i$ . Then, substituting for the  $G_{\alpha_i \alpha_i}^{A_2^*(\bar{k}_i)}$  integral and rearranging, one obtains:

$$\left[ \int_{span} A_2^*(K, x) \alpha_i^2(x) dx \right] \dot{\xi}_i \geq \frac{4I_i \zeta_i}{\rho B^4} \dot{\xi}_i \quad (1-26)$$

Taking the Fourier transform of this equation and multiplying it by its complex conjugate produces:

$$\int_{span} \int_{span} A_2^*(K, x_1) A_2^*(K, x_2) \alpha_i^2(x_1) \alpha_i^2(x_2) dx_1 dx_2 \geq \left[ \frac{4I_i \zeta_i}{\rho B^4} \right]^2 \quad (1-27)$$

A form for the spanwise coherence is then assumed that is similar to that for turbulent velocity coherence as follows:

$$A_2^*(K, x_1)A_2^*(K, x_2) = (A_2^*(K))^2 e^{-c|x_1 - x_2|/L} \quad (1-28)$$

where  $L$  is the bridge span length. It is obvious how the spanwise coherence expression of equation (1-28) will decrease the likelihood of flutter by decreasing the value of the left hand side of the flutter criterion in equation (1-27). This will always be the effect of a diminution of spanwise coherence for a single mode flutter analysis such as this—the effectiveness of the self-excited force is decreased. However, the effects of such spanwise coherence are not so obvious for multi-mode, coupled flutter analyses. While decreases in spanwise coherence may stabilize a deck by reducing negative damping effects, it may also destabilize a deck by reducing favorable damping. The impact of such effects will become more important as bridges with longer spans are designed and multi-mode flutter becomes more probable.

As mentioned above, the spanwise coherence of self-excited forces has never been addressed experimentally before. Experimental work is needed to understand the role that turbulence plays in the spanwise coherence of the self-excited forces not only for the analysis of flutter susceptibility but also for the analysis of buffeting—specifically, how mode coupling and damping are affected by changes in the spanwise behavior of the aeroelastic forces.

The influence of nonlinear effects is another topic requiring further research. The flutter analysis techniques described in section 1.3 are linear. They are based on a linearization of nonlinear aerodynamic phenomena. Their frequency dependent coefficients are experimentally determined for bodies oscillating with small

displacements—essentially a linearization around a specific set of parameter values. This approach captures the nonlinear effects without an explicit nonlinear model.

Studies related to the Messina Straits crossing project (connecting the island of Sicily to the Italian peninsula) have illustrated the importance of nonlinear aerodynamic loading (Diana et al., 1993, 1998, 1999; Falco et al., 1992). Structural changes necessary to extend bridge spans from current distances of 1990m to the 3300m to required cross the Messina Straits complicate the aerodynamic properties of bridges. Therefore experimental investigation of such nonlinear aerodynamic properties is necessary along with complementary analytical techniques to incorporate such data into bridge response estimates. Chen et al. (2000a) have developed a time domain analytical model which incorporates nonlinearities of both structural and aerodynamic origin. An important aspect of this particular approach is that flutter and buffeting analysis is performed simultaneously rather than separately—like the frequency domain approach described in section 1.3. This allows interaction between the response induced by buffeting and that induced by self-excited forces. Without such interaction, importance sources of nonlinear effects are ignored.

In terms of experimental work needed, it is logical to extend the linearization already practiced to a wider range of parameters to gain insight into where nonlinear effects manifest themselves. Analysis with extended linearization means that functions such as flutter derivatives need to be identified for a range of parameters such as angle of attack and vibration amplitude. This type of analysis will show where superposition of aerodynamic loads is warranted, where nonlinearities exist, and hopefully, what nonlinear models might describe the behavior.

Where the flutter derivatives given in equations (1-7) and (1-8) are given only as a function of  $K$ , the larger aerodynamic problem is nonlinear with dependence on a greater number of parameters. This nonlinear dependence might give the flutter derivatives the following representation:

$$H_i^* = f(K, \bar{\alpha}, \alpha_0, h_0, I_i, L_{ij}, S_i) \quad (1-29)$$

$$A_i^* = f(K, \bar{\alpha}, \alpha_0, h_0, I_i, L_{ij}, S_i) \quad (1-30)$$

where  $\bar{\alpha}$  is the average angle of attack of the motion,  $\alpha_0$  is the amplitude of the torsional motion,  $h_0$  is the amplitude of the heaving motion, and  $I_i$ ,  $L_{ij}$ , and  $S_i$  are the turbulence intensity, integral length scale in the  $j^{th}$  direction, and small-scale spectral density parameter of the  $i^{th}$  component of velocity, respectively. A similar parametric study was proposed by Huston (1986) who suggested that an appropriate experimental program might be useful to determine whether the motion-dependent forces are simple functions of the turbulence statistics.

An important application for the work of this study is to improve numerical predictions of bridge responses. Current numerical efforts can be divided into two main groups. The first group attempts to model the actual flow about bridge decks (for a review of computational fluid dynamics in general see Murakami & Mochida, 1999; for an example of the use of discrete vortex simulation, see Larsen & Walther, 1997). These approaches hold great promise as design tools, but prediction accuracy and computational resource requirements remain as significant difficulties to be overcome. An experimental effort such as the current work adds to the base of knowledge from which such methods can be validated.

The second group does not employ traditional CFD methods but rather attempts use experimentally-obtained aerodynamic coefficients and generate stability predictions for a number of turbulent flow scenarios (Beliveau et al., 1977; Lin, 1979; Lin & Ariaratnam, 1980; Tsiatas & Gasparini, 1987; Bucher & Lin, 1988; Tsiatas & Sarkar, 1988; Lin & Li, 1993; Shinozuka & Billah, 1993; Billah & Shinozuka, 1994; Bartoli et al., 1995; Li & Lin, 1995; Pandey & Ariaratnam, 1998). The common thread running through each of these studies is that of modeling the inflow turbulence as a random dynamic pressure. This means replacing  $q = \frac{1}{2} \rho U^2$  with  $q = \frac{1}{2} \rho (U + u(t))^2$  in equations (1-7) and (1-8) where  $u(t)$  is a random variable with characteristics matched to those of the relevant turbulent flow.

Although different researchers may handle the mathematics differently, what is lacking in each is a complete representation of the effects of different scales. While a random dynamic pressure may capture large-scale turbulent fluctuations adequately it cannot include the effects of the smaller scales changing the fundamental flow structure and pressure producing mechanisms. In one of the first attempts at stochastic analysis of the flutter problem in turbulent flow, Y.K. Lin (1979) acknowledges this in the following:

Another important assumption used in the analysis is that the scale of turbulence in the wind is much larger than the lateral dimensions of the bridge. In such a case the flow pattern around the bridge is expected to be similar to that associated with a nonturbulent flow. However, if the turbulence scale is of the same order of magnitude or even smaller than the lateral dimensions of the bridge, the flow pattern, and thus the lift and drag curves, can change greatly.

Thus, the change in flow structure caused by turbulence is not entirely understood and better insight into this phenomenon could be of fundamental importance to stochastic modeling efforts of this type.

## 1.5 Outline for the rest of the dissertation

Inconsistencies such as those mentioned in the previous section exist perhaps because so few studies have been done of the mechanics of how turbulence affects the motion-induced forces on a bridge deck. While several bridge decks have been examined in smooth and a variety of turbulent flows, few studies have been done to understand mechanisms causing the differences. To pursue such an understanding, this dissertation proceeds as follows. Chapter 2 summarizes the approach taken in the current work to address the motivating issues raised in this chapter. This summary includes some discussion of the literature on the effects of turbulence on generic bluff body flow structure and how this work guided the research into motion-induced forces. Chapter 3 outlines the experimental equipment used to implement the work of chapter 2 including the turbulence-generation techniques, the design of the model and its accompanying motion-driving mechanisms, and the velocity and pressure measurement methods.

Chapter 4 presents the velocity measurement data including statistical characteristics of each incident flow used in this study. Results of pressure measurements on stationary models are reported in Chapter 5. These results were used to validate the system integrity, place the current measurements in the context of the existing literature concerning stationary rectangular cylinders, and develop a preliminary picture of the flow

structure about a rectangular cylinder that would be useful for interpreting the results of subsequent dynamic tests. Chapter 6 contains sectional pressure data from dynamic tests. These data include force and pressure spectra, pressure amplitude and phase distributions, flutter derivatives, and other statistical distributions. Spanwise coherence and correlation results are presented in chapter 7.

Although only chapter 8 is formally called a “discussion” chapter, each chapter containing results contains a certain amount of commentary which, when taken as a whole, builds a picture of the “anatomy” of the effects of turbulence on bridge aerodynamics. Chapter 8 brings all of the former three chapters of results together into a more complete picture. Chapter 9 summarizes the major conclusions of the work and proposes research goals for future study.

## CHAPTER 2. APPROACH AND BACKGROUND

The current approach addresses the issues raised in Chapter 1 with a wind tunnel model equipped with a large number of pressure taps, oscillating in a series of smooth and turbulent flow. This chapter describes the approach taken in this project to experimental bridge aerodynamics analysis and then summarizes existing literature on bluff body aerodynamics as background. The synopsis of the approach provided here is an introduction to the various components of the work—each of which will be dealt with in greater depth in subsequent chapters.

### 2.1 The Current Approach

For this study of the effects of turbulence on bridge decks, a section model and accompanying motion-driving mechanisms were constructed. The specifications of this equipment relate back to the problem motivation in Chapter 1. Streamwise pressure distributions were measured—rather than total force—to allow examination of the *anatomy* of the aerodynamic forces rather than just their integrated effects. Pressure taps were arranged to allow measurement of pressures at two spanwise positions simultaneously. Quantifying the spanwise coherence of buffeting and self-excited forces on an oscillating model was thus possible. This study represents the first such study of the spanwise coherence of self-excited forces on oscillating bridge models.

At the outset, one must recognize the host of length scales present in this flow-structure interaction problem. Complex interactions between these fluid and structural scales underlie the measured aerodynamic quantities.

Fluid scales include the thickness of the shear layer and the reattachment length. Scales in the incident turbulent flow include the largest and smallest scales that are present—often quantified using the turbulence integral scales and a small-scale spectral density parameter, respectively. Structural scales include not only the overall dimensions of the bridge deck—it's vertical height, streamwise width, and spanwise length—but also dimensions of various structural members such as trusses, guard rails, and traffic barriers. Even smaller scales are present in terms of surface roughness of the bridge components. For example, the road surface, the presence of railroad tracks, and the use of gratings all play a role in the development of the overall flow structure.

The relative importance of each of these scales is worthy of study, but differentiating the effects of individual scales is problematic. One example of this difficulty is found when trying to identify the effect of turbulence scale while holding turbulence intensity constant. Holding the turbulence intensity constant requires that any increase in, say, large-scale turbulent energy be balanced by decreases in the energy content of different scales. Aerodynamic structure changes resulting from these changes cannot be attributed exclusively to the large-scale increase or the small-scale decrease.

To focus on flow mechanisms without the complexities of actual bridge deck shapes, a rectangular cross section with a smooth surface was studied. This eliminated most of the structural length scales—all but the overall dimensions. The relative importance of every fluid scale, as mentioned above, was not differentiated. Rather,

various flow scales were quantified and reported to provide an overall picture of the various flow scenarios. Further details of these flow parameters are provided in Chapter 4. Detailed studies of each scale's effect would require specialized experiments beyond the scope of this study.

A model of rectangular cross section ( $B/D = 6.67$ , where  $B$  is the streamwise dimension and  $D$  is the frontal dimension of the body) was chosen for two main reasons. It was chosen, as mentioned above, to reduce the number of length scales involved and study flow mechanisms without the geometric complexities of actual bridge decks. It was also chosen to take advantage of the large amount of literature relating to the aerodynamics of rectangular shapes. Because a significant portion of the lift generated over a bridge deck can be attributed to mechanisms involving separated flows, a bluff body with rectangular cross section was used to examine the effects of turbulence on flow structures involving separated flows. Subsequent phases of this work will involve actual bridge deck sections.

To test a wide range of dynamic conditions, the motion driving mechanism designed and built was capable of driving pitching and plunging motions with variable amplitudes at changing mean angles of attack. In this, the first project with this equipment, testing consisted of torsional motion at zero-mean angle of attack. Full integration of all the dynamic capabilities of the system will require further work beyond the scope of this project.

Observing the effects of turbulent scale required that a series of turbulent flows be generated having constant turbulence intensity and varying integral scales. Tests were conducted in each turbulent flow, and analysis techniques were developed to track the

turbulence-induced changes in the unsteady forces. One such technique was the identification of the amplitude and phase of the self-excited pressure signals at each streamwise location. What follows is a brief derivation of this approach and how it also produces conventional flutter derivatives for comparison with the literature.

Rather than extract flutter derivatives directly from free-vibration data, this method obtains streamwise pressure amplitude and phase distributions from forced oscillation experiments. This approach is similar to that of Matsumoto et al. (1996). While these distributions can be integrated to provide conventional flutter derivatives, they also provide insight into the mechanisms involved in the turbulence effects.

The amplitude and phase distributions for the surface pressures are defined according to the following equations. For torsional motion described in terms of the angular position,  $\alpha$ , in equation (2-1), each position along the model has a pressure fluctuation at the model oscillation frequency described by equation (2-2).

$$\alpha(t) = \alpha_0 \cos(2\pi f_\alpha t) \quad (2-1)$$

$$C_p(x, t) = -\alpha_0 C_p^*(x) \cos(2\pi f_\alpha t - \psi(x)) \quad (2-2)$$

where  $\alpha_0$  is the oscillation amplitude,  $f_\alpha$  is the model's torsional oscillation frequency,  $C_p(x, t)$  is the pressure fluctuation function (normalized by the dynamic pressure), and  $\psi(x)$  is the phase defined as the lag between the maximum angle of attack and the maximum negative pressure at a specific location,  $x$ . These quantities are illustrated in Figure 2-1 where the pressure signal is shown together with the angular displacement of the model.

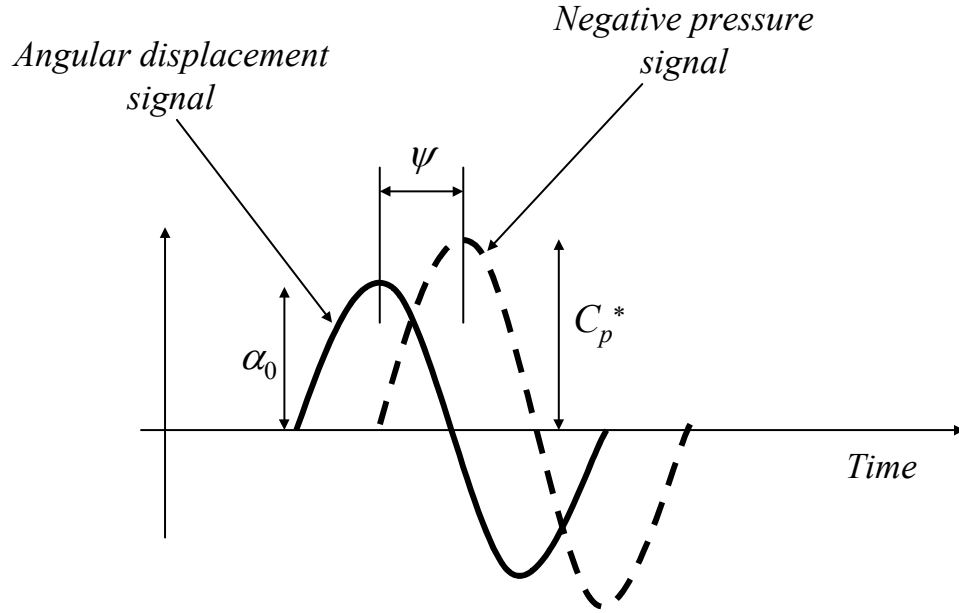


Figure 2-1 Illustration of the definitions of pressure amplitude,  $C_p^*(x)$ , and pressure phase,  $\psi(x)$ , with respect to the body oscillation.

The amplitude of these pressure fluctuations are given in terms of a pressure coefficient,  $C_p^*(x)$ , defined according to equation (2-3).

$$C_p^*(x) = \frac{p^*(x)}{q\alpha_0} \quad (2-3)$$

where  $p^*(x)$  is the amplitude of the pressure fluctuation,  $q$  is the dynamic pressure, and  $\alpha_0$  is the amplitude of the angular oscillation.

Integrating the pressure function, (2-2), over the surface can render the self-excited moment as follows:

$$M_{se}(t) = -q\alpha_0 \int_{-b}^b 2C_p^*(x) \cos(2\pi f_m t - \psi(x)) dx \quad (2-4)$$

Substituting  $x^* = x/b$  and rearranging terms yields:

$$M_{se}(t) = qb^2 \left[ -\alpha(t) \int_{-1}^1 2x^* C_p^*(x^*) \cos \psi(x^*) dx^* + \frac{\dot{\alpha}(t)}{\omega_m} \int_{-1}^1 2x^* C_p^*(x^*) \sin \psi(x^*) dx^* \right] \quad (2-5)$$

The expression for the self-excited lift,  $L_{se}(t)$ , is derived similarly. With self-excited lift and moment defined according to equations (1-7) and (1-8), respectively, torsional motion flutter derivatives can be derived from the amplitude and phase distributions using equations (2-6) through (2-9) as follows:

$$A_2^* = \frac{1}{2k^2} \int_{-1}^1 x^* 2C_p^*(x^*) \sin \psi(x^*) dx^* \quad (2-6)$$

$$A_3^* = \frac{-1}{2k^2} \int_{-1}^1 x^* 2C_p^*(x^*) \cos \psi(x^*) dx^* \quad (2-7)$$

$$H_2^* = \frac{1}{2k^2} \int_{-1}^1 2C_p^*(x^*) \sin \psi(x^*) dx^* \quad (2-8)$$

$$H_3^* = \frac{-1}{2k^2} \int_{-1}^1 2C_p^*(x^*) \cos \psi(x^*) dx^* \quad (2-9)$$

where  $k$  is the reduced frequency defined as  $k = \omega_\alpha b / U$  where  $\omega_\alpha = 2\pi f_\alpha$ .

Pressure amplitude and phase as defined above are discussed at length in subsequent chapters. They complement the statistical and spectral analysis also presented for the unsteady pressures developed by various turbulent flows. The large amount of work done for bluff bodies of rectangular cross section provided a foundation from which the above analysis could extend. This literature is briefly summarized in the following section.

## 2.2 Background of Bluff-Body Aerodynamics

Civil engineering structures provide a wide variety of applications for bluff body aerodynamics. Because bridges and buildings often have rectangular shapes, a large amount of wind tunnel work has been done studying varieties of rectangular bodies and the shear layers separating from them. Most of this work has been done for stationary bodies, but some has been for such prisms in motion. Because this study of turbulence effects on bridge aerodynamics employs a rectangular cylinder, relevant results from the literature are highlighted here. A brief outline of bluff body flow structure about a rectangular body will be followed by a presentation of relevant parameters and a summary of the effects of these parameters on quantities of aerodynamic interest.

To aid the description of parameters and definitions in this summary of bluff-body flow structure, Figure 2-2 shows a schematic diagram of flow over a body with rectangular cross section. The separated shear layers are the most important components of this flow. Shear layers separate from the sharp leading edges, roll up periodically to form vortex-like structures, and usually reattach near some distance,  $x_R$ , downstream. Although this reattachment is highly unsteady—the line in the diagram represents only a time mean separating streamline—it separates the surface of the body into regions of mostly separated and mostly attached flow. The pressure distribution has large negative values in the separated region (i.e. the “separation bubble”) and recovers to much higher pressures downstream of reattachment.

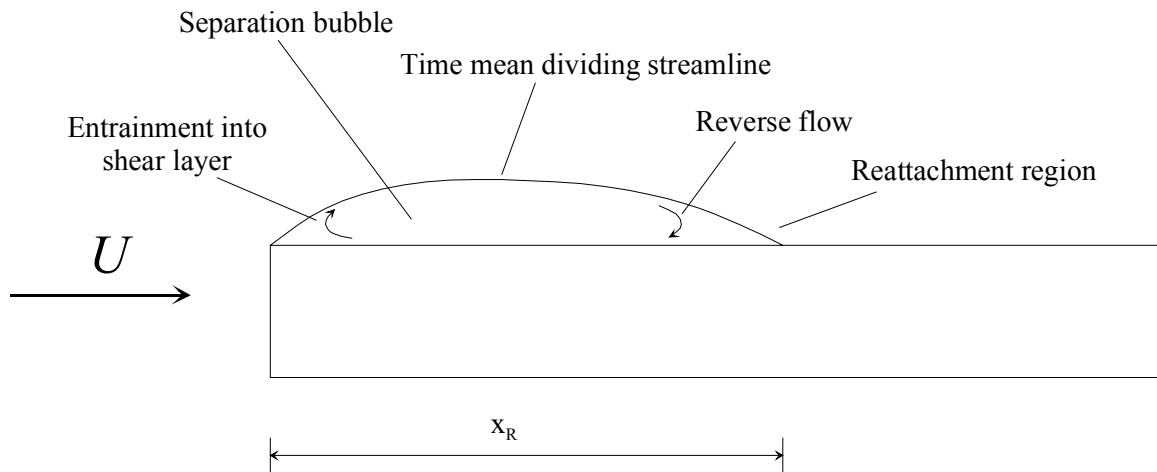


Figure 2-2 Schematic illustration of flow separation and the resulting pressure field around a bluff body with rectangular cross section.

Plotting various statistical distributions of surface pressures versus streamwise position provides insight into the physics of the flow structure. In fact, such distributions are the most common method of tracking turbulence-induced changes in the flow structure. Mean pressure distributions map out the approximate region of separation with large negative pressures within the separation bubble. Saathoff & Melbourne (1989) report that in smooth flow the maximum in the rms pressure distribution is located approximately at the reattachment line. This maximum moves a bit upstream of the reattachment line for turbulent incident flows.

Distributions of the peak pressures give a measure of the greatest pressure magnitudes experienced at any single point. The upstream portion of the separation bubble experiences the largest peak pressures. Saathoff & Melbourne (1989, 1997) attribute this to the rolling up of the separated shear layer into a vortex that causes large negative pressures on the surface beneath it. This phenomenon occurs in both smooth and turbulent flows but creates stronger vortices in turbulent flow. Examining the distribution

of the skewness of the pressure signals at various streamwise locations complements the observations of the peak distribution. Negatively skewed signals correspond to the region near the maximum peak pressures. Nearer the reattachment point, positively skewed pressures occur, which Kiya & Sasaki (1983) suggest is indicative of irrotational fluid from outside the separation bubble crashing down into the surface with the reattaching shear layer.

Studying how turbulence affects the pressure distributions around bluff bodies requires quantification of the turbulence itself. A number of parameters are used for this purpose. Although the importance of the Reynolds number,  $Re$ , will be discussed later, the relevant length scale for its calculation is the frontal dimension of the body,  $D$ . Turbulence intensity, defined as the rms value of a particular velocity component's fluctuation normalized by the mean free stream velocity,  $U$ , is a measure of the total energy of the turbulent fluctuations. Researchers most often report longitudinal turbulence intensity,  $I_u$  because it is the easiest to measure with a hot wire anemometer. For this same reason, the longitudinal integral scale,  $L_{ux}$ , is most often reported as a measure of the average size of the turbulent "eddies." An integral scale,  $L_{ij}$ , is a measure of the dimension in the  $j^{th}$  direction of the eddies  $i^{th}$  responsible for the fluctuations of the  $i^{th}$  velocity component. The autocorrelation coefficient function calculated from a time series of longitudinal velocity fluctuations (again, easily measurable with a hot wire anemometer) can be transformed using Taylor's approximation (Hinze (1959)) into a spatial correlation function. The area under this function is a measure of  $L_{ux}$ .

Spectral shape information—how the energy of a flow is distributed over its various scales—is not often reported in either bridge or bluff body studies. Although the

integral scale—the largest scale present in a flow—is often the only measure of scale reported, research has suggested that energy at smaller scales may be more effective at causing the effects attributed to turbulence in general. A parameter to gage the small-scale content of a turbulent flow is the small-scale spectral density parameter first proposed by Melbourne (1979) and used subsequently by Tieleman & Akins (1990). It is defined as follows:

$$S_u = \frac{fG_{uu}(f)}{U^2}(10^6) \quad (2-10)$$

where  $G_{uu}$  is the power spectral density of the longitudinal velocity fluctuations and  $f$  is the frequency of these fluctuations. This useful parameter is essentially a *scale-specific* turbulence intensity in which the scale is selected with an appropriate value of the parameter  $a$ . In the frequency relation,  $f = aU/D$ ,  $a$  is chosen as an appropriate ratio to the body dimension,  $D$ . Work by Gartshore (1973), Melbourne (1979), Bearman & Morel (1983), and Tieleman & Akins (1990) have emphasized the effectiveness of scales on the order of the thickness of the separated shear layer (which is estimated to be approximately  $D/10$ ) at altering shear layer behavior.

The role of turbulence in the aerodynamics of stationary bluff bodies has been extensively documented in the literature (e.g., Gartshore, 1973; Lee, 1975; Kareem & Cermak, 1979; Hillier & Cherry, 1981; Bearman & Morel, 1983; Nakamura & Ohya, 1984; Kiya & Sasaki, 1983, 1985; Nakamura & Ozono, 1987; Saathoff & Melbourne, 1989, 1997; Kareem, 1990; Nakamura, 1993; Li & Melbourne, 1995; and others). Past research into how turbulence affects the bluff-body flow structure illustrated in Figure 2-2 will now be summarized. Numerous researchers have studied the effects of

turbulence on flows over bluff bodies with rectangular cross sections. Some studies have involved finite afterbodies and some have involved afterbodies of sufficient length—i.e. “infinite” length—to eliminate interaction between the two separated shear layers and to allow study of the separation/reattachment structure exclusively. Data discussed here will include that measured from bodies with “infinite” afterbodies because of the similarity to data from bodies with a sufficient minimum afterbody length ( $4 \leq B/D \leq 6$ ). Because most research in this field has reported only longitudinal turbulence intensities and integral scales, these are the only values referred to in most of this summary. In addition, the terms “turbulence intensity” and “integral scale” will refer to the longitudinal values unless otherwise indicated.

Mean and rms pressure distributions are the two most commonly measured quantities for flow over rectangular bluff bodies. Examples of such distributions for a blunt flat plate—i.e. a rectangular prism with an “infinite” afterbody—from Li & Melbourne (1995) are plotted in Figure 2-3. These distributions exhibit a basic hump shape that is typical of a flow with a separated region followed by reattachment. Increases in turbulence intensity alter mean pressure distributions in two basic ways that have been reported by many number of researchers (e.g. Hillier & Cherry, 1981; Kiya & Sasaki, 1983; Saathoff & Melbourne 1989, 1997; and others). Greater values of  $I_u$  increase the maximum negative pressure experienced on the surface and cause an upstream “shift” in the flow structure. The maximum value occurs closer to the leading edge while the pressure recovery downstream of the maximum becomes steeper. While most researchers have found little effect of integral scale on mean pressures for scales up to  $2D$ , Li & Melbourne (1995) found that scale effects increase in flows of greater

turbulence intensity. Their work, along with that of Nakamura & Ozono (1987) testing values up to  $24D$ , shows that as  $L_u$  increases beyond  $2D$  the trend described above reverses. Instead of greater magnitudes and steeper recoveries, the pressures have smaller magnitudes and more gradual recoveries—a trend toward the distributions observed for smooth flows. One explanation put forth is that turbulent flows with extremely large integral scales behave similarly to smooth flows with slowly varying velocities that are not able to alter the mean flow structure.

Examples of rms pressure distributions are plotted in Figure 2-4. The basic shape of the rms pressure distributions feature an upstream “shift” similar to that observed in the mean pressure distributions. Greater turbulence intensities result in rms pressure distributions with maximum values occurring nearer the leading edge. While this shift does not seem to be significantly affected by scale, the rms values of these distributions increase with both intensity and scale. The most significant increases occurred in the hump region near the leading edge. Like the mean pressures, the rms pressures were increased by turbulence scale increases more dramatically in flows of greater intensity. However, Li & Melbourne (1995) reported that these increases occurred only for scale less than approximately  $3.8D$ . Beyond these scales, no further increase in the rms values was observed (up to integral scales of  $10.2D$ ).

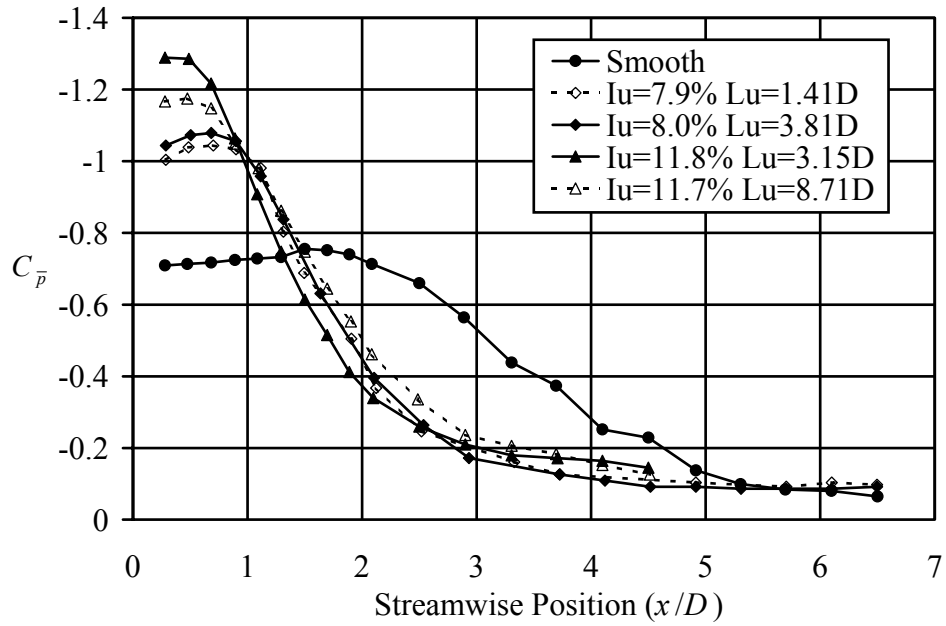


Figure 2-3 Streamwise distribution of mean pressure coefficient for smooth and turbulent flows about a blunt flat plate with “infinite” afterbody (from Li & Melbourne, 1995).

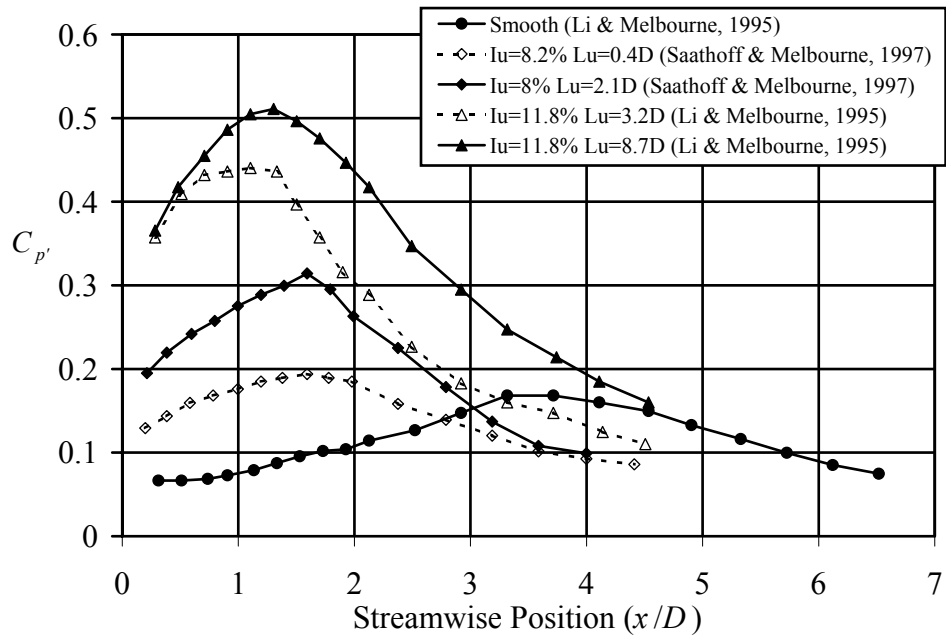


Figure 2-4 Streamwise distribution of rms pressure coefficient for turbulent flows about a blunt flat plate with “infinite” afterbody.

The shift in the statistics described above is accompanied by a shift in the reattachment point. In smooth flow, the mean reattachment point is located near  $4.4D$  and moves upstream with increasing turbulence intensity—near  $2.4D$  for  $I_u = 8\%$ . Figure 2-5 displays reattachment length data from Saathoff & Melbourne (1997). Reattachment is often observed using oil surface-flow visualization—using the upstream and downstream motion of the oil to identify a mean reattachment point within a reattachment zone. Kiya & Sasaki (1983, 1983a) supplemented this technique using a split-film probe to monitor reverse-flow intermittency near the surface. By measuring the integral scales of vortices in the reattachment zone they found that the size of the zone scales with the size of these vortices. Their measurements of surface pressure spectra in the reattachment zone showed a shift in energy from large scales to smaller scales with increased turbulence intensity. Kiya & Sasaki (1983) also observed that pressures in the reattachment zone exhibited a positive skewness. Probability density functions (PDF's) of pressure signals in separated regions are in general negatively skewed. The positive skewness of the reattachment zone was postulated is due to the flux of outer irrotational fluid toward the surface (Kiya & Sasaki, 1983).

Physically, the shifts in the mean and rms pressure distribution are associated with increased curvature of the separating shear layer. As already described, a shorter reattachment length accompanies this increased curvature. A number of researchers have attributed these shear layer behavior changes to the increased entrainment of the shear layer due to free stream turbulence (Gartshore, 1973; Bearman & Morel, 1983; Kiya & Sasaki, 1983). Enhanced entrainment draws more fluid out of the separation bubble thus lower pressure within the bubble and shortening the reattachment length. Employing

pulsed-wire anemometry in the separation bubble of a flat plate normal to the free stream (with a long splitter plate), Castro & Haque (1987, 1988) found that entrainment from the separation bubble is, in fact, increased with increased free stream turbulence.

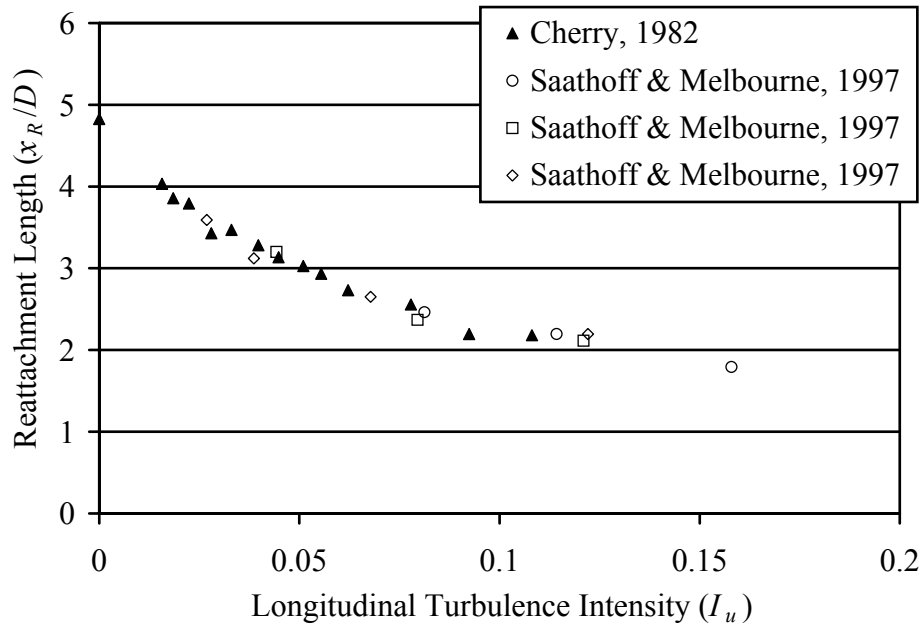


Figure 2-5 Reattachment length versus longitudinal turbulence intensity for a blunt flat plate.

Negative peak pressure magnitudes generated beneath the separated shear layers of bluff bodies also has engineering significance—both for estimating maximum structural loads and for understanding the flow physics. Saathoff & Melbourne (1989, 1997) have studied these maximum pressures for blunt flat plates. Their work shows that the maximum peak pressures occur near  $0.25x_R$ —thus showing the familiar “shift” toward the leading edge observed in the mean and rms distributions. The values of the peak pressures increase with both turbulence intensity and integral scale.

Using flow visualization obtained simultaneously with surface pressure signals, Saathoff & Melbourne (1997) observed that peak pressures occurred when a strong vortex was formed from the rolling up of the separating shear layer. It was hypothesized that incident turbulence modifies this process by controlling the perturbations of the shear layer that create the vortices. Higher turbulence intensities create stronger perturbations of the shear layer creating larger vortices. Larger vortices generate greater pressure magnitudes. Larger turbulence scales were hypothesized to increase the time of the perturbation thus increasing the total amount of shear layer vorticity entrained into the vortices.

The same mechanism hypothesized for the increase in peak pressures also contributes to the increased spanwise correlation of surface pressures—that is, increased strength of vortices shed from the leading edge shear layers corresponds to greater organization in the spanwise direction. Saathoff & Melbourne (1995, 1997) found spanwise correlations to increase with integral scale. This was not a new finding. A number of researchers have studied the relationship between incident flow scales and the spanwise pressure correlations measured on bluff bodies. In addition to the work of Saathoff & Melbourne, Sankaran & Jancauskas (1993) and Kimura et al. (1996) have studied spanwise pressure correlation on rectangular cross sections. Larose et al. (1993) and Larose & Mann (1998) have studied spanwise force correlation on bridge deck sections. In each case, it is reported that as incident turbulent scales increase, spanwise coherence increases. Perhaps more importantly, turbulent scales greater than some minimum produced spanwise surface pressure coherence greater than that of the incident flow. Because spanwise correlations play such an important role in gust loading of

structures and in the extrapolation of section model results to full scale, turbulence effects on the correlation of pressures along the span must be understood. Again, it should be mentioned that the above studies of spanwise coherence and correlation were all conducted on stationary bodies.

With respect to turbulence scales, two items are worthy of mention before proceeding. As mentioned previously, the work of Gartshore (1973), Melbourne (1979), Bearman & Morel (1983), and Tieleman & Akins (1990) have emphasized the effectiveness of scales on the order of the thickness of the separated shear layer. In particular, Gartshore (1973) showed that a small rod upstream of the stagnation streamline of a bluff body was sufficient to produce drag behavior similar to that of bodies in grid-generated turbulent flow. The relative importance of the various turbulent scales would be valuable knowledge when planning an experiment.

Quantifying the relative importance of turbulent scales is problematic. To isolate the effect of scale, one should keep the turbulence intensity constant. With turbulence intensity constant, however, increases in the energy associated with large scales must be offset by decreases in small-scale energy. As a result, flow structure changes due to large-scale energy increases cannot be differentiated from changes due to small-scale energy decreases. With this in mind, the approach taken for this project was to report all such scales and refrain from assigning causal relationships between specific scales and specific aerodynamic effects.

With this background of the current approach and of turbulence effects on bluff body aerodynamics as a foundation, subsequent chapters of this dissertation will describe this project in detail.

## CHAPTER 3. EXPERIMENTAL SETUP

This chapter describes the equipment used in the present study including the facilities, the model and its motion-driving system, the computer data acquisition system, and all relevant instrumentation.

### 3.1 The Atmospheric Wind Tunnel

Both the atmospheric wind tunnel and the turbulence-generation equipment are described in this section. The basic layout of the atmospheric wind tunnel is shown in Figure 3-1 below. A 5 ft. by 5 ft. by 49 ft. open-return test section is connected to a centrifugal fan powered by a 30 hp motor. Air entering the inlet passes through two anti-turbulence screens and a set of flow straighteners, through a 3.48:1 contraction section and, finally, through an additional set of flow straighteners. The turbulence intensity of the resulting flow in the test section is less than 0.5%.

Turbulent flows were generated using conventional biplane, square-mesh grids. Constructed of wood, these grids each had a solidity ratio of 0.32 (where solidity ratio is the projected solid area of the grid per unit total area) but had mesh sizes of 7.5 and 21.25 inches (where mesh size,  $M$ , is the center to center distance of the grid bars). The smaller and larger mesh grids were constructed from conventional 2x2 and 2x6 lumber, respectively (the actual dimensions of 2x2's are 1.5 in. by 1.5 in. while the dimensions of 2x6's are 1.5 in. by 5.375 in.). Grids of different geometries at various distances upstream

of the model generated a wide range of turbulence parameters. Figure 3-1 indicates the grid positions used in this study. The smaller-mesh grid generated an  $I_u = 6\%$  and an  $I_u = 12\%$  case using the two grid positions closest to the model —  $x = 14.1M$  and  $x = 6.67M$ , respectively. The larger-mesh grid generated  $I_u = 6\%$  and  $I_u = 12\%$  cases from the two further grid positions —  $x = 21.9M$  and  $x = 13.5M$ , respectively. Chapter 4 will present velocity measurements and a complete analysis of these four turbulent flows.

Figure 3-1 also shows that this wind tunnel is equipped with a “turbulence generating box” where turbulence can be generated using lateral jets (as shown in the figure). This technique was not employed for the present study.

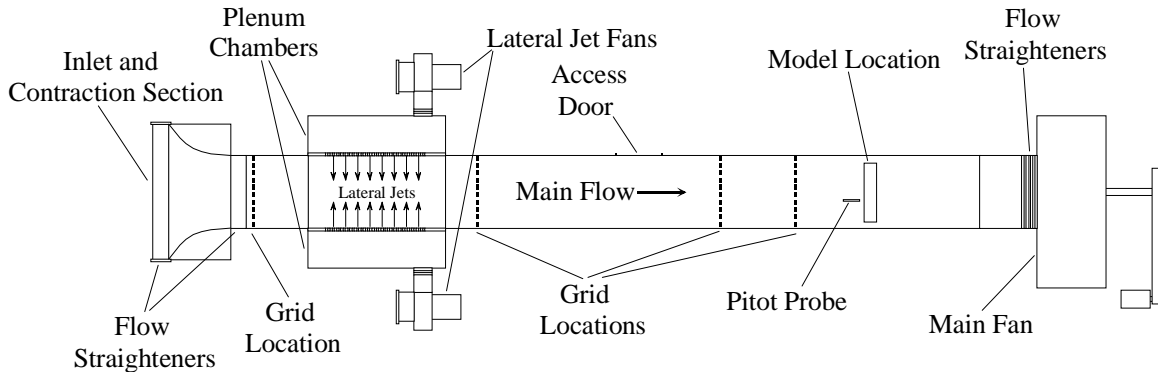


Figure 3-1 Top view schematic diagram of the atmospheric wind tunnel (dimensions are to scale).

### 3.2 Model

All pressure measurements were made on a model having a rectangular cross section. Constructed of Plexiglas, the model had a frontal height,  $D$ , of 1.5 in., a streamwise width,  $B$ , of 10 in., and a span,  $L$ , of 42 in. End plates of height  $7D$

extended  $2.5D$  and  $5D$  from the model's leading and trailing edges, respectively. A drawing and a picture of the model are shown in Figure 3-2. The top face of the model is fixed in place with screws and is removable to allow for placement and connection of pressure sensors and tubing.

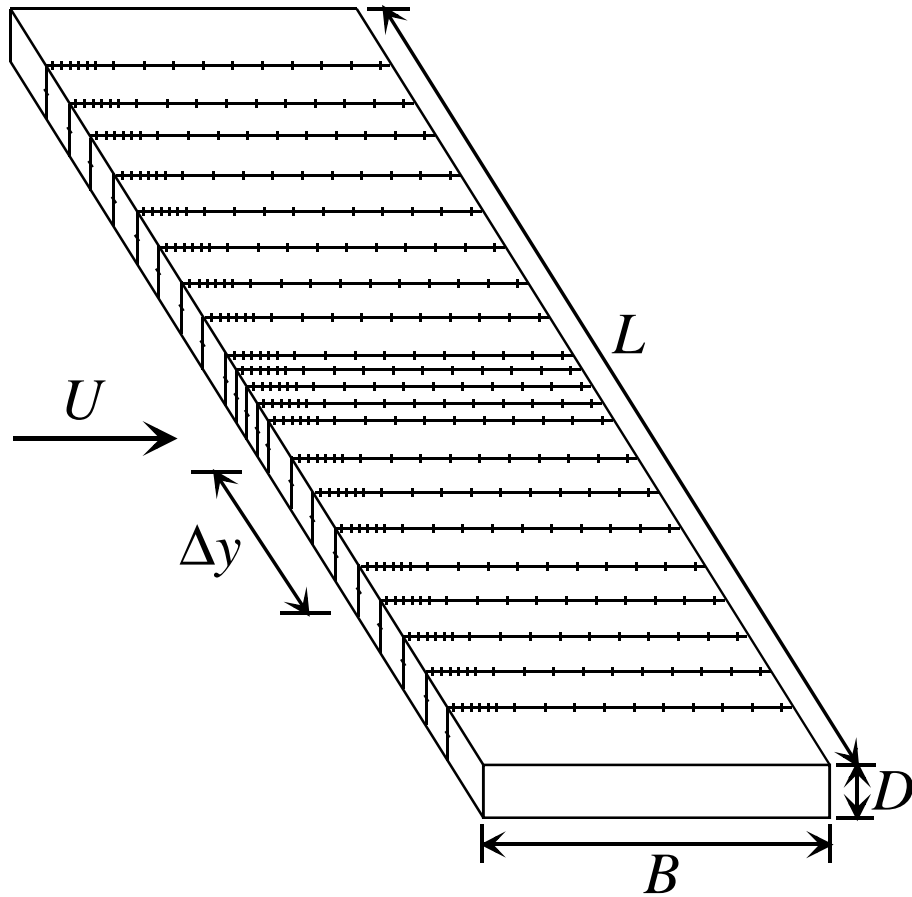


Figure 3-2 Diagram showing the layout of pressure taps on the surface of the model.

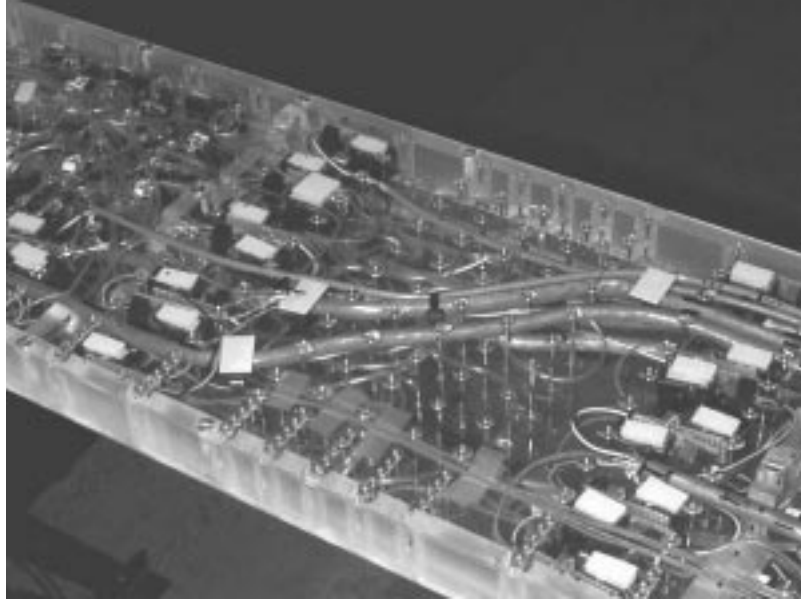


Figure 3-3 Photograph of the upper surface of the model. Through the upper surface, the pressure taps, pressure transducers, and all associated wiring is visible.

Figure 3-2 shows the locations of a large number of pressure taps on the model's surface. Twenty-one streamwise sets of taps were distributed across the span—both top and bottom. The middle five rows are separated by 1 in. while the outer rows have a 2 in. separation. Each row consists of 32 taps—16 on top and 16 on the bottom. Six taps were distributed in the first  $1D$  of the streamwise width,  $B$ , while the remaining 10 taps were equally spaced across the rest of the width. The photograph in Figure 3-3 shows the top surface of the model showing the arrangement of pressure transducers and wiring inside. A schematic view of the model's cross section is illustrated in Figure 3-4 to show explicitly how the pressure taps are distributed in the streamwise direction.

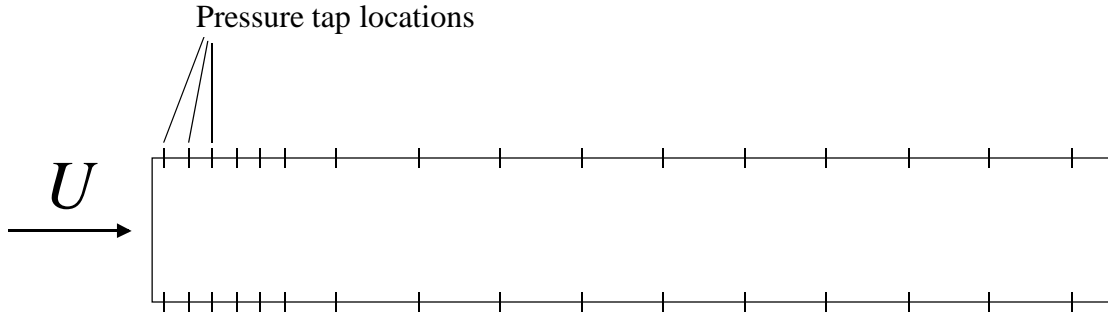


Figure 3-4 Diagram of pressure model cross section showing streamwise placement of pressure taps.

Sixty-four pressure sensors were fixed inside the model connected to the pressure taps with 14-in. lengths of plastic tubing (inner diameter 0.050 in.). Because the number of sensors accommodates the taps of two different spanwise positions at once, the taps were constructed with stainless steel tubes to allow for convenient rearranging of the tubing to vary the spanwise separation. Unfortunately, the large number of tubes in the relatively small model increased the probability of crimping the tubes when the cover was replaced following rearrangement. When a signal was lost due to crimping, one of two actions was taken. Either the pressure distribution containing the lost signal was ignored, or the lost signal was accounted for by interpolating between adjacent pressure signals. Appendix A contains further details involving the tubing and describes the calibration procedures for both the sensors and the tubing.

### 3.3 Motion Driving Equipment

To fulfill the goals expressed in Chapter 2, the motion driving mechanism had to meet several specifications. Pitching and heaving motion was required at variable

amplitudes and at variable mean angles of attack. This section describes the equipment designed and built to meet these needs.

Linkages driven by electric servo motors drove the motion. Figure 3-5 shows a schematic of these electro-mechanical mechanisms, and Figure 3-6 shows a picture of the pressure model mounted in this apparatus. The model was mounted between two “carriage pieces” containing bearings to allow both pitching motion and linear motion along guide rails. Both the pitching motion and the plunging motion were driven using specially-designed linkages. The plunging motion was created using push rods driven eccentrically from a motor mounted beneath the tunnel. Pitching motion was driven from a motor mounted to the outside wall of the wind tunnel. This motor was connected to a four-bar linkage mechanism designed to rotate a shaft sinusoidally. This shaft was then connected to the center shaft of the model for pitching. To allow for both pitching and plunging motions simultaneously, this shaft connection was made through a double U-joint. This joint could then flex with the plunging motion and still allow pitching control. Extensive linkage analysis (Kimbrell, 1991) was performed on these mechanisms to predict force and torque requirements and to insure that the motion would be sinusoidal.

The two servomotors were controlled using a National Instruments PC-based controller board (Model PCI-Servo-4A) which can be programmed from LabVIEW (software which will be described in more detail in the next section). This allowed versatile integration and coordination of the model motion with the data acquisition process.

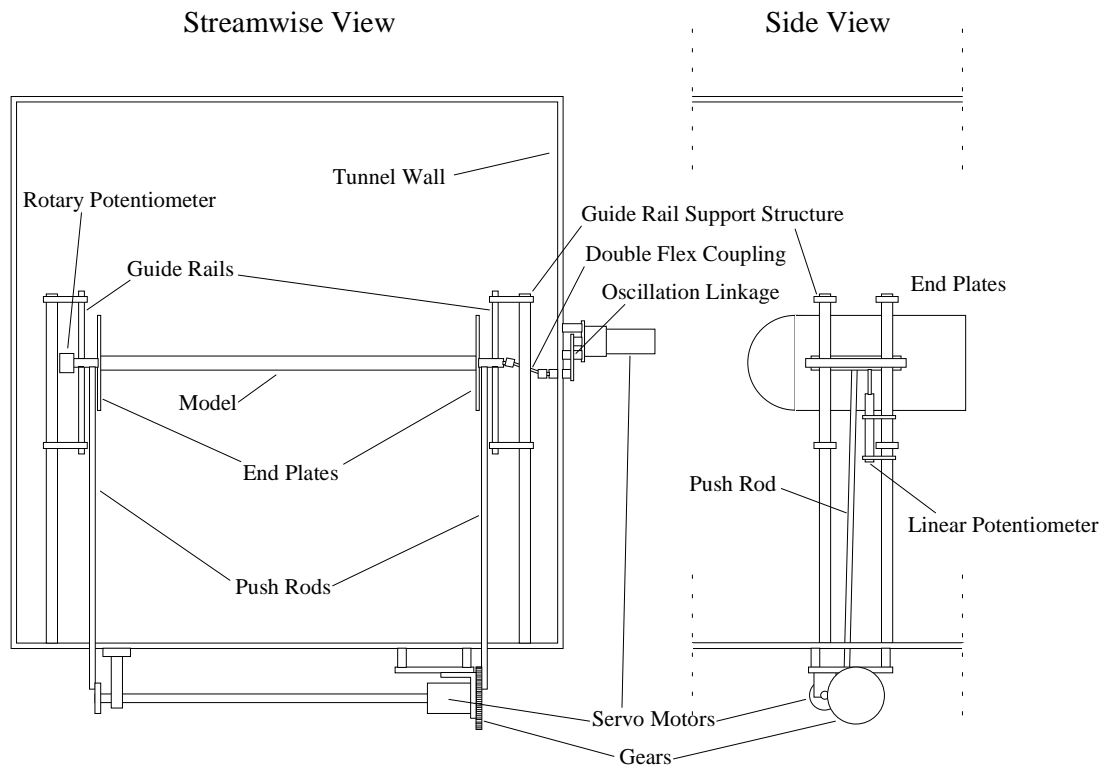


Figure 3-5 Schematic diagram of mechanisms for pitching and plunging the section model.

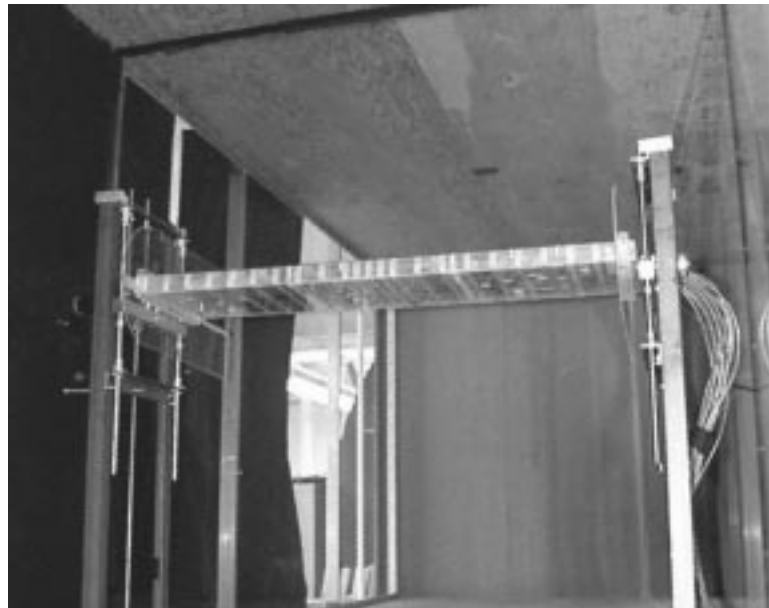


Figure 3-6 Picture of pressure model mounted on its motion driving mechanisms in the atmospheric wind tunnel.

Position information for the two degrees of freedom was obtained in two different ways. The vertical position of the model was measured using a linear potentiometer. With its resistance varying with the position of the piston, it produced a voltage proportional to vertical position of the model. Angular position was acquired using a rotational potentiometer mounted to the end of the model opposite of the drive end. Calibrations of these measurement techniques are described in Appendix D.

The flexible coupling driving the pitching motion proved to be a difficult design problem. To reach low reduced velocities, the frequency of oscillation had to be quite high (for example, the lowest reduced velocity considered in this case was  $U_r = 3.1$  which required an oscillation frequency of  $f_\alpha = 7.5\text{Hz}$ ). The couplings tested were either showing too much play or exhibiting resonance behavior within the frequency range to be tested. After a number of different design iterations—including double U-joint couplings, several sizes of flexible couplings, and a rigid shaft—a design was chosen that would allow testing, but under less than optimal conditions. The design involved flexible couplings which when combined with the pressure model exhibited a resonant response peak near 5.5 Hz. This resulted in a change in oscillation amplitude as the frequency was changed. Figure 3-7 shows how this dependence on frequency translated into an amplitude dependence on reduced velocity over the range tested for this project. For most aspects of this research, this amplitude change was unimportant. Discussions of subsequent chapters will make clear where having non-constant amplitude was an important issue with respect to the analysis.

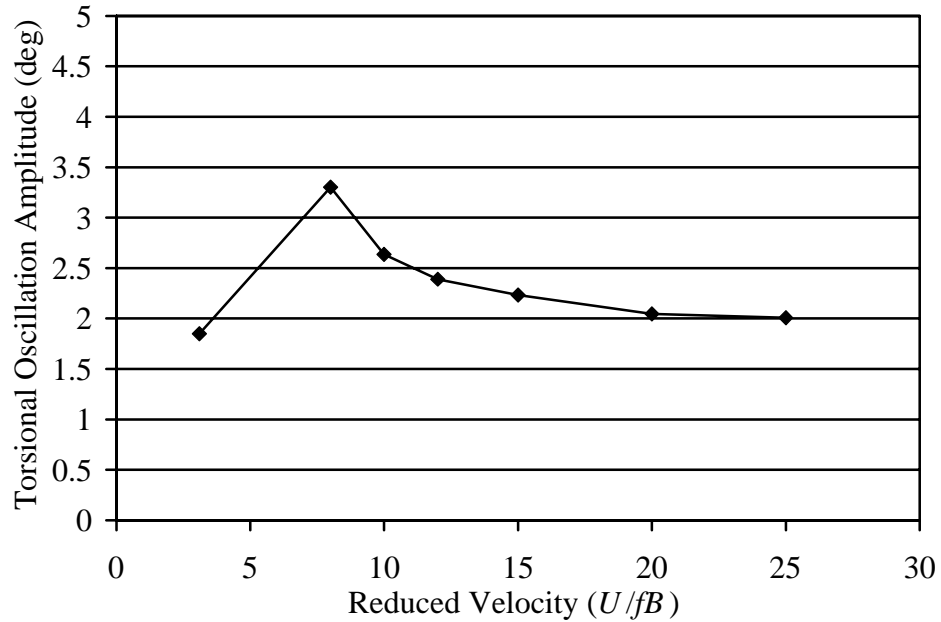


Figure 3-7 Torsional oscillation amplitude versus reduced velocity.

### 3.4 Data Acquisition Equipment

A computer data acquisition system was used for all the experiments. The subsequent sections describing velocity and pressure measurement transducers all terminate with the computer hardware described here.

A Pentium Pro PC formed the heart of the system running data acquisition hardware made by National Instruments (NI). To accommodate the high channel count required for this work, the hardware consisted of both a 16-bit multifunction board (Model PCI-MIO-16XE-10) residing in the computer and nine boards (Model SCXI-1140) that simultaneously sample and hold (SSH) multiple channels of voltages in a stand-alone chassis. This system “holds” 72 channels of voltages simultaneously while the computer board digitizes each one sequentially. This holding circuitry allowed each

channel to be sampled with minimal time lag between the first and last channels. Because the maximum sampling rate of the analog-to-digital converter (ADC) was 100 kHz, the maximum sampling rate for any one of the 72 channels was 1388 Hz (the sampling rate used for this study was 1000 Hz). The SSH hardware's droop rate—a measure of how quickly a voltage decays once it is “held”—is specified as 10 mV/sec, which is insignificant for these sampling rates. The hardware was controlled with NI's LabVIEW software, a graphical programming language enabling interactive data acquisition.

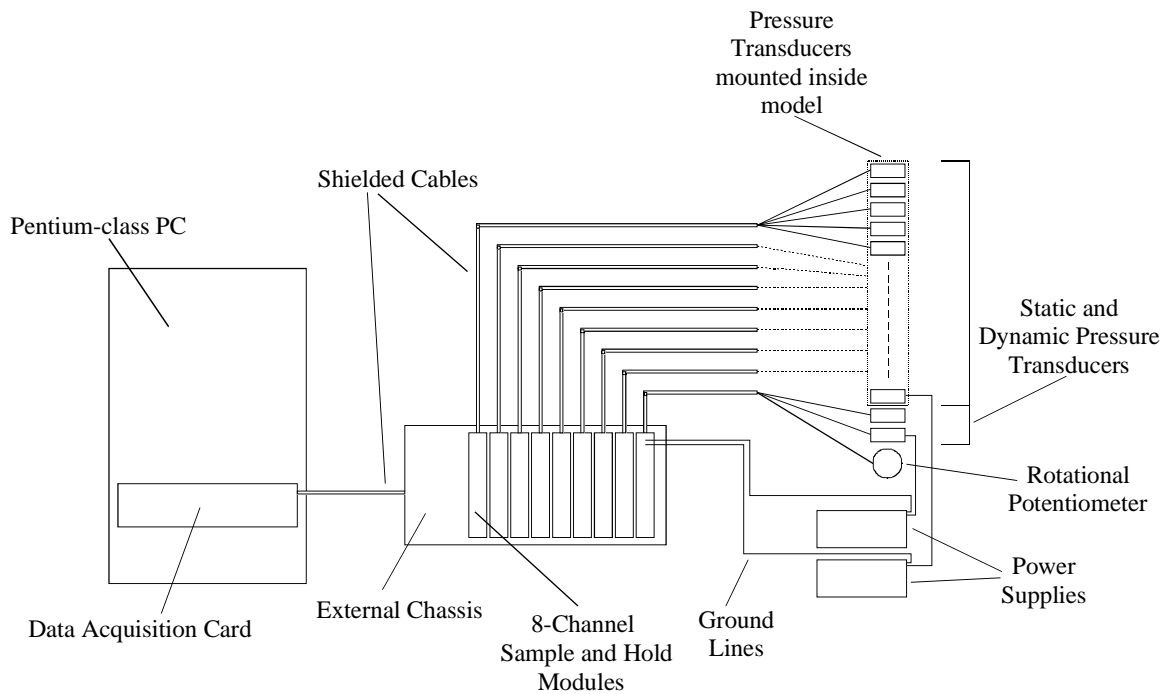


Figure 3-8 Schematic diagram of the data acquisition system including the 72-channel sample and hold equipment and the PC-based data acquisition card.

### 3.5 Pressure Measurements

Sixty-six pressure transducers were utilized to measure the dynamic and static pressures in the wind tunnel and the pressure distributions about the model. Two types of pressure transducers were used: Honeywell Microswitch sensors (Model 163PC) with a range of 620 Pa and SenSym sensors (Model ASCX01DN) with a range of 6900 Pa. Both sensors measured differential pressures, were temperature compensated, and had onboard voltage amplification. The Sensym transducers were mounted within the model to measure pressure distributions while the Honeywell sensors were used to measure the static and dynamic pressures of the flows with a Pitot-static probe. Appendix A describes the sensors in greater detail and the calibration procedures followed for each.

The dynamic pressure—used to normalize all the model pressure measurements and to calculate mean flow velocity—was measured using a Pitot probe (of diameter  $D_p = 5/16$  in.) mounted  $8D$  upstream of the model,  $6.67D$  down vertically from the center of the tunnel, and  $3.33D$  laterally from the center of the tunnel. The static pressure line of this same Pitot probe was connected via long plastic tubing to the static pressure ports of the pressure transducers inside the model.

All pressure data were acquired in ensembles of 4096 points sampled at 1000 Hz. Stationary model tests consisted of 60 ensembles (245.8 seconds) while oscillating model tests consisted of 12 ensembles (49.2 seconds). The effective number of ensembles for calculation of sectional quantities, however, was greatly increased because of the four different measurement locations and the five repetitions of the experiments for the different spanwise separations (see Appendix D).

### 3.6 Velocity Measurements

Velocity measurements were made two ways. One is the well-known method using a Pitot-static probe to measure mean dynamic pressure (as described in the previous section) and obtain velocity with the use of Bernoulli's equation. This method was only used to set the mean flow speed in the wind tunnel.

Thermal anemometry was the other velocity measurement technique employed, and was used for measuring all the turbulence quantities. Hot film probes of X configurations were used to measure two components of turbulent velocity fluctuations—the streamwise component and the vertical component. TSI's IFA 100 anemometer was used with TSI Model 1241 X probes. More details concerning this equipment—including descriptions of calibration methods—can be found in Appendix B.

To measure horizontal or vertical profiles of turbulence parameters, the probes could be mounted on a velocity traverse mechanism as shown in Figure 3-9. This traverse mechanism, driven with a stepper motor, was mounted vertically or horizontally in the tunnel depending on the profile to be measured. Velocity coherence measurements—requiring two probes—were made by mounting one probe on a fixed support and the other on the traverse. The geometry of the probe holders required that the stationary probe be mounted with a 90°-angle adapter to allow the probes to come within 0.25 in of each other. Computer control of the traverse allowed for automated traverse runs.

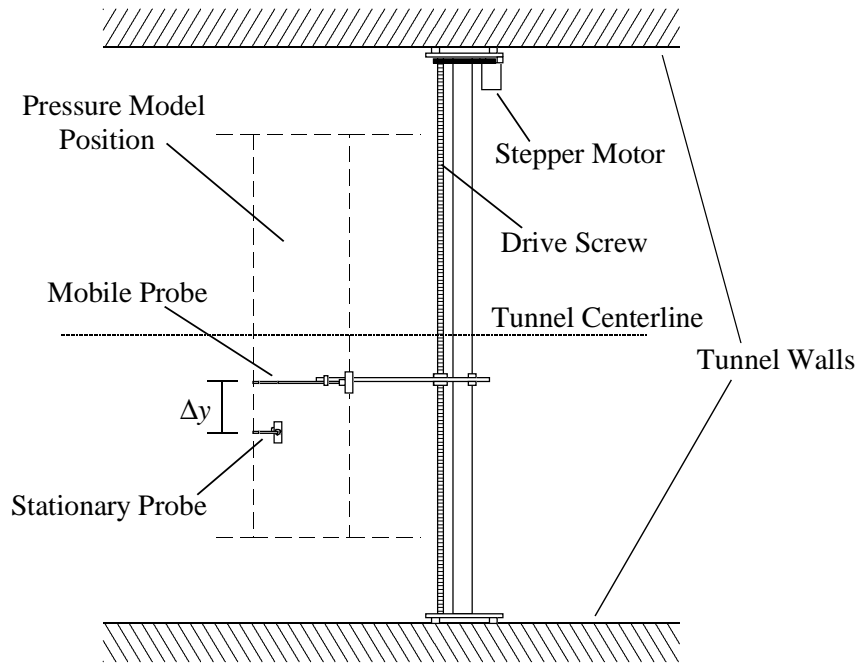


Figure 3-9 Top view schematic diagram of the traverse mechanism for hot film probes set up for horizontal traverses in the wind tunnel.

## CHAPTER 4. VELOCITY MEASUREMENTS

A host of different velocity measurements were taken to quantify the characteristics of the turbulent flows used in this study. This chapter summarizes flow characteristics using a number of commonly-used parameters, reports on flow profiles indicative of wind tunnel test section uniformity, and provides spectral data on each flow to show how turbulent energy is distributed among the various scales present in the flow.

### 4.1 Summary of Incident Turbulent Flows

As described in Chapter 3, the turbulent flows used in this study were generated with biplane grids. Grids of different sizes generated various integral scales while different grid-to-model distances controlled the turbulence intensity. To study the effect of the various turbulent scales, flows of different integral scales but constant turbulence intensity were produced. Table 1 lists the longitudinal and vertical turbulence intensities, the longitudinal and transverse integral scales, and the small-scale spectral density parameters for each flow. Each turbulent flow is referred to with a number corresponding to its turbulence intensity (e.g. “6” for 6%) and a letter corresponding to flows with different integral length scales for that turbulence intensity. Except for  $S_u$ , all values reported in the table result from averaging over the middle  $2B$  of the test section.

Table 4-1 TURBULENT FLOW PARAMETERS

	$I_u$	$I_w$	$L_{ux}$	$L_{uy}$	$L_{wx}$	$L_{wy}$	$S_u$
Smooth	0.4%	0.3%	N/A	N/A	N/A	N/A	N/A
$I_u = 6\%$							
Case 6a	6.1%	5.7%	1.81D	1.69D	0.86D	1.34D	2.3
Case 6b	5.8%	5.1%	4.9D	2.68D	2.56D	2.21D	0.3
$I_u = 12\%$							
Case 12a	11.7%	11.1%	1.34D	1.14D	0.61D	0.83D	53
Case 12b	11.6%	10.2%	4.89D	3.33D	2.66D	2.52D	6.0

#### 4.2 Velocity Profiles

To quantify the wind tunnel’s flow uniformity, flow profiles were measured with the model absent. Although the flow’s behavior in the lateral direction is of primary interest in this study, preliminary vertical profiles were measured to validate the existence of a reasonably sized region of uniform flow. Figure 4-1 contains vertical profiles of mean longitudinal velocity. These profiles, measured at the center of the tunnel and at distances of  $1B$  and  $2B$  to either side, show uniformity well within  $\pm 2\%$  in the  $4B$  by  $4B$  center region of the test section. Longitudinal turbulence intensity profiles—measured at the same positions as mean velocity—are shown in Figure 4-2. Most of the center region has a turbulence intensity at or below 0.5%, but near  $y = -2B$

it rises to more than 1.0%. This may be caused by the difference in tunnel walls from one side to the other. While the  $y = +3B$  wall is made of Plexiglas, the  $y = -3B$  wall consists of plywood with the access door. It is reasonable to assume that the rougher  $y = -3B$  wall would generate a thicker boundary layer and increase the turbulence intensity on that side. Efforts to reduce the turbulence intensity by sealing and smoothing the access door's seam were unsuccessful, so the slightly larger turbulence intensity was accepted as an unavoidable characteristic of the wind tunnel.

Once the uniformity of the atmospheric tunnel's flow was verified for the vertical direction, attention was focused on lateral flow profiles. Lateral profile measurements were taken along the stagnation line of the model—with the model absent—for each flow considered. Profiles of mean velocity, mean flow angle, turbulence intensity, and integral length scale are presented here.

The mean flow profile for smooth flow is shown in Figure 4-3. This profile shows an excellent uniform profile—within  $\pm 2\%$ —in the spanwise direction over the middle  $4B$  of the test section. The edges of the profile exhibit slightly higher velocities before decreasing to zero in the wall boundary layers. These higher velocities can most likely be attributed to imperfect design of the inlet section of the wind tunnel itself.

Inserting grids into the wind tunnel exaggerated the high-velocity edges seen in the smooth-flow profile. Removing the inlet section of the tunnel, however, improved the profiles somewhat, so for each subsequent test involving grids, the inlet was removed. Grids without the inlet produced mean velocity profiles as shown in Figure 4-4 and Figure 4-5, for 6% and 12% turbulence intensities, respectively. While the smaller scale cases (the “a” cases) have quite a uniform profile for both turbulence intensities, the

larger scale cases—generated by the larger grid—show some significant spanwise velocity variations. Considering the velocity differences between each spanwise pressure measurement location, the greatest velocity difference was 10%. As stated, these nonuniformities are a characteristic of the facility and were unavoidable for this study.

The use of an X-probe allowed measurement of profiles of the mean flow angles. Smooth flow angle profiles are shown in Figure 4-6. Flow angle profiles for the “6” cases and the “12” cases are shown in Figure 4-7 and Figure 4-8, respectively. In most cases the angles were within  $\pm 0.5^\circ$  and in every case were within  $\pm 1.0^\circ$ .

Both longitudinal and vertical turbulence intensities were quantified for each flow using local rms values of velocity fluctuations and local mean velocities. Figure 4-9 shows that smooth flow turbulence intensities were less than 0.4% over the majority of the span. Longitudinal turbulence intensity profiles are shown in Figure 4-10, and vertical intensity profiles are shown Figure 4-11. The nonuniformities in these profiles are quite similar to those of the mean velocity profiles which could be expected since local mean velocities were used to normalize them.

Integral scale variations over the model span can be observed from the profiles of  $L_{ux}$  and  $L_{wx}$  in Figure 4-12 and Figure 4-13, respectively.  $L_{ux}$  is a measure of the longitudinal dimension of the eddies responsible for longitudinal velocity fluctuations, while  $L_{wx}$  is a measure of the longitudinal dimension of eddies responsible for vertical velocity fluctuations. Each of these quantities was estimated from the areas under the autocorrelation curves of the associated velocity fluctuations. This area—integrated to the first zero-crossing—is associated with a time scale which was converted to a length

scale by multiplying by the mean velocity (Taylor’s approximation). Each autocorrelation curve is shown in Section 4.4.

The longitudinal scales of the larger grid cases—the “b” cases—varied as much as  $1.5D$  while the smaller grid cases varied only  $0.3D$ . The vertical scales, however, did not vary as much—only  $0.7D$  for the larger grid and  $0.1D$  for the smaller grid. Profiles such as these were only possible for the longitudinal integral scales because they could be done with single-probe time series. The transverse scales reported in Table 4-1 have single values because they required two-probe experiments at a number of spanwise separations.

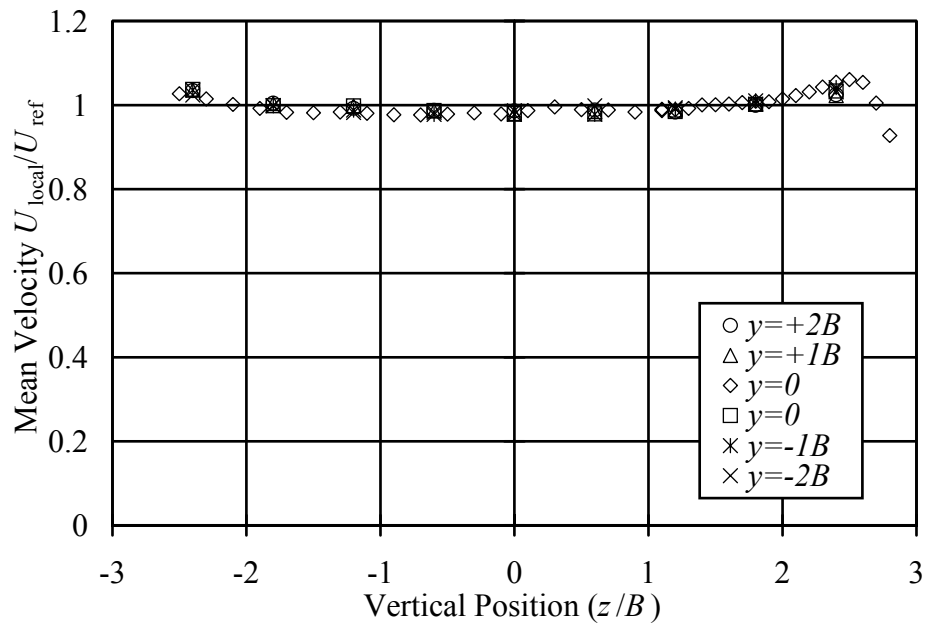


Figure 4-1 Vertical profiles of mean longitudinal velocity in smooth flow at various lateral distances from the center of the tunnel.

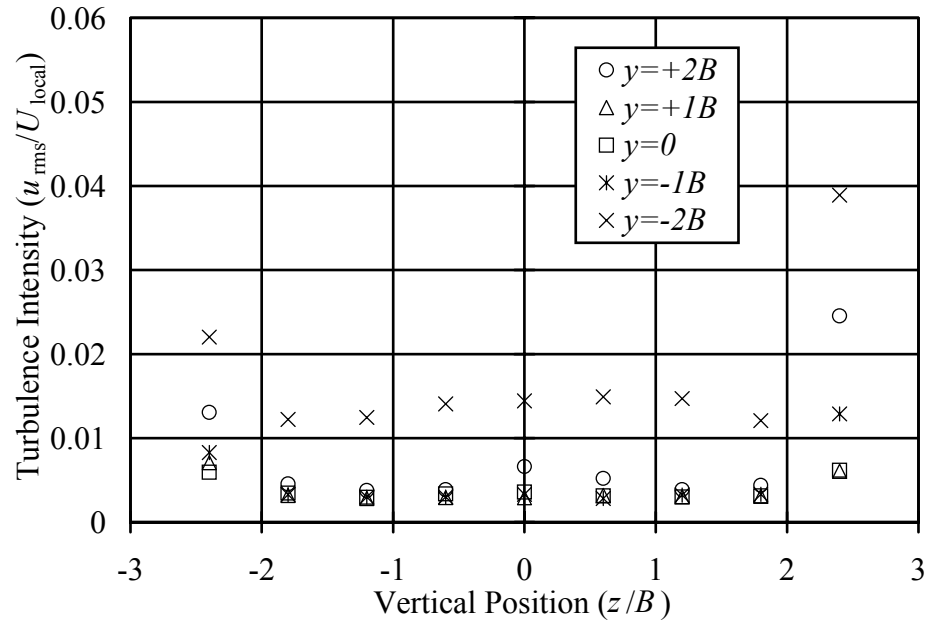


Figure 4-2 Vertical profiles of longitudinal turbulence intensity in smooth flow at various lateral distances from the center of the tunnel.

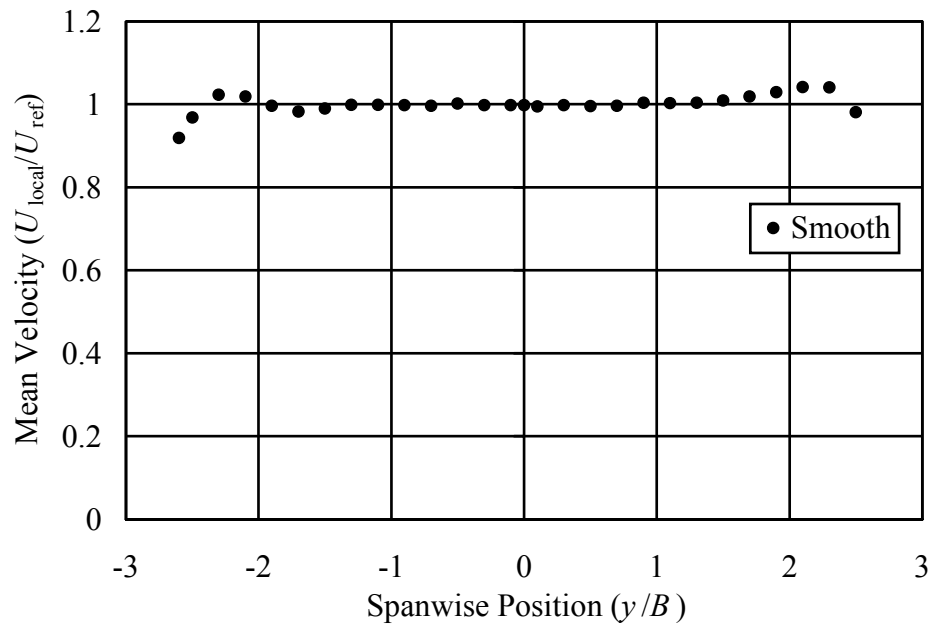


Figure 4-3 Spanwise profile of mean longitudinal velocity for smooth flow

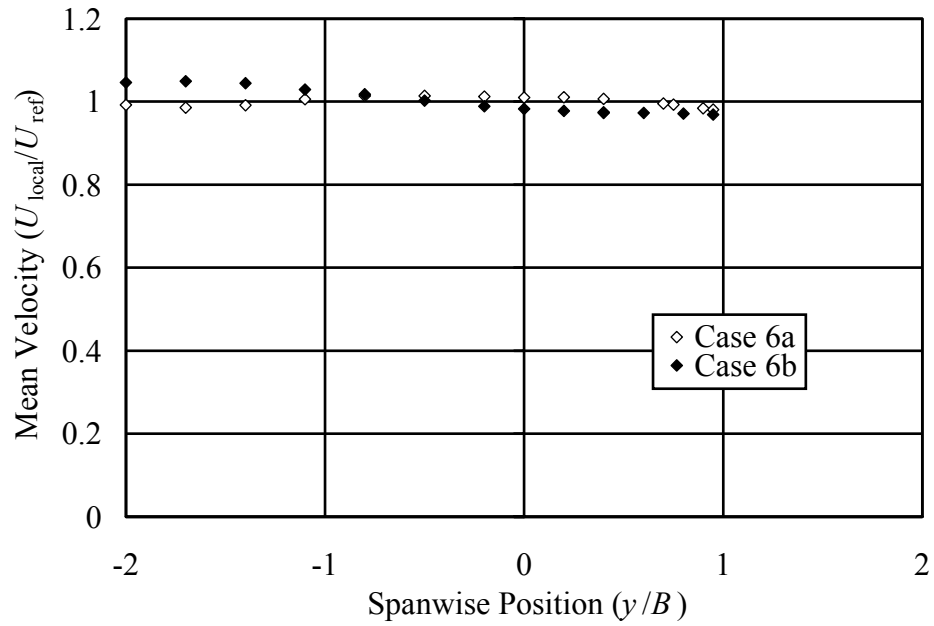


Figure 4-4 Spanwise profile of mean longitudinal velocity for turbulent flows with turbulence intensity of 6%

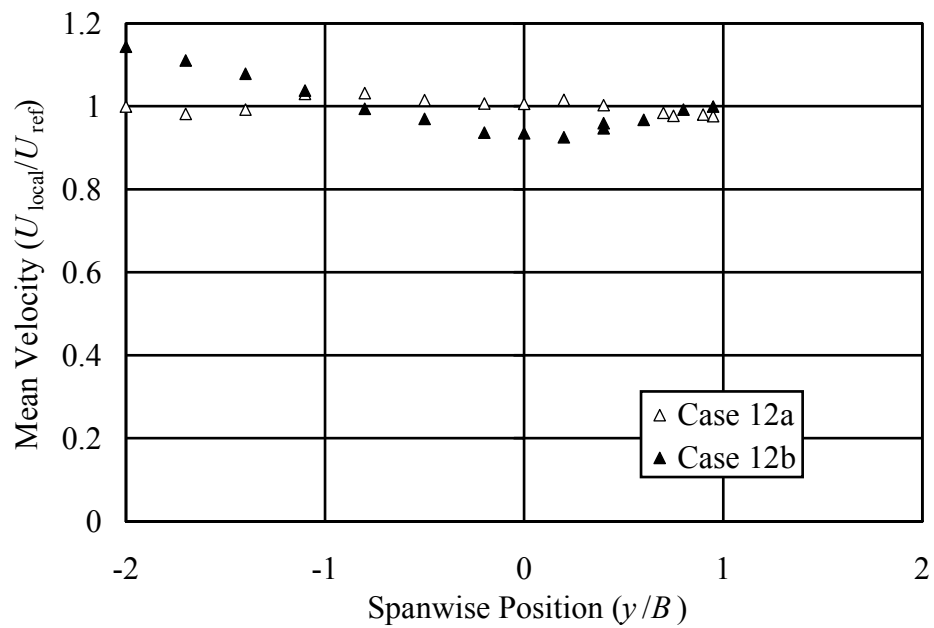


Figure 4-5 Spanwise profile of mean longitudinal velocity for turbulent flows with turbulence intensity of 12%

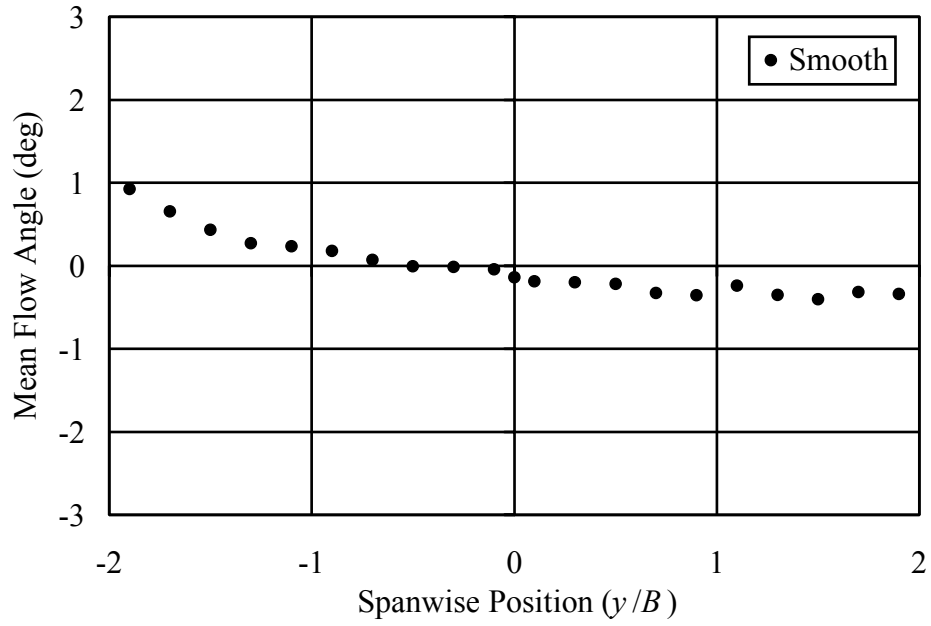


Figure 4-6 Spanwise profile of mean flow angle for smooth flow

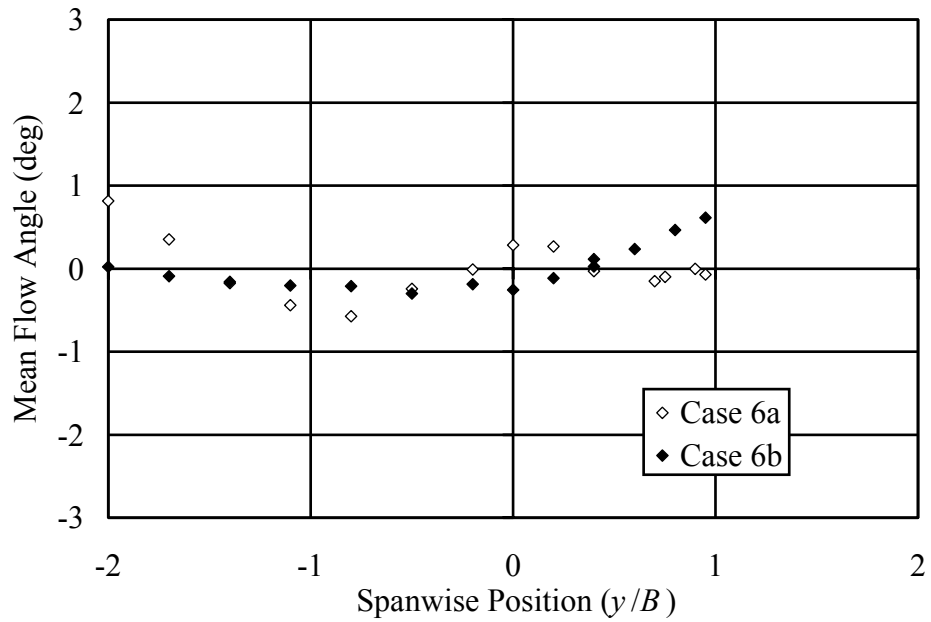


Figure 4-7 Spanwise profiles of mean flow angle for turbulent flows with turbulence intensity of 6%

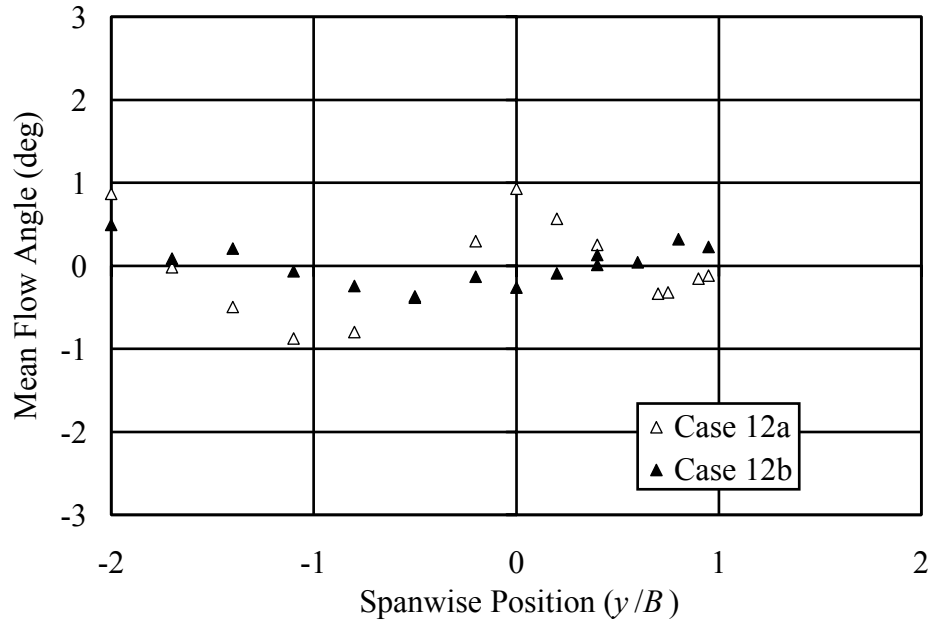


Figure 4-8 Spanwise profiles of mean flow angle for turbulent flows with turbulence intensity of 12%

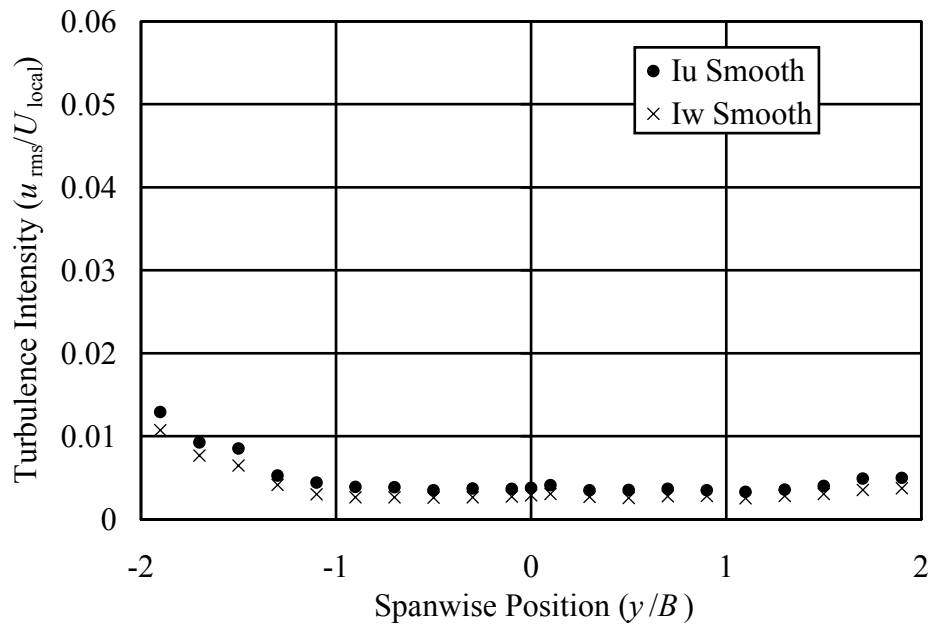


Figure 4-9 Spanwise profile of turbulence intensity for smooth flow

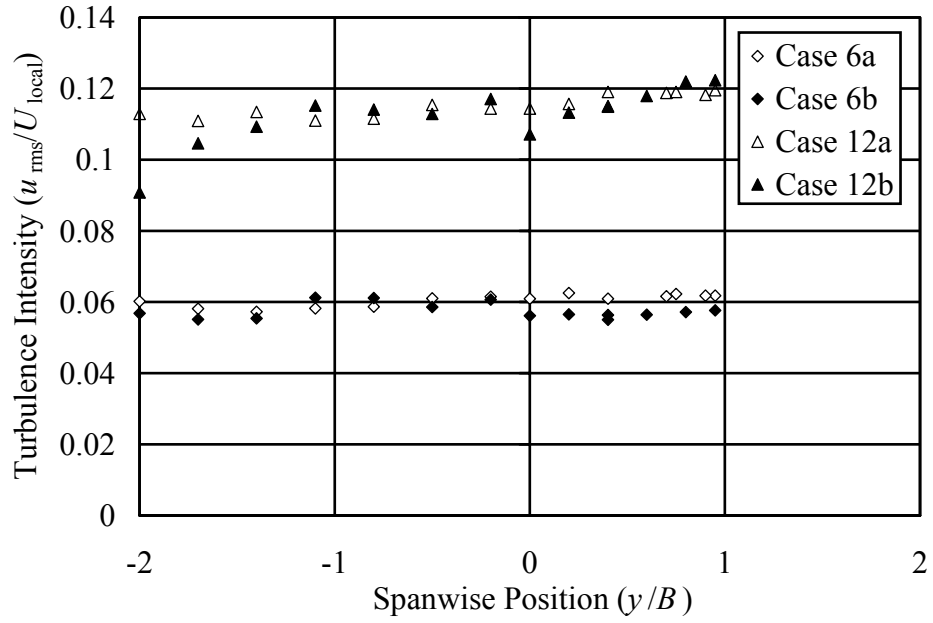


Figure 4-10 Spanwise profiles of longitudinal turbulence intensity for all turbulent flows

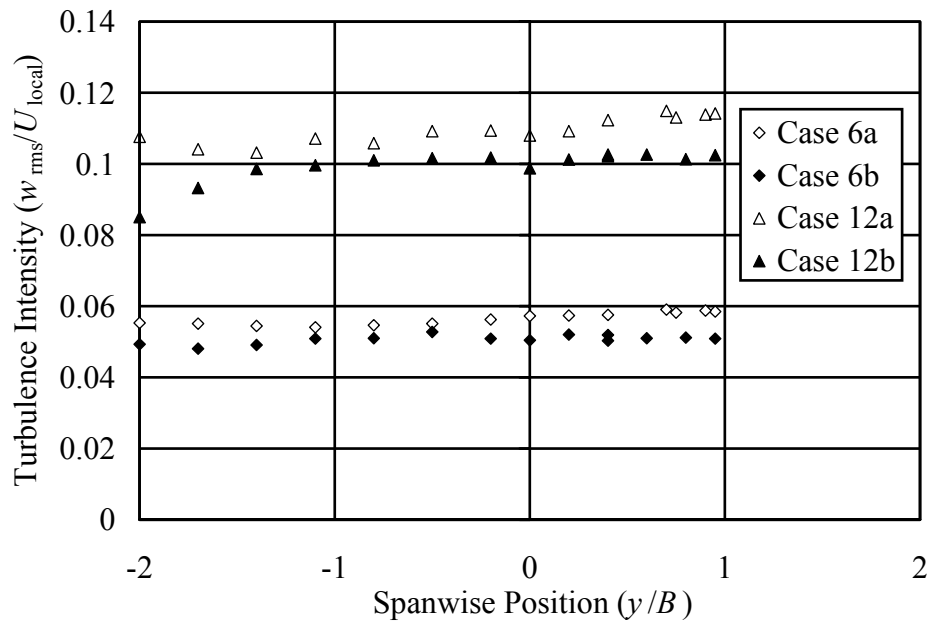


Figure 4-11 Spanwise profiles of vertical turbulence intensity for all turbulent flows

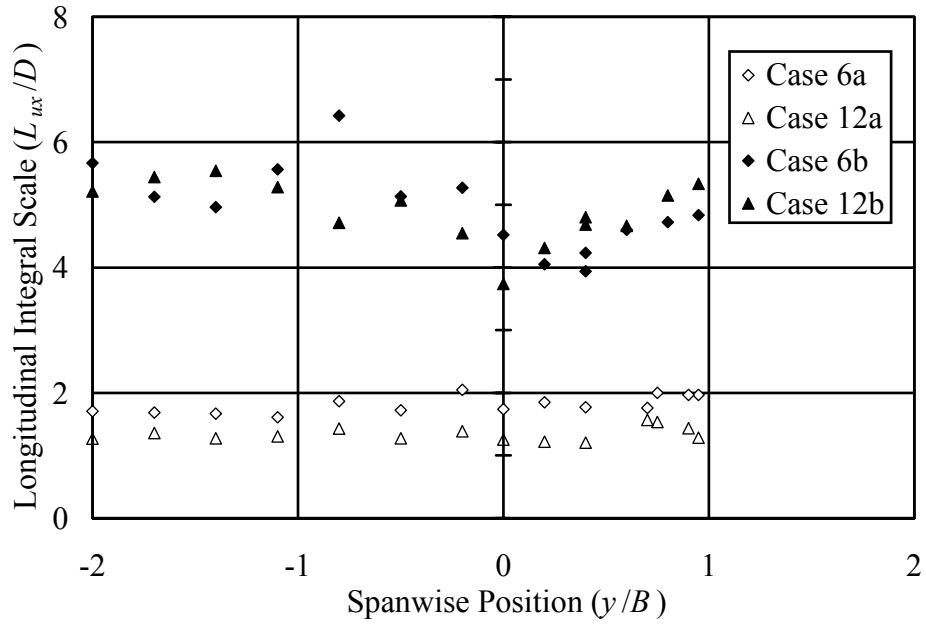


Figure 4-12 Spanwise profiles of longitudinal integral scale for each turbulent flow

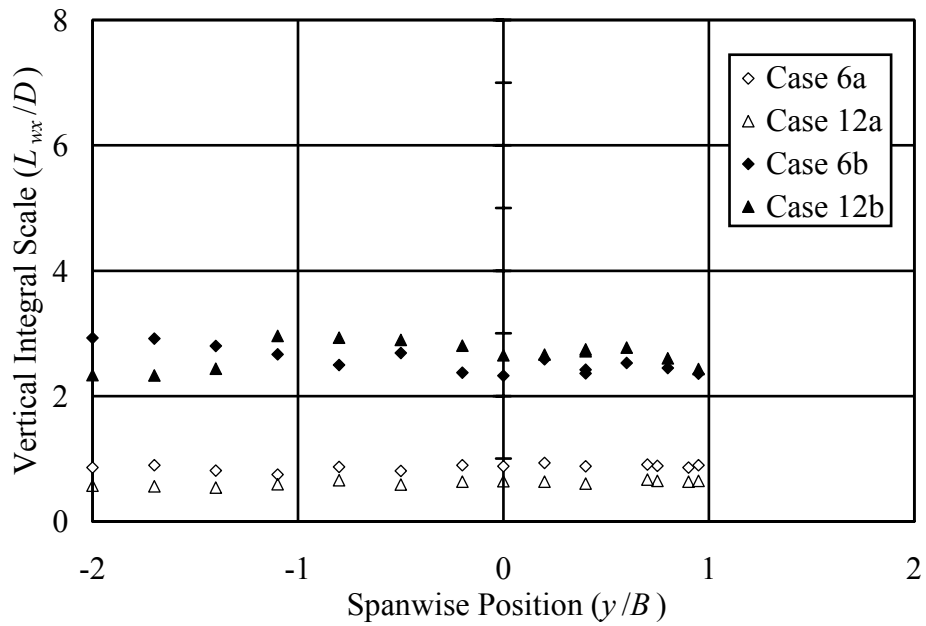


Figure 4-13 Spanwise profiles of vertical integral scale for each turbulent flow

### 4.3 Spectral Measurements

As discussed in Chapter 2, the turbulence intensity and integral scale do not fully describe a turbulent flow. Because studies of bluff-body aerodynamics have shown the strong influence that small-scale turbulence can have, the spectral distribution of turbulence scales was also quantified for this study. Power spectral density plots for the  $u$  component of velocity at 6% and 12% turbulence intensity are shown in Figure 4-14 and Figure 4-15, respectively. Each figure shows curves with equal areas beneath them and demonstrates how the energy is redistributed among scales when the integral scale is changed with the turbulence intensity held constant.

The ordinate in each case is  $fD/U$ . This allows easy location of the reference point for the small-scale spectral density parameter. Choosing scales on the order of the thickness of the separated shear layer means this parameter is calculated from values at  $fD/U = 10$ . The plot shows how significantly the small scale energy content of the flow changes when the integral scale is changed (also shown in Table 4-1).

Figure 4-16 and Figure 4-17 show the power spectral density functions of the  $w$  component of velocity for the Case 6 and Case 12 flows, respectively. Spectral shapes and magnitudes are quite similar to their  $u$  component counterparts, except for slightly less low-frequency content for the  $w$  fluctuations. This difference is also reflected in Table 4-1 where the  $L_{wx}$  and  $L_{wy}$  integral scales are also smaller than the corresponding  $u$  component scales.

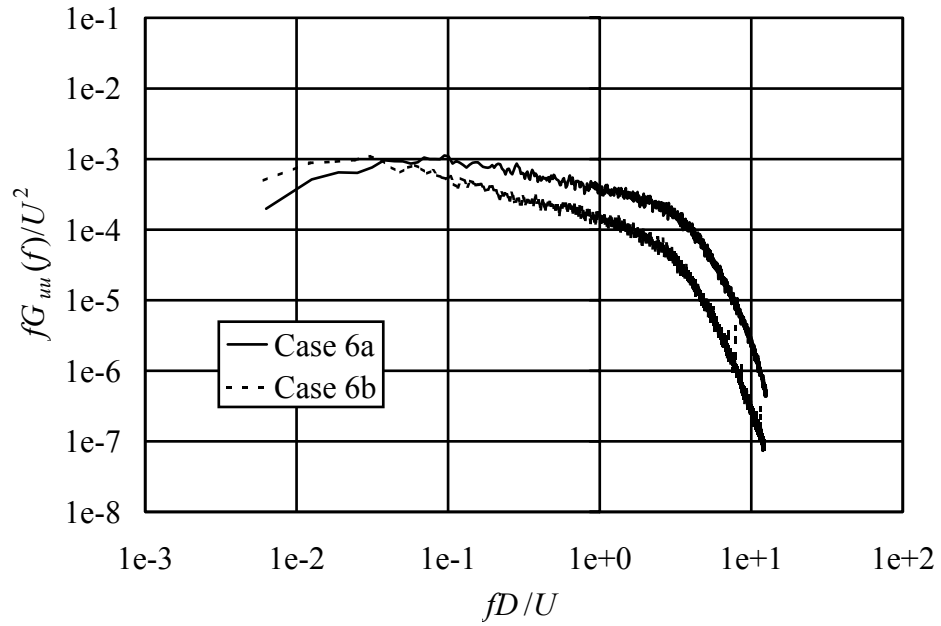


Figure 4-14 Power spectral density plots of the  $u$  velocity component for the Case 6 flows.

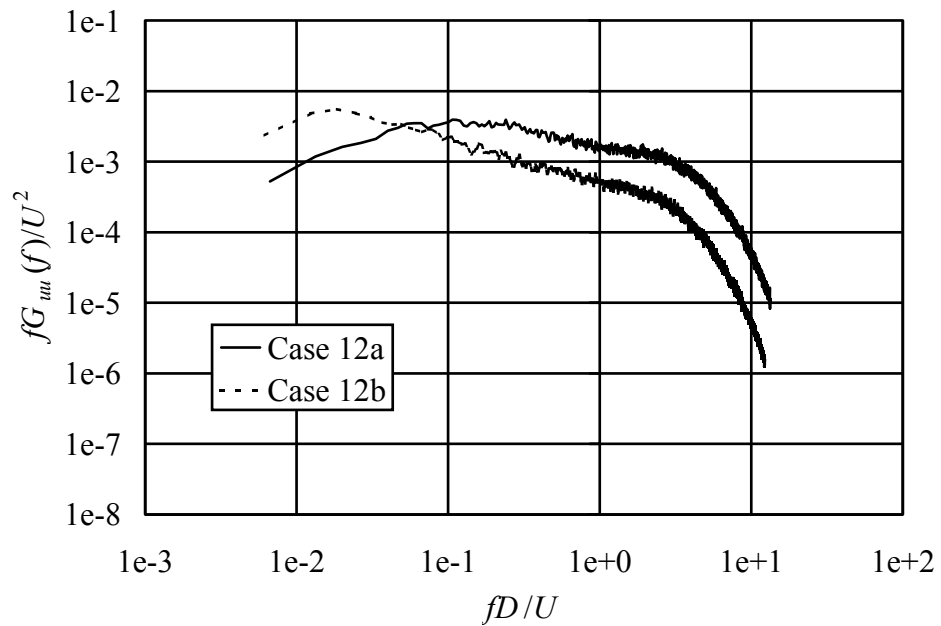


Figure 4-15 Power spectral density plots of the  $u$  velocity component for the Case 12 flows.

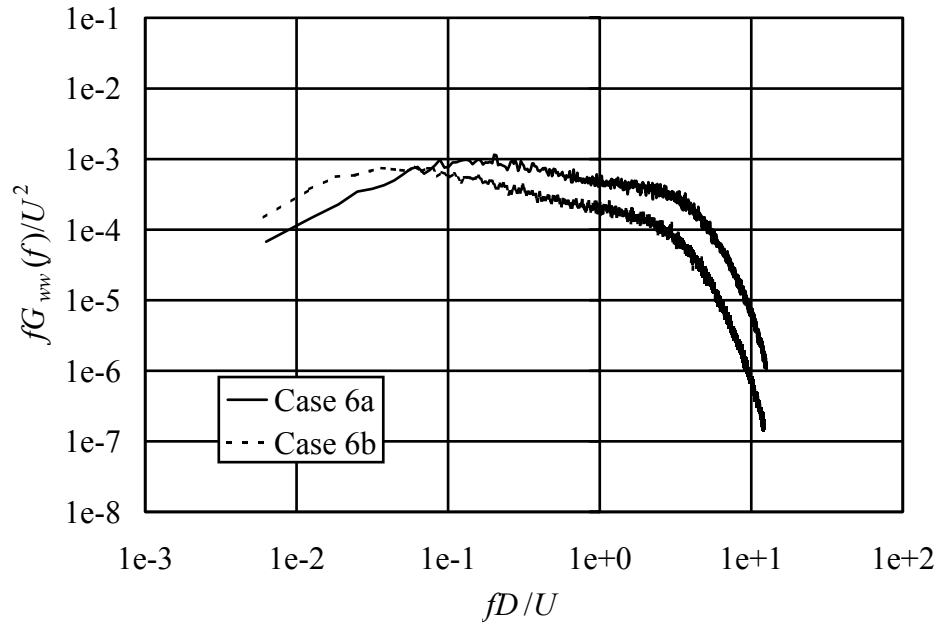


Figure 4-16 Power spectral density plots of the  $w$  velocity component for the Case 6 flows.

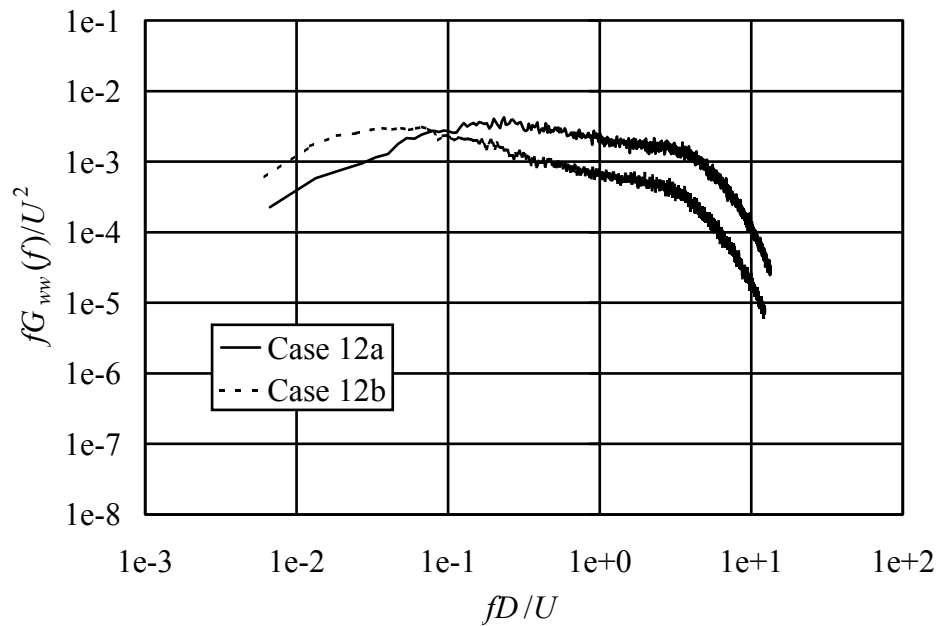


Figure 4-17 Power spectral density plots of the  $w$  velocity component for the Case 12 flows.

#### 4.4 Correlation Measurements

The importance of the spanwise correlation of aerodynamic forces in extrapolating section model tests to full-scale predictions has already been discussed. Because the relation between the spanwise correlation between the incident flow field and that of the forces on the body is important to clarify, streamwise and spanwise velocity correlations were measured.

The autocorrelation coefficient functions for the longitudinal velocity fluctuations for flows of 6% and 12% turbulence intensity are displayed in Figure 4-18 and Figure 4-19, respectively. Of course, given the larger grid size the “b” case curves have greater areas beneath them than the curves for the “a” cases. Also, comparing cases 6a to 12a and cases 6b to 12b, one finds very similar curves—which should be the case for flows generated using the same grids. Analogous observations can be made from Figure 4-20 and Figure 4-21, the autocorrelation curves for the vertical velocity fluctuations for 6% and 12%, respectively.

To quantify incident flow correlation in the bridge model’s spanwise direction, two-probe velocity coherence measurements were made for several spanwise separations. To aid comparison to the streamwise correlation functions, these coherence functions were converted with an inverse fast Fourier transform (IFFT) to correlation functions. Plotting the maxima of these correlation functions at each separation renders the spanwise correlation curves shown in Figure 4-22 to Figure 4-25. Figure 4-22 and Figure 4-23 show the curves for  $u$ , and Figure 4-24 and Figure 4-25 the curves for  $w$ .

In each case, an exponential curve has been fit to the data. From these fits, values of the integrals of these curves were made to estimate the spanwise length scales listed in Table 4-1.

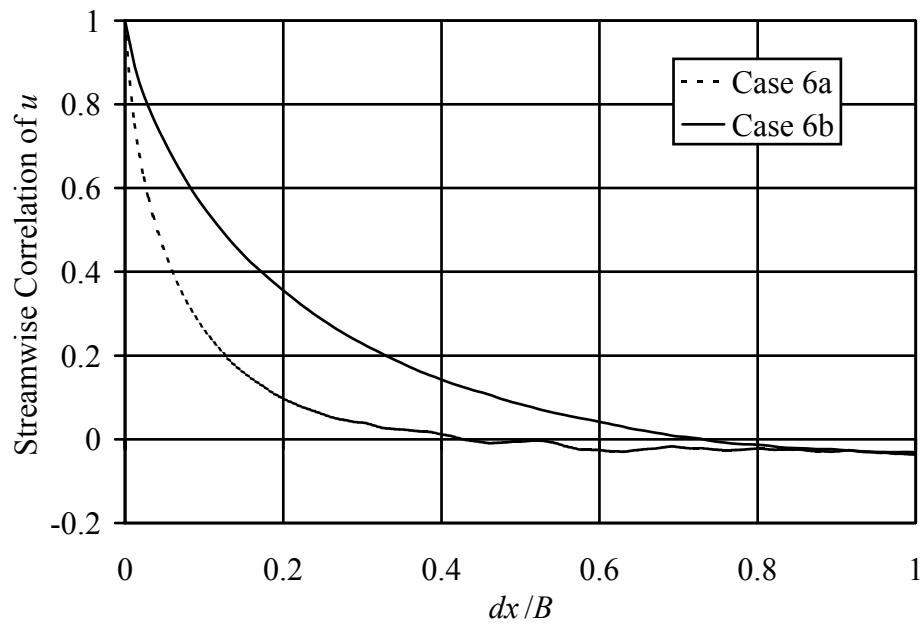


Figure 4-18 Streamwise correlation coefficients for  $u$ -components of flows with 6% turbulence intensity.

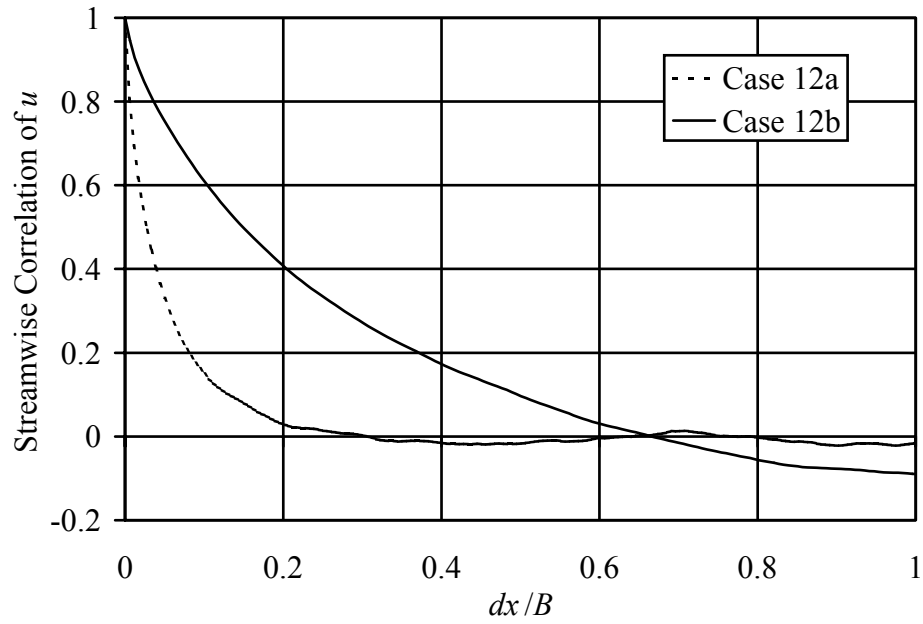


Figure 4-19 Streamwise correlation coefficients for  $u$ -components of flows with 12% turbulence intensity.

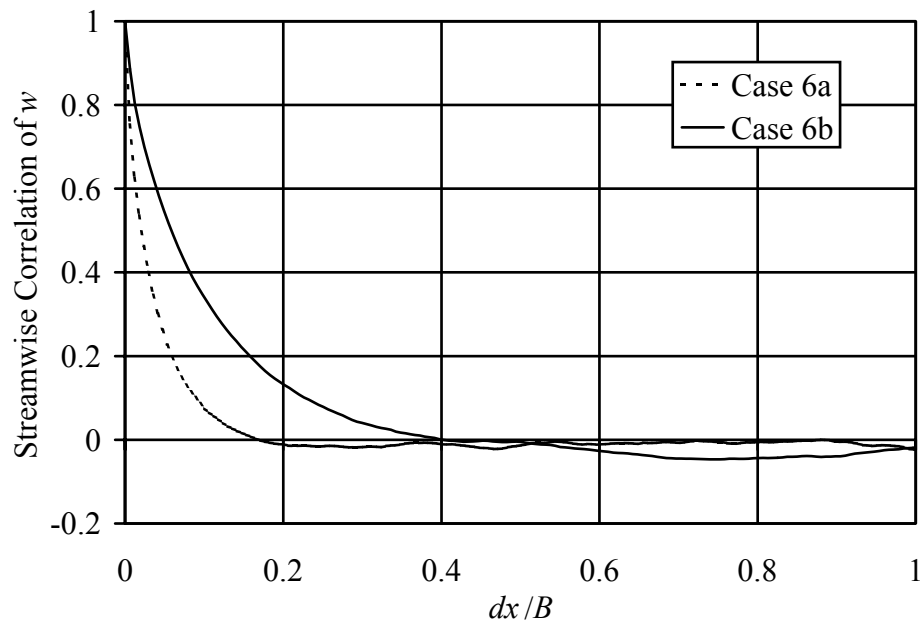


Figure 4-20 Streamwise correlation coefficients for  $w$ -components of flows with 6% turbulence intensity.

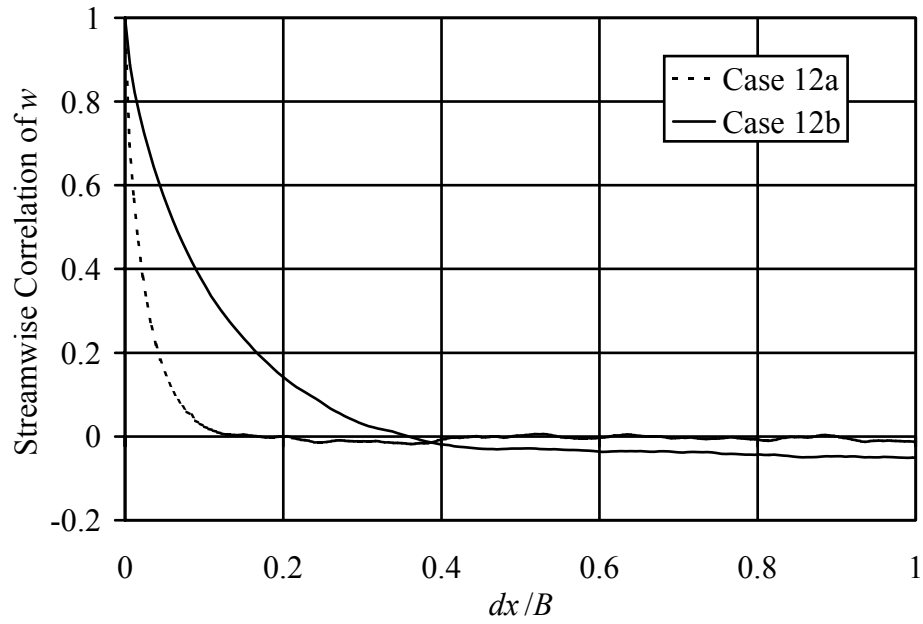


Figure 4-21 Streamwise correlation coefficients for  $w$ -components of flows with 12% turbulence intensity.

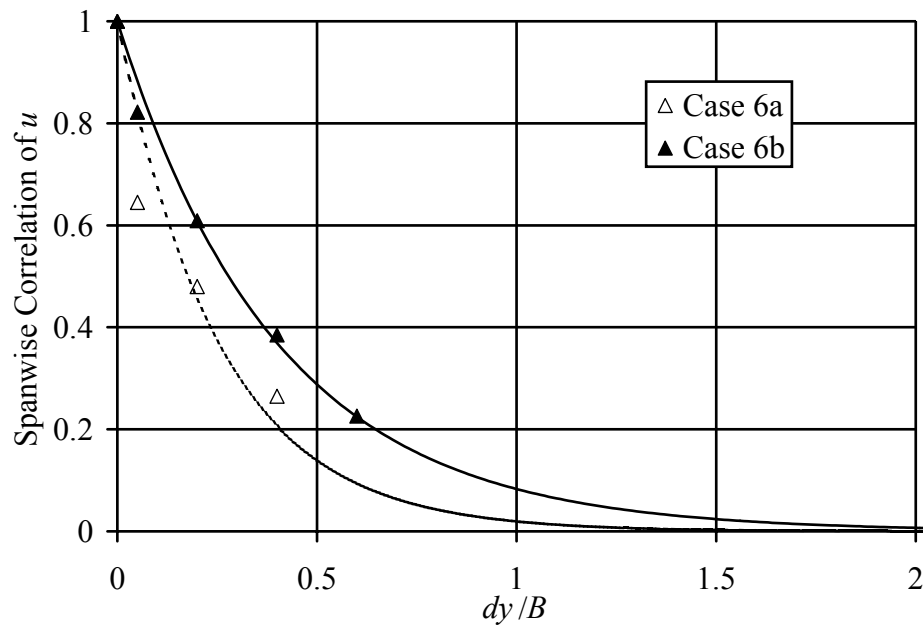


Figure 4-22 Spanwise correlation coefficients with exponential curve fits for  $u$ -components of flows with 6% turbulence intensity.

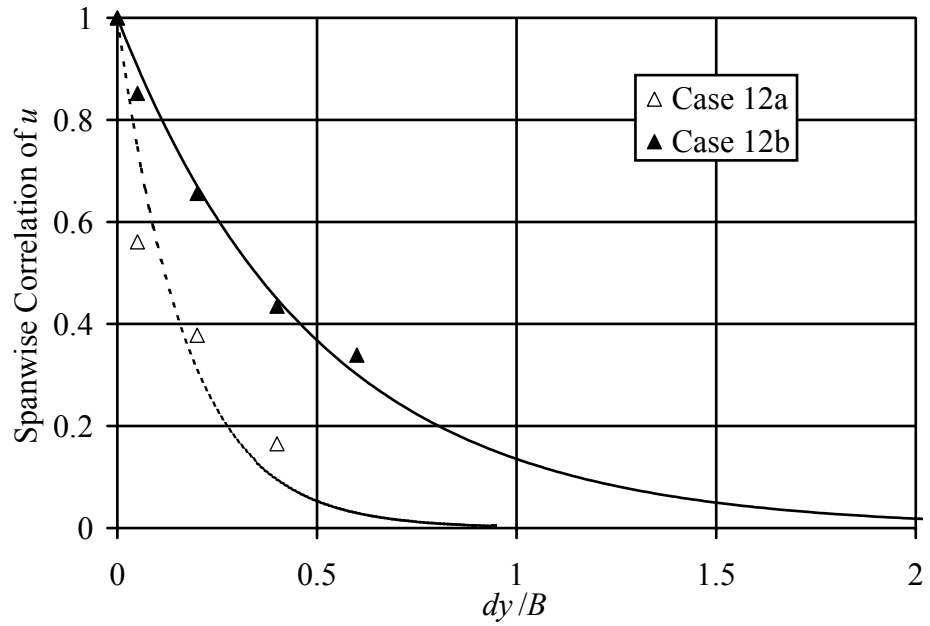


Figure 4-23 Spanwise correlation coefficients with exponential curve fits for  $u$ -components of flows with 12% turbulence intensity.

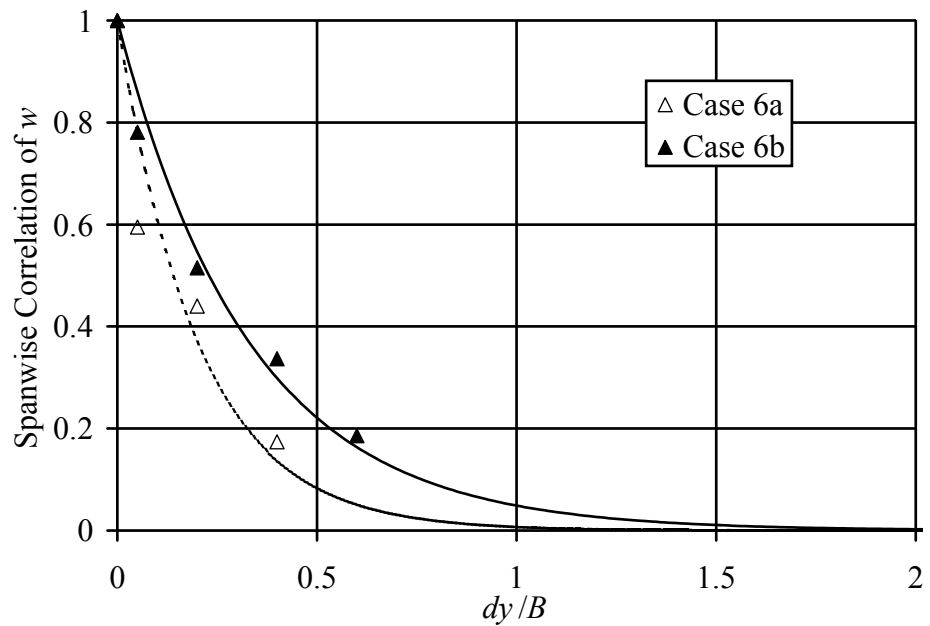


Figure 4-24 Spanwise correlation coefficients with exponential curve fits for  $w$ -components of flows with 6% turbulence intensity.

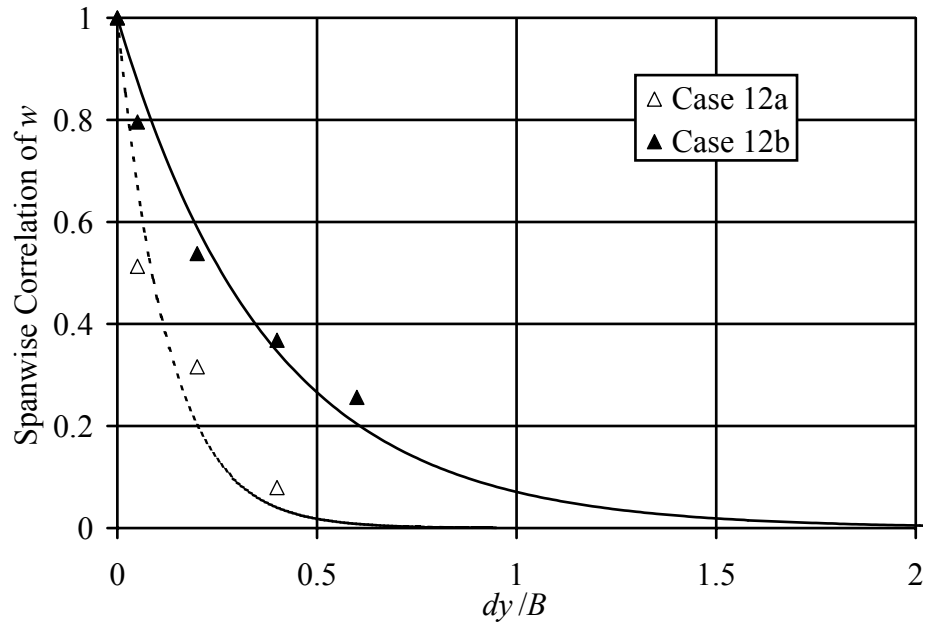


Figure 4-25 Spanwise correlation coefficients with exponential curve fits for  $w$ -components of flows with 12% turbulence intensity.

## CHAPTER 5. PRESSURE FIELDS ON STATIONARY MODEL

### 5.1 Summary of Pressure Analysis Methods

This chapter discusses the measurements made on stationary models. These tests had two purposes. The first goal was mainly for validation—not only to meet certain obvious physical specifications but also to compare measurements made for this study with the current literature. With this accomplished, the more important goal of gleaning flow structure information pertinent to the physical mechanisms of the dynamic forces was pursued. In this chapter, results of preliminary tests of the measurement system integrity are presented, statistical quantities corresponding to the pressure fluctuations are given, and pressure spectra are presented.

### 5.2 Preliminary Tests

Stationary model tests were conducted for several reasons. The effectiveness of the end plates was ascertained from spanwise pressure measurements on a stationary model. The mean angle of attack for the tests was set using stationary-model pressure distributions. Finally, pressure statistics measured on stationary models in the various flow fields yielded a data set with which both the work of other researchers and the subsequent dynamic test results could be compared.

Tests of end-plate effectiveness consisted of spanwise pressure distributions on the upper and lower surfaces at two spanwise locations— $x/B = 0.11$  and  $x/B = 0.79$ . These two locations were chosen so that one profile would be from inside the separation bubble and one profile would be from outside it. Reattachment is generally observed to occur just upstream of the peak in the RMS pressure distribution (see for example, Kiya & Sasaki (1983)). In this case, this peak occurs near  $x/B = 0.56$  as shown later in Figure 5-6 of the next section.

Figure 5-1 shows spanwise mean pressure profiles at the above-mentioned locations. Two objectives were to be met with this test. First, a reference angle of attack for the model had to be located such that the mean pressures on the upper and lower surfaces were equal, i.e. such that the mean lift was zero. This criterion was met—as shown in the figure—with a geometric angle of attack,  $\alpha_G$ , of  $-1^\circ$ . Geometric angle of attack refers to the angle measured with a protractor on the surface of the model. All subsequent mention of angle of attack will correspond to angles measured with respect to this geometric reference. This determination of the reference angle of attack was repeated with spanwise tests as described later in this section.

The second objective was to verify a uniform pressure profile along the span. Variations near  $x/B = 0.11$  amounted to about 3% while those near  $x/B = 0.79$  were greater than 10%—the greater percentage for the latter due in part to smaller mean values at  $x/B = 0.79$ . With respect to the dynamic pressure, these variations were less than 4%. The profile also suggests that there may be some slight periodicity to the variations, particularly for the downstream case. This periodicity may be a result of incoming flow

nonuniformities (including variations in the incident flow described in Chapter 4) and/or of endplate effects.

Figure 5-2 contains spanwise profiles of the RMS pressure distributions corresponding to the same position as the mean values in Figure 5-1. Within the spanwise range of  $+1.0B$  to  $-1.4B$  (the range where spanwise coherence measurements—presented in Chapter 7—were taken), these values have a standard deviation of 6% with respect to local mean pressures and less than 1% with respect to the dynamic pressure.

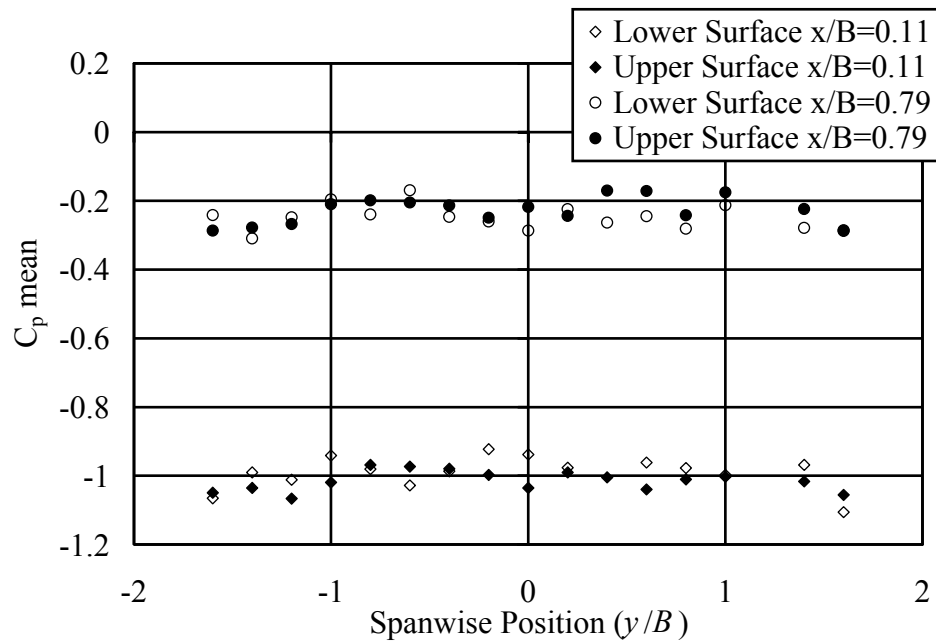


Figure 5-1 Spanwise distributions of mean pressure coefficients at two streamwise locations,  $x/B = 0.11$  and  $x/B = 0.79$ .

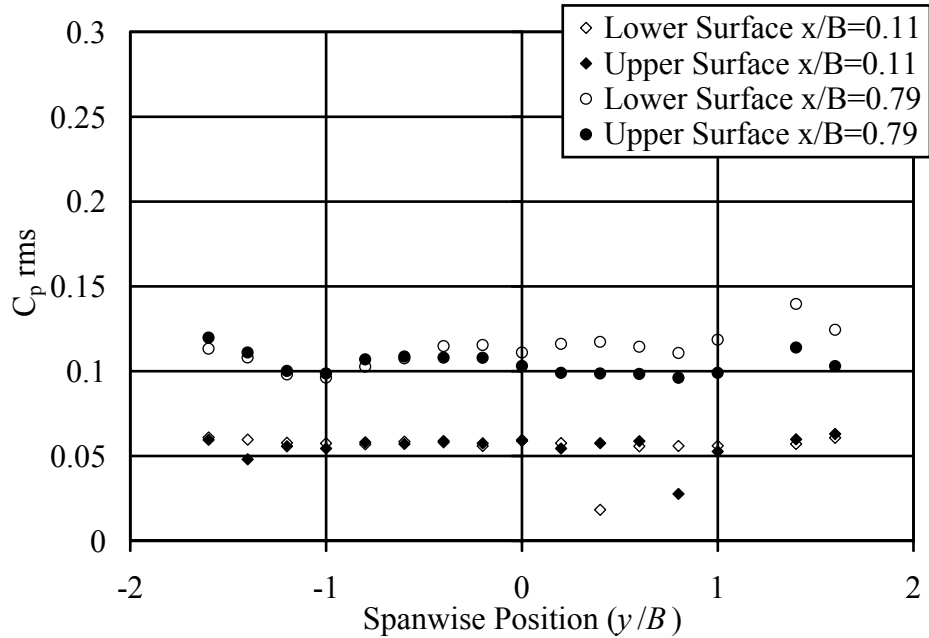


Figure 5-2 Spanwise distributions of RMS pressure coefficients at two streamwise locations,  $x/B = 0.11$  and  $x/B = 0.79$ .

Because of the possibility that incident flow angles could vary from one flow to another, tests were done to verify the reference angle of attack (as discussed above) for each flow. Because the work in this study focuses mainly on dynamic pressures, the RMS distributions were examined for this test. Good matches for the upper and lower surface RMS pressure distributions were obtained with a geometric angle of attack of  $-1^\circ$  for each case. One example of these tests is shown in Figure 5-3 where the upper and lower surface distributions for Case 12b are plotted. Except for one value near the peak where the mismatch was near 3% of dynamic pressure, the match was excellent.

Figure 5-4 presents the RMS pressure coefficients along with data from the literature. The data from the current project compare well with previous research. More specifically, the various data sets show consistency in terms of the location of the

maximum in the distribution moving toward the leading edge with increasing turbulence intensity and in terms of greater turbulence scales resulting in greater RMS values.

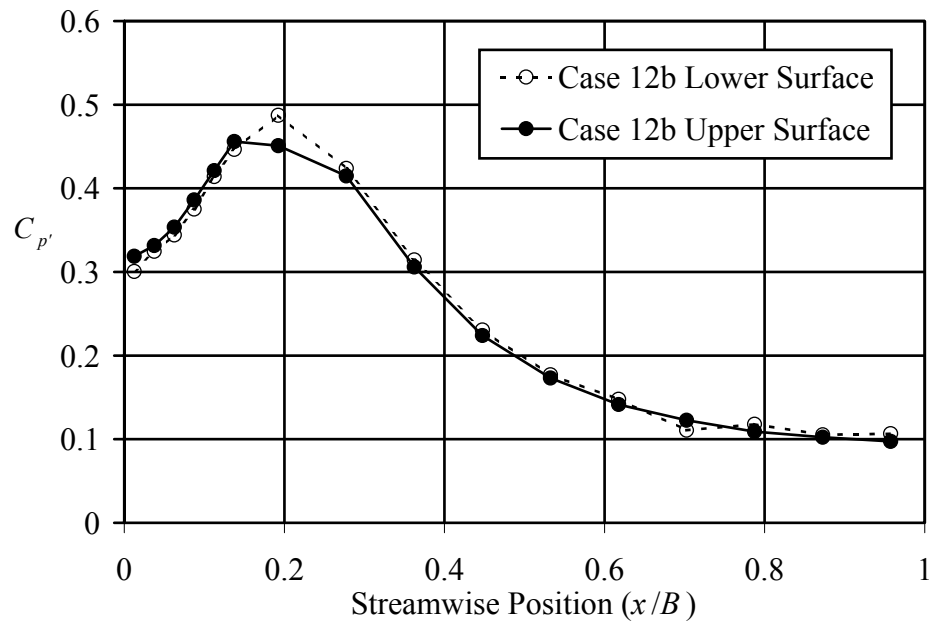


Figure 5-3 Streamwise distribution of RMS pressures for upper and lower surfaces at the model centerline measured to set the reference angle of attack.

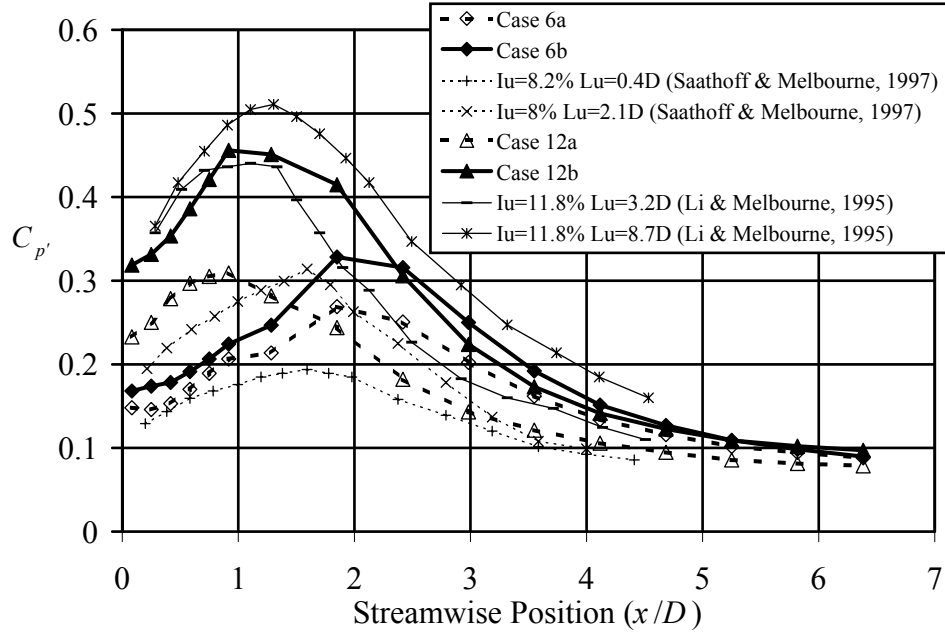


Figure 5-4 Streamwise distributions of RMS pressure fluctuations compared with data from the literature.

### 5.3 Statistical Distributions of Pressure

An understanding of the behavior of the statistical pressure distributions in turbulent flows provides a foundation for studying the behavior of dynamic pressures. This section shows the distributions of the mean, RMS, and peak pressure coefficients,  $C_p = 2(p - p_\infty) / \rho U^2$ . The distributions of the skewness and kurtosis coefficients are also shown to provide information on the non-Gaussian characteristics of the pressures along the streamwise direction.

Figure 5-5 shows the streamwise distribution of mean pressure values for each of the five flow cases. As the turbulence intensity is increased from smooth flow, the minimum pressure decreases and occurs nearer to the leading edge. The pressure recovery also becomes steeper. From their extreme values, the pressure coefficients

return to  $-0.4$  near  $0.6B$  in smooth flow, near  $0.4B$  for  $I_u = 6\%$ , and near  $0.3B$  for  $I_u = 12\%$ . For the range of integral scales included in these cases, there is only a slight effect of scales. With increasing integral scale, the pressure values increased slightly without changing the shape or the steepness of the curve significantly.

Figure 5-6 and Figure 5-7 show the distributions of the RMS and peak pressure coefficients, respectively. Both of these distributions show similar behavior with respect to turbulence intensity and scale. In both cases, increasing turbulence intensity corresponds to larger magnitudes in the distribution and to the location of maxima moving nearer the leading edge. The general hump-like shape of the distributions does not change—rather, they can be described as being “compressed” toward the leading edge. In this sense, the behavior is similar to that observed for the mean pressure distributions.

With respect to scales, however, the RMS and peak pressure distributions have a greater sensitivity to turbulence scale than do the mean pressure distributions. While turbulence intensity changes the streamwise position of the distribution maxima, turbulence scale changes the amplitudes of the distributions. For example, this behavior can be seen in Figure 5-6 for the Case 6 distributions—both having a turbulence intensity of 6%. Both maxima are located near  $0.28B$  but the change in  $L_{ux}$  from  $1.8D$  to  $4.9D$  corresponds to a change in the RMS value from 0.27 to 0.33 (an increase of  $\sim 20\%$ ). This same trend also manifests itself in the peak pressure distributions as shown in Figure 5-7. Data from a number of other sources show these same trends for RMS and peak pressures with respect to turbulence intensity and scale (Hillier & Cherry, 1981; Kiya & Sasaki, 1983; Saathoff & Melbourne, 1985, 1997; Li & Melbourne, 1995). The physical

significance of these trends for this study is that the location of the maximum in the RMS distributions occurs just upstream of the mean reattachment position (Kiya & Sasaki, 1983).

The skewness and kurtosis coefficients for the pressure fluctuations were also quantified. These distributions are shown in Figure 5-8 and Figure 5-9, respectively. The skewness coefficient is defined as the third central moment, the skewness, of a random variable normalized by that variable's standard deviation raised to the third power. This can be written as:

$$S_k = \frac{\sum (p_i - \bar{p})^3 / N}{[\sum (p_i - \bar{p})^2 / N]^{3/2}} = \frac{\sum (p_i - \bar{p})^3 / N}{\sigma_p^3} \quad (5-1)$$

where  $p_i$  represents individual pressure samples,  $\bar{p}$  is the mean pressure,  $N$  is the number of samples in the data set, and  $\sigma_p$  is the standard deviation of the pressure data.

The kurtosis coefficient,  $K_u$ , is calculated similarly but with the fourth moment normalized by the fourth power of the standard deviation. The skewness coefficient is a measure of the degree of symmetry or lack of symmetry of a random variable about its mean. While a symmetric probability distribution has a skewness of zero, a positive or negative skewness is possible. The kurtosis coefficient quantifies how narrow or how flat the probability distribution is. A Gaussian distribution has a kurtosis coefficient of three—a coefficient greater than three corresponds to a distribution more peaked than Gaussian while a coefficient less than three corresponds to a distribution flatter than Gaussian.

Figure 5-8 shows the distribution of the skewness coefficient for each flow case. As discussed in Chapter 2, regions of negative skewness are associated with separated

flow, and positive skewness has been observed in regions of flow reattachment. The basic shape of the distributions is that of a negative skewness near the leading edge followed by an increase in values toward zero followed further downstream by another decrease to negative values. Only the smooth flow and  $I_u = 6\%$  cases show regions of positive skewness. Scale effects manifested themselves as shifts toward more negative values for greater turbulence scales. These shifts were small near the leading edge, but downstream of the “rise toward zero” mentioned above, they were quite significant with greater changes occurring for  $I_u = 12\%$  than for  $I_u = 6\%$ . For Case 12, these downstream skewness values went from  $-0.33$  to  $-1.33$  for a scale change from  $1.3D$  to  $4.9D$ .

Kurtosis values, Figure 5-9, also showed significant changes with turbulence scale. Like the other statistical distributions, these scale effects were also more pronounced in flows of greater turbulence intensity. Maximum Case 12 kurtosis values increased from 4.6 to 6.8 from the “a” to the “b” case. The skewness and kurtosis distributions share the trait that their regions of greatest sensitivity to turbulence scale are further downstream than those of the RMS and peak distributions. The kurtosis values showed the greatest changes with different inflow conditions beyond  $x = 0.3B$ .

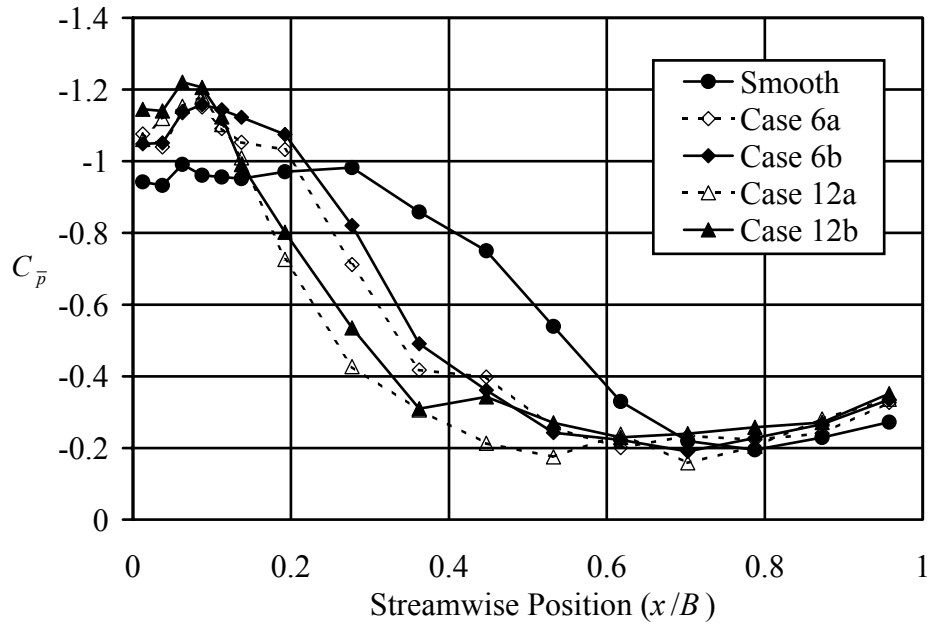


Figure 5-5 Mean pressure distributions for a stationary model in all flow cases.

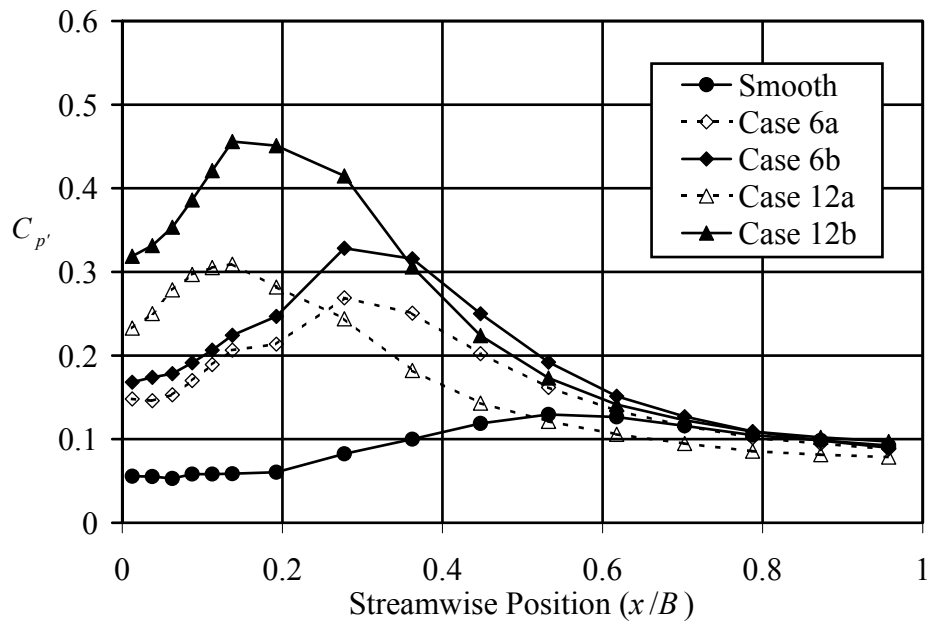


Figure 5-6 RMS pressure distributions for a stationary model in all flow cases.

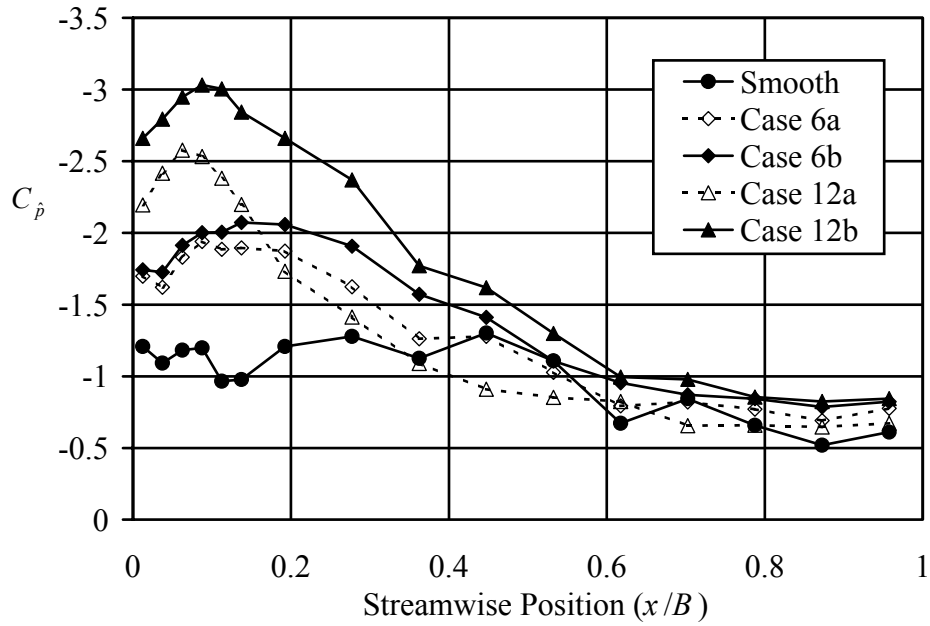


Figure 5-7 Peak pressure distribution for a stationary model in all flow cases.

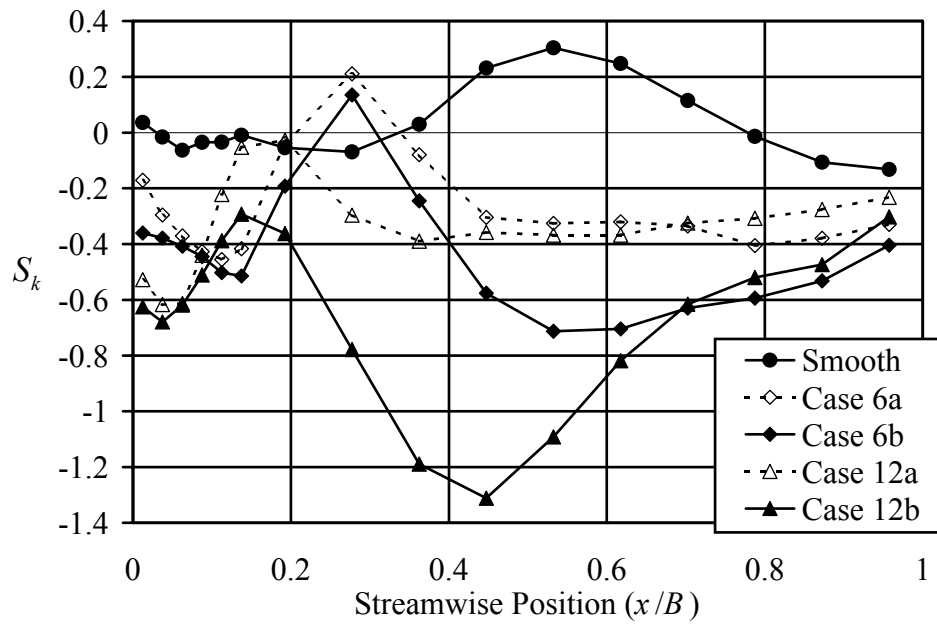


Figure 5-8 Skewness coefficient distribution for a stationary model in all flow cases.

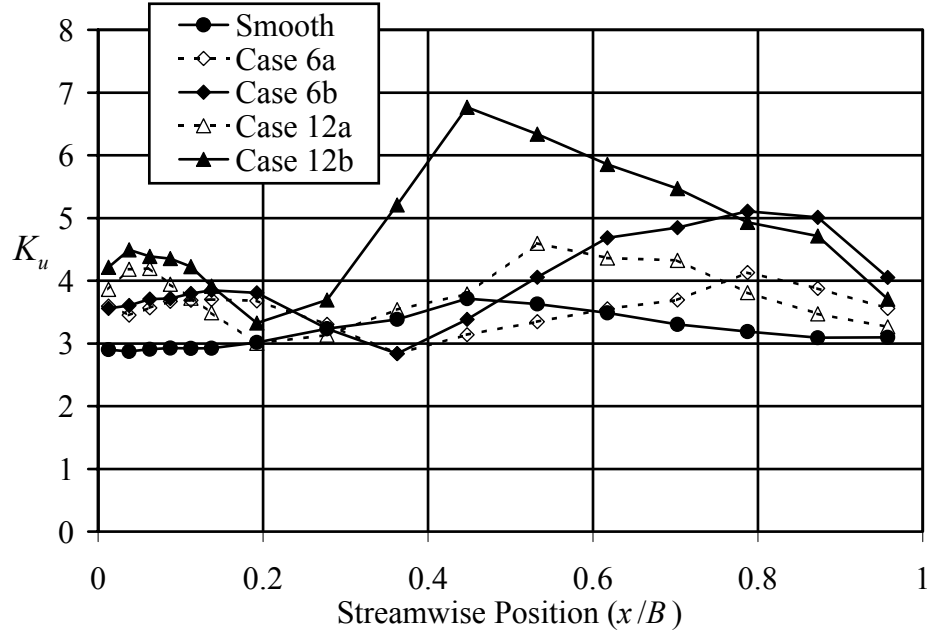


Figure 5-9 Kurtosis coefficient distribution for a stationary model in all flow cases.

#### 5.4 Pressure Spectra

Pressure spectra were calculated from the signals at each pressure tap. These spectra are presented in figures containing two rows of eight spectra each. These spectra correspond to streamwise positions from the leading edge to the trailing edge of the model.

Figure 5-10 contains the spectra for a stationary model in smooth flow. Every streamwise position shows a significant peak near  $fD/U = 0.02$  (in this case,  $f = 3.2\text{Hz}$ ). This frequency lies in the same range as the “low frequency flapping” motion measured by Cherry et al. (1984) in their studies of the separated shear layer about a blunt flat plate. They reported the frequency of this motion with the expression  $F_{\text{flap}} = 0.11U/x_R$  (where  $F_{\text{flap}}$  is the frequency in Hz,  $U$  is the mean freestream velocity,

and  $x_R$  is the reattachment length). For a reattachment length of  $x_R = 4.9D$  (Cherry et al., 1984), this expression predicts a low-frequency shear layer motion for the current tests to be 3.6 Hz. Cherry et al. (1984) suggested that this was related to some overall bubble growth-decay mechanism. The presence—and significance—of unsteadiness in this frequency range is discussed in Chapter 8.

A second distinct peak at  $fD/U = 0.19$  is prominent for all locations up to  $x = 0.19B$ . Increases in broad band energy levels for  $fD/U > 0.06$  bury this peak for all locations downstream of  $0.19B$ . Further downstream—beyond the probable location of reattachment ( $x \cong 0.6B$ )—a broader peak emerges near  $fD/U = 0.17$ . Near reattachment, the broad band energy levels for  $fD/U > 0.06$  reach a maximum from which they decrease further downstream. This fact was also reflected in the RMS pressure distributions already presented in section 5.3.

Spectra for Case 6a and 6b flows are presented in Figure 5-11 and Figure 5-12, respectively. Broad band energy levels are higher than those for smooth flow over the entire frequency range with Case 6b exhibiting higher energy at the lower frequencies than Case 6a. As in smooth flow, the broad band energy reaches a maximum near reattachment (i.e. near the location of maximum RMS pressure fluctuations) which is near  $x \cong 0.28B$ . Away from this location the broad band levels decrease enough to reveal the various salient peaks under consideration here. The Case 6a results show a broad peak near  $fD/U = 0.20$  for  $x > 0.87B$ . Case 6b results in this region exhibit an even broader peak with a slightly higher middle frequency of about  $fD/U = 0.21$ . Similar statements can be made of the Case 12a and 12b results in Figure 5-13 and Figure 5-14,

respectively. Case 12a flow produces a peak near  $fD/U = 0.20$  while the larger scales of Case 12b flow resulted in a broader peak near  $fD/U = 0.21$ .

These frequencies are higher than those found near the trailing edge of the model in smooth flow. Some sense can be made of this frequency shift when one considers the scaling relationship suggested by Sigurdson (1995) for the shedding of large scale structures from a separation bubble. Although this relationship was the result of work on a flat faced circular cylinder aligned coaxially with the free stream, the scaling was shown to apply to a wide range of separating and reattaching flow scenarios. This scaling relationship can be written as follows:

$$\frac{F_{\text{shed}} h}{U_s} = \text{constant} \quad (5-2)$$

where  $F_{\text{shed}}$  is the shedding frequency,  $h$  is the maximum height of the shear layer above the surface of the model, and  $U_s$  is the separation velocity (the velocity just outside the shear layer at separation). The separation velocity can be estimated from the following equation using Bernoulli's equation:

$$\frac{U_s}{U_\infty} = (1 - C_{p_s})^2 \quad (5-3)$$

where  $U_\infty$  is the mean freestream velocity and  $C_{p_s}$  is the pressure coefficient at separation (which, in this case, is estimated from the pressure coefficient measured nearest to the leading edge). From the mean pressure coefficients of Figure 5-5 and equation (5-3), one can predict that the separation velocity will be higher for the turbulent flows than for smooth flow. Also, due to the turbulence-induced reduction of the radius of curvature of the separated shear layer (as discussed in Chapter 2), the height of the

shear layer from the body,  $h$ , will be less. Both of these trends, when viewed in light of the scaling of equation (5-2), result in a higher frequency of shedding as observed for the turbulent-flow cases.

In addition to the effect that incident flow turbulence has on the shedding peak near  $fD/U = 0.20$ , it also changes the behavior near the low-frequency peak near  $fD/U = 0.02$  discussed earlier. In each turbulent flow, a harmonic of this peak appears at  $fD/U = 0.04$ . This harmonic was present but far weaker in smooth flow. In turbulent flow, this harmonic has an amplitude nearly the same as the primary peak. This may be the result of the invigorating effects of the perturbations of the shear layer due to turbulence.

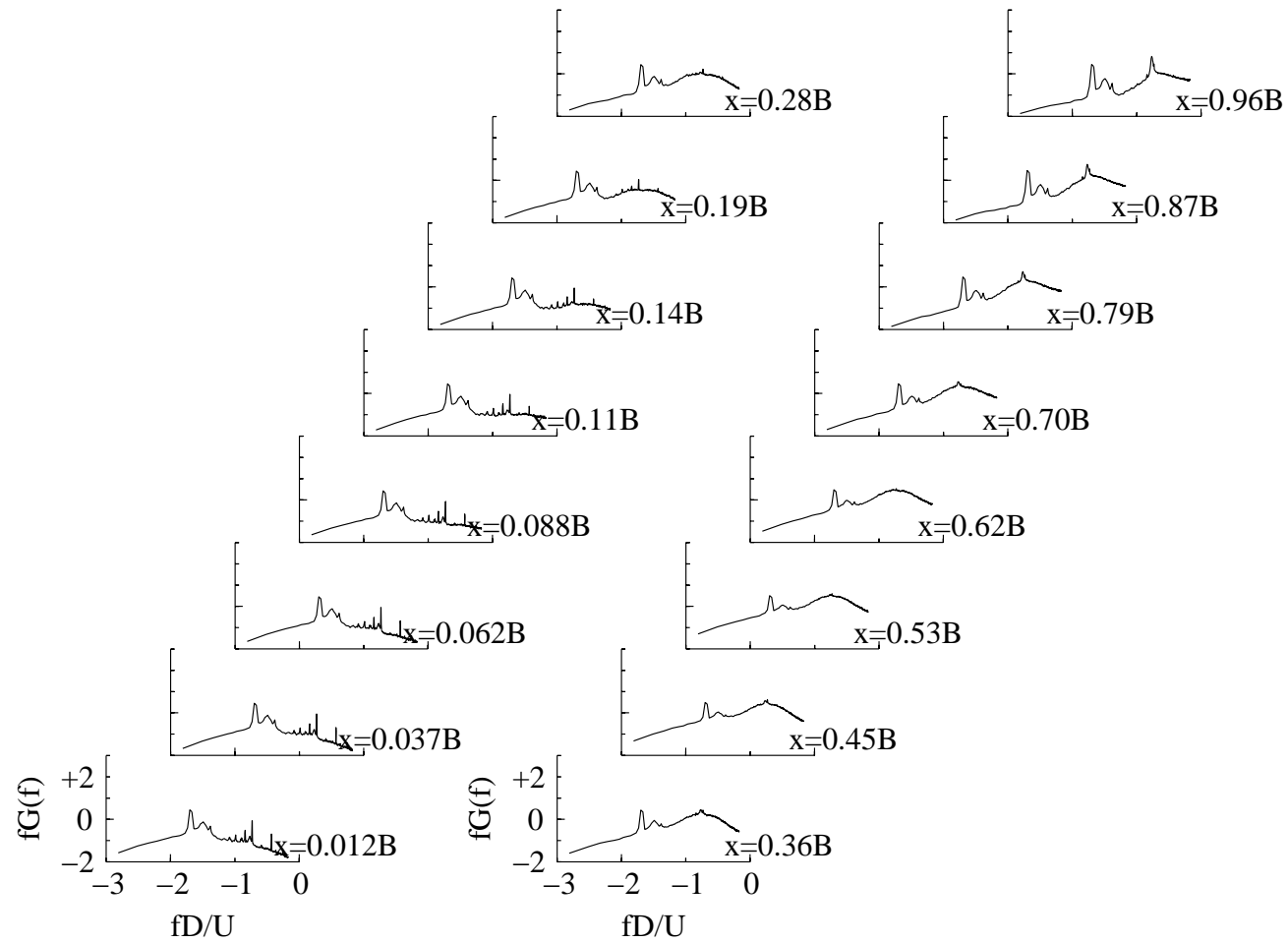


Figure 5-10 Power spectral densities for pressure signals on a stationary body in smooth flow.

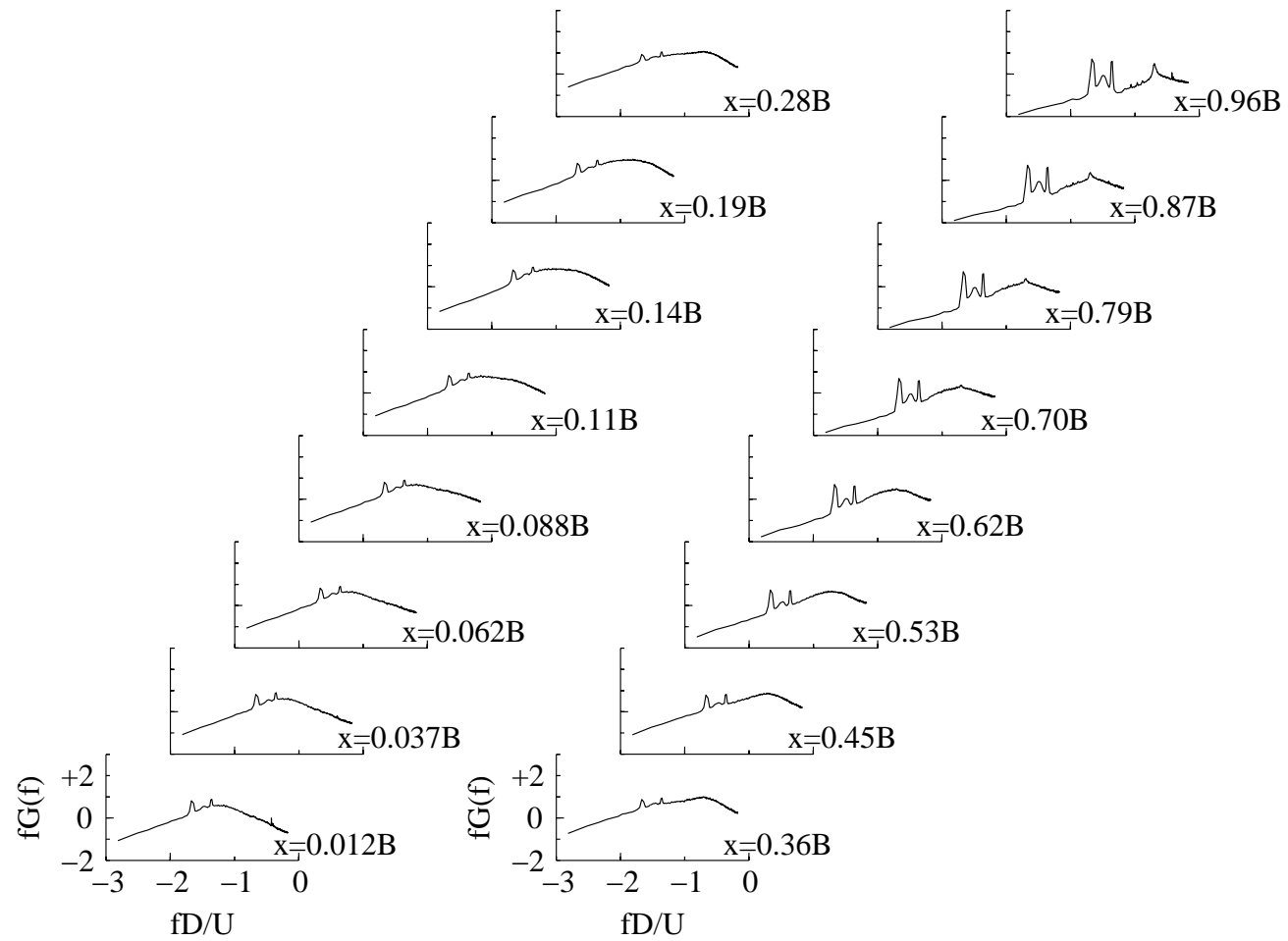


Figure 5-11 Power spectral densities for pressure signals on a stationary body in Case 6a flow.

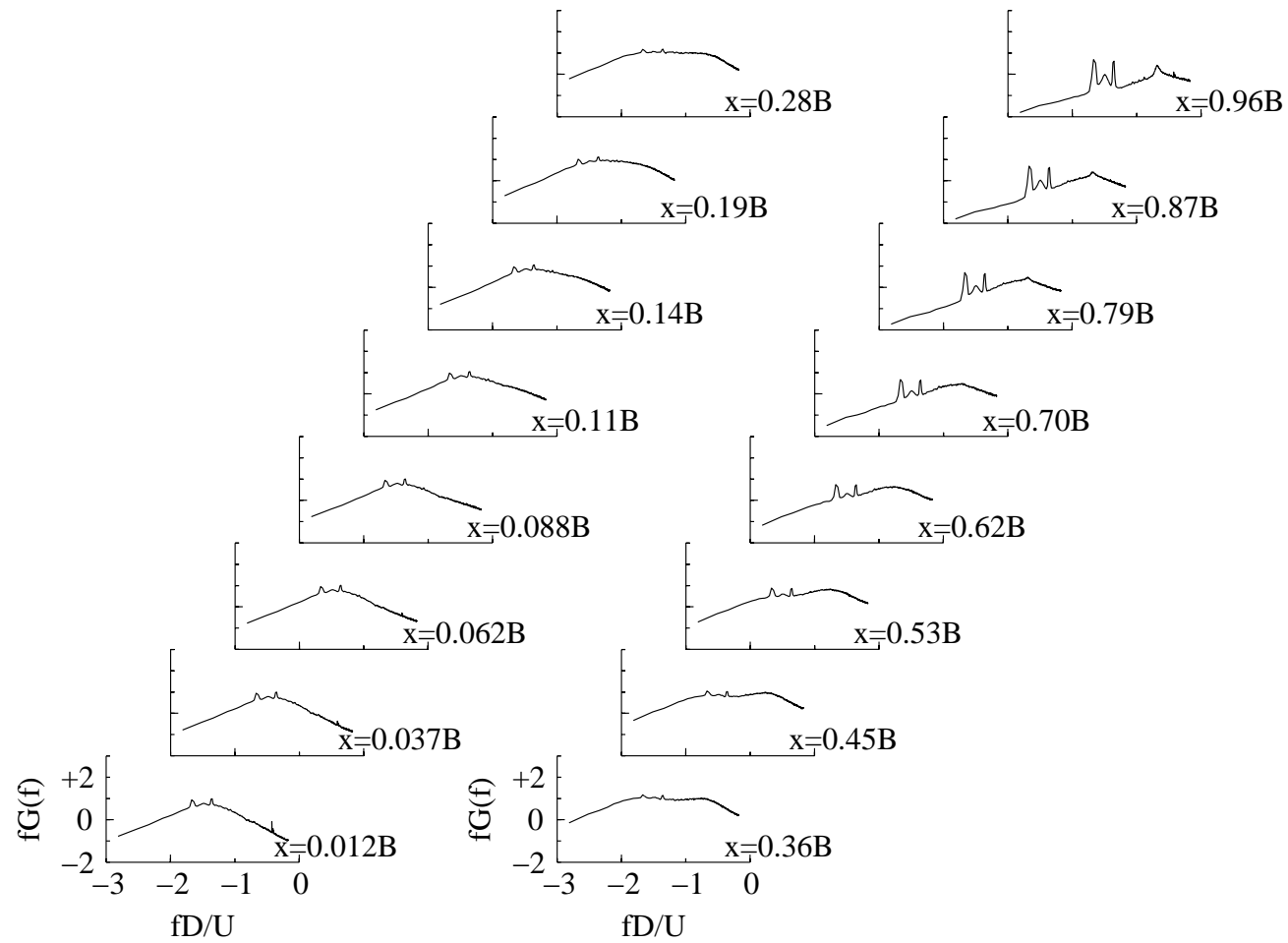


Figure 5-12 Power spectral densities for pressure signals on a stationary body in Case 6b flow.

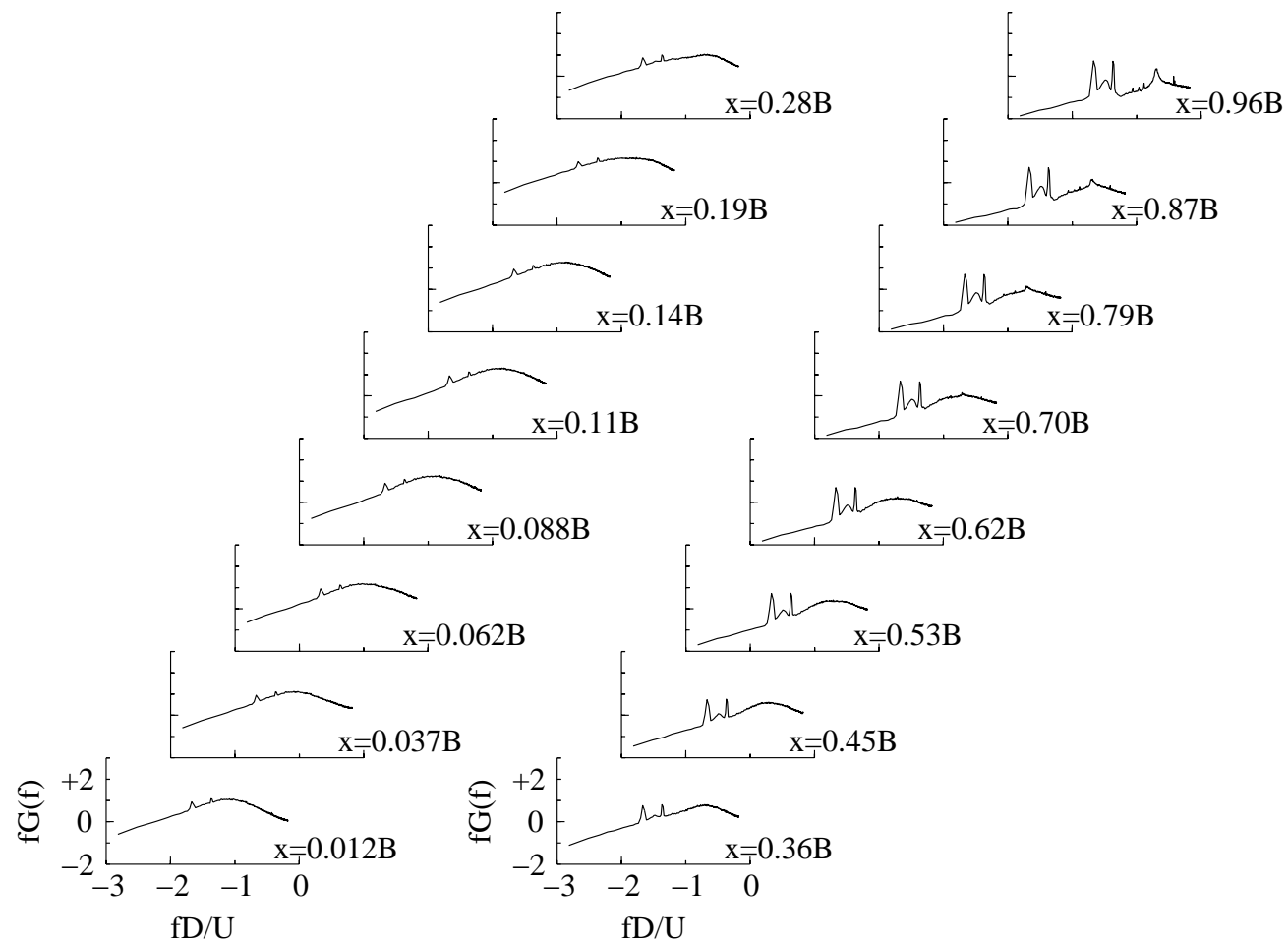


Figure 5-13 Power spectral densities for pressure signals on a stationary body in Case 12a flow.

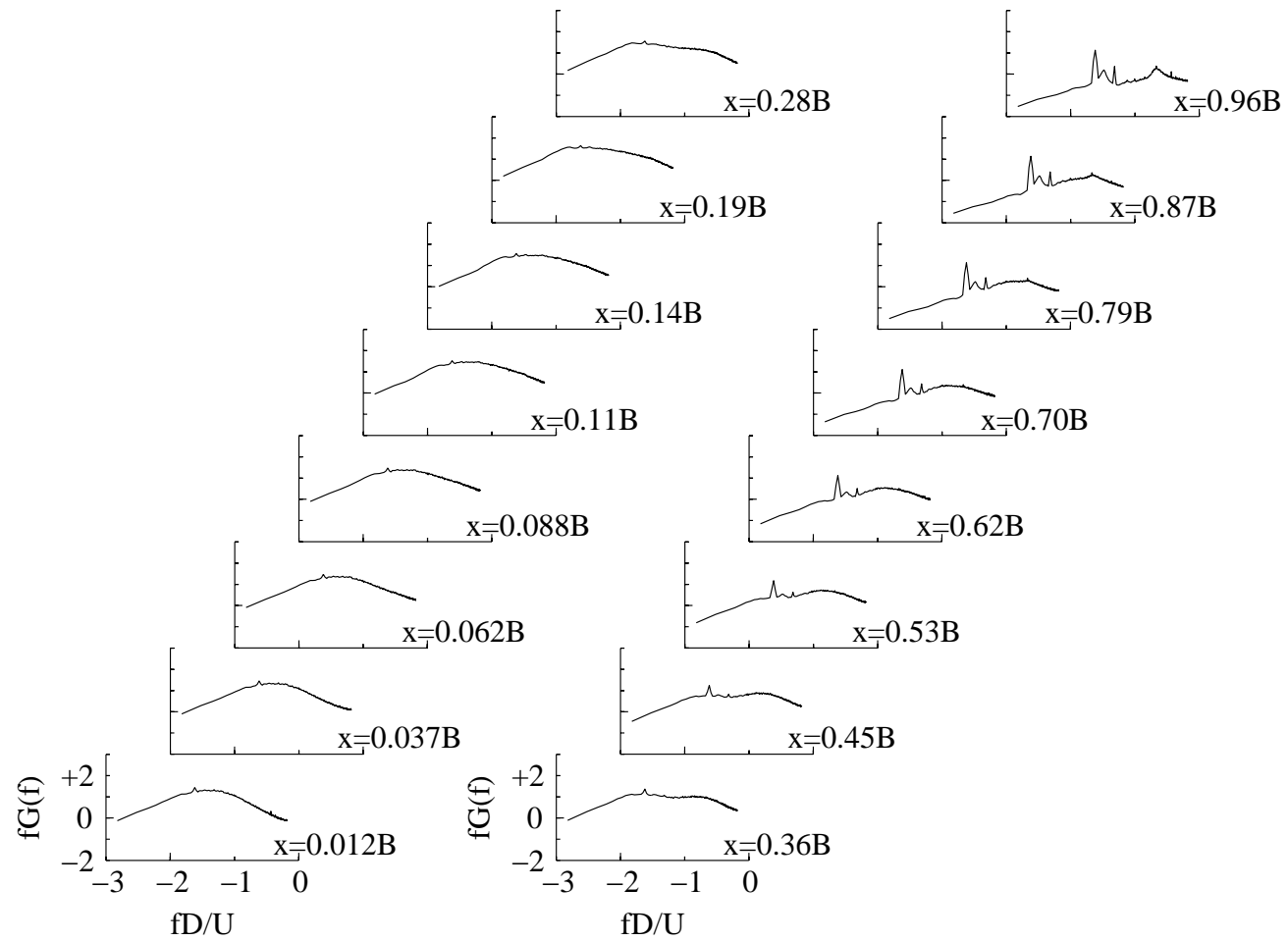


Figure 5-14 Power spectral densities for pressure signals on a stationary body in Case 12b flow.

## CHAPTER 6. PRESSURE FIELDS ON OSCILLATING MODELS—SECTION RESULTS

The primary goal of the experiments with dynamic models was to identify turbulence-induced modifications to the self-excited forces observed at a single section. Experiments consisted of measuring pressure during pitching motions in the series of turbulent flows described in Chapter 4. This chapter includes a short summary of the pressure analysis methods used here followed by a presentation of the results of these analyses. These results include the power spectral densities of both the integrated forces and the individual pressure signals, the pressure amplitude and phase distributions, the flutter derivatives corresponding to these amplitudes and phases, and the streamwise distributions of various statistical quantities of the pressure fluctuations.

### 6.1 Summary of Pressure Measurement Experiments

The test data in this chapter were taken during torsional oscillations of the model at various reduced velocities,  $U_r$ . Reduced velocity is defined as:

$$U_r = \frac{U}{f_\alpha B} \quad (6-1)$$

where  $U$  is the mean free stream velocity,  $f_\alpha$  is the model's torsional oscillation frequency, and  $B$  is the model dimension in the streamwise direction (the "bridge deck width"). Altering either the oscillation frequency or the flow velocity can vary the

reduced velocity. Because of the possibility that Reynolds number changes could alter the flow structure in a way indistinguishable from that of turbulence-induced modifications, the reduced velocity was always varied by changing the oscillation frequency.

The mean flow velocity for all tests reported in this dissertation was 6.0 m/s. This value was chosen as a balance between the need for large dynamic pressures to get good signals from the pressure transducers and the need for a low velocity to reach the desired range of  $U_r$ . The dynamics of the servo motor and oscillation mechanism dictated a maximum torsional oscillation frequency of 7.5 Hz which set the minimum reduced velocity at 3.1—a satisfactory value for this study. The range of  $U_r$  tested was then 3.1-25 with a gap between 3.1 and 8 determined by the resonance of the oscillation mechanism described in Chapter 3.

## 6.2 Force and Pressure Spectra

Examination of the lift and moment spectra give a unique picture of the force decomposition described in Chapter 1. Bridge analysis techniques often assume that aerodynamic lift and moment can be expressed as the sum of self-excited and buffeting components. Power spectral densities of lift and moment are presented on the following pages. In each case, the stationary model test results are plotted together with the oscillating model results to examine the merits of decomposing the forces.

Smooth flow spectra for reduced velocities of 3.1, 8, and 20 are presented in Figure 6-1 through Figure 6-3. It should be noted here that for these and all force and

pressure spectra presented in this chapter, the 95% confidence intervals are approximately the thickness of the thick shaded line of the stationary model results. In each case, the spectra of the oscillating models consist of broad band levels somewhat similar to the stationary model results with large peaks at the model oscillation frequency and its harmonics. Significant differences between the stationary and oscillating model broad band levels are evident. Although noteworthy, these differences do not significantly affect the validity of the decomposition of forces because the very low turbulence levels result in low levels of buffeting force. Buffeting forces in smooth flow result mainly of the turbulence generated by the body itself—commonly known as “signature turbulence.” When the model oscillates, the energy of this “signature turbulence” is increased mainly for frequencies above  $fD/U = 0.01$ .

Another effect of the oscillation is the shift of the shedding frequency peak near  $fD/U = 0.2$ . Stationary model pressure spectra presented in Chapter 5 exhibited a shift of this peak to higher frequencies when turbulence was added to the incident flow. In this case, the oscillation of the model caused a similar shift of this peak to higher frequency.

Spectra for the corresponding moments corresponding to these same smooth flow tests are presented in Figure 6-4 through Figure 6-6. General behavior of the moment spectra was similar to that of the lift spectra, but the discrepancy between stationary and oscillating model broad bands levels was more pronounced. Increases in broad band levels due to oscillation was not limited to  $fD/U > 0.01$  as for the lift spectra. Increases occurred over the entire frequency range. The same shift of the shedding peak at  $fD/U = 0.2$  also occurred.

Spectra for turbulent flow cases are presented in pairs corresponding to equal turbulence intensity and different turbulence scale. Lift spectra stationary and oscillating models ( $U_r = 3.1$ ) in Case 6 flows are plotted in Figure 6-7. Broad band energy levels are much larger than for the smooth flow cases as expected. Larger turbulence scales in the incident flow also shift the maximum in the psd to lower frequencies. The similarity between the stationary and oscillating test broad band levels is much closer than for the smooth flow cases, and the broad band levels of the larger scale “b” case match better than those of the “a” case. When the turbulence intensity is increased to 12%, as in the Case 12 results plotted in Figure 6-8, the broad band levels match even better.

Figure 6-9 and Figure 6-10 show the moment spectra for these same turbulence cases. The general shape of these psd’s was similar to that of lift. The broad band levels for moment also matched better for increased turbulence intensity—just as in the case of the lift spectra.

Lift and moment spectra are also presented for  $U_r$  values of 8 and 20. Figure 6-11 through Figure 6-14 contain the groups of spectra for  $U_r = 8$ , and Figure 6-15 through Figure 6-18 contain those for  $U_r = 20$ . To summarize the dependence on reduced velocity, Figure 6-19 and Figure 6-20 plot the rms lift and moment coefficients, respectively, versus reduced velocity for each of the spectra plotted. The rms lift coefficient is defined as  $C_{L_{rms}} = L_{rms}/qB$  where  $q$  is the dynamic pressure. The moment coefficient is defined as  $C_{M_{rms}} = M_{rms}/qB^2$ . For  $U_r > 12$ , the rms lift was relatively constant, but a maximum occurred in the range  $3.1 < U_r < 8$ . The general shape of the  $U_r$  dependence of the force amplitudes was similar to that of the angular amplitude

dependence on  $U_r$ , (see Chapter 3). Although oscillation amplitude dependence may explain some or most of the aerodynamic force dependence on reduced velocity, Chapter 8 also discusses this problem with respect to the dynamics of the shear layer.

The match between stationary model buffeting spectra and the buffeting components of the oscillation model spectra did not depend significantly on reduced velocity. The various spectra described above were integrated and compared to quantify the differences between stationary and oscillating model broad band levels. To compare only broad band levels, the oscillating test spectra were integrated without the peak associated with the oscillation frequency. Comparisons of such differences are plotted in Figure 6-21 and Figure 6-22 for lift and moment, respectively. These plots show the difference between the rms values of the broad bands normalized by the stationary model values. Difference range from as small as 2% to just over 10%, although no apparent trends exist for reduced velocity dependence. As observed in the spectra themselves, the broad bands matched better for higher turbulence intensity and for larger integral scales.

For more detailed examination of the spectral character of the aerodynamic forces, power spectral density functions for the pressure signals at each of the sixteen streamwise positions are presented here for several reduced velocities. In each case, the PSD's for both the stationary model tests (already presented in Chapter 5) and the oscillating model tests are plotted together for comparison. The spectral character of the pressure fluctuations shown here exhibit behaviors influenced not only by the shear layer behavior and the corresponding effects of turbulence but also by the influence of the forced oscillation of the body.

Three groups of five figures each will be presented. Each group consists of the results from a particular reduced velocity in every incident flow case. Figure 6-23 through Figure 6-27 present the PSD's for tests at a reduced velocity of 3.1 in each flow. Stationary model PSD's are shaded and plotted thicker than the oscillating model results. What is remarkable is the similarity between the broad band spectra of the stationary and oscillating cases—particularly for the turbulent flow tests. For the most part, the oscillating model pressures have the same spectra as the stationary model except for a peak at the model oscillation frequency.

The smooth flow spectra of Figure 6-23 exhibits a number of aspects worth noting. As in the case of the stationary model results of Chapter 5, behavior of the peaks can be divided into two regions—upstream and downstream of  $x \cong 0.28B$ . This is also the approximate location of the maximum RMS pressure values (complete statistics will be presented later in the chapter) and the approximate location of reattachment.

The pressure signals upstream of reattachment show three salient peaks. Two of these, at  $fD/U = 0.02$  (the low-frequency unsteadiness of the shear layer) and at  $fD/U = 0.19$  (the shedding frequency of large-scale structures from the separation bubble), were also observed in the stationary model tests. The largest peak is at  $fD/U = 0.048$ —the model oscillation frequency. The broad band levels increase from the leading edge to reattachment and decrease from reattachment to the trailing edge. This increase obscures the peak at 0.19. Beyond reattachment, two harmonics of the model oscillation frequency appear at  $fD/U = 0.095$  and 0.14.

Figure 6-24 and Figure 6-25 show the spectral for Case 6a and Case 6b flows, respectively. In both cases, broad band power levels are much higher than those in

smooth flow, and the shedding peak located at  $fD/U = 0.19$  in smooth flow is no longer visible. Downstream of reattachment—which occurs near  $x \cong 0.16B$ —only the model oscillation frequency and the low-frequency unsteadiness show pronounced peaks. Turbulence in the incident flow prevents the formation of the harmonics seen in the smooth flow.

Case 12a and Case 12b spectra are shown in Figure 6-26 and Figure 6-27, respectively. Like the Case 6 flows, the model oscillation frequency is the only spectral peak upstream of reattachment. Downstream of reattachment both the model oscillation frequency and the low-frequency unsteadiness ( $fD/U = 0.02$ ) produces pronounced peaks.

The group of five spectra for the various flow cases at  $U_r = 8$  is presented from Figure 6-28 to Figure 6-32. Most aspects of these spectra are the same as those for  $U_r = 3.1$ . The smooth flow spectra show a vortex shedding peak at  $fD/U = 0.19$  upstream of reattachment. All five cases basically have the model oscillation frequency— $fD/U = 0.019$ —as the only peak upstream of reattachment. Downstream of reattachment, harmonics form. In smooth flow, up to four harmonics of the oscillation frequency manifest themselves in the spectra. Turbulent flow virtually eliminated the oscillation frequency harmonics as it did for the lower reduced frequency.

Unlike the  $U_r = 3.1$  cases, however, the  $U_r = 8$  turbulent cases show harmonics of both the oscillation frequency and the low-frequency unsteadiness downstream of reattachment. The 6% turbulence cases, Figure 6-29 and Figure 6-30, show how close the model oscillation frequency is to that of the low-frequency unsteadiness. A pair of double peaks form downstream of reattachment and differentiate from each other further

downstream. The first double peak is composed of the model oscillation frequency,  $fD/U = 0.019$ , and the low-frequency unsteadiness,  $fD/U = 0.022$ . The second double peak is made up of harmonics of these first two frequencies, 0.037 and 0.043, respectively. This same behavior is evident in the Case 12 spectra (Figure 6-31 and Figure 6-32) although the harmonics are much less pronounced in the larger scale turbulence of Case 12b. The ramifications of forcing the model motion near this shear layer unsteadiness are discussed in Chapter 8.

As the reduced velocity increases further to  $U_r = 20$  another change occurs for the spectra—see Figure 6-33 through Figure 6-37. Most aspects are the same as the lower  $U_r$  cases, but the behavior downstream of reattachment is different. All four turbulent flow cases for  $U_r = 20$  show the peak at the oscillation frequency decrease significantly toward the trailing edge. The dominant peaks far downstream of reattachment are the low-frequency unsteadiness and its first harmonic. This occurs for Case 6a, 6b, and 12a. Case 12b in Figure 6-37 only shows a peak at the low-frequency unsteadiness frequency. The larger integral scale of Case 12b suppressed its harmonic also—as seen in the other cases.

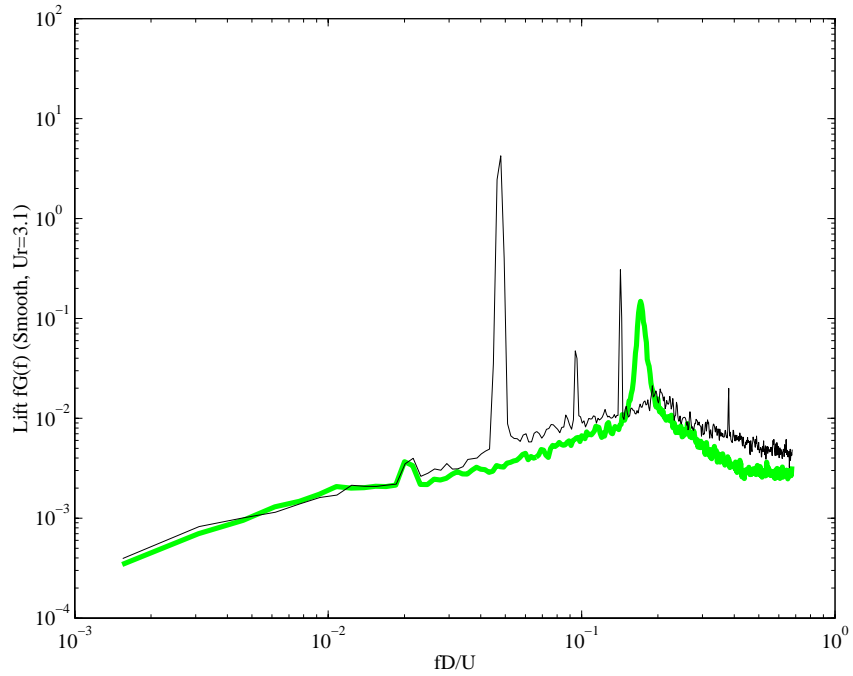


Figure 6-1 Lift force spectra in smooth flow for both stationary and  $U_r = 3.1$  tests (stationary results shaded).

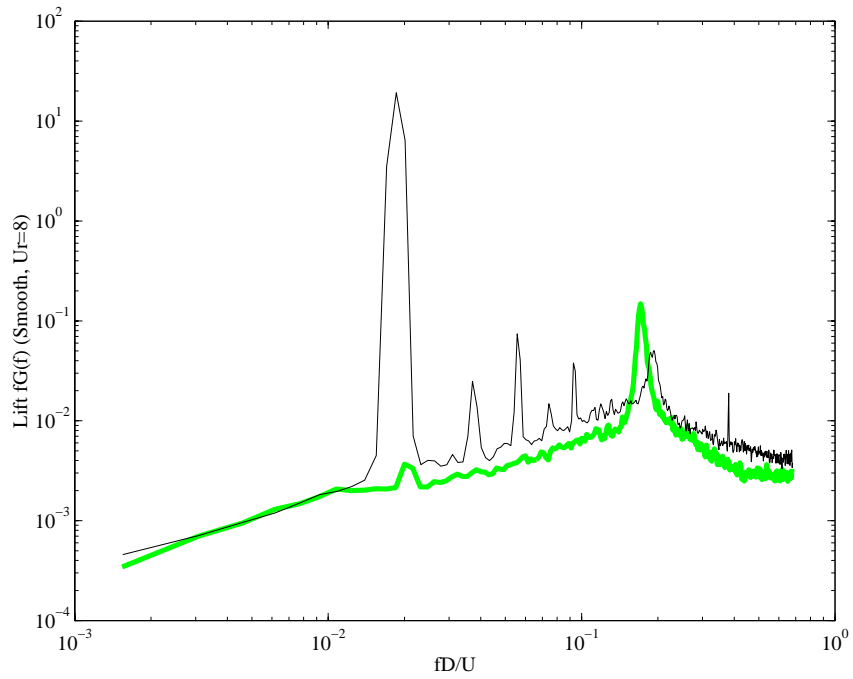


Figure 6-2 Lift force spectra in smooth flow for both stationary and  $U_r = 8$  tests (stationary results shaded).

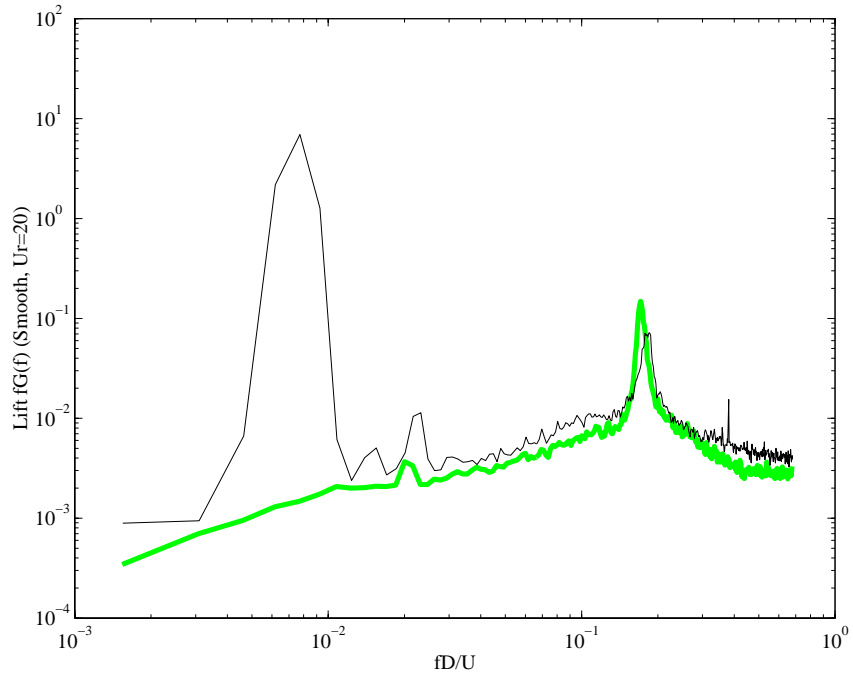


Figure 6-3 Lift force spectra in smooth flow for both stationary and  $U_r = 20$  tests (stationary results shaded).

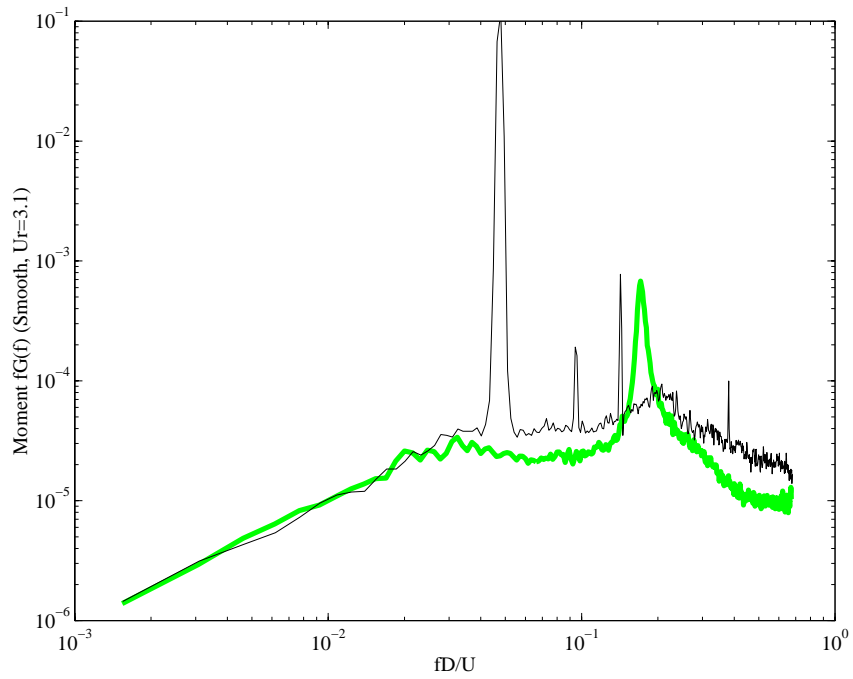


Figure 6-4 Moment spectra in smooth flow for both stationary and  $U_r = 3.1$  tests (stationary results shaded).

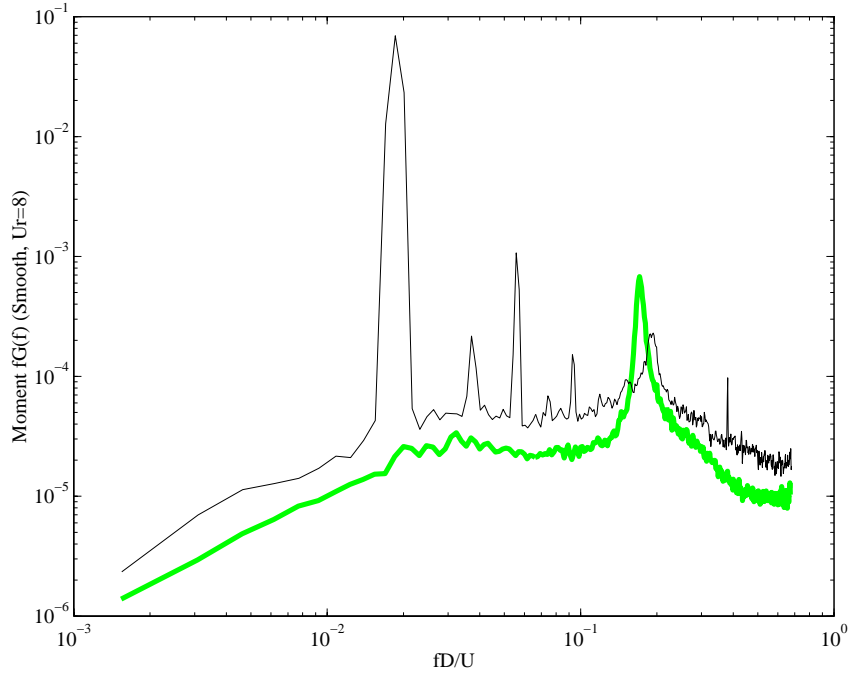


Figure 6-5 Moment spectra in smooth flow for both stationary and  $U_r = 8$  tests (stationary results shaded).

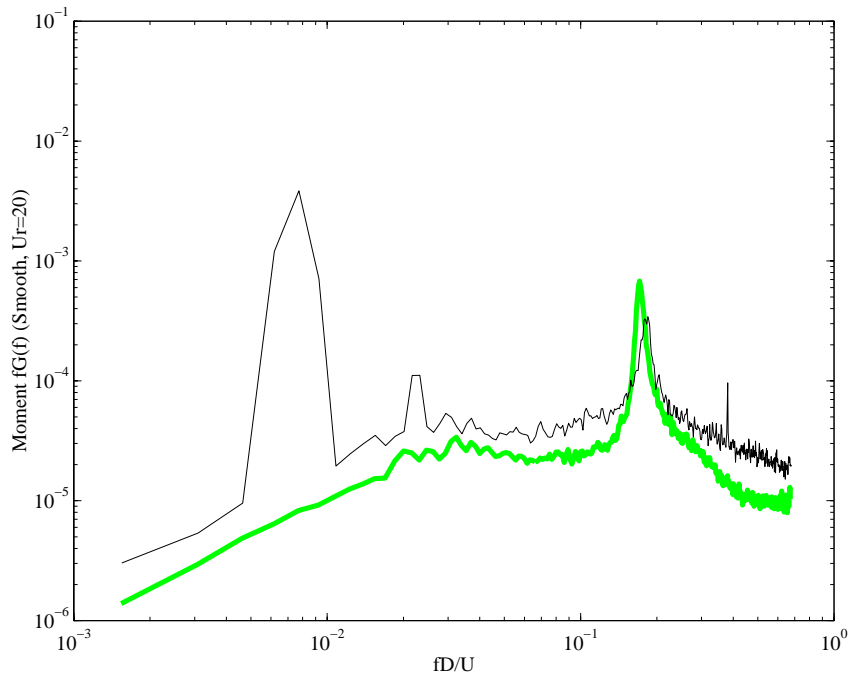


Figure 6-6 Moment spectra in smooth flow for both stationary and  $U_r = 20$  tests (stationary results shaded).

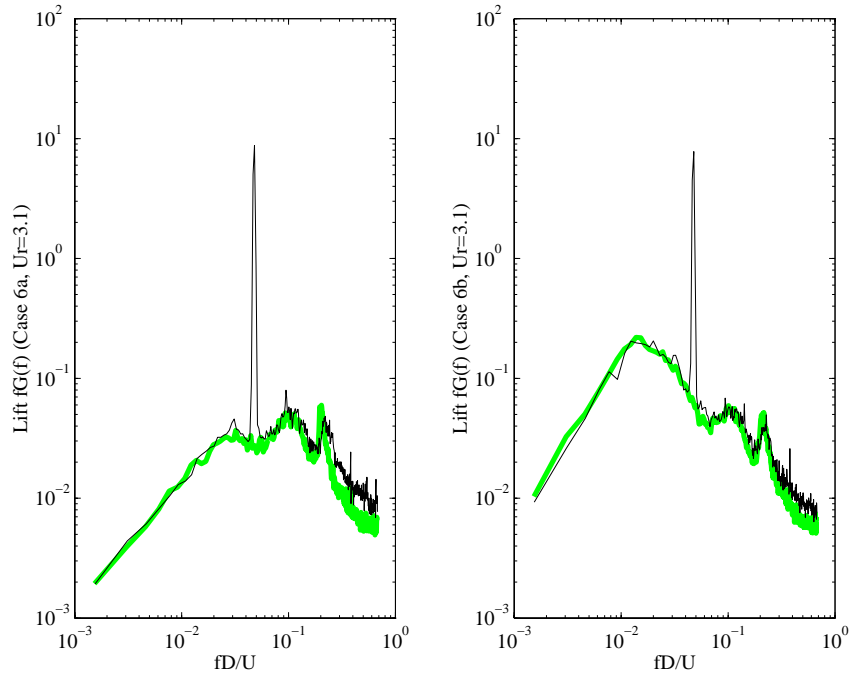


Figure 6-7 Lift force spectra for  $I_u = 6\%$  for both stationary and  $U_r = 3.1$  tests (stationary results shaded).

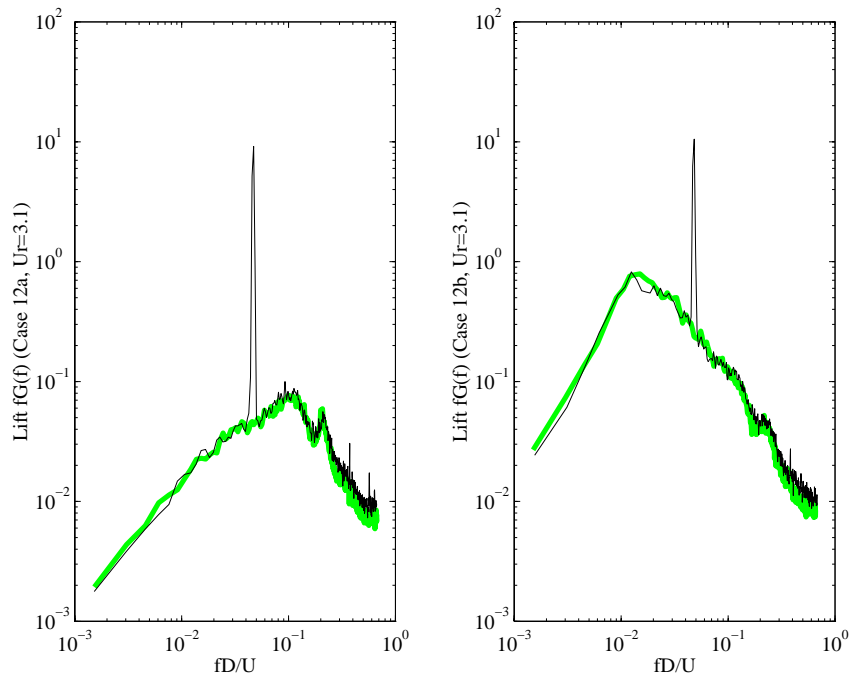


Figure 6-8 Lift force spectra for  $I_u = 12\%$  for both stationary and  $U_r = 3.1$  tests (stationary results shaded).

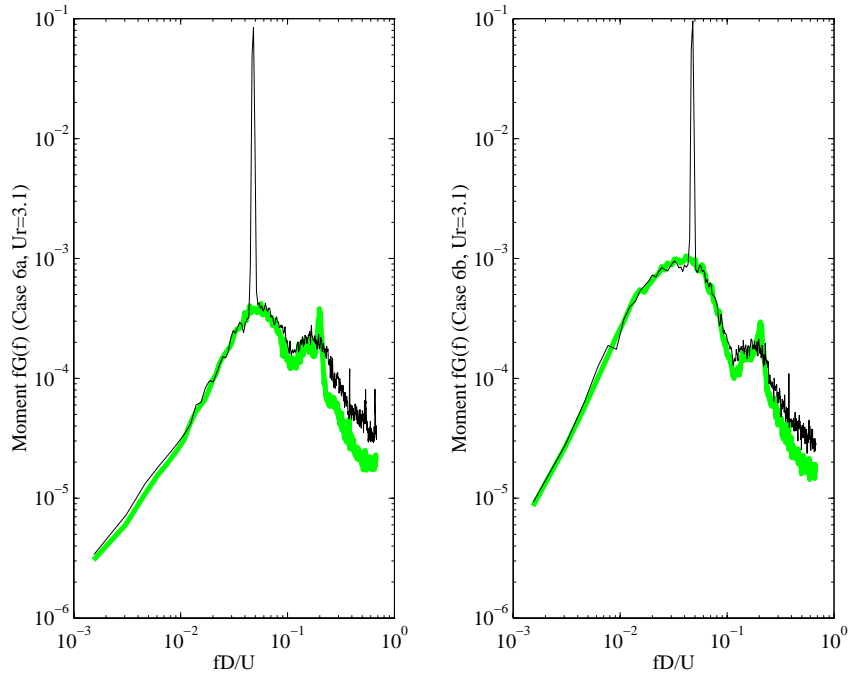


Figure 6-9 Moment spectra for  $I_u = 6\%$  for both stationary and  $U_r = 3.1$  tests (stationary results shaded).

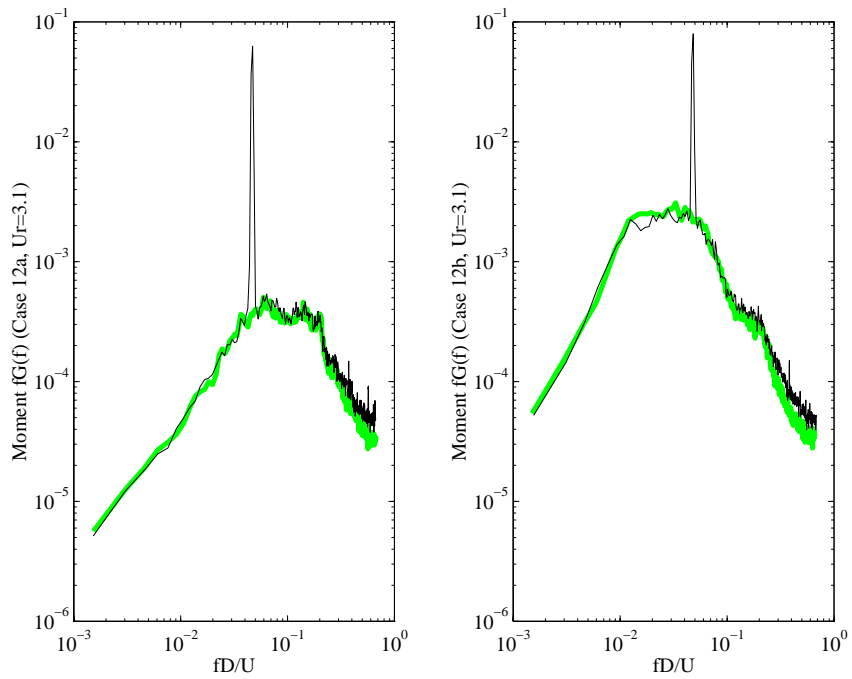


Figure 6-10 Moment spectra for  $I_u = 12\%$  for both stationary and  $U_r = 3.1$  tests (stationary results shaded).

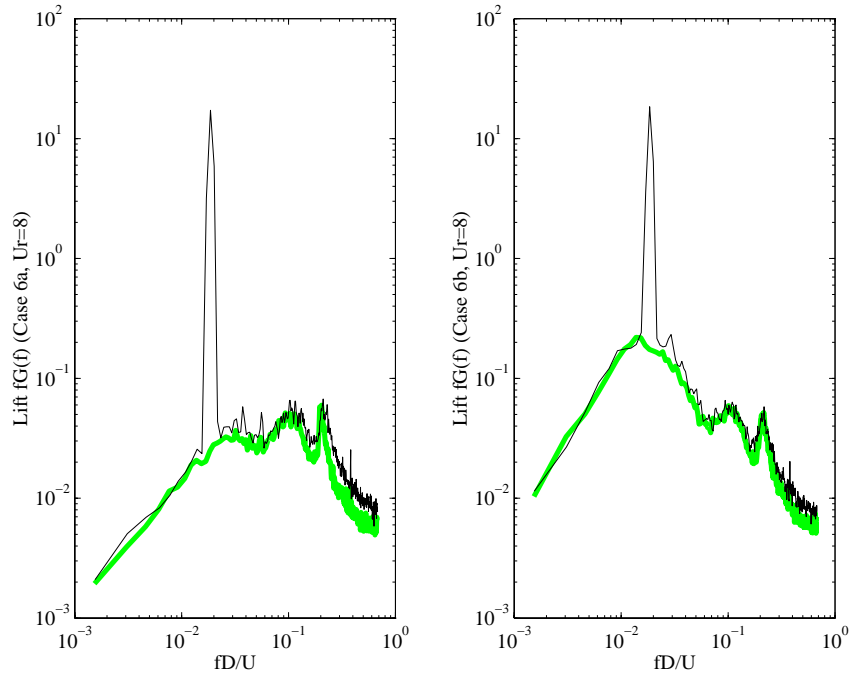


Figure 6-11 Lift force spectra for  $I_u = 6\%$  for both stationary and  $U_r = 8$  tests (stationary results shaded).

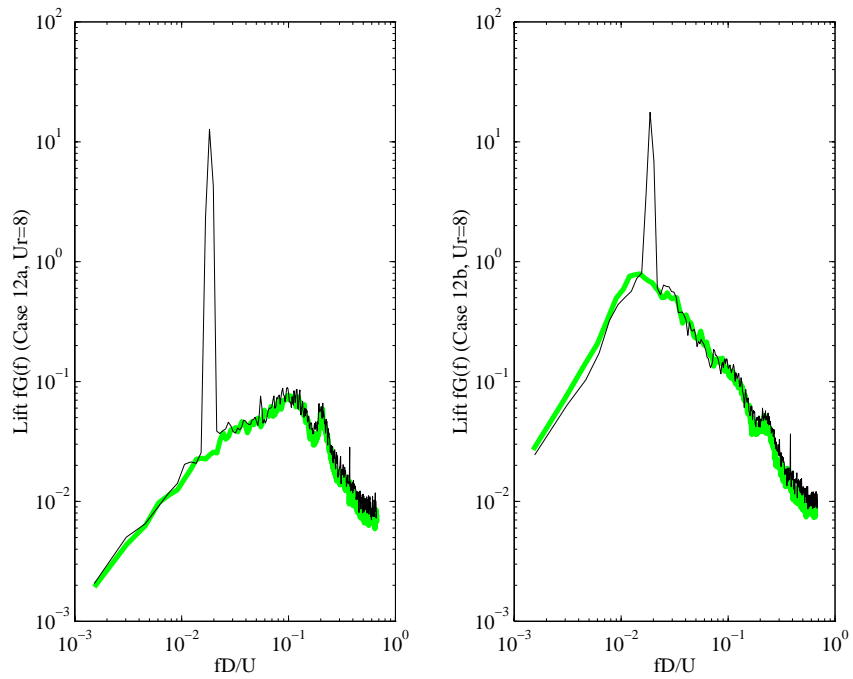


Figure 6-12 Lift force spectra for  $I_u = 12\%$  for both stationary and  $U_r = 8$  tests (stationary results shaded).

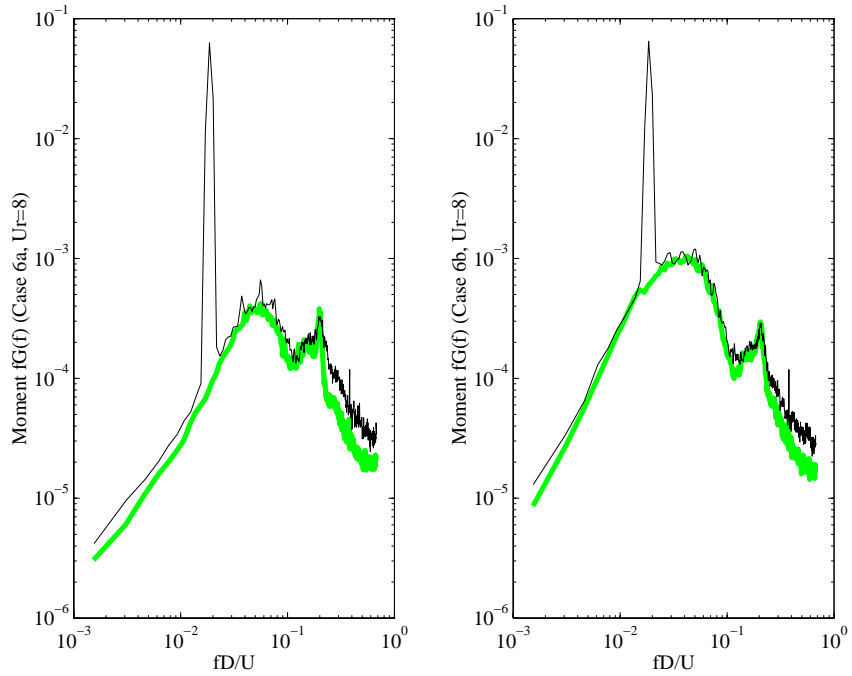


Figure 6-13 Moment spectra for  $I_u = 6\%$  for both stationary and  $U_r = 8$  tests (stationary results shaded).

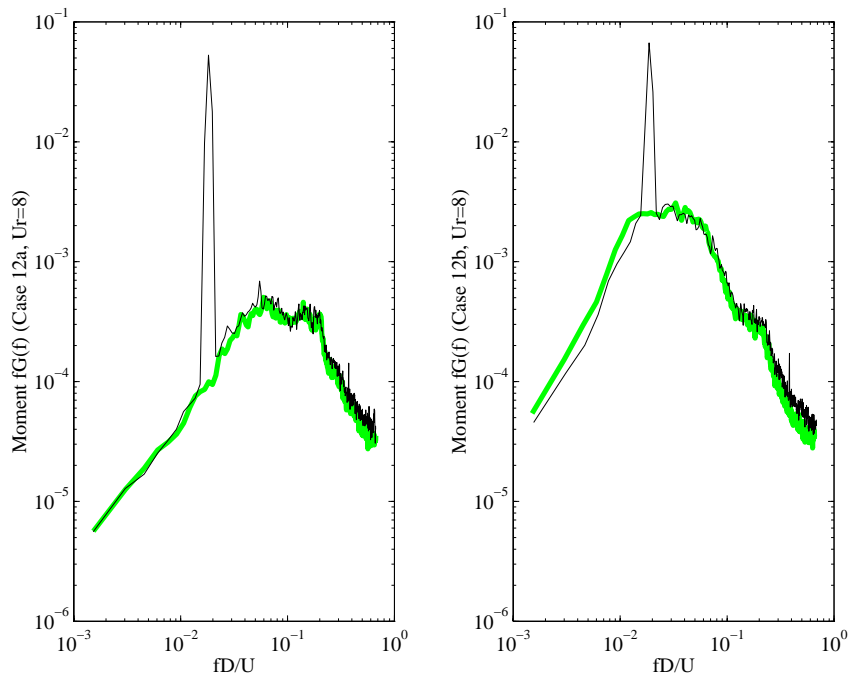


Figure 6-14 Moment spectra for  $I_u = 12\%$  for both stationary and  $U_r = 8$  tests (stationary results shaded).

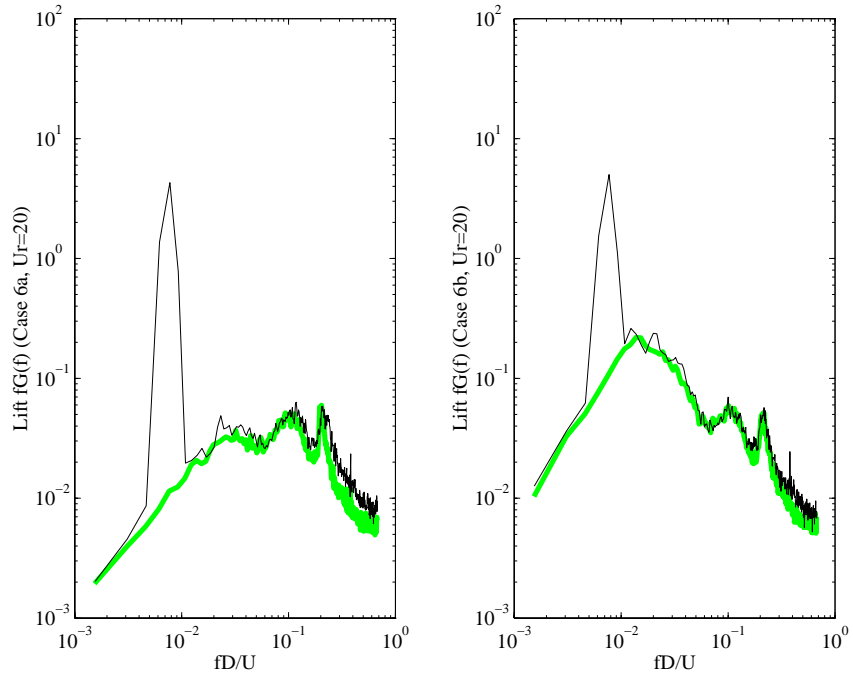


Figure 6-15 Lift force spectra for  $I_u = 6\%$  for both stationary and  $U_r = 20$  tests (stationary results shaded).

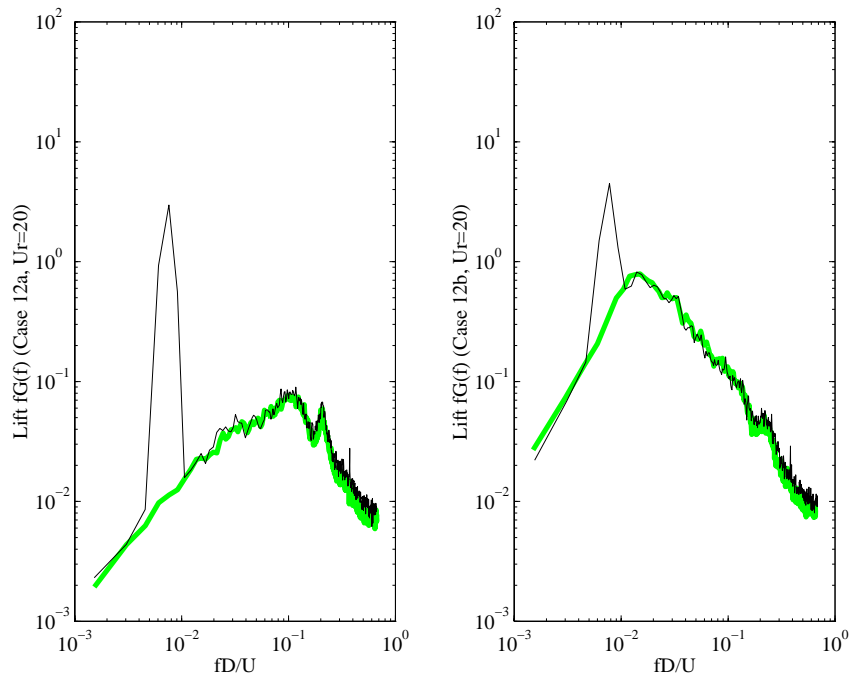


Figure 6-16 Lift force spectra for  $I_u = 12\%$  for both stationary and  $U_r = 20$  tests (stationary results shaded).

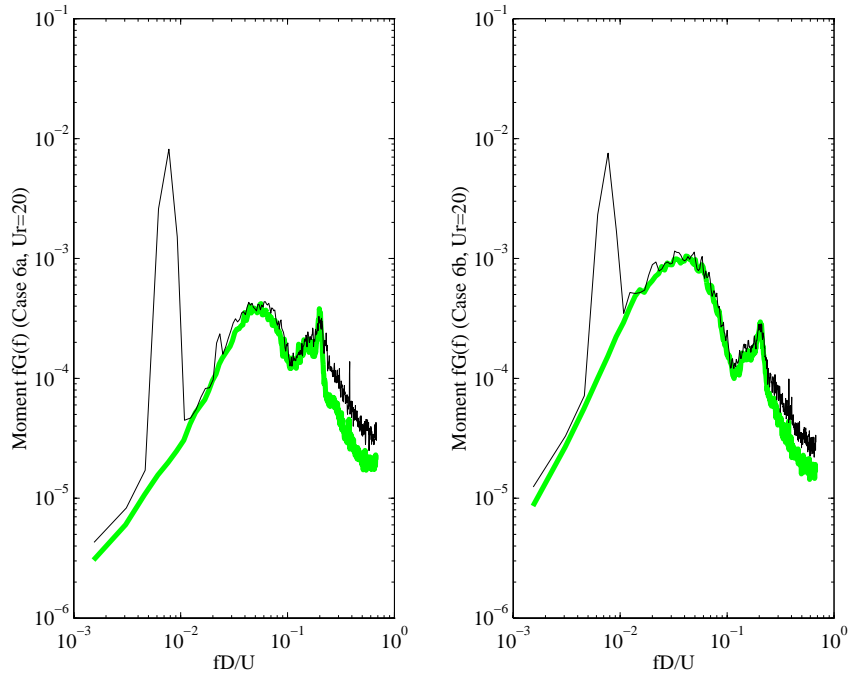


Figure 6-17 Moment spectra for  $I_u = 6\%$  for both stationary and  $U_r = 20$  tests (stationary results shaded).

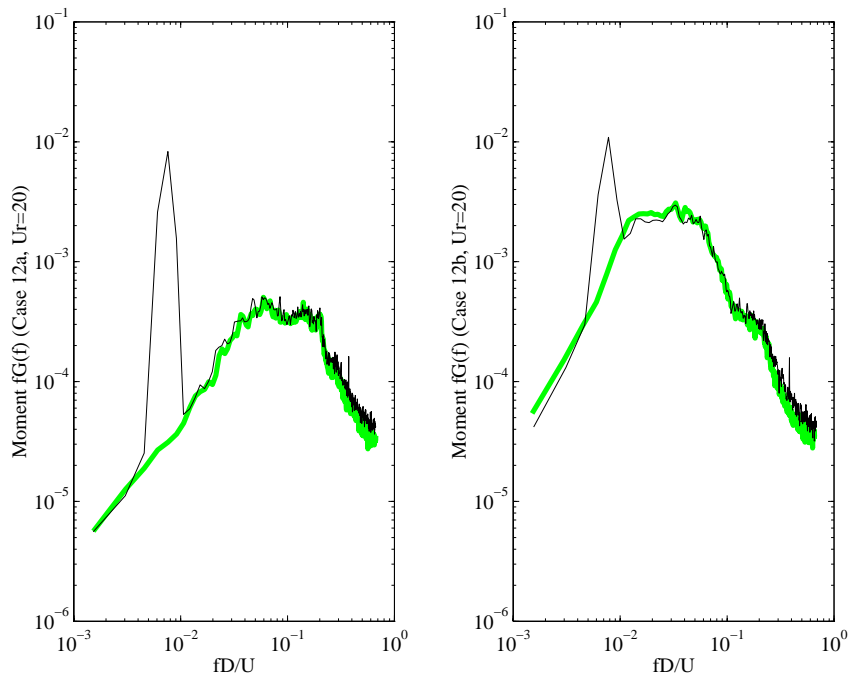


Figure 6-18 Moment spectra for  $I_u = 12\%$  for both stationary and  $U_r = 20$  tests (stationary results shaded).

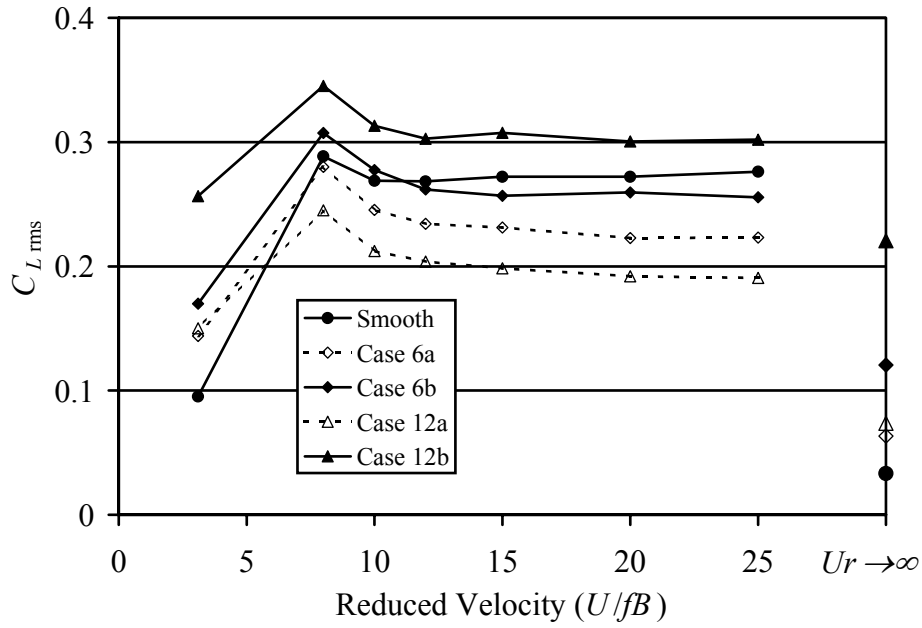


Figure 6-19 RMS lift coefficient versus reduced velocity. Stationary model results are presented on the far right.

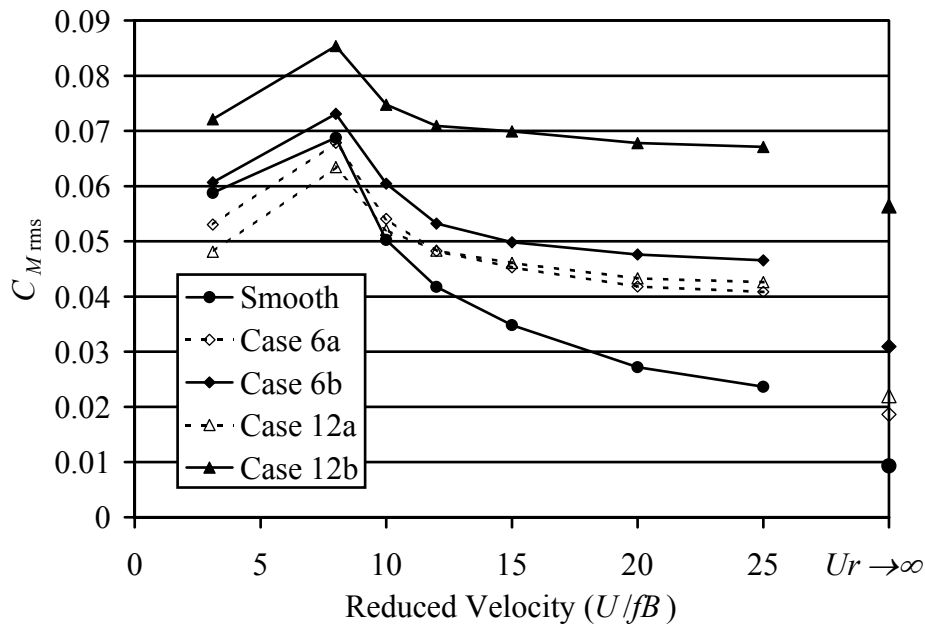


Figure 6-20 RMS moment coefficient versus reduced velocity. Stationary model results are presented on the far right.

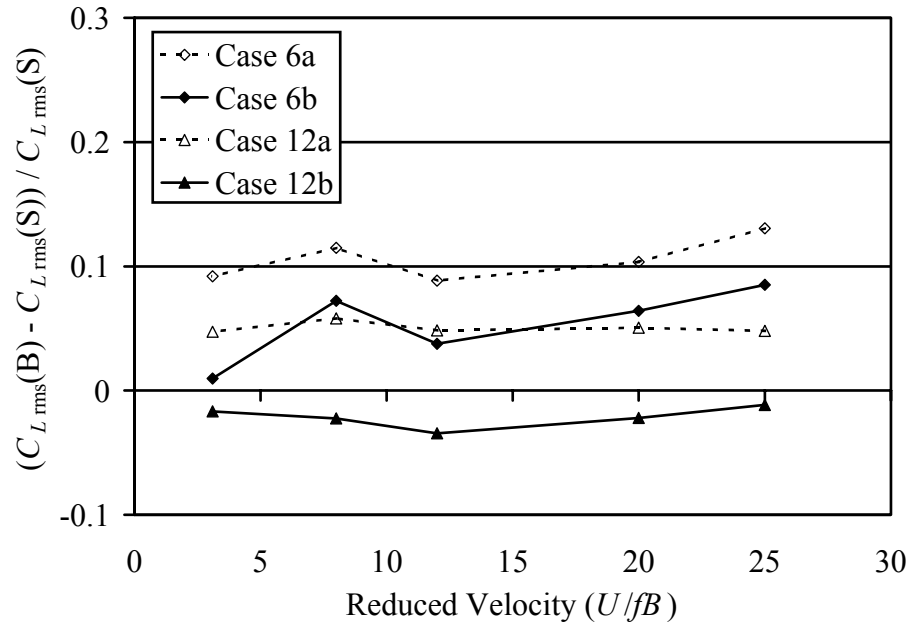


Figure 6-21 Relative differences between RMS lift coefficient for stationary (S) and the buffeting lift component (B) of the oscillating model tests.

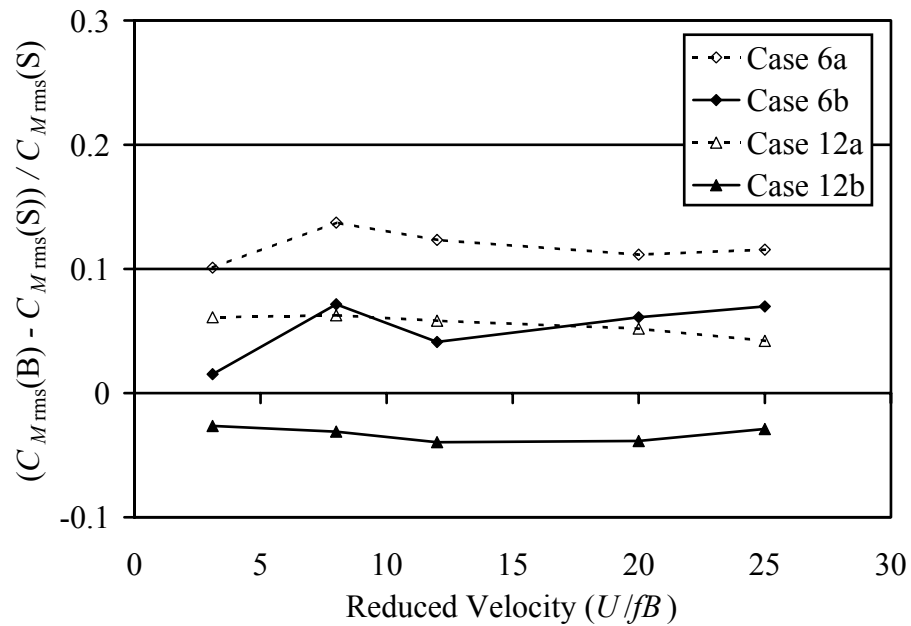


Figure 6-22 Relative differences between RMS moment coefficient for stationary (S) and the buffeting moment component (B) of the oscillating model tests.

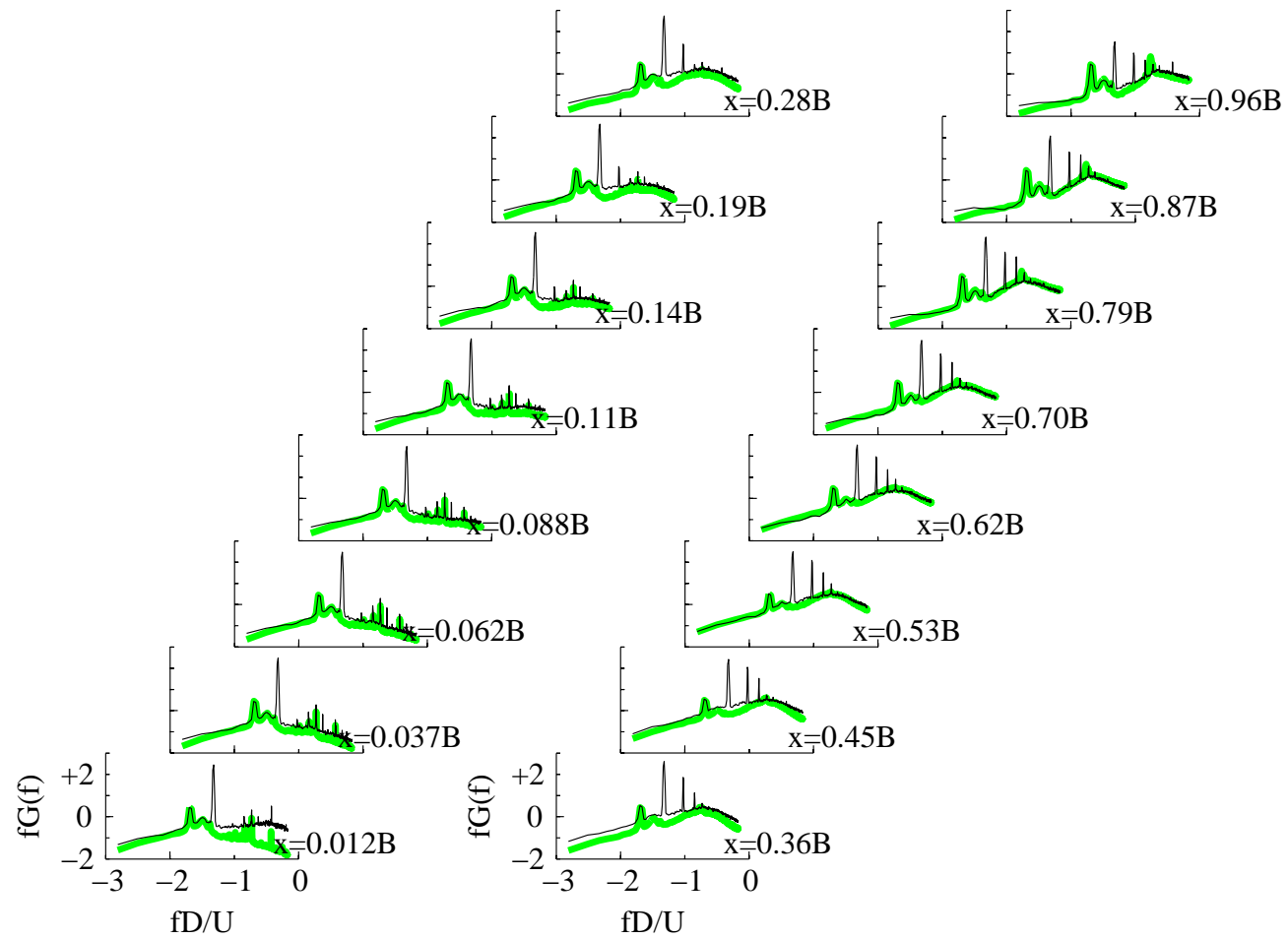


Figure 6-23 Power spectral density functions for pressure signals in smooth flow for both stationary and  $U_r = 3.1$  tests (stationary results shaded).

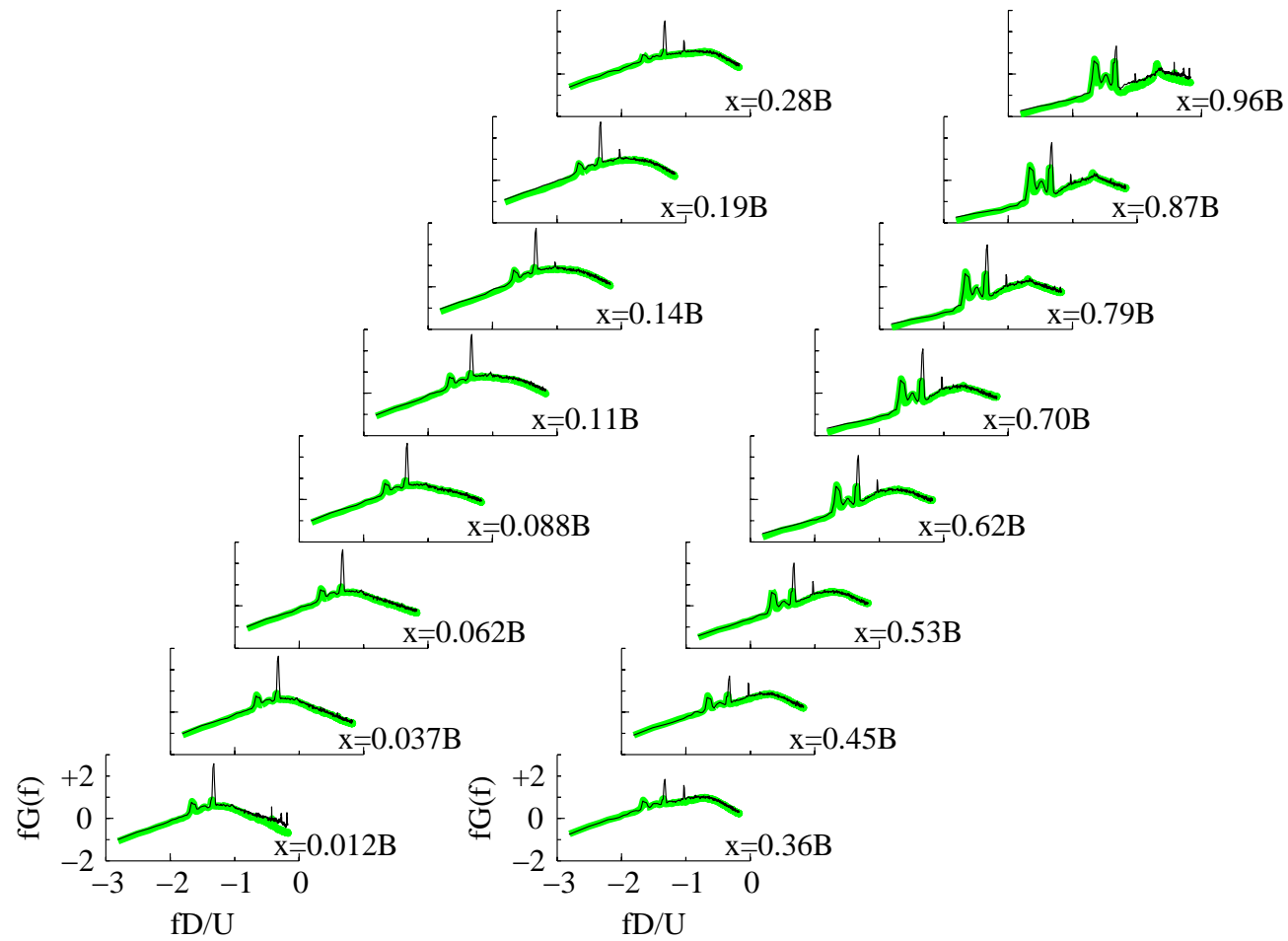


Figure 6-24 Power spectral density functions for pressure signals in Case 6a flow for both stationary and  $U_r = 3.1$  tests (stationary results shaded).

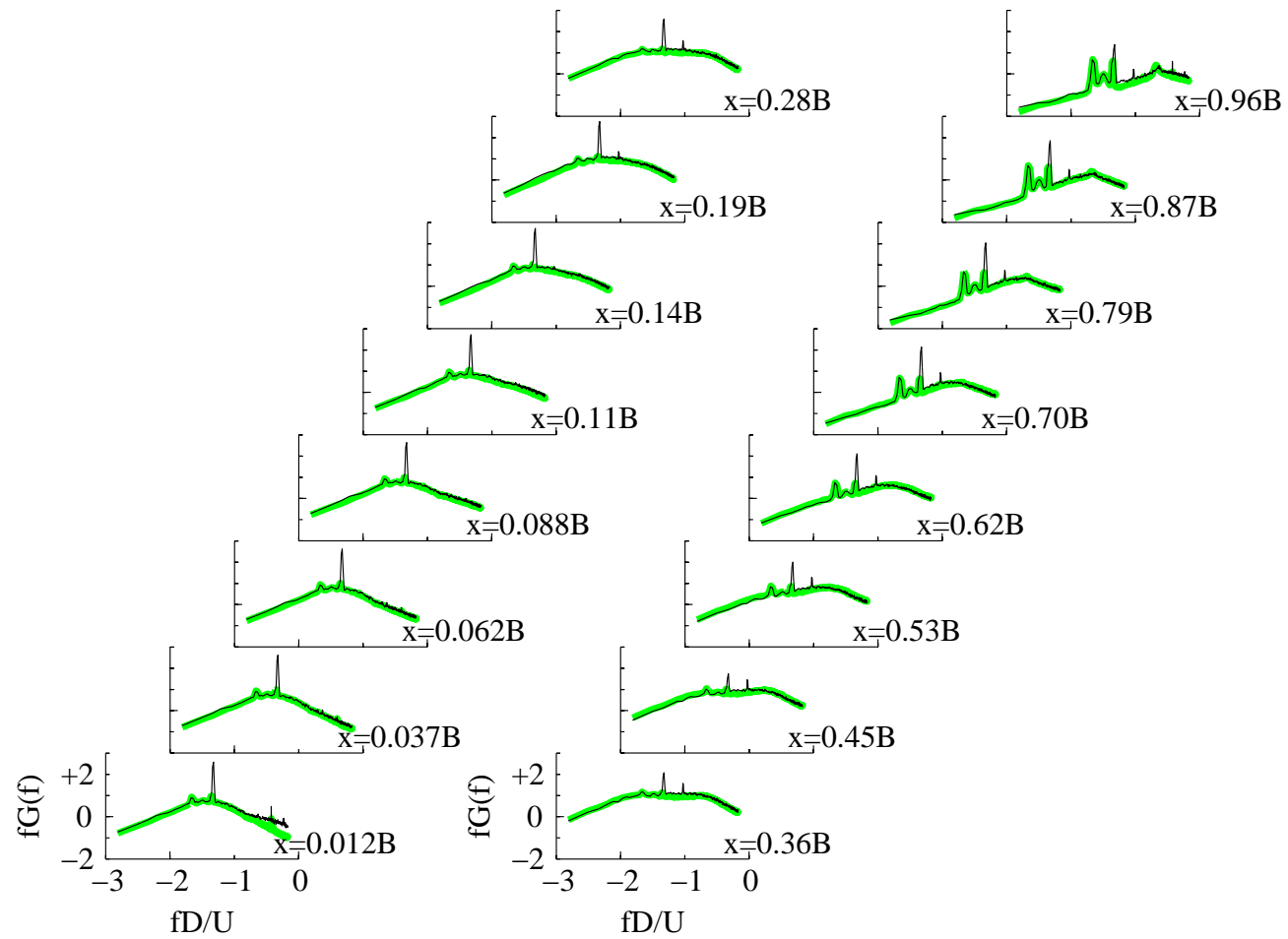


Figure 6-25 Power spectral density functions for pressure signals in Case 6b flow for both stationary and  $U_r = 3.1$  tests (stationary results shaded).

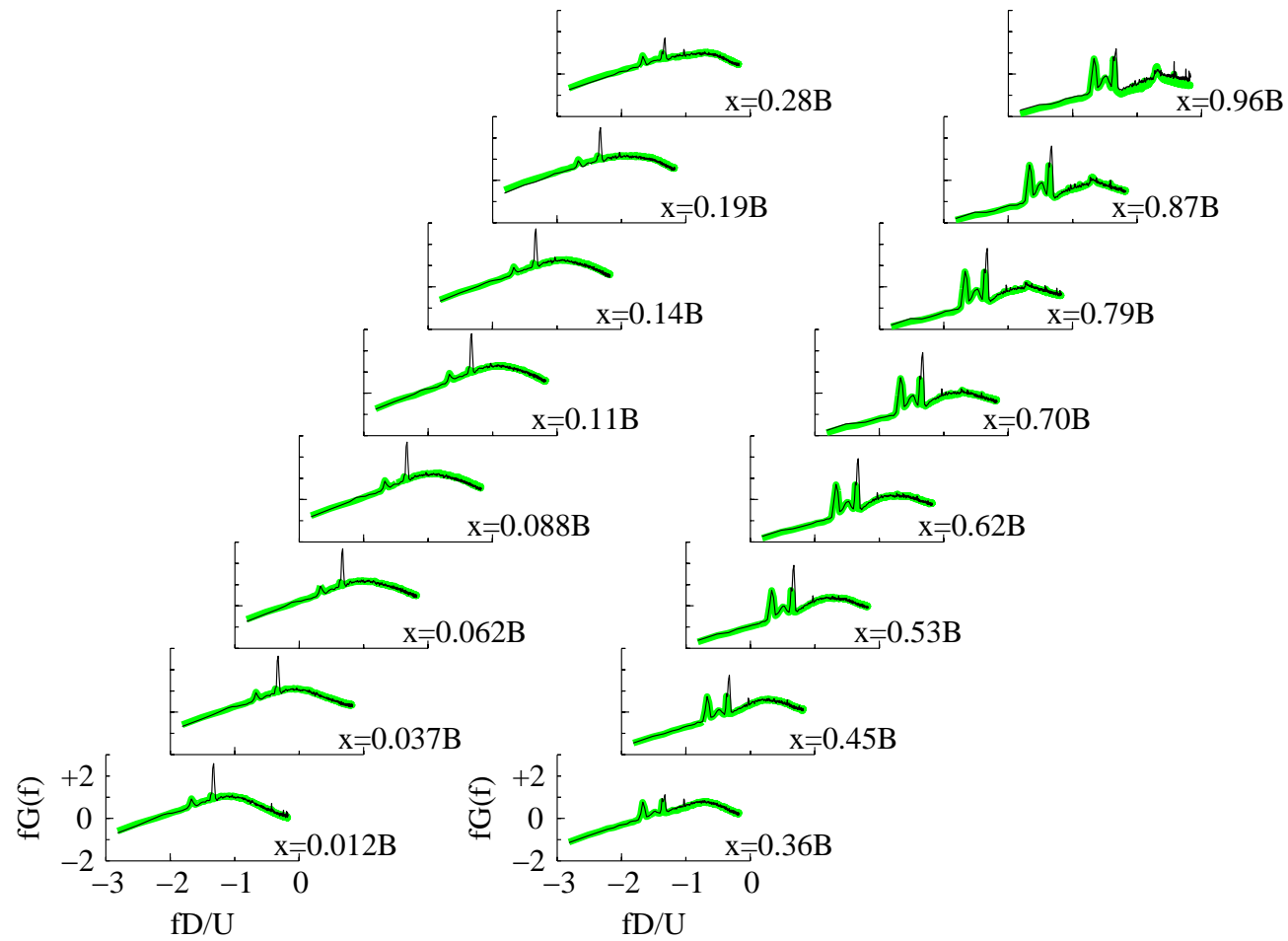


Figure 6-26 Power spectral density functions for pressure signals in Case 12a flow for both stationary and  $U_r = 3.1$  tests (stationary results shaded).

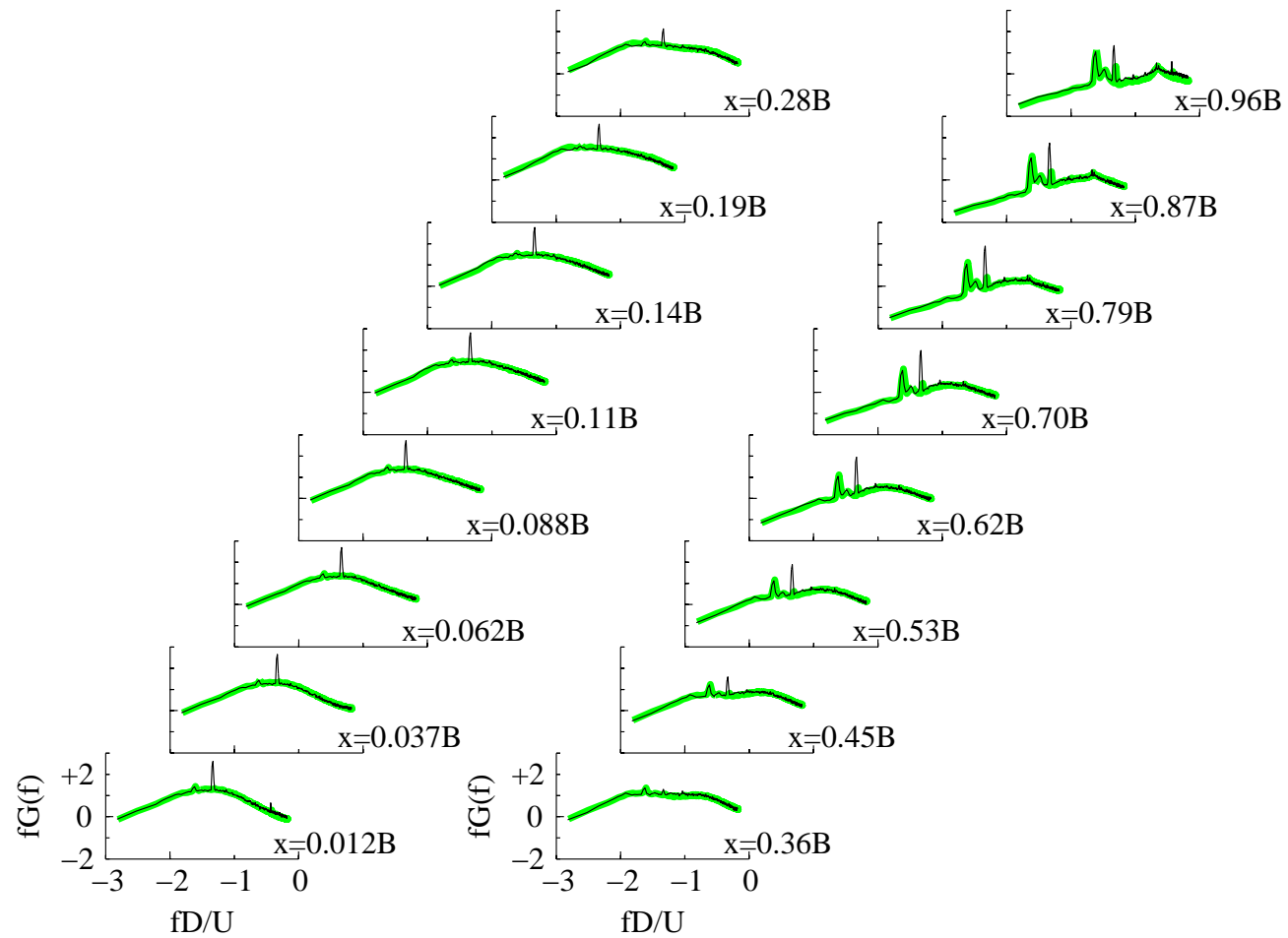


Figure 6-27 Power spectral density functions for pressure signals in Case 12b flow for both stationary and  $U_r = 3.1$  tests (stationary results shaded).

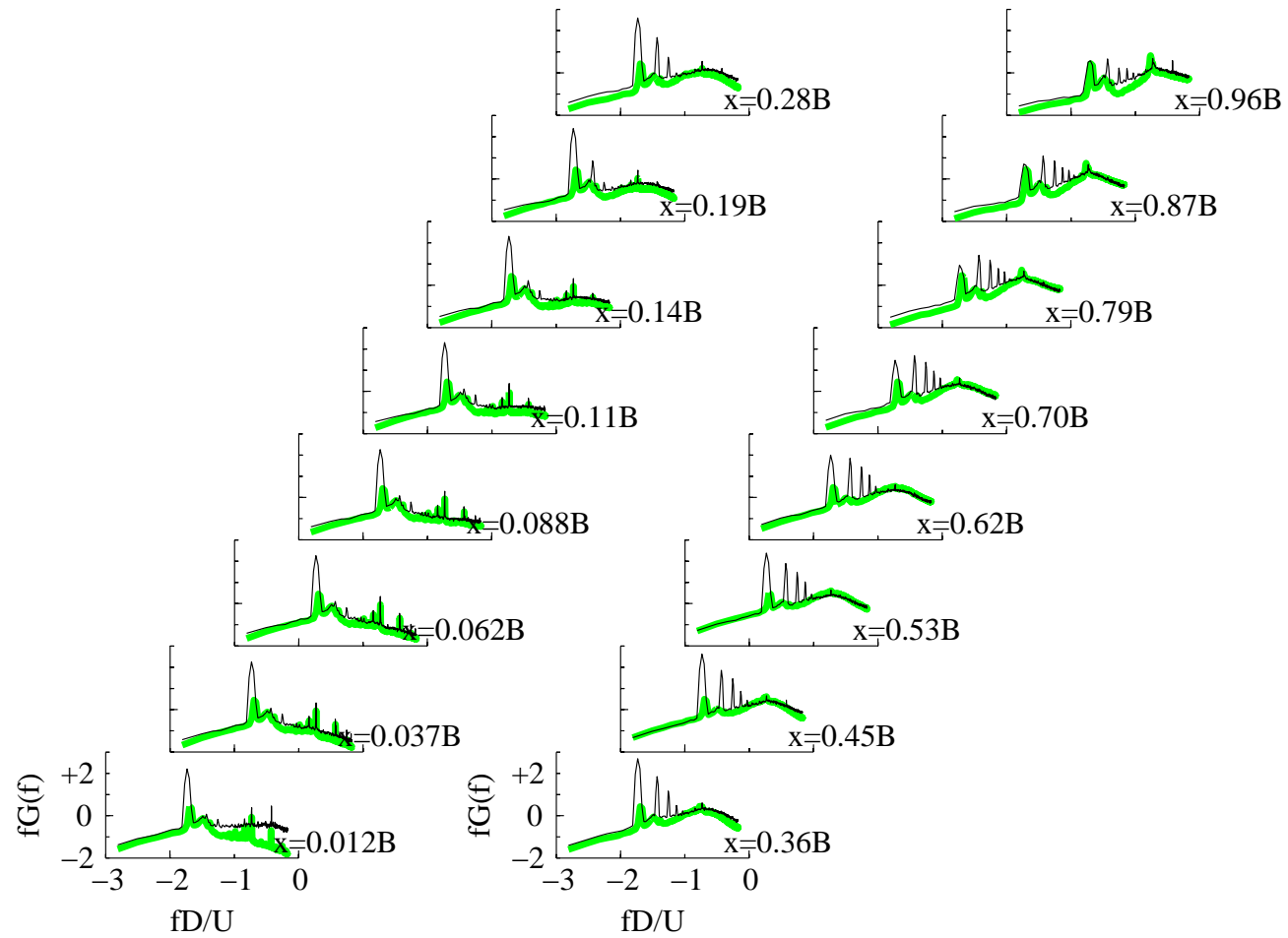


Figure 6-28 Power spectral density functions for pressure signals in smooth flow for both stationary and  $U_r = 8$  tests (stationary results shaded).

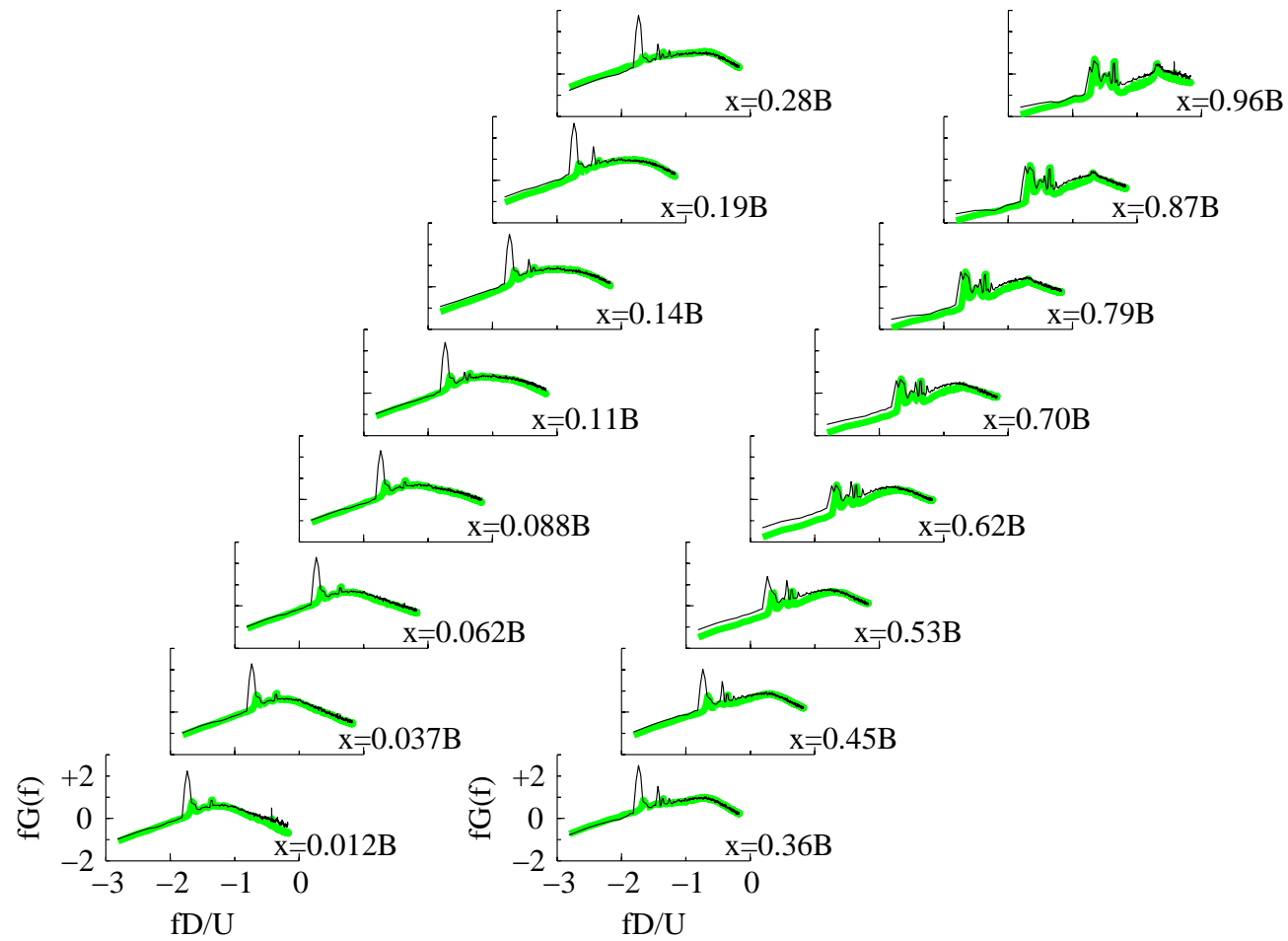


Figure 6-29 Power spectral density functions for pressure signals in Case 6a flow for both stationary and  $U_r = 8$  tests (stationary results shaded).

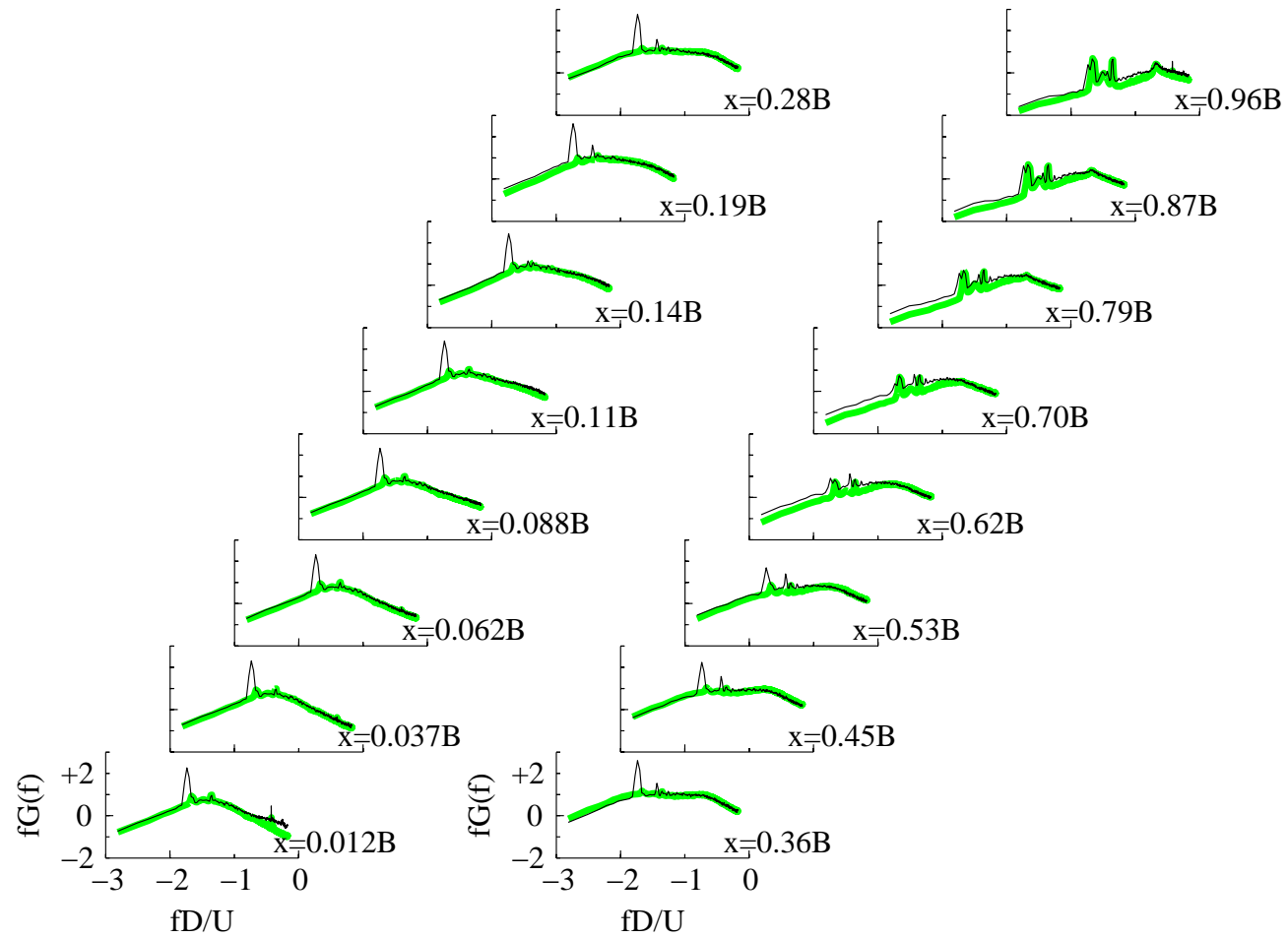


Figure 6-30 Power spectral density functions for pressure signals in Case 6b flow for both stationary and  $U_r = 8$  tests (stationary results shaded).

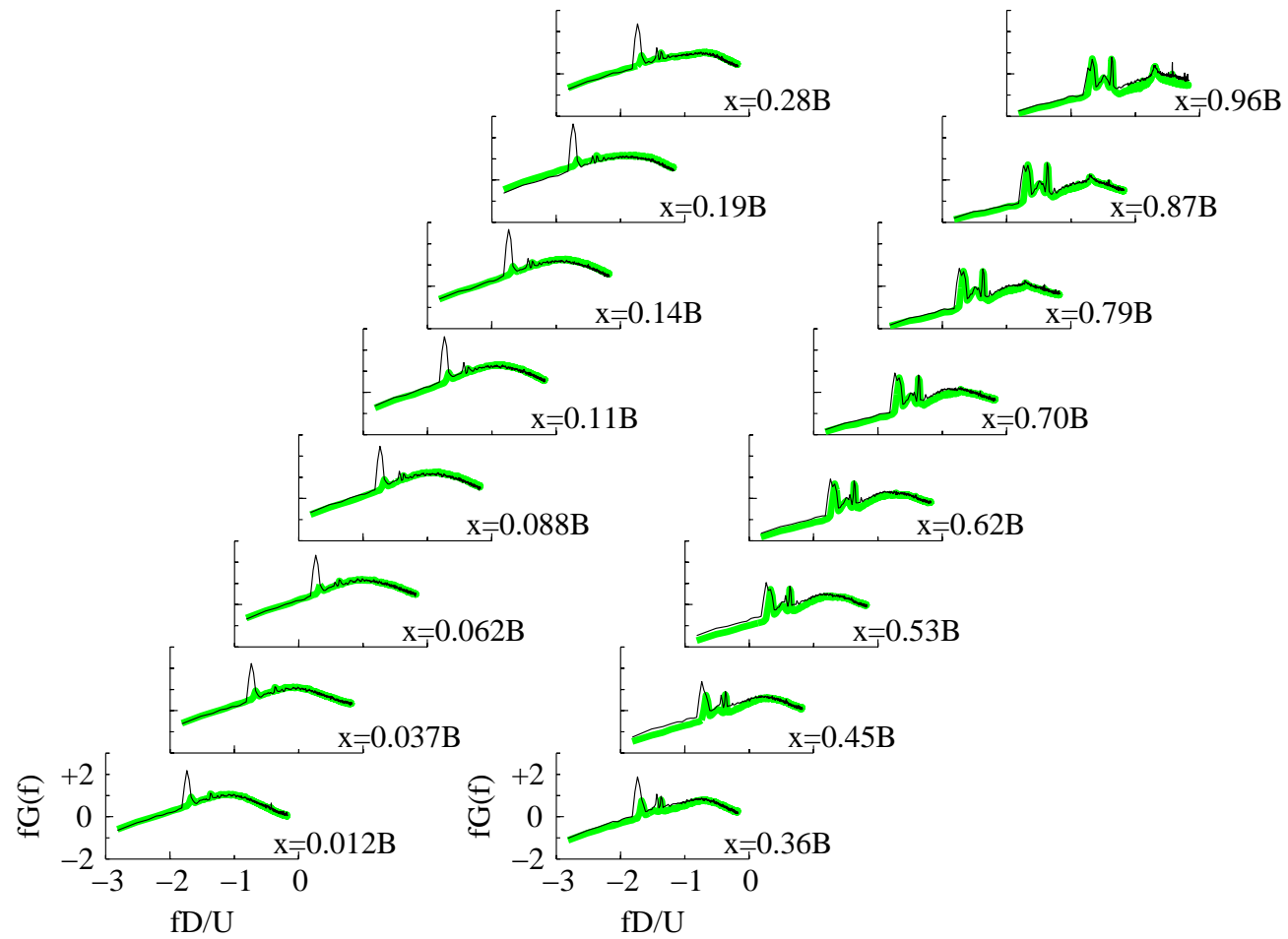


Figure 6-31 Power spectral density functions for pressure signals in Case 12a flow for both stationary and  $U_r = 8$  tests (stationary results shaded).

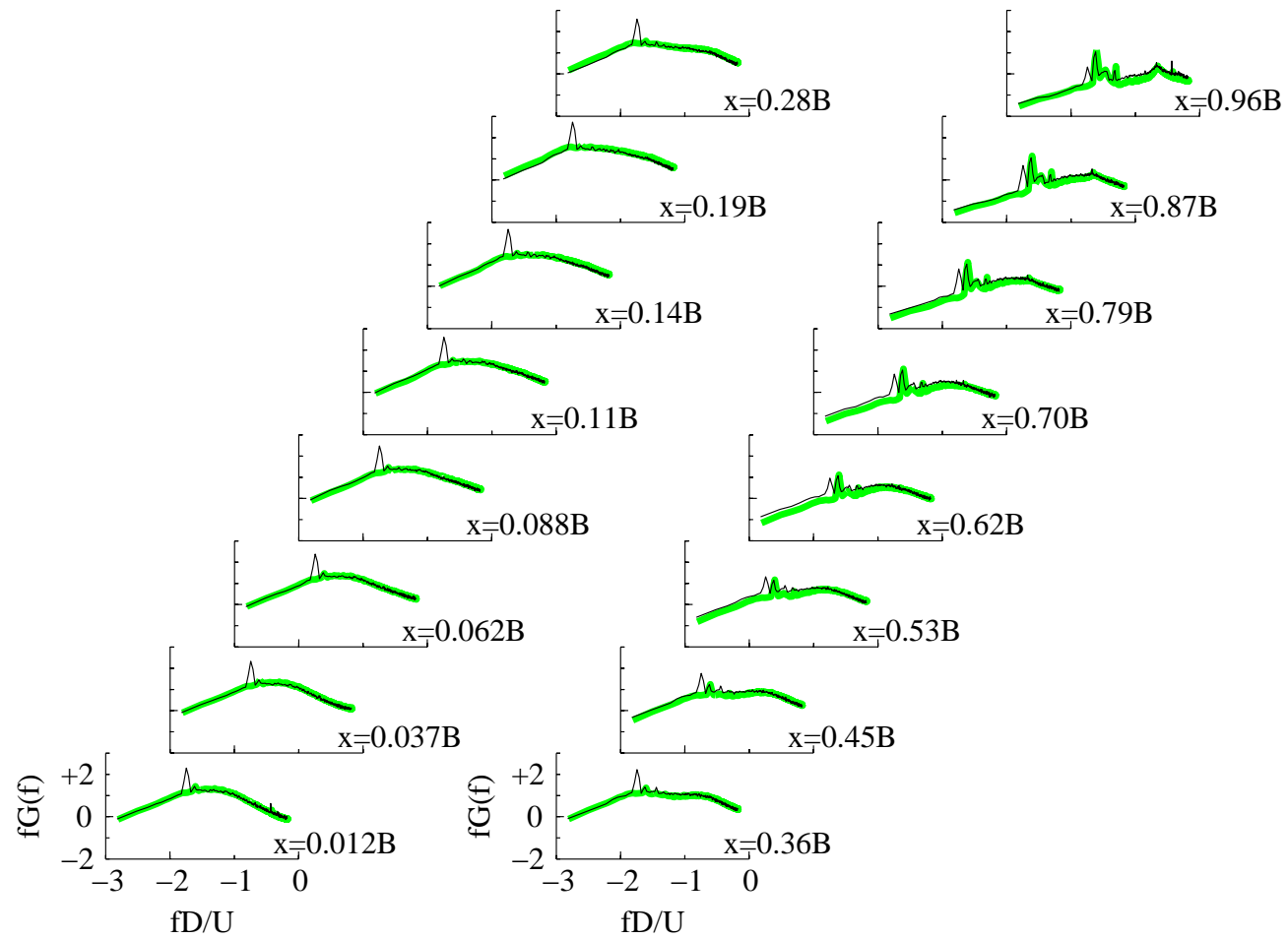


Figure 6-32 Power spectral density functions for pressure signals in Case 12b flow for both stationary and  $U_r = 8$  tests (stationary results shaded).

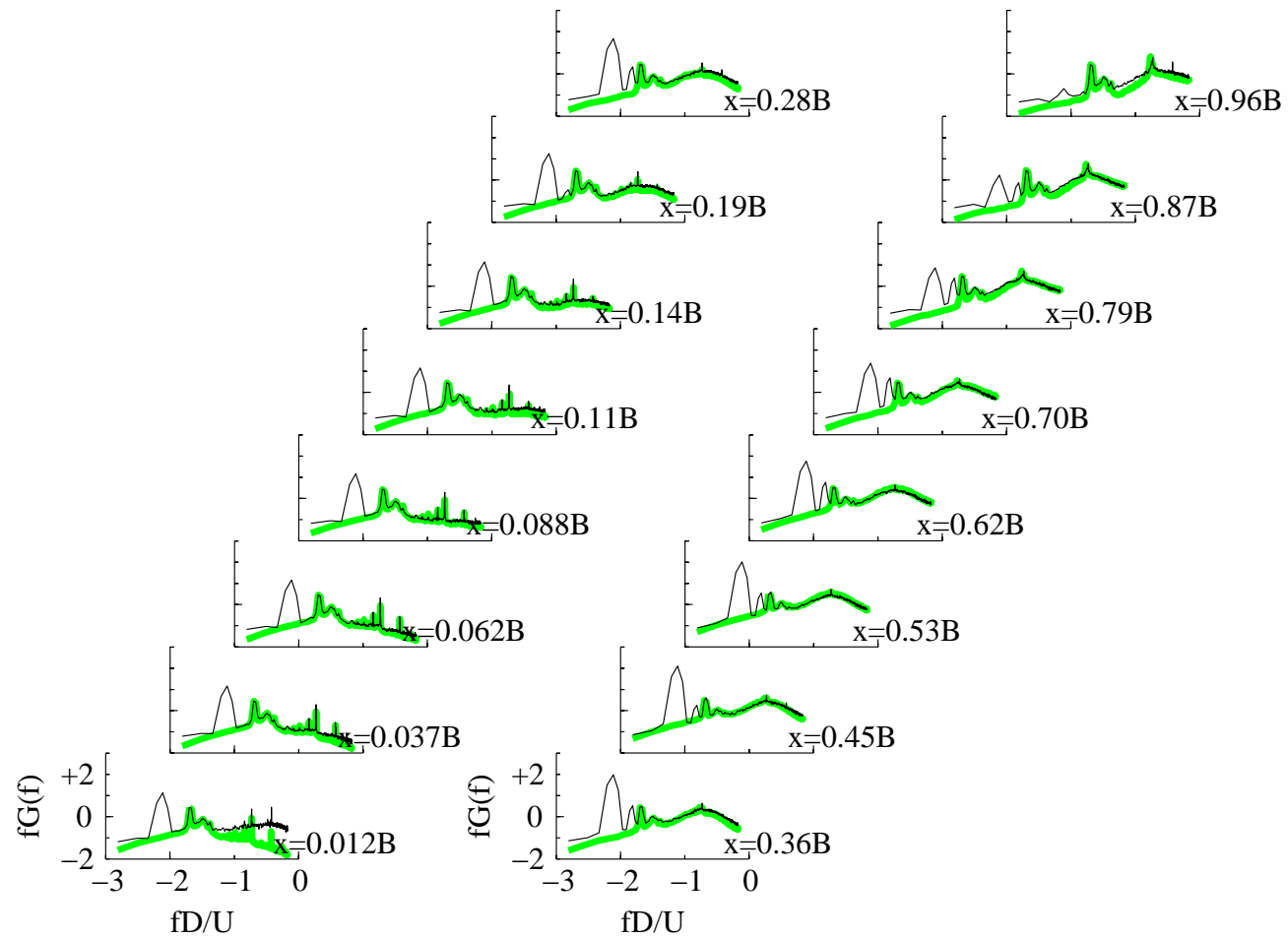


Figure 6-33 Power spectral density functions for pressure signals in smooth flow for both stationary and  $U_r = 20$  tests (stationary results shaded).

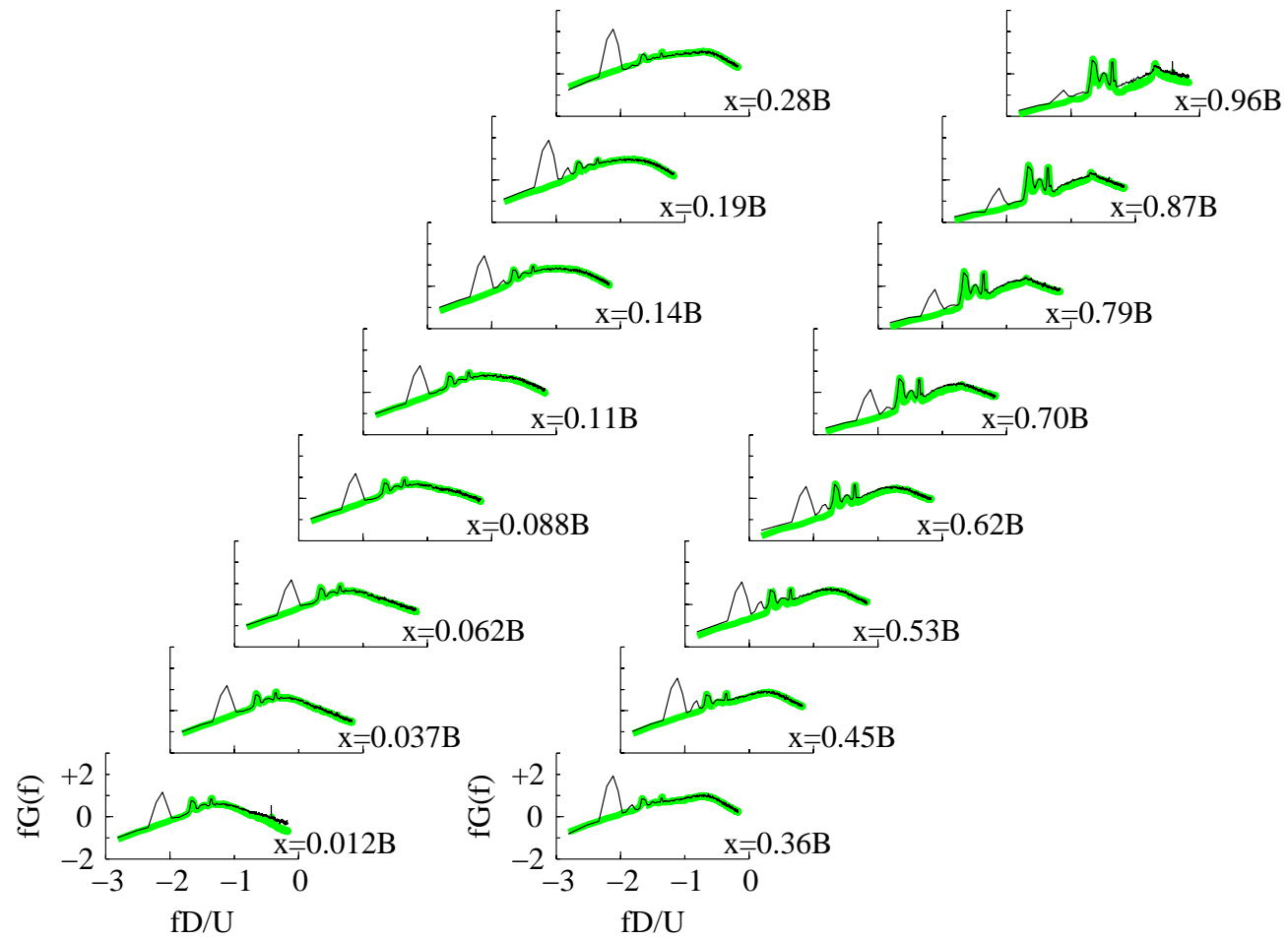


Figure 6-34 Power spectral density functions for pressure signals in Case 6a flow for both stationary and  $U_r = 20$  tests (stationary results shaded).

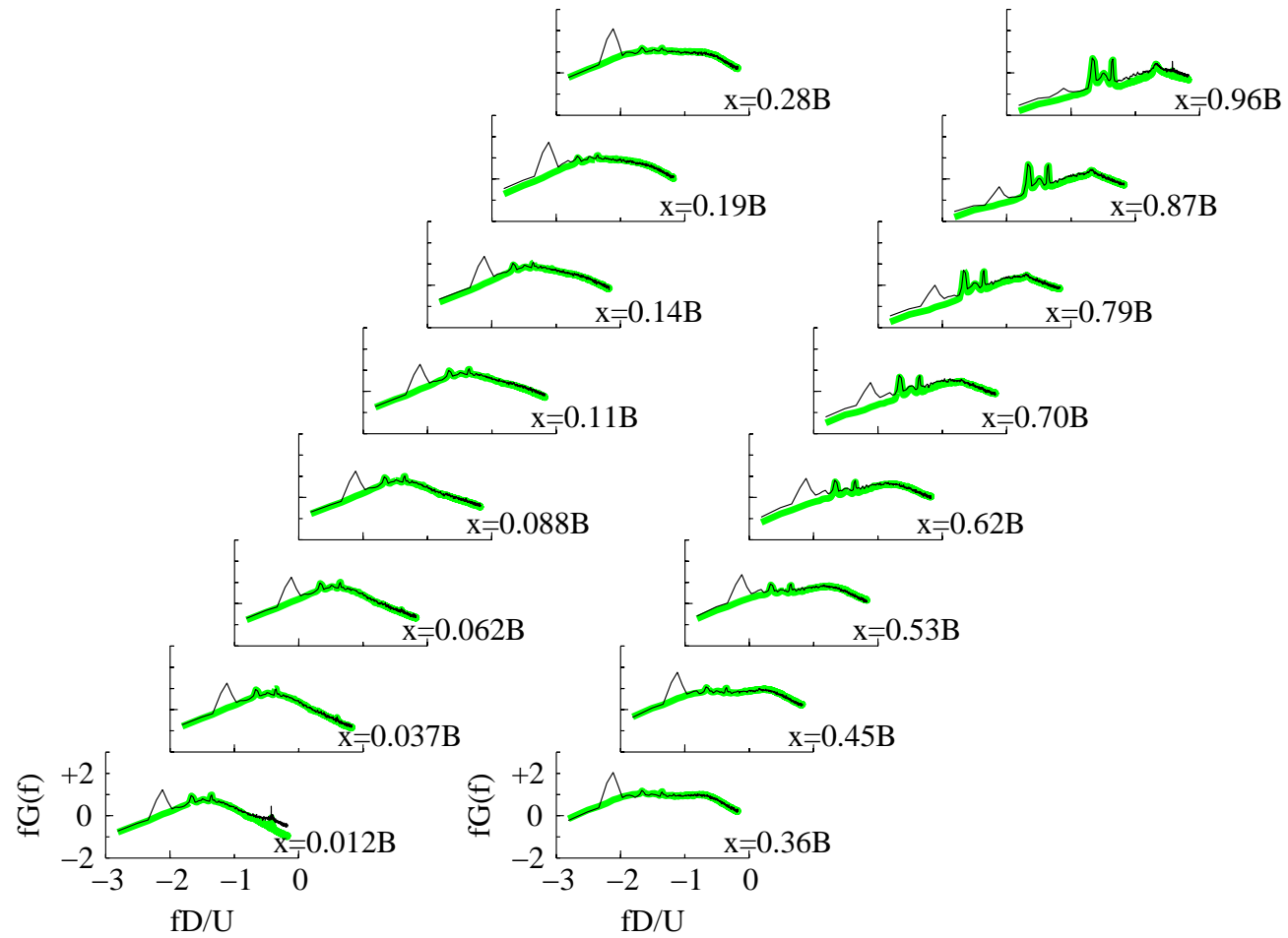


Figure 6-35 Power spectral density functions for pressure signals in Case 6b flow for both stationary and  $U_r = 20$  tests (stationary results shaded).

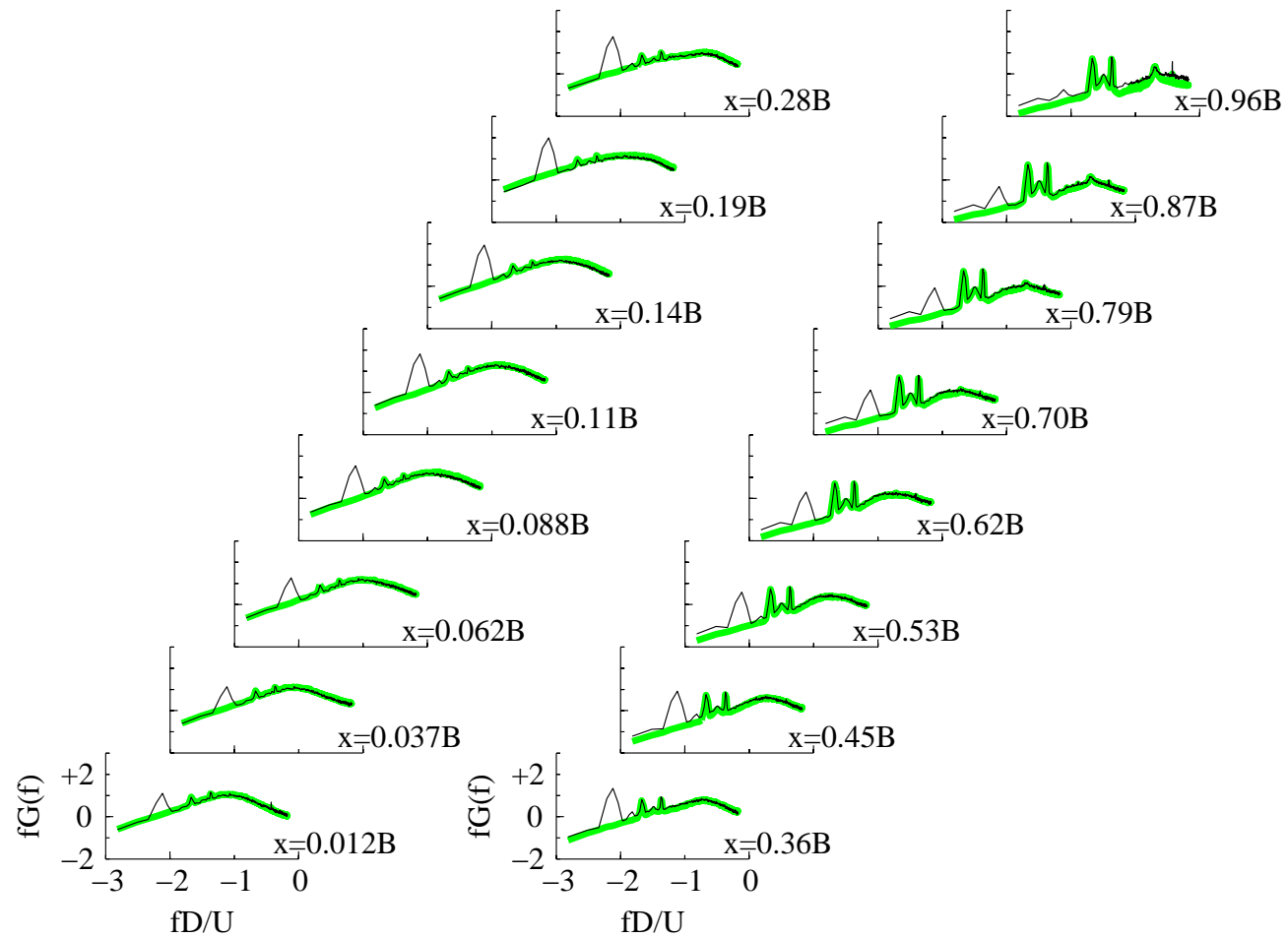


Figure 6-36 Power spectral density functions for pressure signals in Case 12a flow for both stationary and  $U_r = 20$  tests (stationary results shaded).

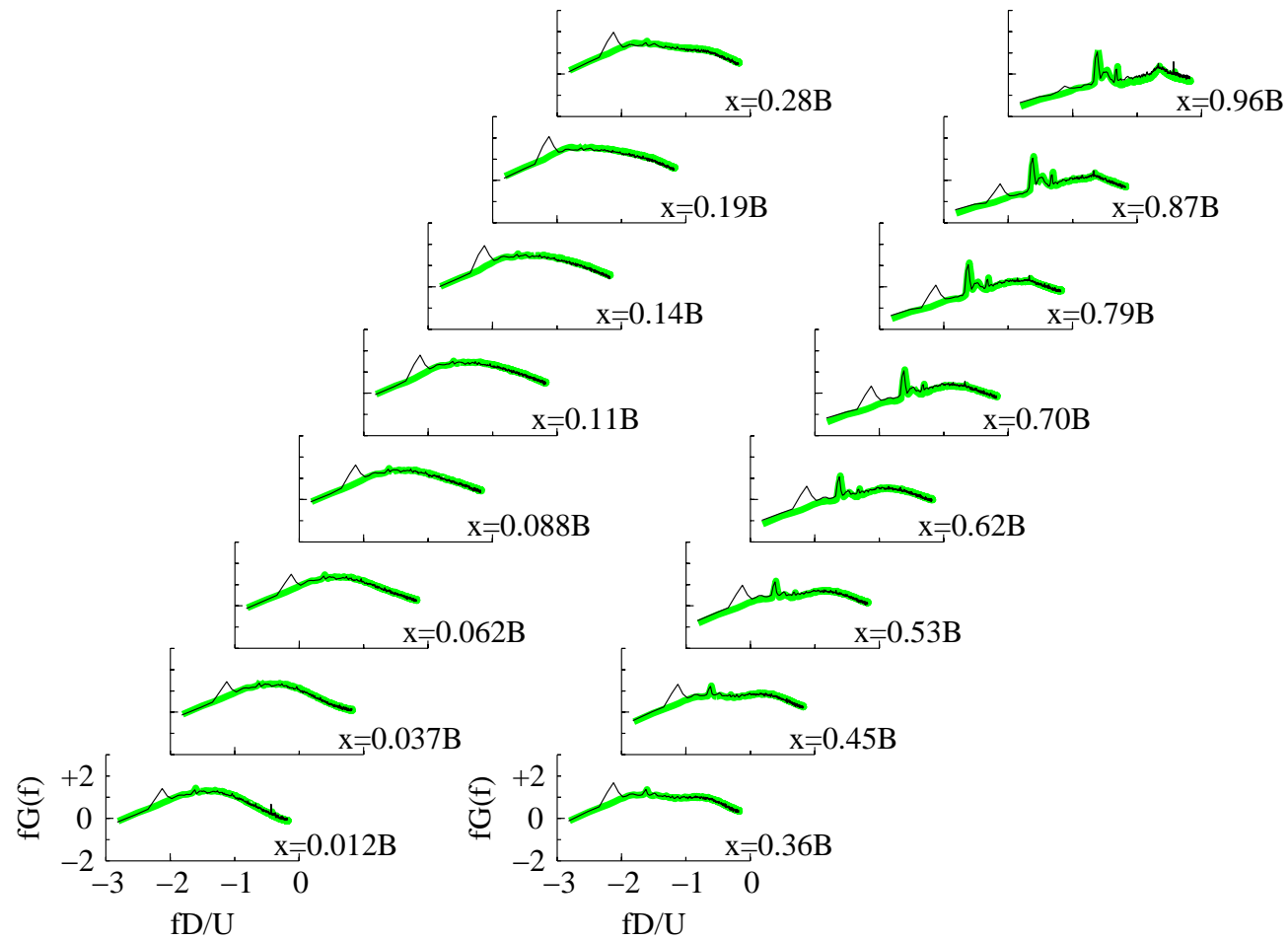


Figure 6-37 Power spectral density functions for pressure signals in Case 12b flow for both stationary and  $U_r = 20$  tests (stationary results shaded).

### 6.3 Streamwise Distributions of Amplitude and Phase

The major portion of the analysis of the self-excited forces was the examination of the amplitudes and phases of the components of the pressure signals at the model driving frequencies. Although the signals at each pressure tap were relatively broad band, each signal had a salient peak at the frequency of the model's motion. As discussed in Chapter 1, the self-excited and buffeting forces are conventionally separated as follows:

(6-2)

$$L(t) = L_{se}(t) + L_b(t)$$

where  $L$  is the total lift force,  $L_{se}$  is the self-excited lift force, and  $L_b$  is the buffeting lift force. The self-excited lift is associated with the peak in the lift force spectrum while the buffeting force is associated with the spectrum's broad band energy.

The pressure amplitudes were then calculated by finding the energy in the peak and subtracting the broad band energy at that frequency. The energy in the peak was calculated from oscillating model tests while the broad band energy at the same frequency was obtained from stationary model tests. This concept is illustrated in Figure 6-38 which shows stationary and oscillating test spectra for the pressure at  $x = 0.012B$  in Case 6b flow. Specific details of these calculations are provided in Appendix C.

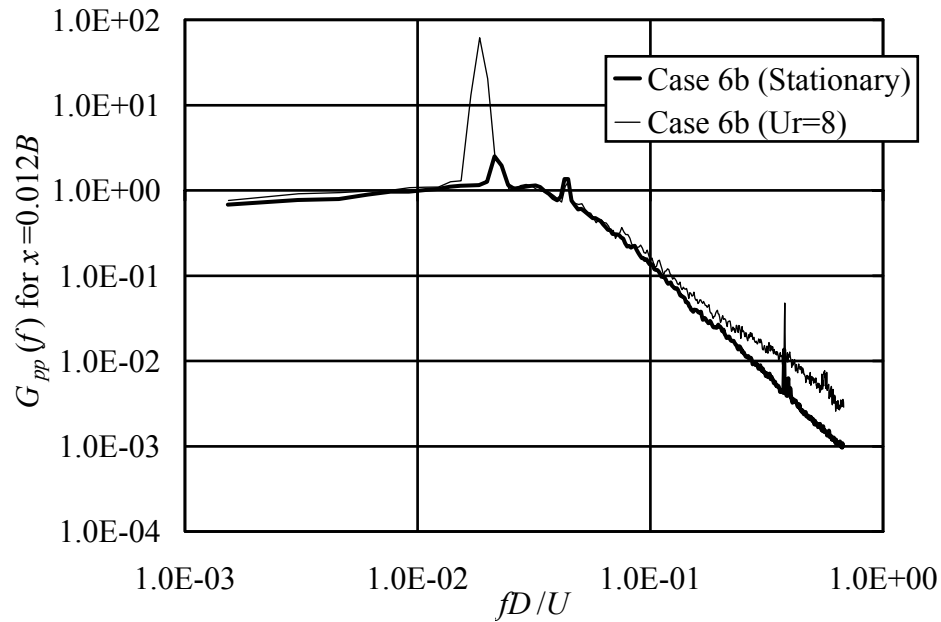


Figure 6-38 Example power spectral density functions for pressure signals at  $x = 0.012B$  for stationary and oscillating model tests.

Figure 6-39, Figure 6-40, and Figure 6-41 show the pressure amplitude distributions for reduced velocities of 3.1, 8, and 20, respectively. Each plot includes all five flow cases. In each case, a basic “hump” shape is evident in the distribution. For each reduced velocity, this shape is “compressed” toward the leading edge with increasing turbulence intensity. This compression is more evident in the two cases of greater reduced velocity perhaps simply because the “hump” distribution is stretched in the downstream direction when reduced velocity increases.

Considering the effect of scales on the amplitudes one can see that greater scale in most cases decreases the amplitude. Figure 6-40 and Figure 6-41 show that a greater integral scale results in smaller amplitudes within the region of the “hump” but not nearly

so much further downstream. Figure 6-39, the  $U_r = 3.1$  case, does not show as much of a scale effect as the other  $U_r$  cases.

To examine the effects of scale more closely and to present uncertainty estimates more clearly, the pressure amplitude data were also plotted in pairs corresponding to equal turbulence intensity and different turbulence scale. Figure 6-42 and Figure 6-43 contain the  $U_r = 3.1$  pressure amplitudes for Case 6 and Case 12, respectively. Neither case showed a significant effect of scale, but the uncertainty bounds did widen slightly with increasing  $L_{ux}$ . This effect was greater at the greater value of  $I_u$  as well.

Scale effects became more pronounced as  $U_r$  increased. Figure 6-44 and Figure 6-45 show the  $I_u = 6\%$  and  $I_u = 12\%$  amplitude distributions for  $U_r = 8$ . Near the peak in the distribution larger integral scales decreased the amplitudes. This effect was greater for greater turbulence intensity—the maximum decrease for the Case 6 flows was  $\sim 10\%$  while the maximum decrease for the Case 12 flows was  $\sim 15\%$ . Downstream of the region of maximum amplitudes increasing scale increased the amplitude very slightly.

Increasing reduced velocity increased the turbulence scale effects on pressure amplitudes up to approximately  $U_r = 10$ . Beyond  $U_r = 10$  amplitude reduction due to scale remained constant. Figure 6-46 and Figure 6-47 show the  $U_r = 20$  pressure amplitudes for Case 6 and Case 12, respectively. Amplitude reduction with increasing  $L_{ux}$  was again found to be dependent on  $I_u$ . For  $I_u = 6\%$  the amplitude reduction was about 22% while for  $I_u = 12\%$  it was about 30%. In addition, the uncertainty bounds were again observed to increase with both turbulence intensity and scale.

The pressure amplitude behavior with respect to turbulence scale was similar to that discussed in Chapter 2 and observed in Chapter 5 for RMS pressure distributions over stationary bluff bodies. Changes in integral scale seemed mainly to cause increases in RMS values at a given streamwise location without significantly changing the streamwise position of the maximum of the distribution.

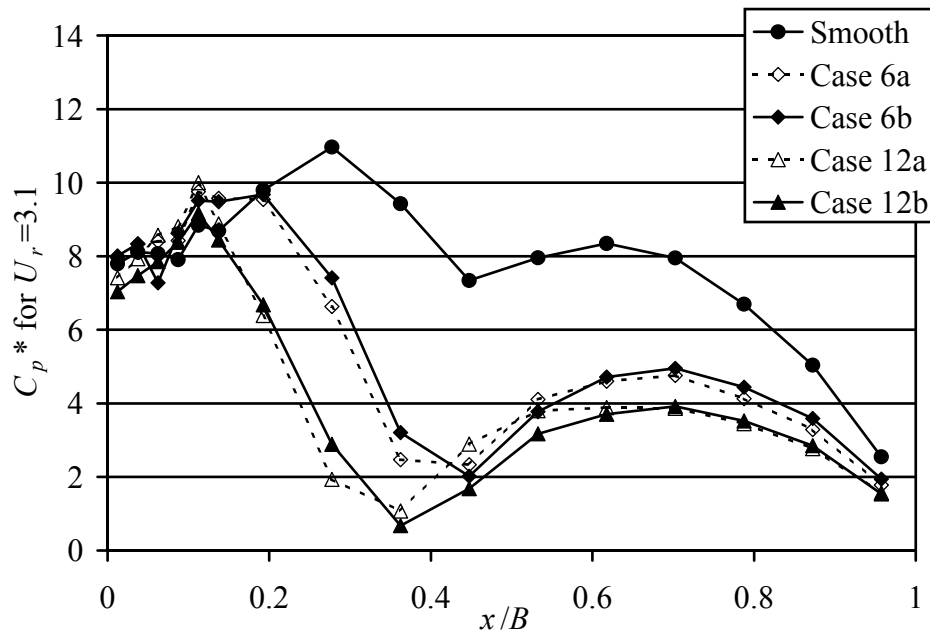


Figure 6-39 Pressure amplitude distributions for a reduced velocity of 3.1.

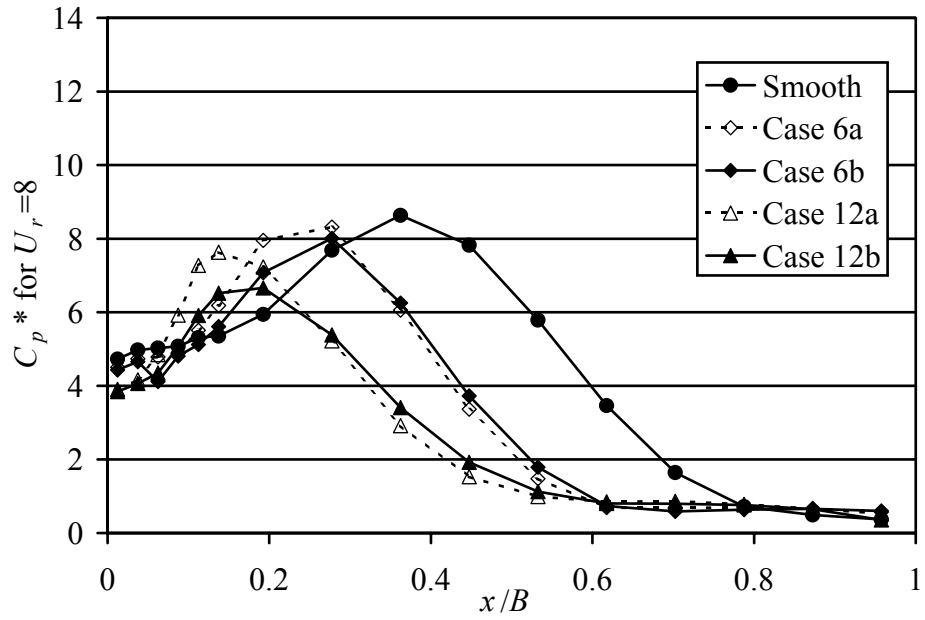


Figure 6-40 Pressure amplitude distributions for a reduced velocity of 8.

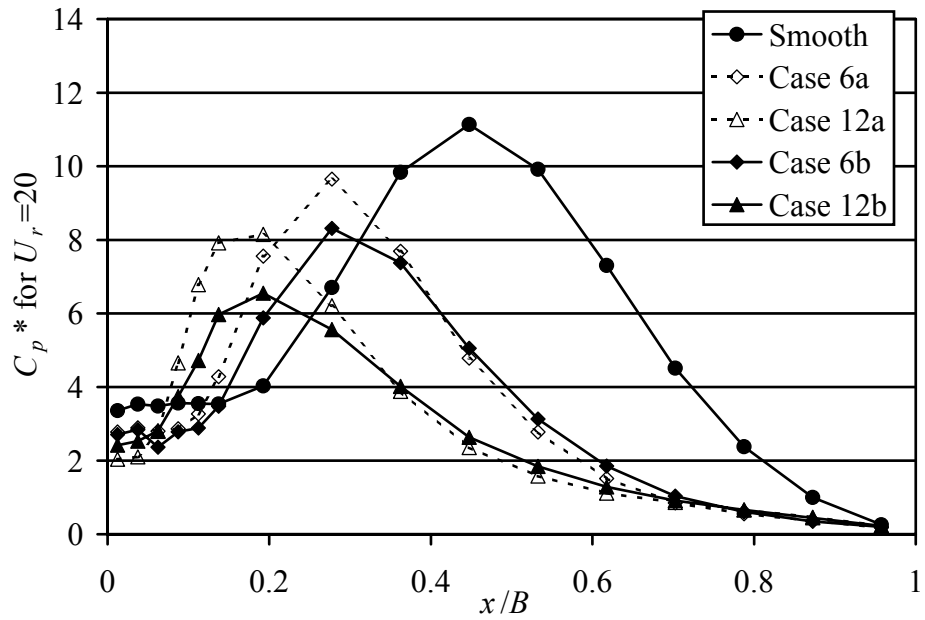


Figure 6-41 Pressure amplitude distributions for a reduced velocity of 20.

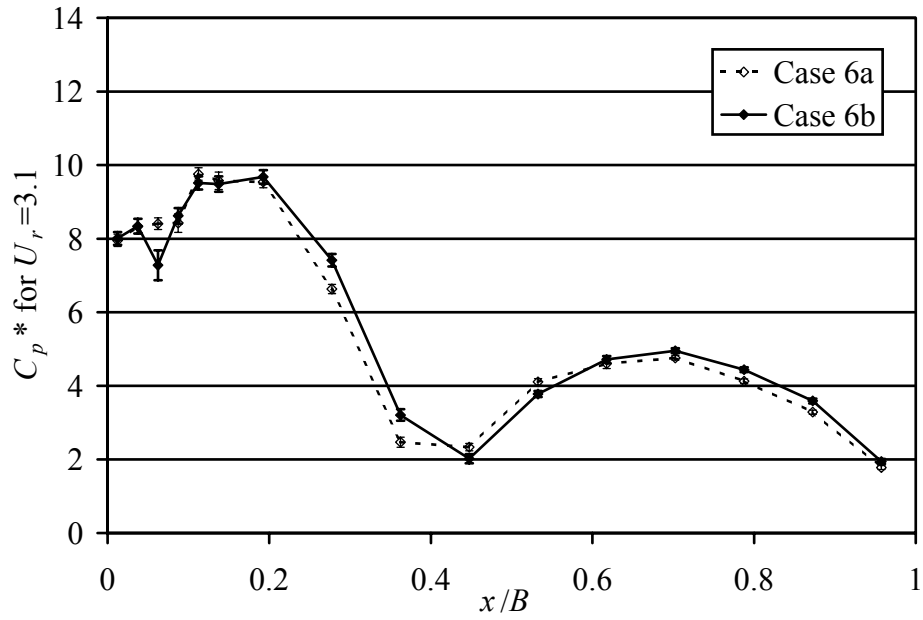


Figure 6-42 Pressure amplitude distributions at a reduced velocity of 3.1 in Case 6 flows (error bars represent 95% confidence intervals).

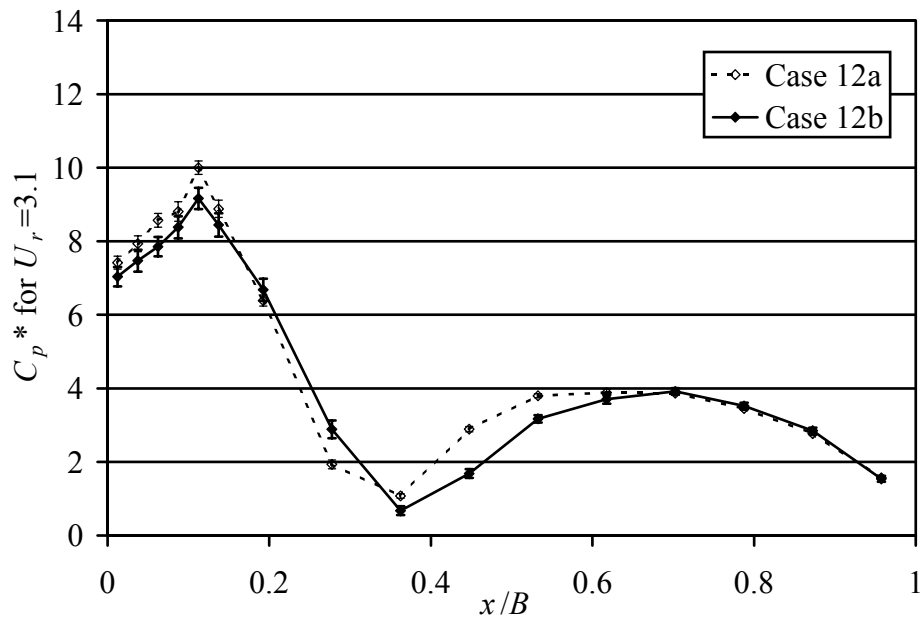


Figure 6-43 Pressure amplitude distributions at a reduced velocity of 3.1 in Case 12 flows (error bars represent 95% confidence intervals).

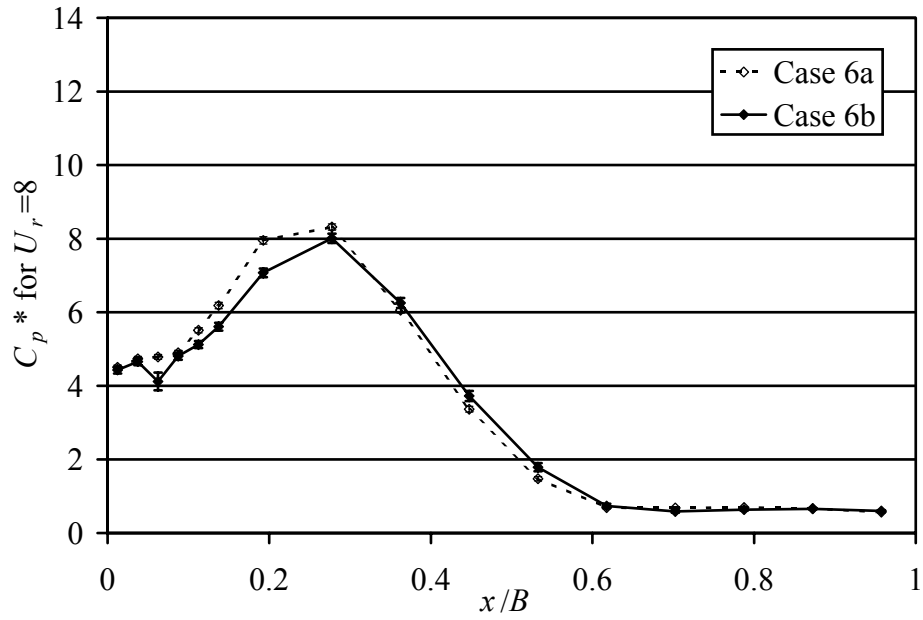


Figure 6-44 Pressure amplitude distributions at a reduced velocity of 8 in Case 6 flows (error bars represent 95% confidence intervals).

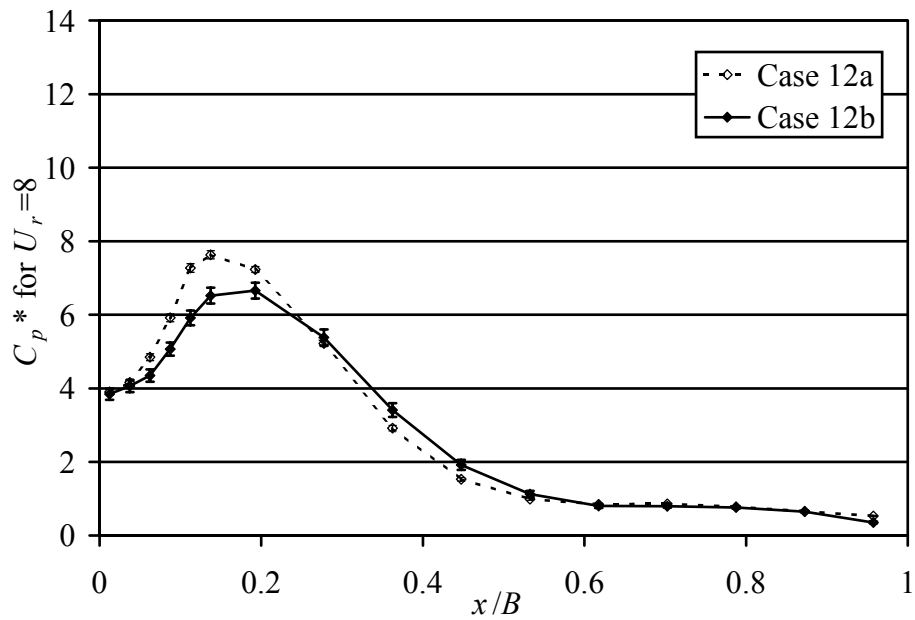


Figure 6-45 Pressure amplitude distributions at a reduced velocity of 8 in Case 12 flows (error bars represent 95% confidence intervals).

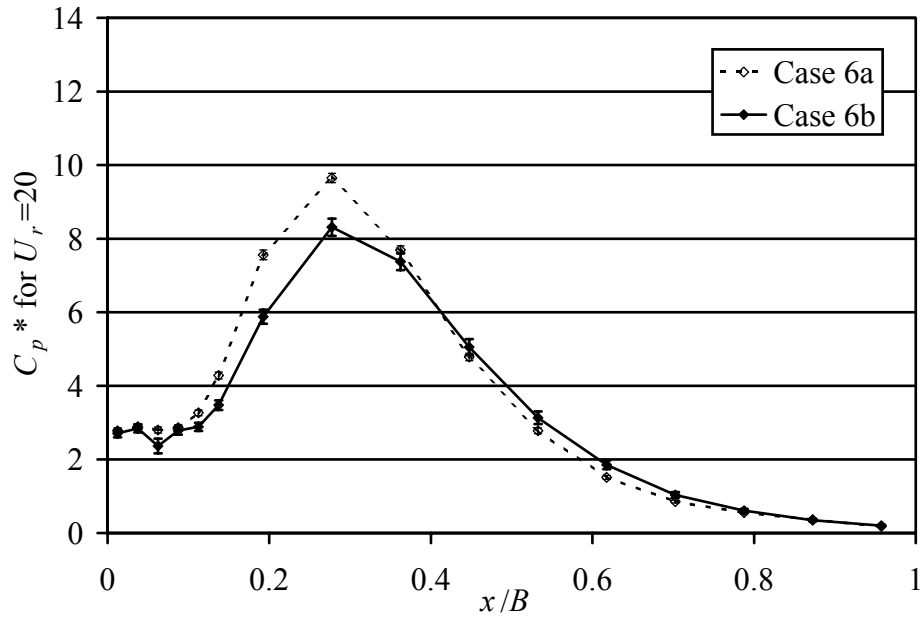


Figure 6-46 Pressure amplitude distributions at a reduced velocity of 20 in Case 6 flows (error bars represent 95% confidence intervals).

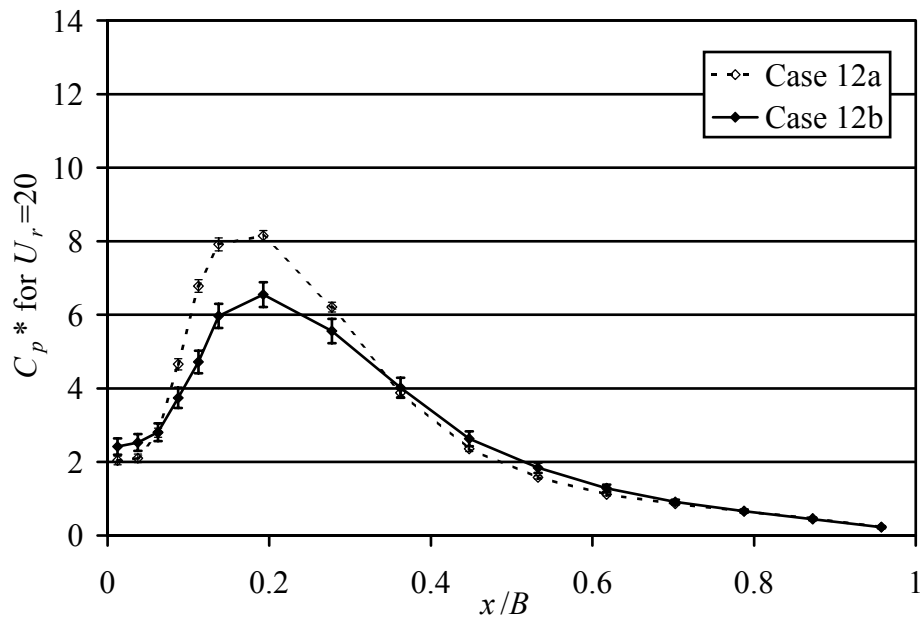


Figure 6-47 Pressure amplitude distributions at a reduced velocity of 20 in Case 12 flows (error bars represent 95% confidence intervals).

Phase distributions for  $U_r = 3.1$ ,  $U_r = 8$ , and  $U_r = 20$  are shown in Figure 6-48, Figure 6-49, and Figure 6-50, respectively. Like the amplitude distributions, the smooth flow phase distributions are seen to have a basic structure that stretches in the streamwise direction as the reduced velocity increases. This basic structure includes a region of nearly constant phase near the leading edge. The downstream extent of this constant-phase region was observed to be the portion of the distribution most affected by free stream turbulence. As the turbulence intensity was increased, the extent of this region was reduced for every reduced velocity tested. In each case, a zone of rapidly increasing phase was observed just downstream of the constant phase region. Beyond this rapidly changing zone, the slope of the phase decreased and the phase values often decreased. Chapter 8 will discuss the overall structure of the phase distributions in more detail.

To illuminate the effects of turbulence scale on these phase distributions, each pair of constant turbulence intensity cases was plotted on a separate plot in Figure 6-51 through Figure 6-56. This made comparisons between large and small integral scale cases easier. In each case, the effect of scale on the downstream extent of the constant phase region is negligible. Most of the distributions show very little change with integral scale.

For the two  $U_r = 3.1$  cases (Figure 6-51 and Figure 6-52), turbulence scale had little discernible effect. The only region affected by scale at all was downstream of the rapidly increasing phase region. Increasing scale increased the phase values somewhat, but this region also experienced greater spread in the experimental phase values which increased the uncertainty bounds. Overall, the effect of increasing scale was minimal.

Comparing the  $U_r = 8$  phase plots (Figure 6-53 and Figure 6-54) with the  $U_r = 3.1$  phase plots, one can see that the slope of the phase values in the rapidly

increasing phase region decreases with increasing  $U_r$ . For 12% turbulence intensity, this slope change was accompanied by lower phase magnitudes as well. As before, uncertainty bounds and scale effects decrease downstream of this region. Increasing turbulence scale increased the phase values for these downstream positions.

When the reduced velocity was increased further to  $U_r = 20$  (Figure 6-55 and Figure 6-56) overall phase values decreased even more. Maximum magnitudes were less than  $20^\circ$ , and turbulence scale showed negligible effects. The impact of this decrease in phase magnitudes will be discussed in Chapter 8.

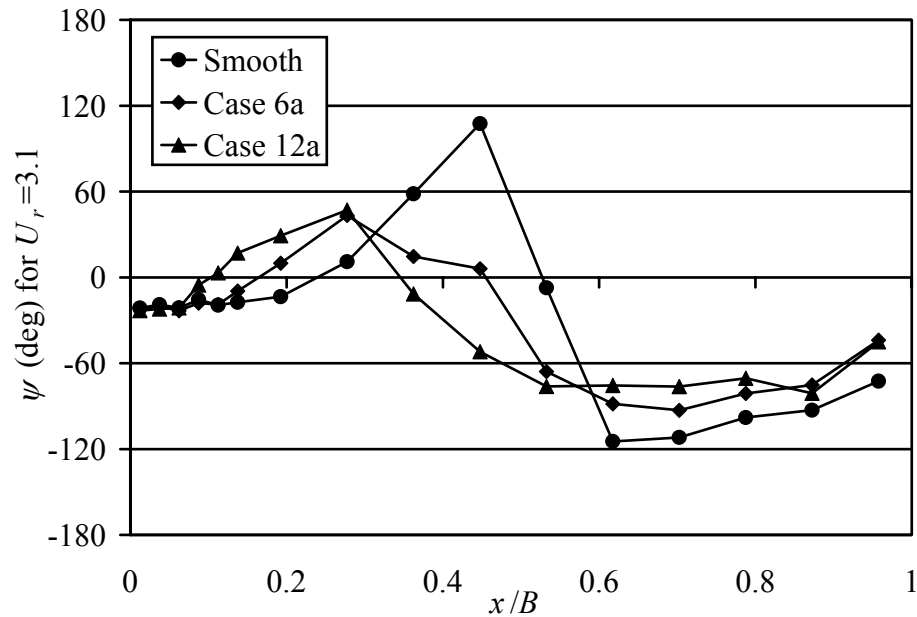


Figure 6-48 Pressure phase distributions in smooth flow and small-scale turbulent flows at a reduced velocity of 3.1.

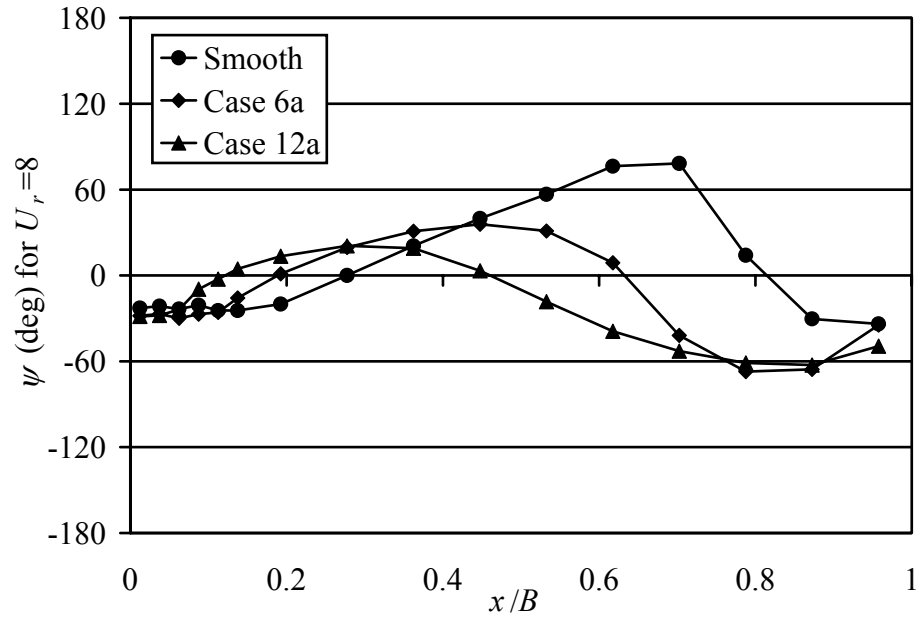


Figure 6-49 Pressure phase distributions in smooth flow and small-scale turbulent flows at a reduced velocity of 8.

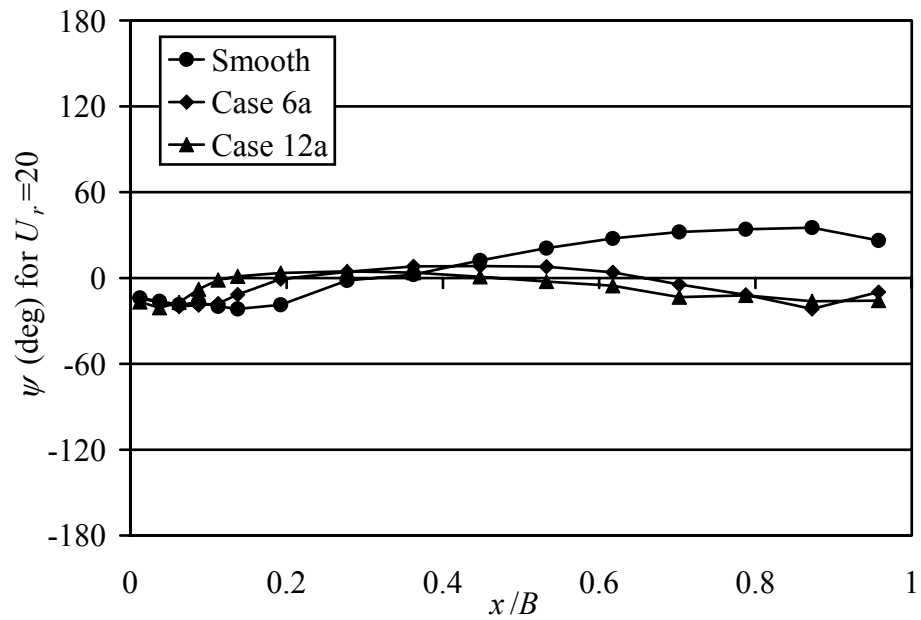


Figure 6-50 Pressure phase distributions in smooth flow and small-scale turbulent flows at a reduced velocity of 20.

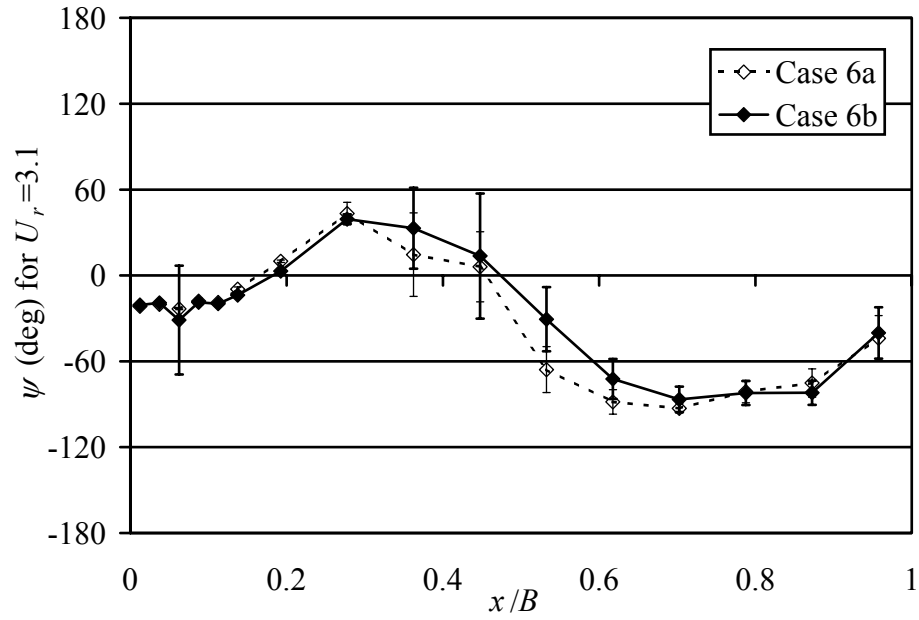


Figure 6-51 Pressure phase distributions for  $U_r = 3.1$  and  $I_u = 6\%$  showing the effect of changing scales (error bars represent 95% confidence intervals).

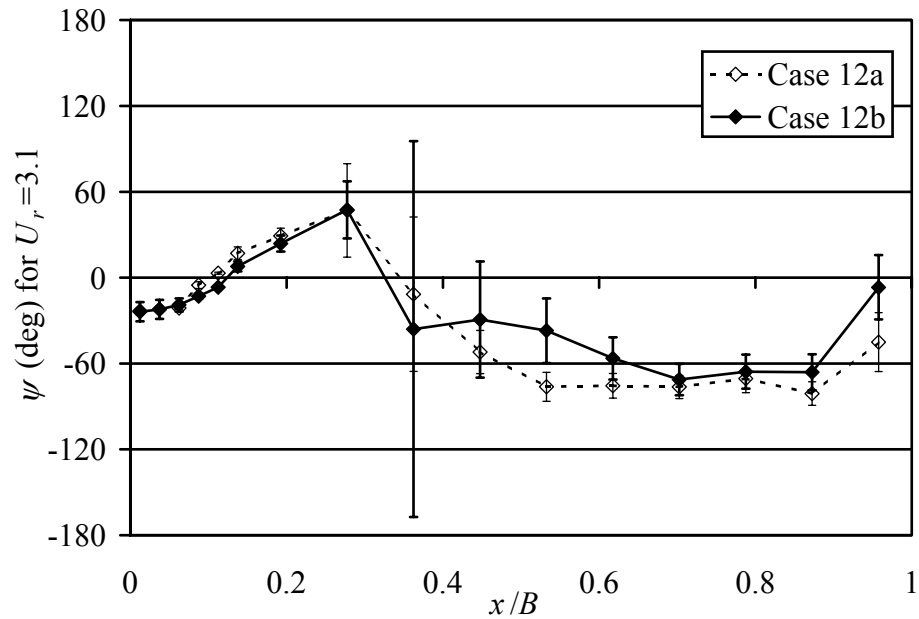


Figure 6-52 Pressure phase distributions for  $U_r = 3.1$  and  $I_u = 12\%$  showing the effect of changing scales (error bars represent 95% confidence intervals).

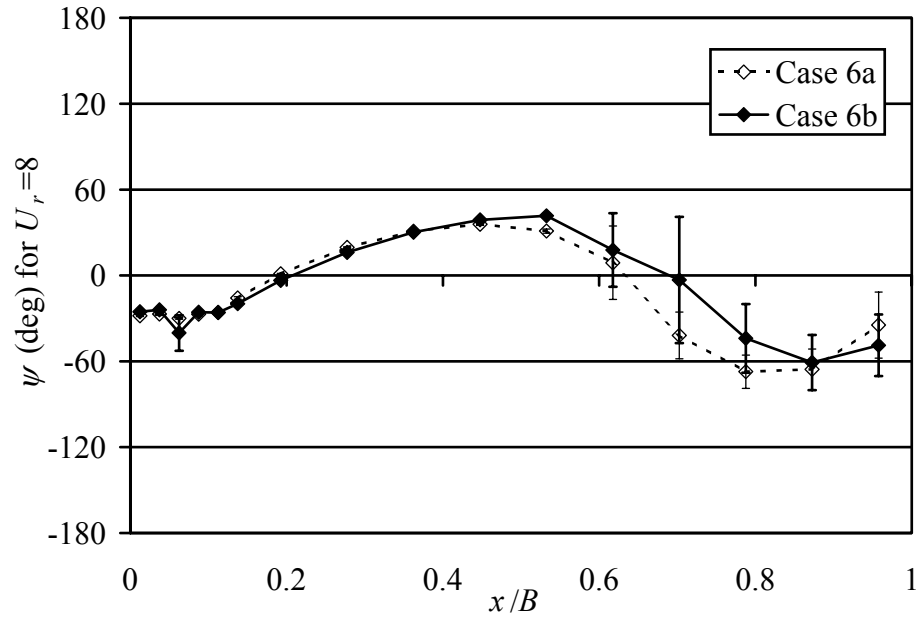


Figure 6-53 Pressure phase distributions for  $U_r = 8$  and  $I_u = 6\%$  showing the effect of changing scales (error bars represent 95% confidence intervals).

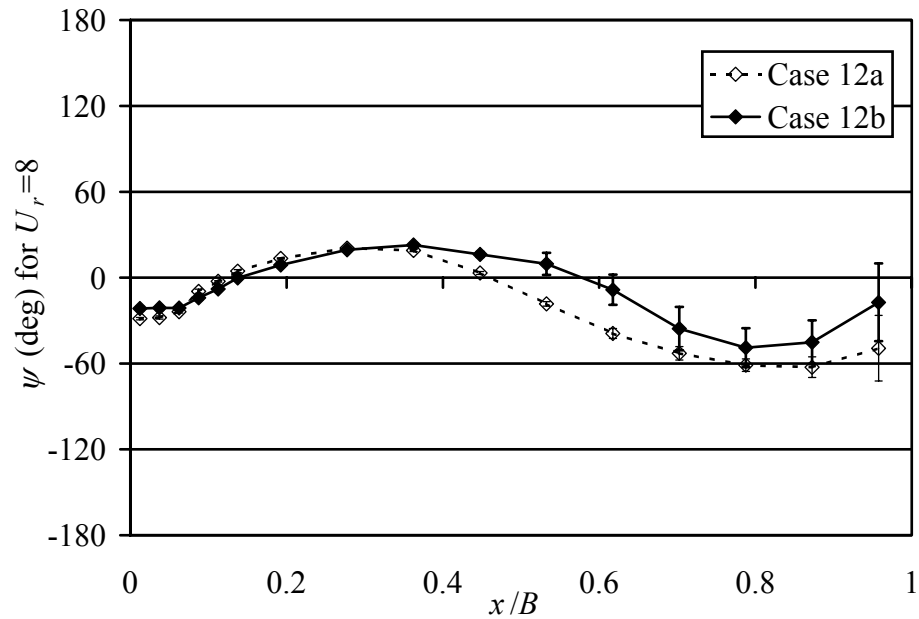


Figure 6-54 Pressure phase distributions for  $U_r = 8$  and  $I_u = 12\%$  showing the effect of changing scales (error bars represent 95% confidence intervals).

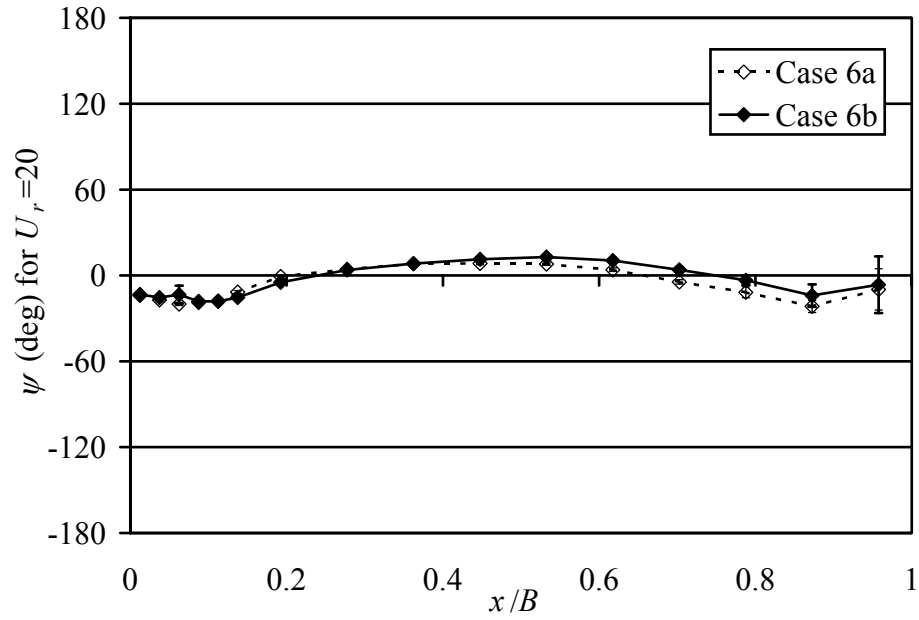


Figure 6-55 Pressure phase distributions for  $U_r = 20$  and  $I_u = 6\%$  showing the effect of changing scales (error bars represent 95% confidence intervals).

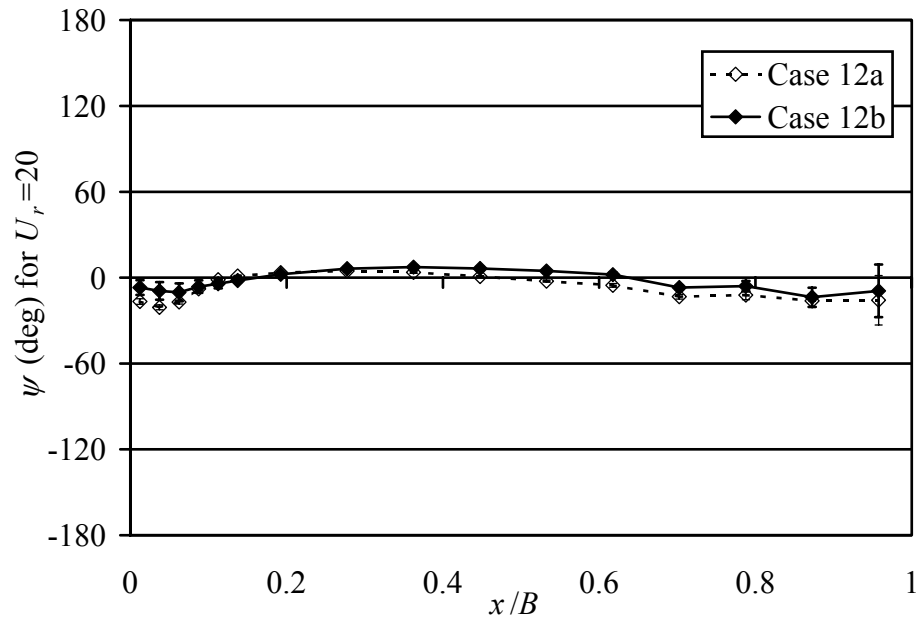


Figure 6-56 Pressure phase distributions for  $U_r = 20$  and  $I_u = 12\%$  showing the effect of changing scales (error bars represent 95% confidence intervals).

## 6.4 Flutter Derivatives

The pressure distributions of section 6.3 can be integrated as described in Chapter 2 to obtain flutter derivatives. Figure 6-23 shows the flutter derivative  $A_2^*$  calculated from pressure measurements in each incident flow considered. Turbulence was observed to have a stabilizing effect on the values of  $A_2^*$ . These effects are considered stabilizing because, as discussed in Chapter 1,  $A_2^*$  is associated with the aerodynamic damping for the torsional motion. Large positive values of  $A_2^*$  correspond to “negative damping” effects. Turbulence of 6% intensity reduced  $A_2^*$  considerably, the turbulence intensity of 12% continued this trend even resulting in negative  $A_2^*$  values. Scale effects were not particularly significant for the range of scales considered.

Values of  $A_3^*$  are presented in Figure 6-58. Turbulence-induced changes in  $A_3^*$  were different than those in  $A_2^*$ . While  $A_2^*$  curves were similar for similar turbulence intensities,  $A_3^*$  curves were similar for similar turbulence scales. For example, both the smaller scale turbulence cases increased the magnitude of  $A_3^*$  at  $U_r = 20$  by about 65% but the two larger scale flows increased  $A_3^*$  by only 40%.

The aerodynamic coupling terms of  $H_2^*$  and  $H_3^*$  are plotted in Figure 6-59 and Figure 6-60, respectively. The magnitudes of both are significantly decreased from their smooth flow values by incident turbulence. Although  $H_2^*$  exhibited no clear trend with respect to turbulence scale, the overall behavior was similar to that of  $A_2^*$  where increasing turbulence intensity resulted in lower values of  $H_2^*$ . As demonstrated in Chen et al. (2000), the shift in the  $H_3^*$  values is a stabilizing effect when considering coupled,

multi-mode problems.  $H_3^*$  curves were also grouped approximately by turbulence intensity. Greater turbulence intensity resulted in lower magnitudes. When comparing values for equal  $I_u$ , greater turbulence scales also lowered  $H_3^*$  magnitudes.

A more detailed analysis of the behavior of the flutter derivatives in turbulent flow is part of Chapter 8. This discussion will include how specific changes in pressure distributions alter the flutter derivatives.

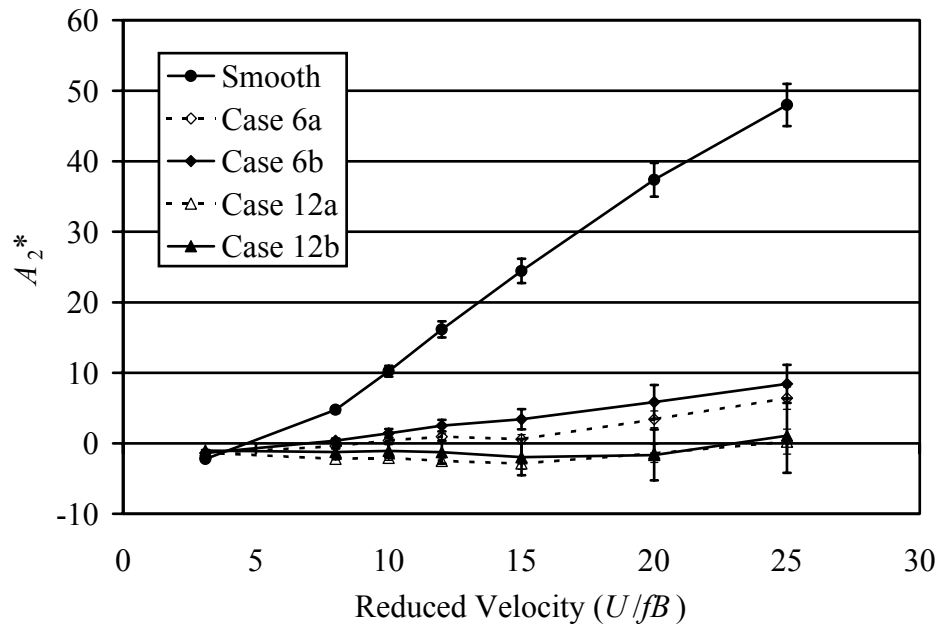


Figure 6-57 Flutter derivative  $A_2^*$  in smooth and turbulent flow.

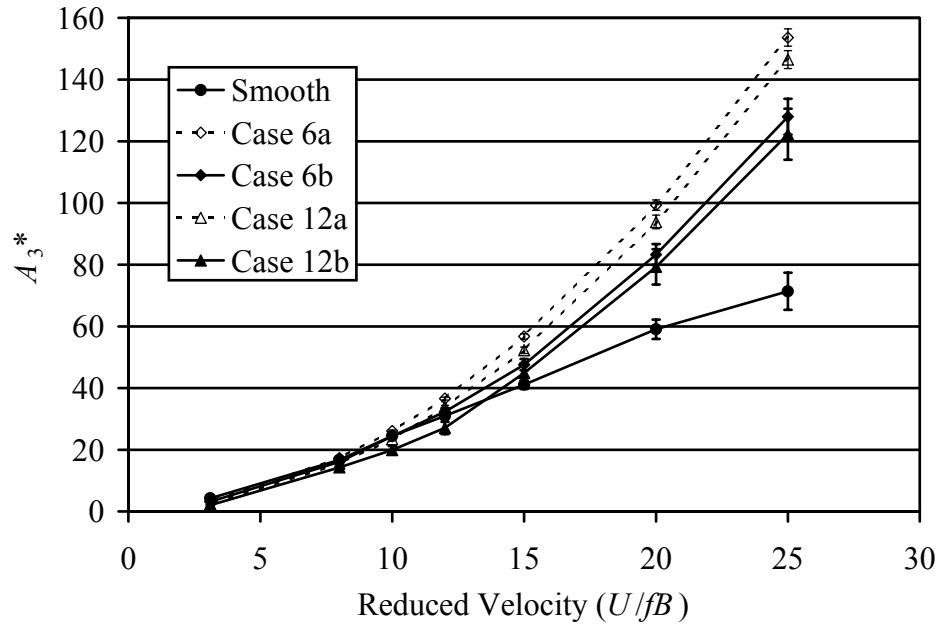


Figure 6-58 Flutter derivative  $A_3^*$  for smooth and turbulent flow.

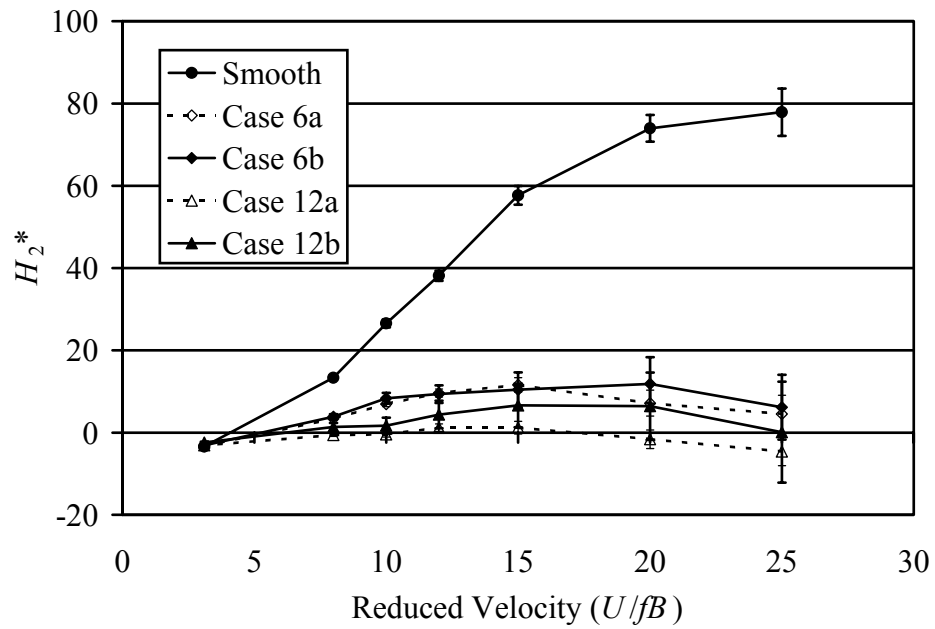


Figure 6-59 Flutter derivative  $H_2^*$  in smooth and turbulent flow.

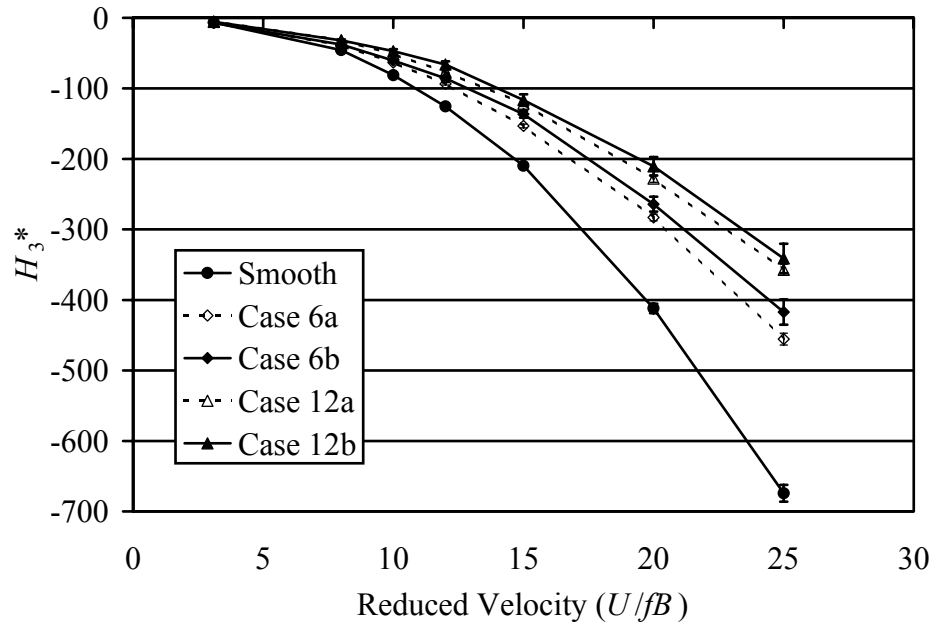


Figure 6-60 Flutter derivative  $H_3^*$  in smooth and turbulent flow.

### 6.5 Aerodynamic Admittance Functions

Having addressed the self-excited forces in the preceding two sections, data pertaining to the buffeting forces are now presented. Specifically, aerodynamic admittance functions are plotted and compared with their stationary model counterparts. While this section presents frequency-dependent functions of force and moment data, section 6.6 will present various statistical quantities of individual pressure signals that provide a more fundamental perspective on the overall forces. As introduced in Chapter 1, aerodynamic admittance functions are essentially frequency response functions describing well turbulent velocity fluctuations translate into buffeting lift and moment forces on the body. The expressions presented in Chapter 1 were employed in a modified

form to quantify admittance for this project. While those expressions were in the time domain, frequency domain expressions were used here as follows:

$$G_{LL}(f) = \left( \frac{1}{2} \rho U^2 2b \right)^2 \left( (C'_L)^2 |\chi_{L_{bw}}|^2 \frac{G_{ww}(f)}{U^2} \right) \quad (6-3)$$

$$G_{MM}(f) = \left( \frac{1}{2} \rho U^2 (2b)^2 \right)^2 \left( (C'_M)^2 |\chi_{M_{bw}}|^2 \frac{G_{ww}(f)}{U^2} \right) \quad (6-4)$$

where  $G_{LL}$  and  $G_{MM}$  are the power spectral density functions of lift and moment, respectively,  $C'_L$  and  $C'_M$  are the slopes, at zero angle of attack, of the static lift and moment curves, respectively, and  $|\chi_{L_{bw}}|^2$  and  $|\chi_{M_{bw}}|^2$  are the aerodynamic admittance functions relating vertical velocity fluctuations to lift and moment, respectively. Because it is dominant, only admittance for  $w$  fluctuations was calculated here using the velocity spectra reported in Chapter 4. Values for the slopes of the lift and moment slopes were found using results of stationary model tests at various angles of attack. Values of  $C'_L = 9.5$  and  $C'_M = 1.15$  were used for each case.

In the following plots “lift admittance” refers to  $|\chi_{L_{bw}}|^2$ , and “moment admittance” refers to  $|\chi_{M_{bw}}|^2$ . An admittance plot is presented here for each of the spectra presented in section 6.2. This includes a comparison of stationary model admittance with oscillating model admittance in each case. Lift and moment admittance functions for  $U_r = 3.1$  are presented in Figure 6-61 through Figure 6-64; admittance functions for  $U_r = 8$  are given in Figure 6-65 through Figure 6-68; and admittance functions for  $U_r = 20$  are given in Figure 6-69 through Figure 6-72.

Little discernable dependence of broad band admittance on reduced velocity was evident. This follows from the results of section 6.2 where negligible reduced velocity dependence was found for the broad band force and moment spectra. In general, admittance was observed here to decrease with greater turbulence intensity. This agrees with the turbulence intensity trends reported by Sankaran & Jancauskas (1992). With greater turbulence scale, admittance values increased particularly for the lower frequency range.

As discussed previously, turbulent buffeting analysis of long-span bridges is generally conducted using experimental data obtained from stationary bridge models. The buffeting forces are assumed to be independent of any deck motion. The data acquired for this project allows an examination of this assumption. In each figure of this section, both stationary and oscillating model admittance functions are plotted together. As with the force spectra results of section 6.2, matches were quite good. In most cases, however, admittance functions were slightly increased by the model motion. The majority of this increase was for frequencies above  $fB/U = 0.1$ . This increase became less significant with increased turbulence intensity and increased turbulence scale. In addition to this frequency-domain analysis of the buffeting decomposition assumption, section 6.6 examines this assumption with statistics of individual pressure signals.

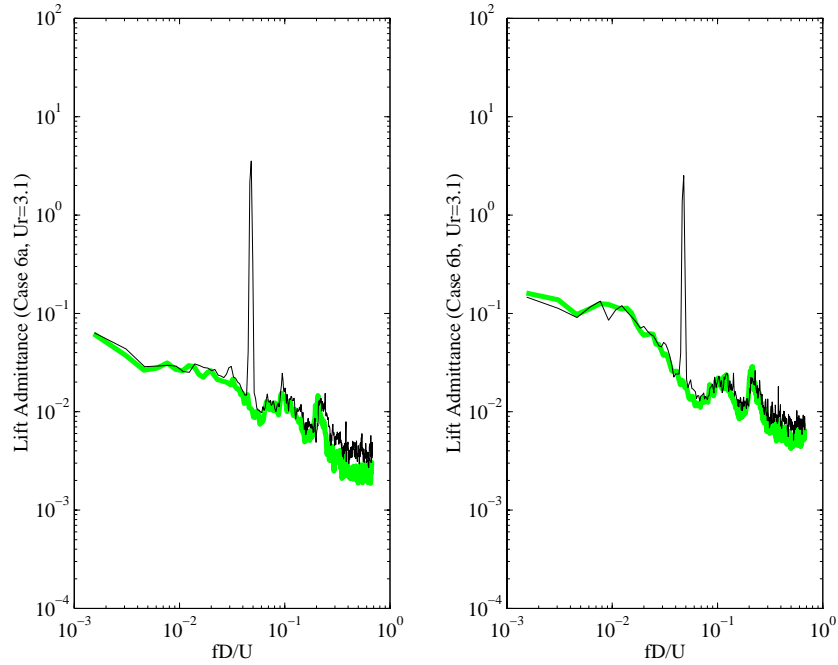


Figure 6-61 Lift admittance functions for  $I_u = 6\%$  for both stationary and  $U_r = 3.1$  tests (stationary results shaded).

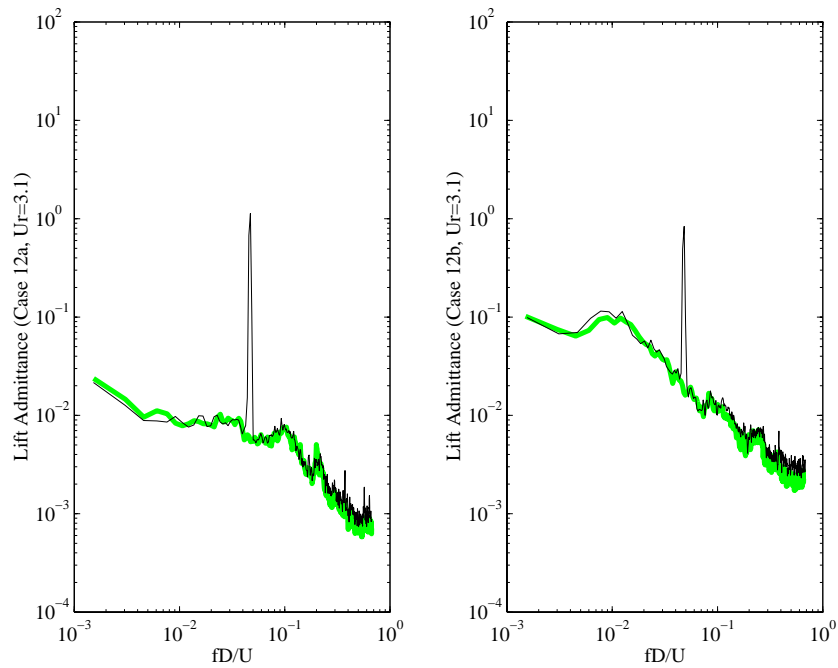


Figure 6-62 Lift admittance functions for  $I_u = 12\%$  for both stationary and  $U_r = 3.1$  tests (stationary results shaded).

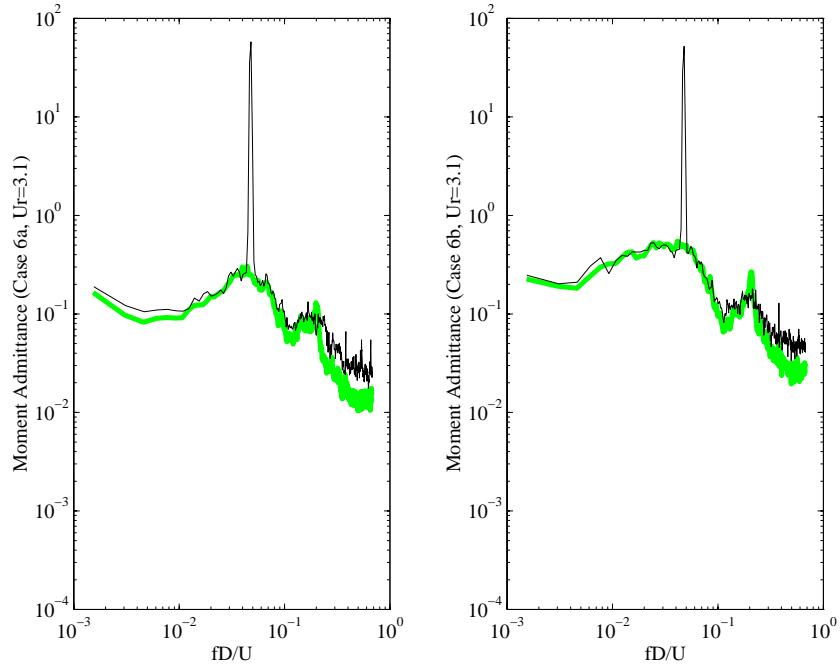


Figure 6-63 Moment admittance functions for  $I_u = 6\%$  for both stationary and  $U_r = 3.1$  tests (stationary results shaded).

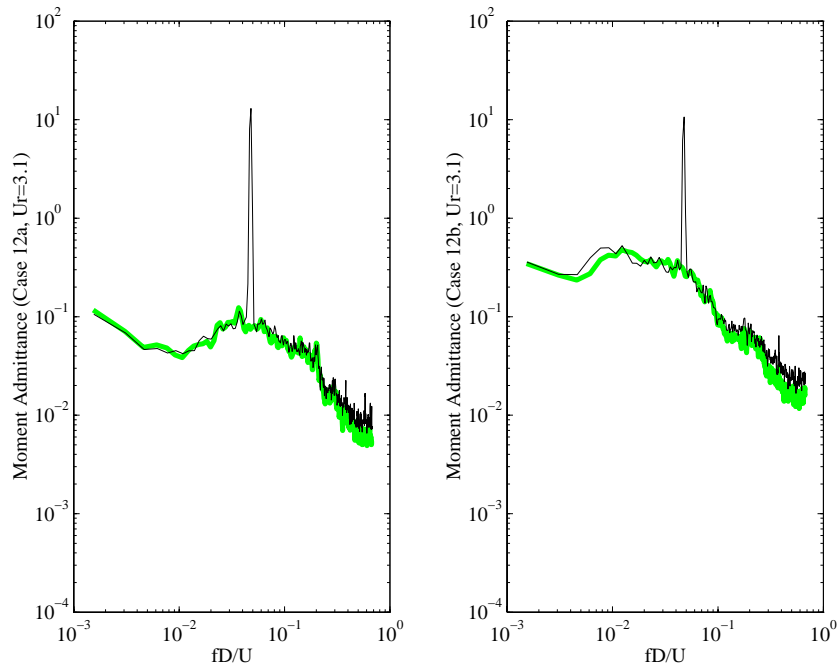


Figure 6-64 Moment admittance functions for  $I_u = 12\%$  for both stationary and  $U_r = 3.1$  tests (stationary results shaded).

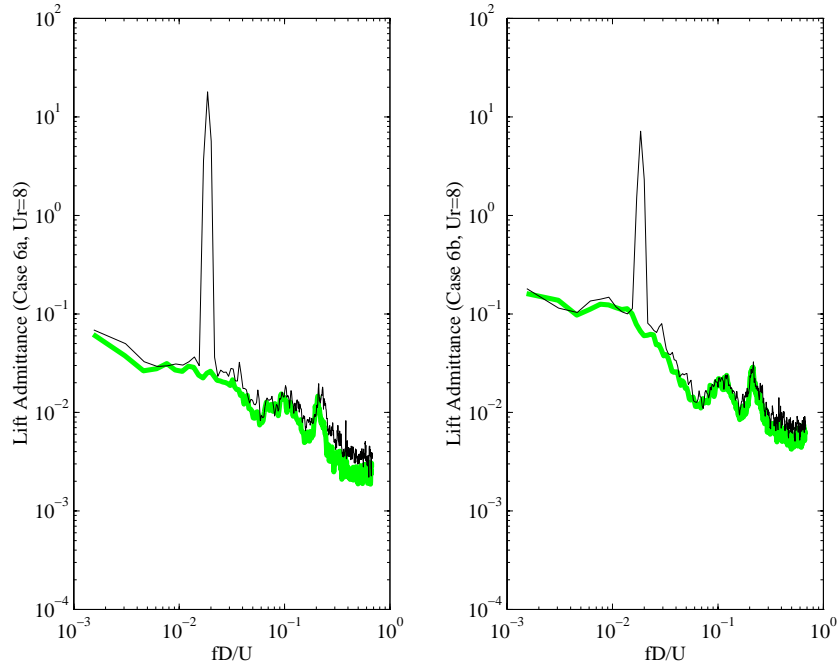


Figure 6-65 Lift admittance functions for  $I_u = 6\%$  for both stationary and  $U_r = 8$  tests (stationary results shaded).

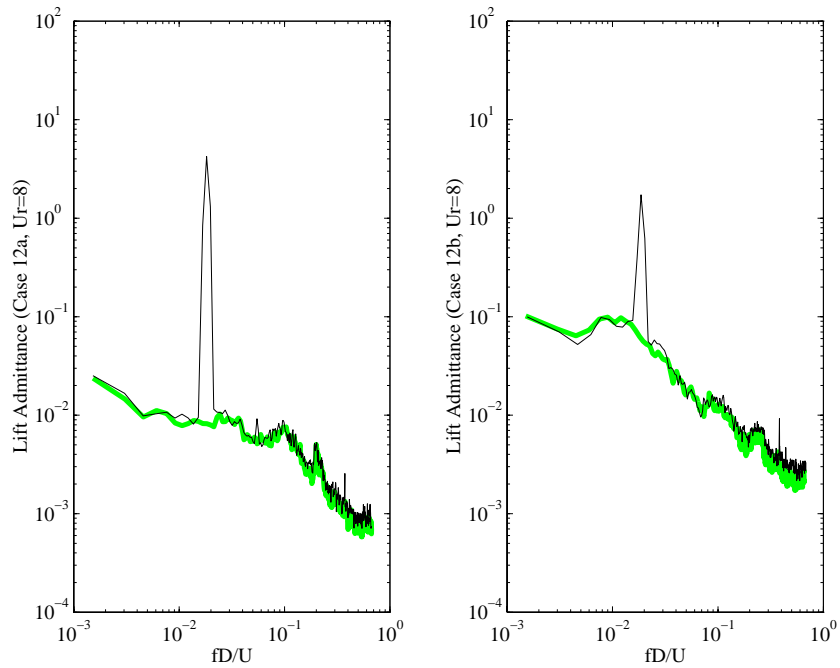


Figure 6-66 Lift admittance functions for  $I_u = 12\%$  for both stationary and  $U_r = 8$  tests (stationary results shaded).

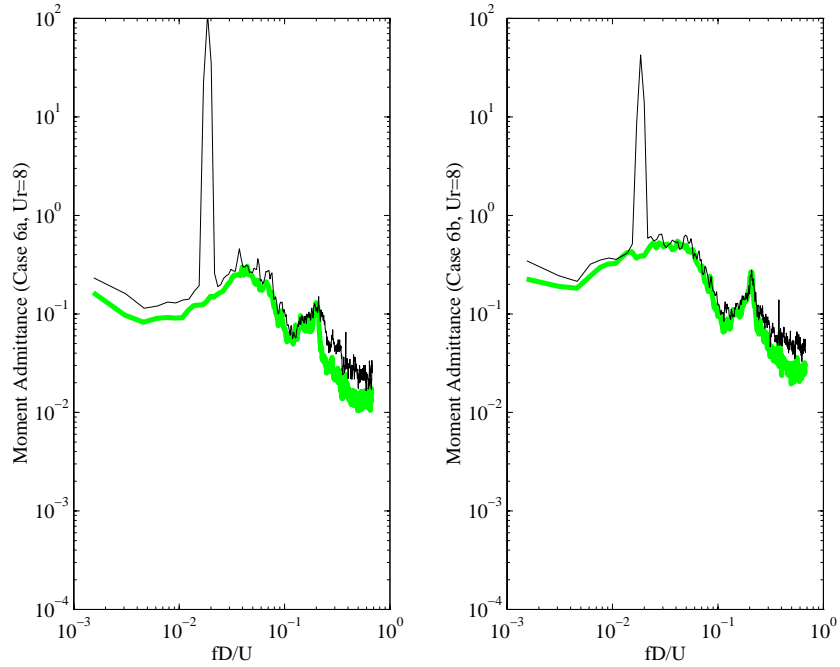


Figure 6-67 Moment admittance functions for  $I_u = 6\%$  for both stationary and  $U_r = 8$  tests (stationary results shaded).

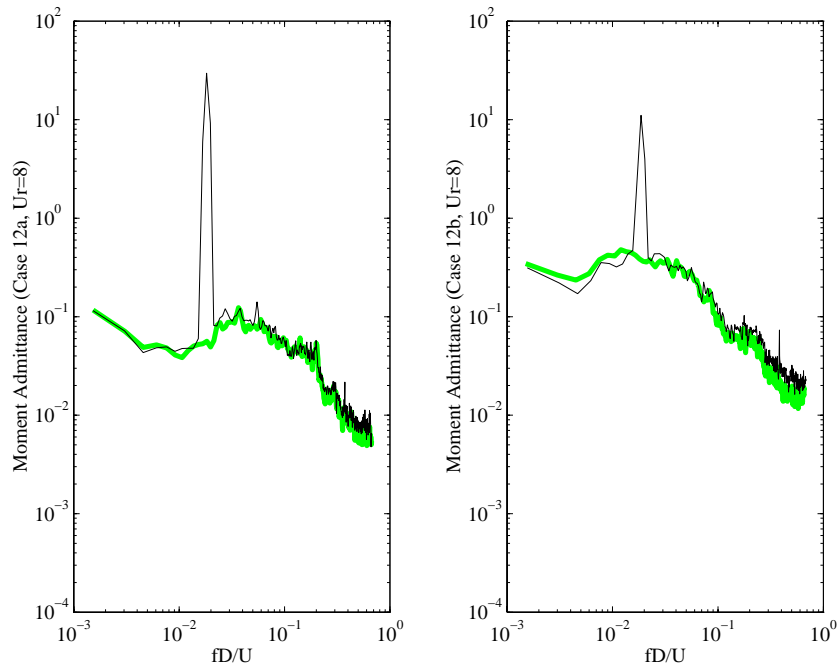


Figure 6-68 Moment admittance functions for  $I_u = 12\%$  for both stationary and  $U_r = 8$  tests (stationary results shaded).

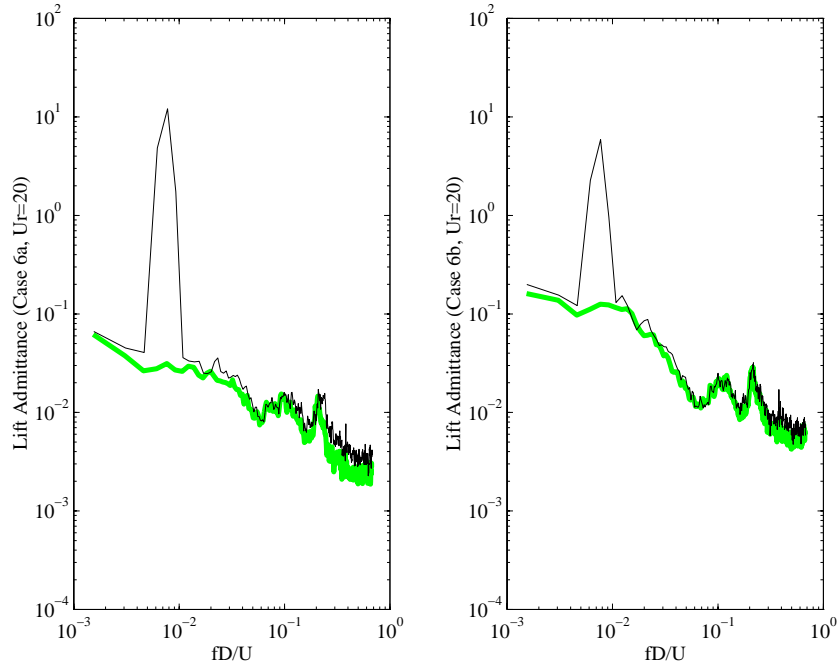


Figure 6-69 Lift admittance functions for  $I_u = 6\%$  for both stationary and  $U_r = 20$  tests (stationary results shaded).

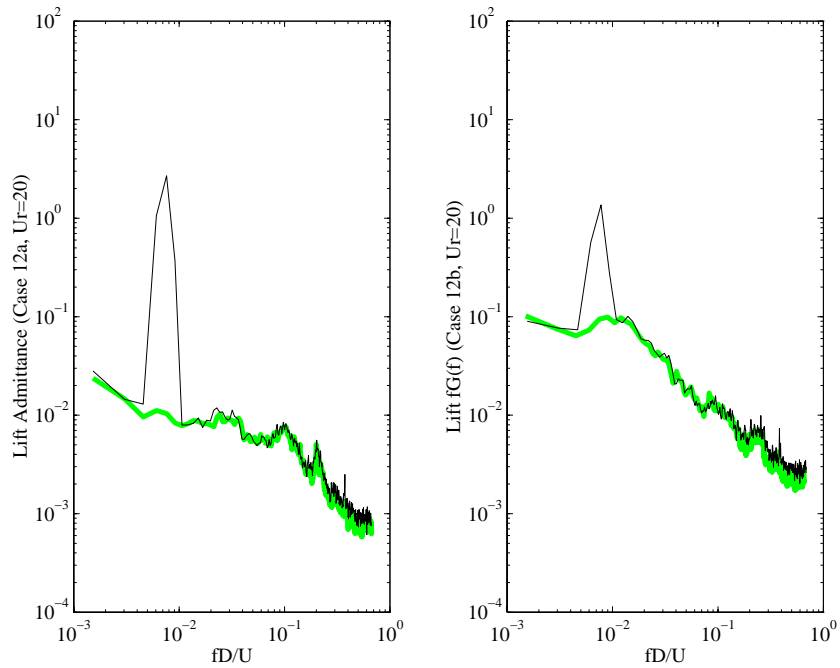


Figure 6-70 Lift admittance functions for  $I_u = 12\%$  for both stationary and  $U_r = 20$  tests (stationary results shaded).

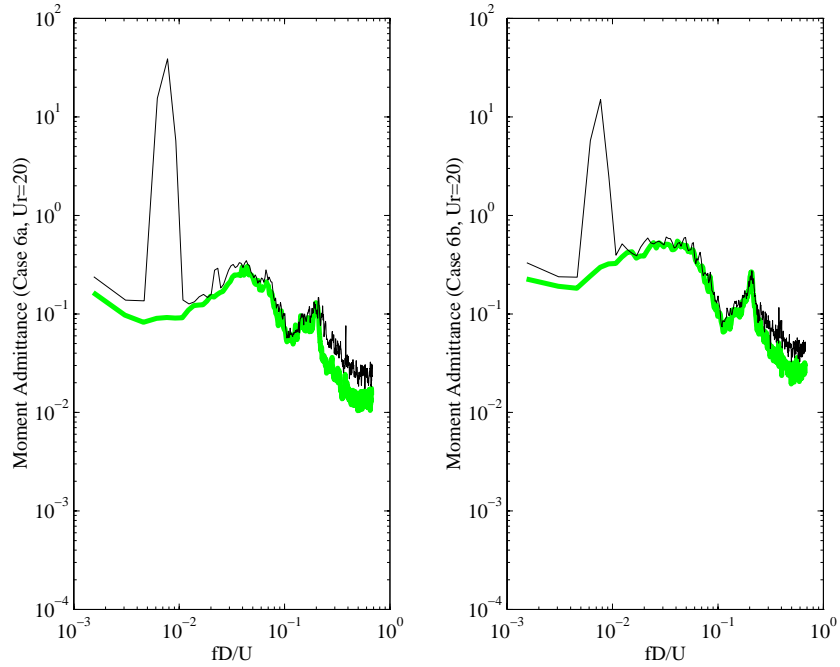


Figure 6-71 Moment admittance functions for  $I_u = 6\%$  for both stationary and  $U_r = 20$  tests (stationary results shaded).

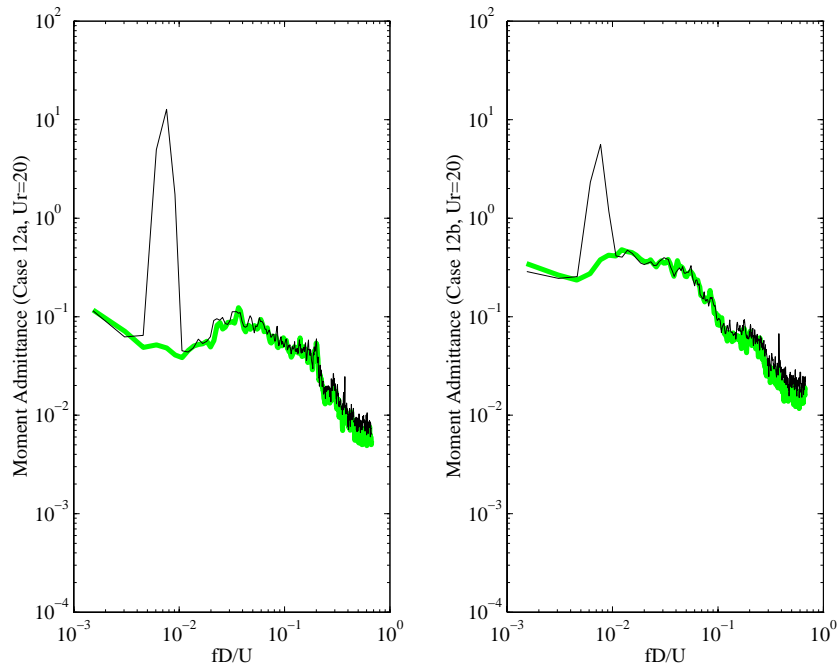


Figure 6-72 Moment admittance functions for  $I_u = 12\%$  for both stationary and  $U_r = 20$  tests (stationary results shaded).

## 6.6 Statistical Distributions of Pressure

Streamwise variation of various statistical distributions are presented here to provide a more fundamental picture of the aerodynamics than that provided by lift and moment data. Streamwise distributions of rms pressures, skewness coefficients, and kurtosis coefficients are plotted for each flow case at reduced velocities of 3.1, 8, and 20.

The distributions of rms pressures are presented in two different ways. For each reduced velocity, three plots are provided. The first plot contains the streamwise distributions of rms pressure for each flow condition. These plots are generated from complete oscillating model pressure signals. The second two plots compare stationary model rms values with oscillating model rms values from which the content of the oscillation frequency peak has been subtracted.

Figure 6-73 presents rms pressure distributions for  $U_r = 3.1$ . As discussed for the stationary model values of Chapter 5, the peak in the rms pressure distribution shifts upstream for increasing turbulence intensity. The magnitudes of the peak values increase with turbulence scale—with such increase being greater for greater turbulence intensities. This is reasonable considering the larger buffeting forces generated when turbulence scale increases. When the rms content at the model oscillation frequency is removed from the rms values oscillating model rms values approximate the broad band buffeting content of the signals. The degree of similarity between this buffeting content for oscillating models and those for stationary model is an important issue when considering the current practice of analyzing buffeting response from stationary model buffeting measurements.

Figure 6-74 and Figure 6-75 show the results of comparing stationary and oscillating model buffeting forces for small and large scale turbulent flows, respectively. Observations of spectra in section 6.2 found that model motion increased the broad band energy levels of the aerodynamic forces. These figures show a similar increase. Smooth flow results show the most significant changes with respect to model motion. Being able to see the streamwise distribution of the changes due to model motion allows one to see that most changes occur upstream of the peak in the rms distribution—in the region most likely associated with the separation bubble. This fact, of course, was not discernible from the lift and moment spectra presented earlier. Greater turbulence intensities and larger turbulence scales reduced the mismatch—relative to the stationary values—between oscillating and stationary results.

Figure 6-76 through Figure 6-78 present similar results for  $U_r = 8$ . Total rms values in Figure 6-76 were greater than for  $U_r = 3.1$ , but all the trends with respect to turbulence were the same. Comparison of the broad band content with stationary results showed very similar results to those of  $U_r = 3.1$ . The same trends were found in the distribution for  $U_r = 20$  plotted in Figure 6-79 through Figure 6-81. Trends in buffeting load comparisons with respect to reduced velocity were discussed section 6.2.

In addition to rms values, peak pressure coefficient distribution were measured as well. Figure 6-82 through Figure 6-84 present peak distributions for reduced velocities of 3.1, 8, and 20, respectively. In each case, the same general trends were observed with respect to turbulence as found for stationary models. Greater turbulence intensity and greater turbulence scale both increase the magnitudes of the peak pressures. With respect to reduced velocity, distributions were quite similar.

As done in Chapter 5 for the stationary model results, the non-Gaussian character of the oscillating model pressure signals were also quantified. Skewness and kurtosis coefficient distributions were calculated for each flow and for each reduced velocity. Figure 6-85 through Figure 6-87 plot the skewness coefficient distributions in the streamwise direction for reduced velocities of 3.1, 8, and 20, respectively. Skewness coefficient values,  $S_k$ , started negative at the leading edge, increased to a maximum further downstream, and then decreased again. For stationary cylinders, the increase toward zero skewness is associated with reattachment. This seems to hold for oscillating cylinders as well—the increase toward zero occurred near the location of the maximum in the rms pressure distribution. As with the stationary model values, the greatest effects of scale were manifested downstream of reattachment. Increasing scale values greatly increased the magnitudes of  $S_k$ . Skewness magnitudes were greater when the model was oscillating. Where stationary model skewness coefficients were mostly  $>-0.6$ , oscillating model values for  $U_r \geq 8$  were mostly at or below  $S_k = -1$ .

Figure 6-88 through Figure 6-90 plot the kurtosis coefficient distributions for the same values of  $U_r$ . For  $U_r = 3.1$ ,  $K_u$  varied only about  $\pm 1.0$  from the Gaussian value of 3.0. For greater reduced velocities, kurtosis values became significantly greater reaching 7.0 for Case 12b. As was the case with  $S_k$ , the  $K_u$  values were most affected by scale downstream of reattachment. Increased scale always increased the magnitudes of  $K_u$ .

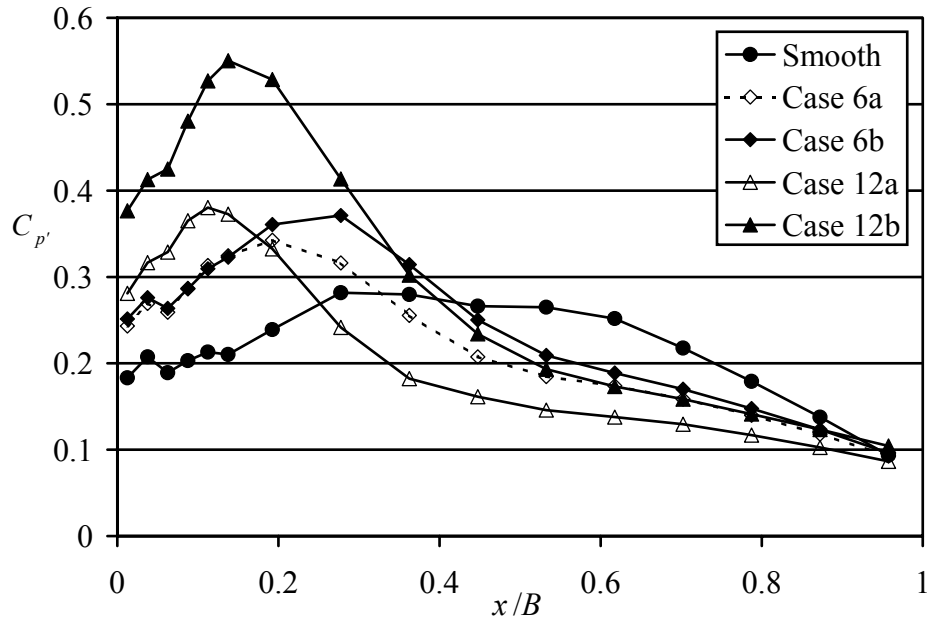


Figure 6-73 RMS pressure distributions for model oscillating at  $U_r = 3.1$  in each flow case.

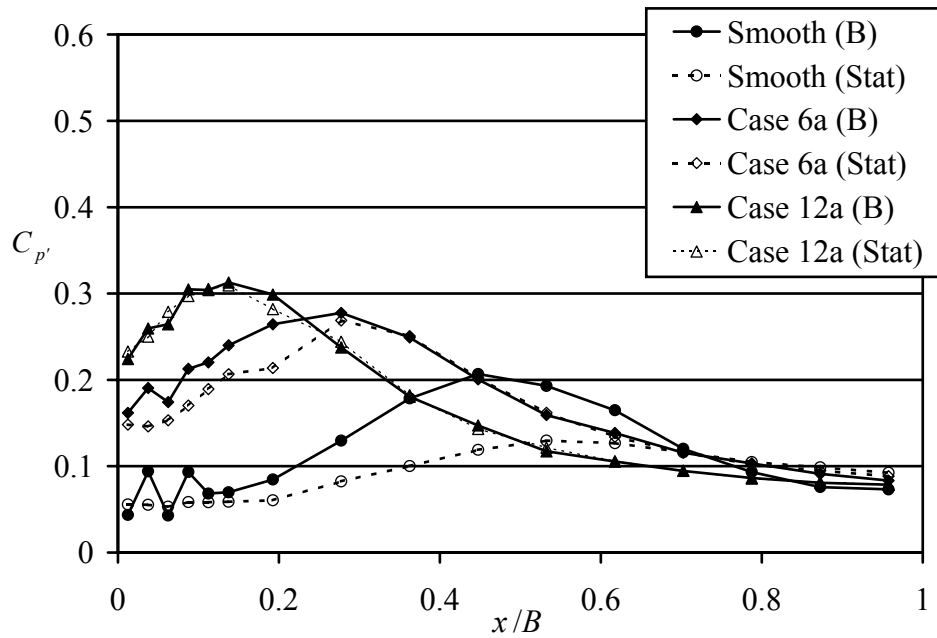


Figure 6-74 Stationary model RMS pressure values (Stat) and oscillating model RMS values with peak content subtracted (B) for small-scale turbulence at  $U_r = 3.1$ .

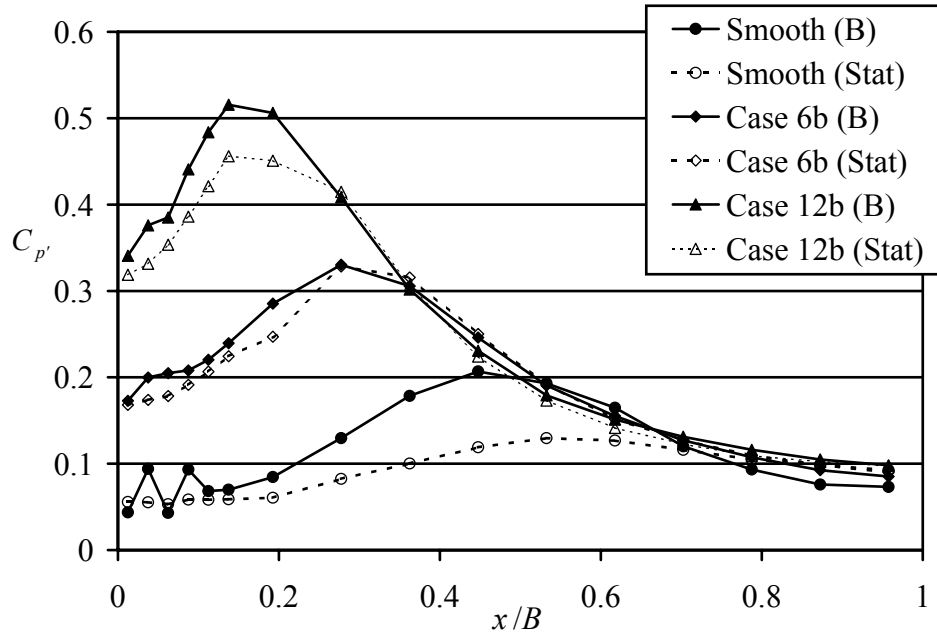


Figure 6-75 Stationary model RMS pressure values (Stat) and oscillating model RMS values with peak content subtracted (B) for large-scale turbulence at  $U_r = 3.1$ .

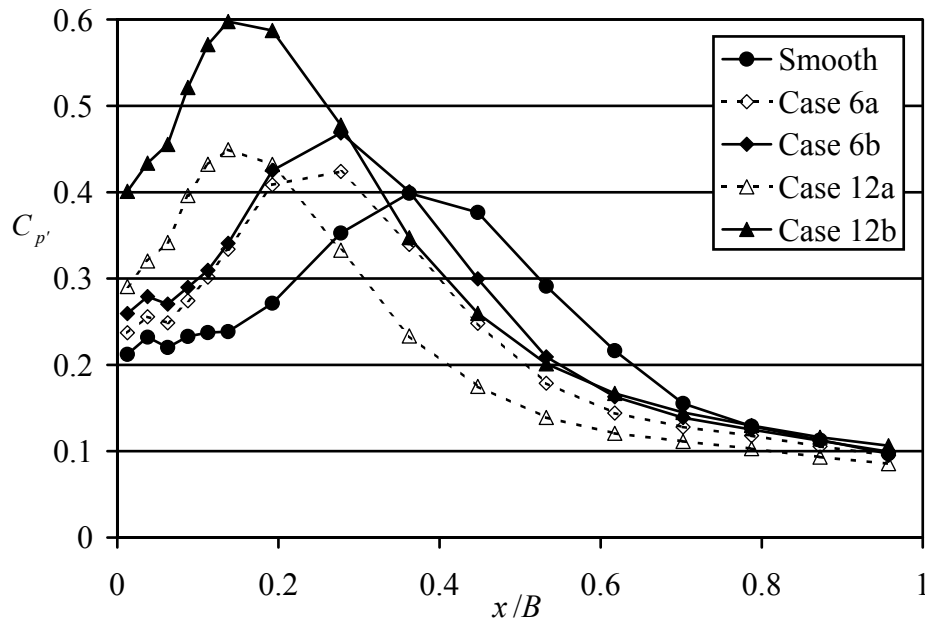


Figure 6-76 RMS pressure distributions for model oscillating at  $U_r = 8$  in each flow case.

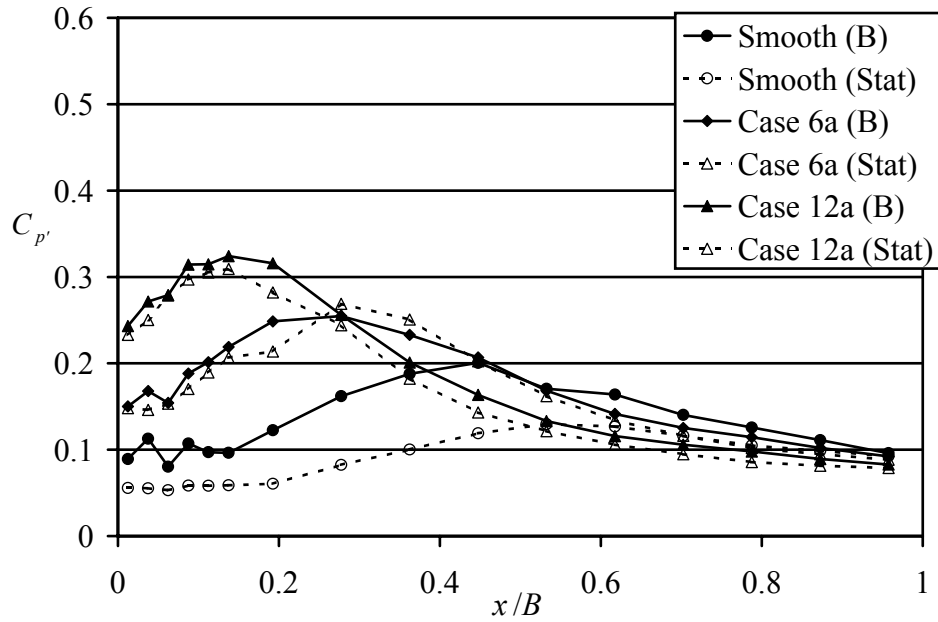


Figure 6-77 Stationary model RMS pressure values (Stat) and oscillating model RMS values with peak content subtracted (B) for small-scale turbulence at  $U_r = 8$ .

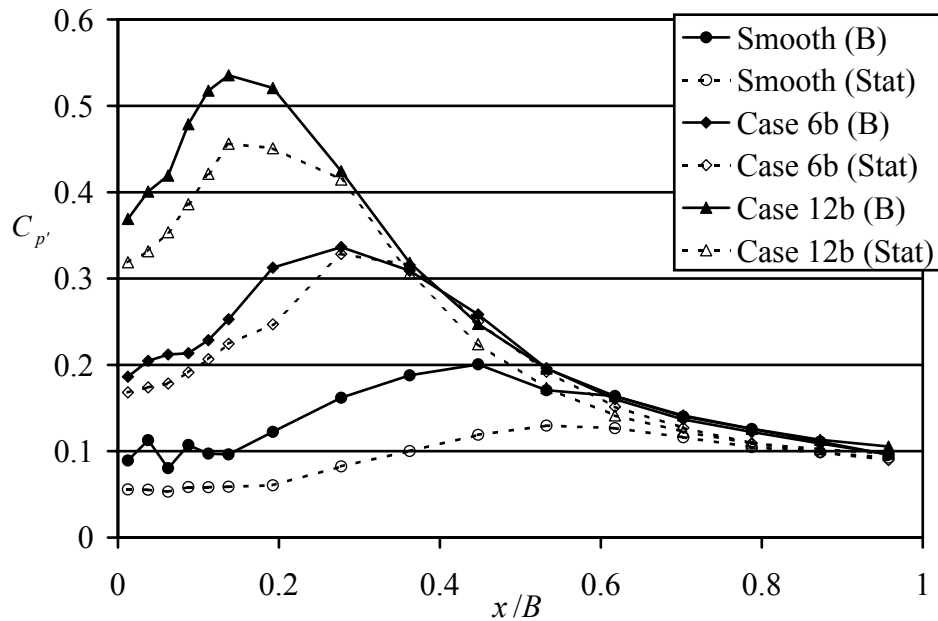


Figure 6-78 Stationary model RMS pressure values (Stat) and oscillating model RMS values with peak content subtracted (B) for large-scale turbulence at  $U_r = 8$ .

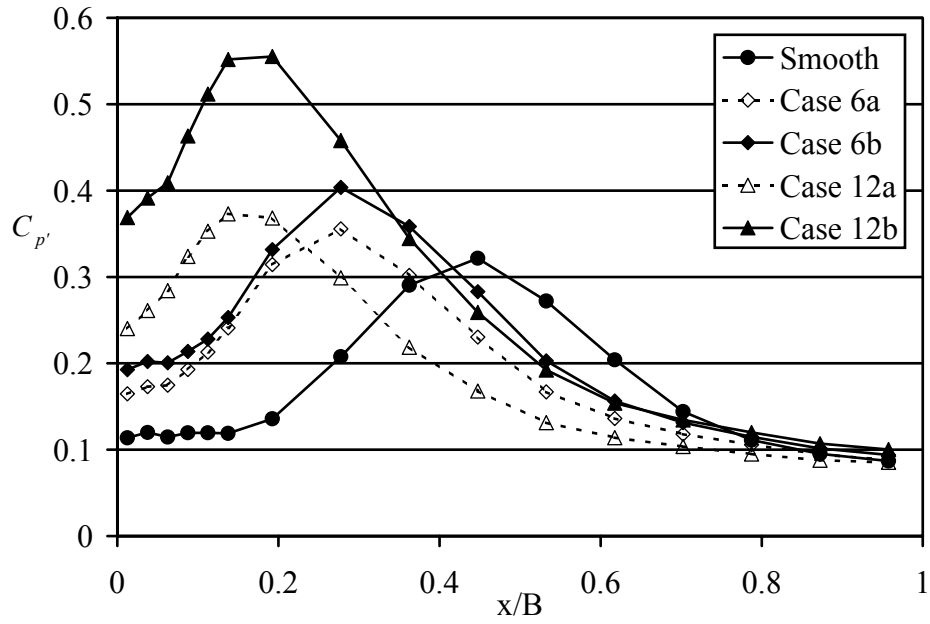


Figure 6-79 RMS pressure distributions for model oscillating at  $U_r = 20$  in each flow case.

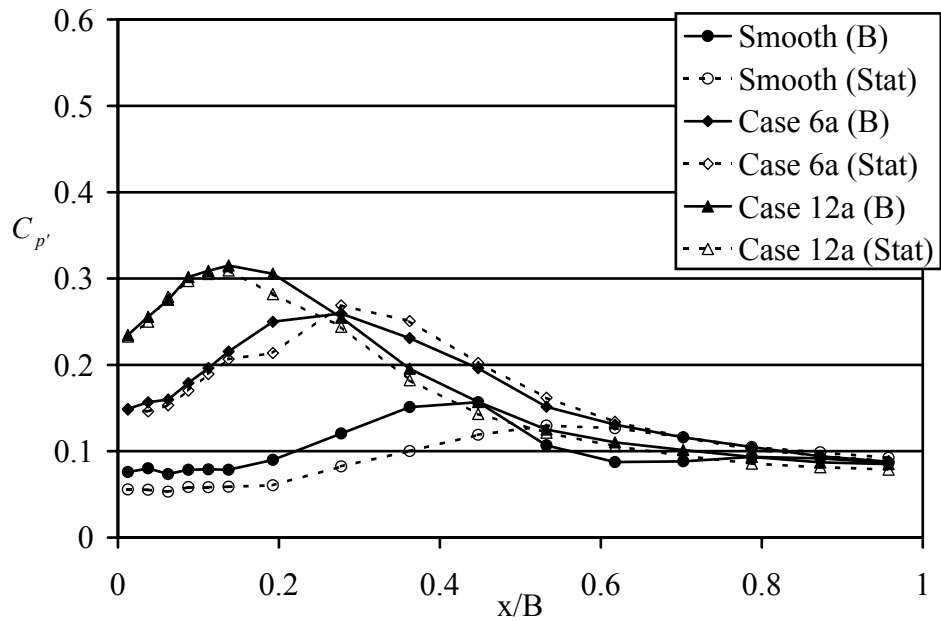


Figure 6-80 Stationary model RMS pressure values (Stat) and oscillating model RMS values with peak content subtracted (B) for small-scale turbulence at  $U_r = 20$ .

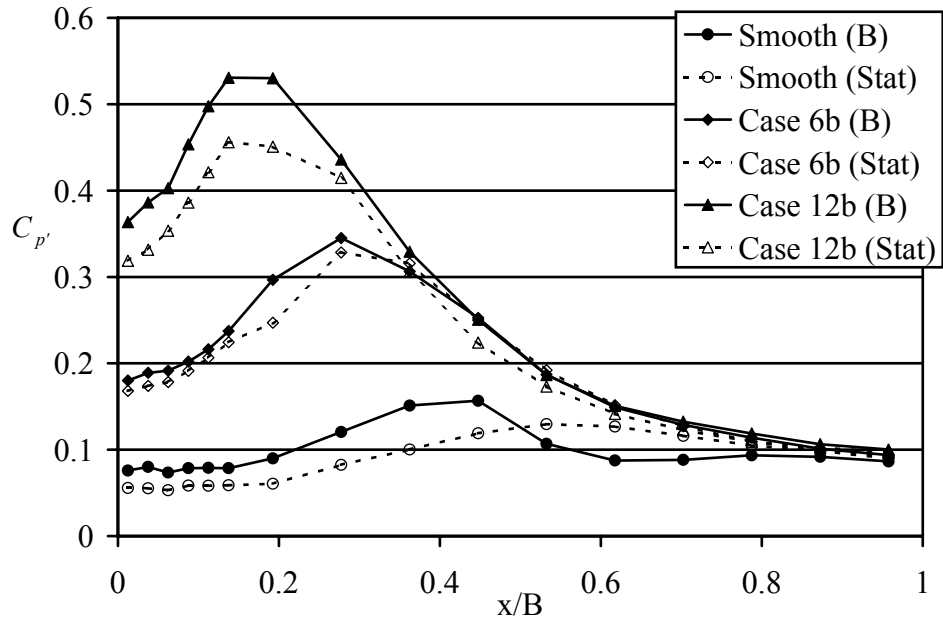


Figure 6-81 Stationary model RMS pressure values (Stat) and oscillating model RMS values with peak content subtracted (B) for large-scale turbulence at  $U_r = 20$ .

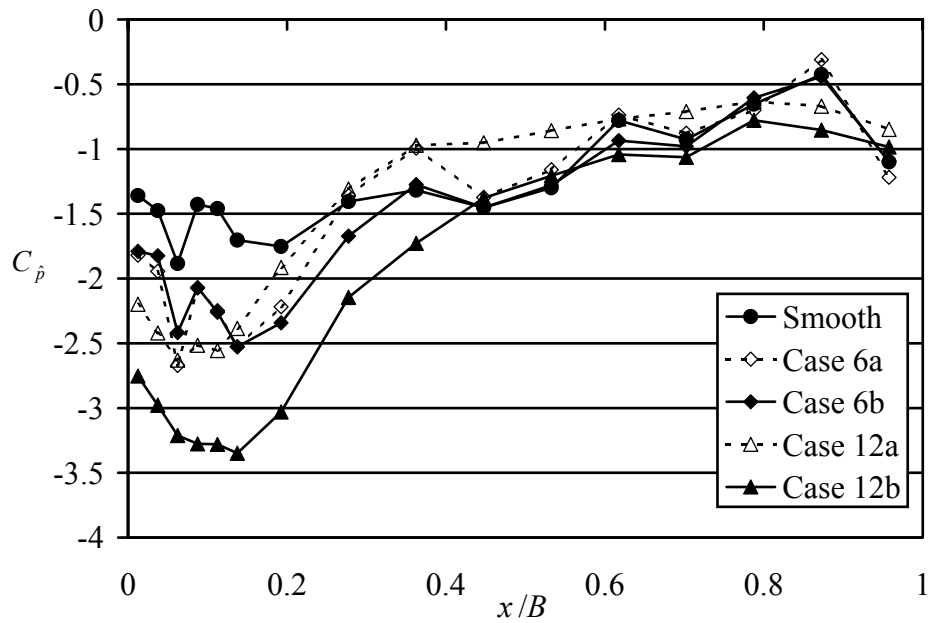


Figure 6-82 Peak pressure distributions for model oscillating at  $U_r = 3.1$  in each flow case.

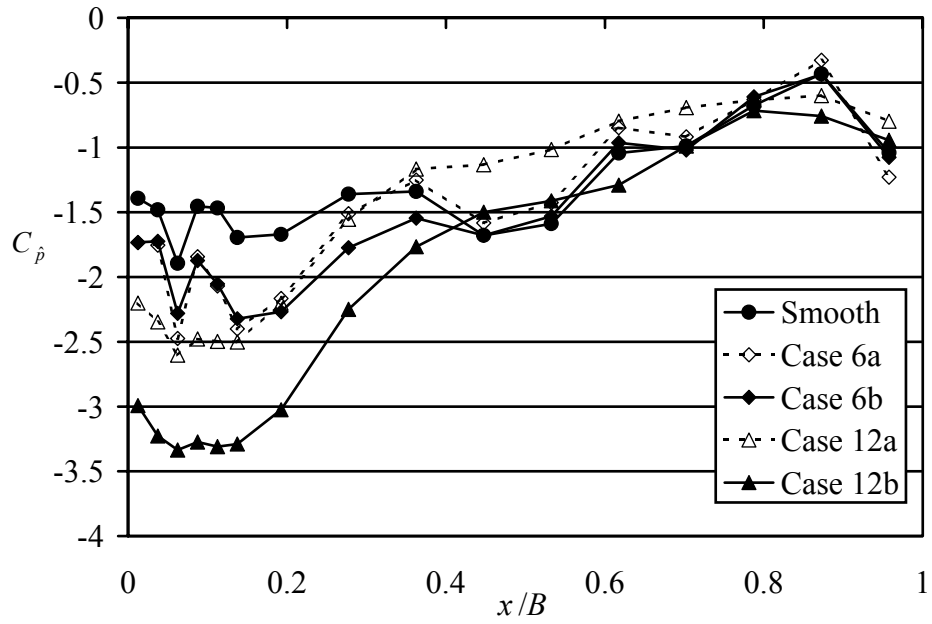


Figure 6-83 Peak pressure distributions for model oscillating at  $U_r = 8$  in each flow case.

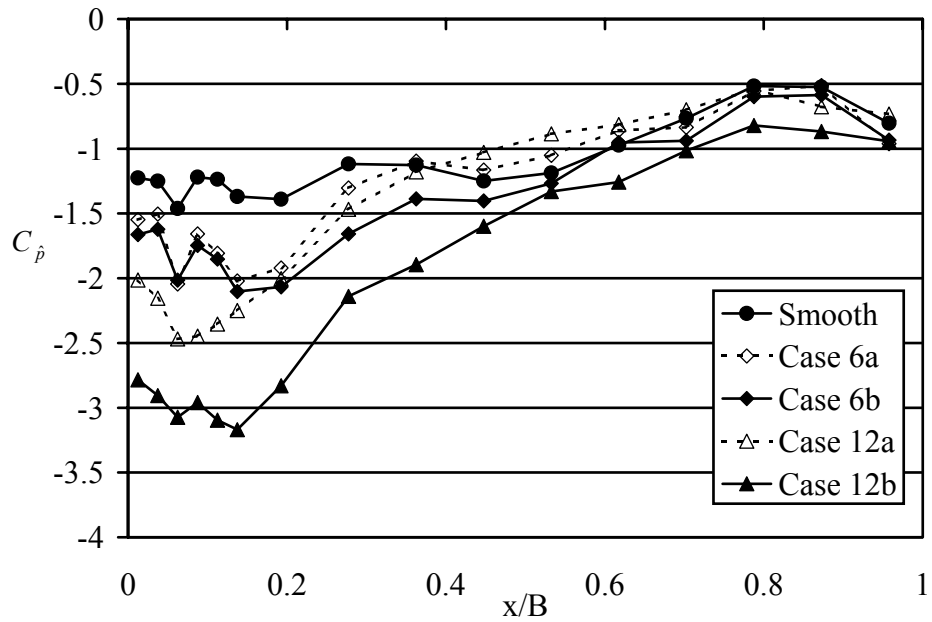


Figure 6-84 Peak pressure distributions for model oscillating at  $U_r = 20$  in each flow case.

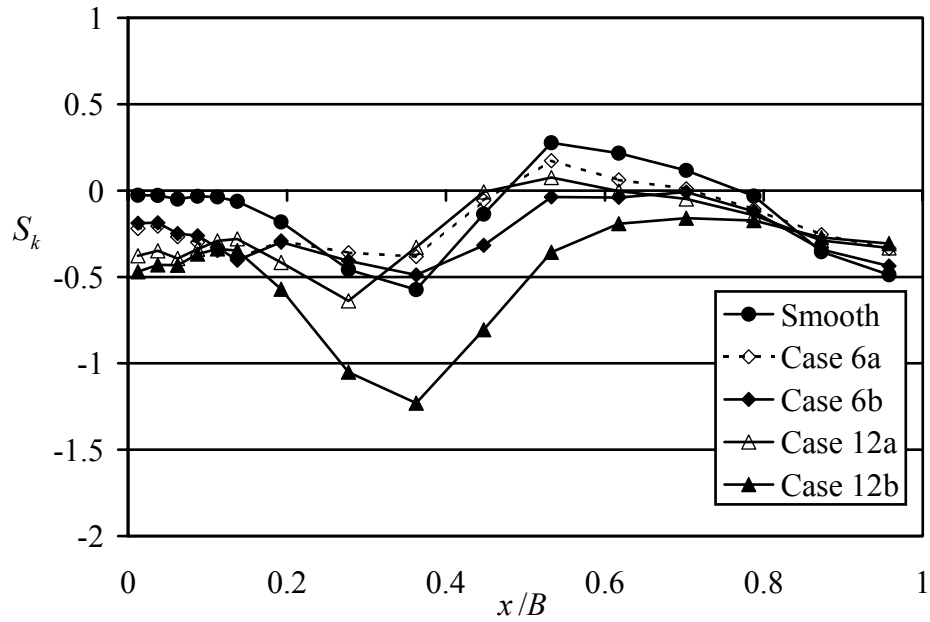


Figure 6-85 Skewness coefficient distributions for model oscillating at  $U_r = 3.1$  in each flow case.

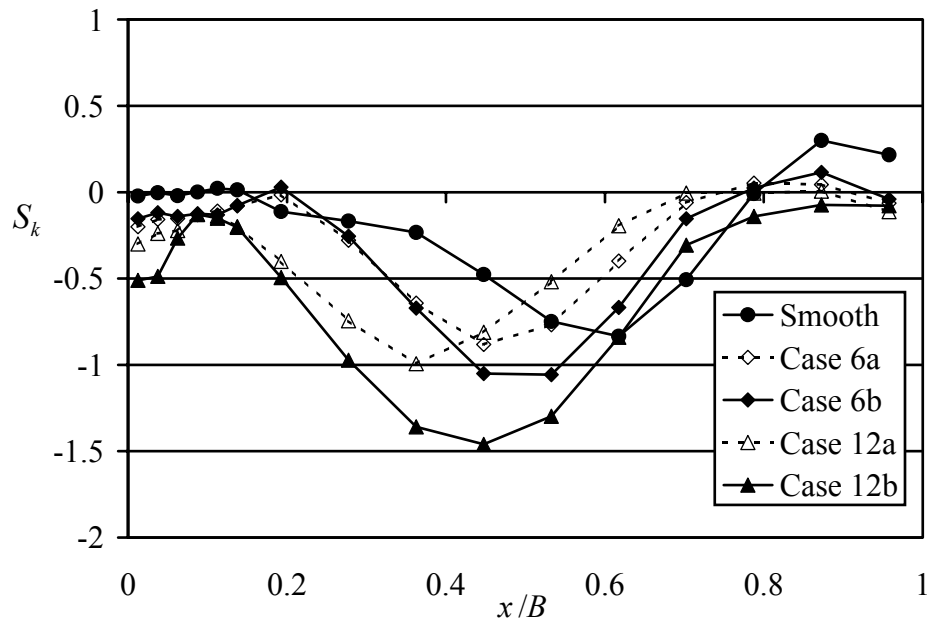


Figure 6-86 Skewness coefficient distributions for model oscillating at  $U_r = 8$  in each flow case.

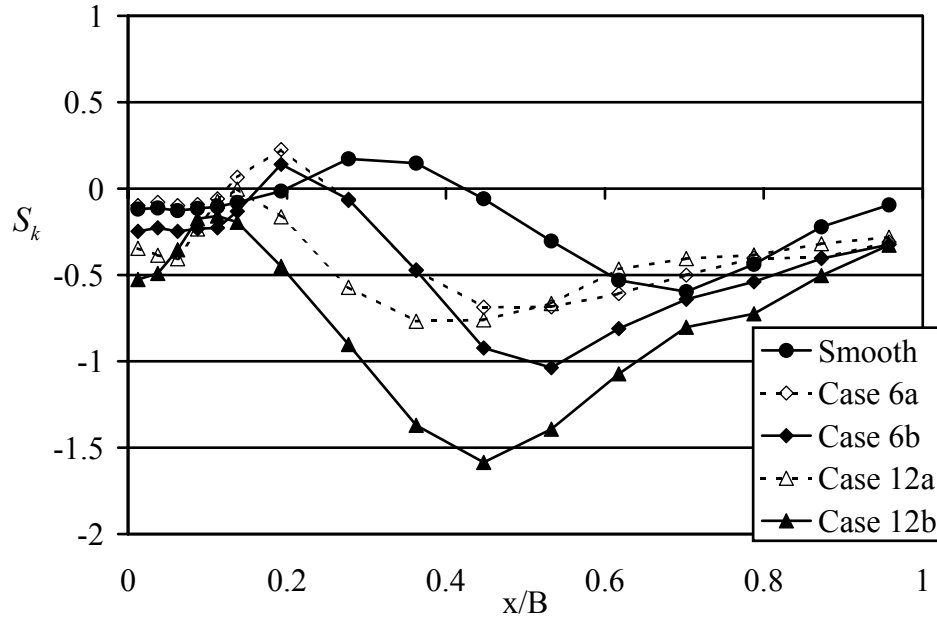


Figure 6-87 Skewness coefficient distributions for model oscillating at  $U_r = 20$  in each flow case.

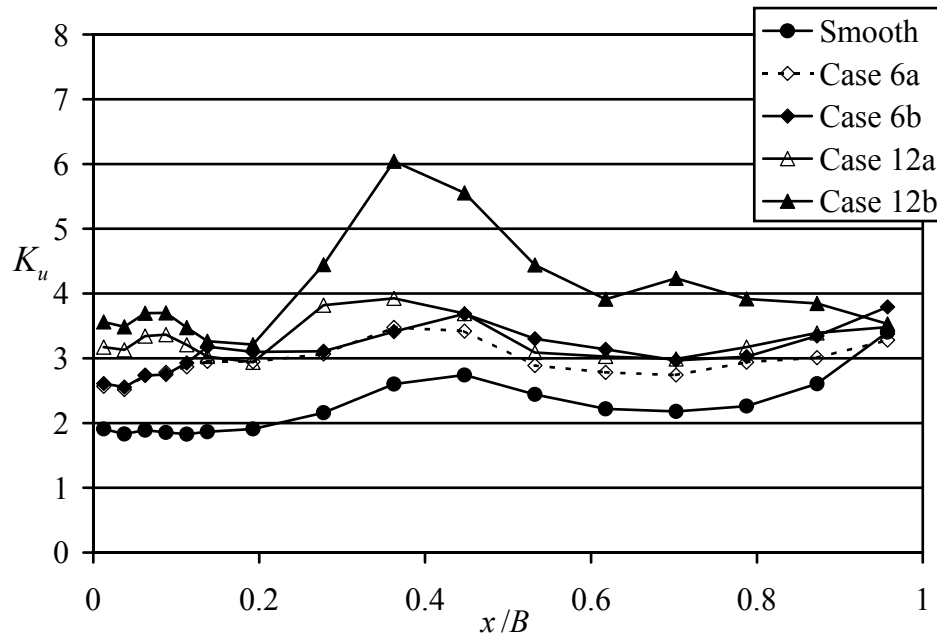


Figure 6-88 Kurtosis coefficient distributions for model oscillating at  $U_r = 3.1$  in each flow case.

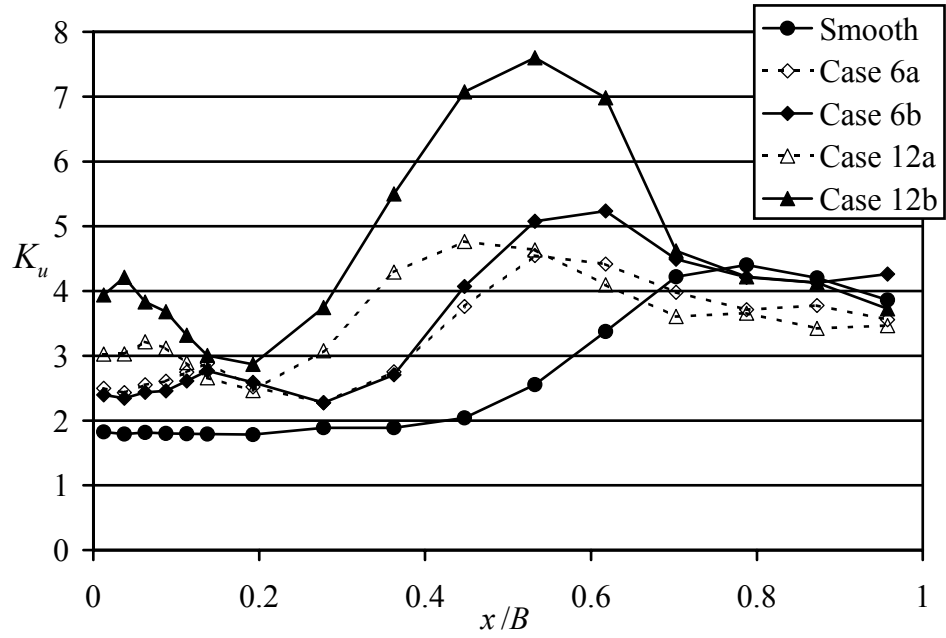


Figure 6-89 Kurtosis coefficient distributions for model oscillating at  $U_r = 8$  in each flow case.

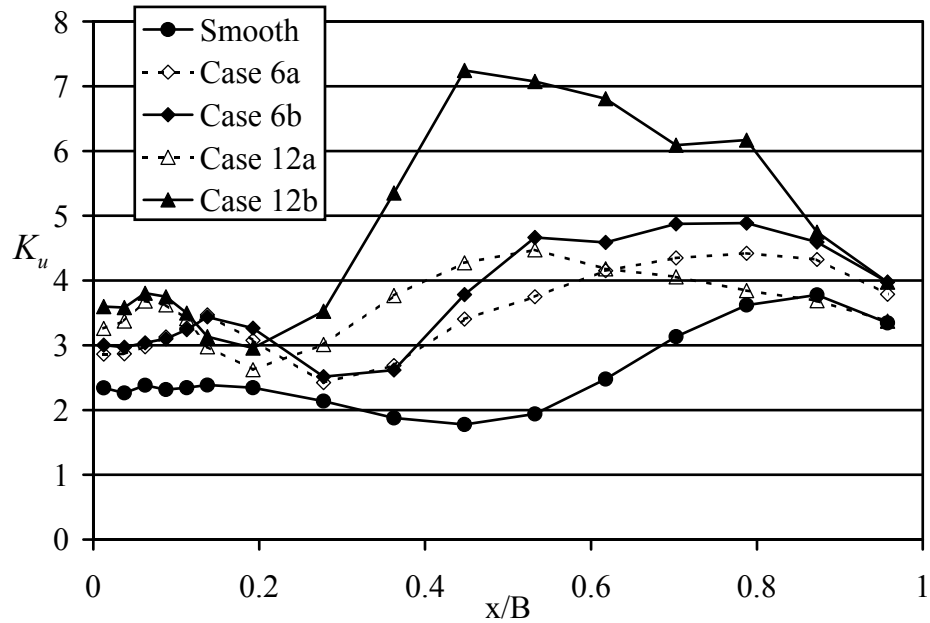


Figure 6-90 Kurtosis coefficient distributions for model oscillating at  $U_r = 20$  in each flow case.

## CHAPTER 7. SPANWISE COHERENCE AND CORRELATION RESULTS

### 7.1 Summary of Measurements of Spanwise Behavior

This chapter presents the measurements of the spanwise correlation of the self-excited forces. Spanwise correlation was examined in two ways on both stationary and oscillating models. First, cross correlation between the integrated quantities of lift and moment was calculated. Second, the cross correlation between individual pressure signals was examined to understand the streamwise position dependence of the spanwise correlation. This chapter presents the correlation calculations for the stationary model tests in the following two sections and the calculations for the oscillating model tests in the two subsequent sections. The dynamic pressure calibration section of Appendix A discusses some potential sources of extraneous pressure coherence, and further details of the coherence calculation procedures can be found in Appendix C.

### 7.2 Spanwise Correlation and Coherence of Forces—Stationary Model

This section presents the data for coherence and correlation of the lift and moment on a stationary model. Pressure signals were integrated at two different spanwise locations to produce time-varying lift and moment functions. Cross correlation and coherence functions were calculated between these lift and moment functions, as shown schematically in Figure 7-1.

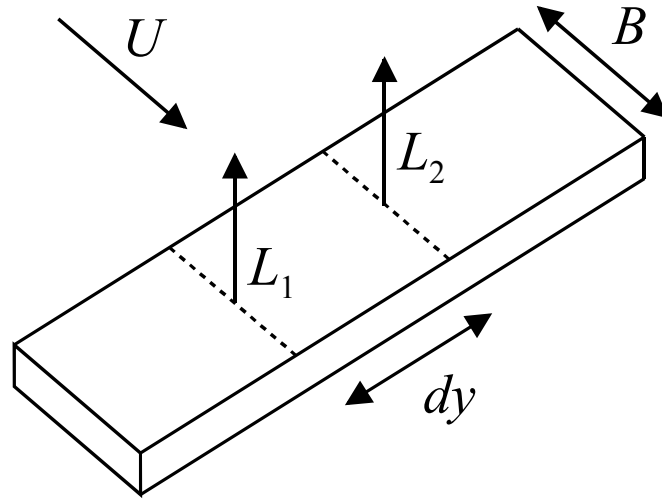


Figure 7-1 Cross correlation and coherence were calculated between lift functions at two different spanwise locations as shown in the diagram above.

Figure 7-2 shows the cross correlation values for lift in each of the flow conditions. The most notable trend is that the correlation curves show more of a dependence on turbulence scale than on turbulence intensity. Both the “a” pair and the “b” pair of flow cases have similar values throughout the range of spanwise separation considered despite the fact that one of each pair corresponds to a flow having double the other’s turbulence intensity. The increase in spanwise correlation values for greater incident turbulence scale is a trend reported by researchers investigating both bluff bodies and bridge deck sections (e.g. Larose et al., 1993; Sankaran & Jancauskas, 1993; Kimura et al., 1996; Saathoff & Melbourne, 1997; Larose & Mann, 1998). Figure 7-3 shows the corresponding spanwise moment correlation curves. Each of these curves, while following the same trends as those for lift, has slightly lower values than their complementary lift correlation curves.

What is also worthy of note is that the spanwise correlation scales of the lift are greater than those of the incident turbulent flow by a factor 3 to 4. Exponential functions were fit to the spanwise correlation data and then integrated to obtain a scale estimates. Table 7-1 lists these spanwise correlation scales for both the incident turbulence and the lift and moment. This ratio drops only slightly, to 2 or 3, when considering the correlation scales of the moment in the various incident flows.

Correlation functions can illustrate the general relationships of pressures to each other, but prediction of dynamic response due to turbulent buffeting requires frequency information (as described, for example, in Davenport, 1962). Coherence functions provide such frequency information. The plots that follow present coherence functions computed for lift and moment on stationary models according to the following expression:

$$\gamma^2(f) = \frac{|G_{L_1L_2}(f)|^2}{G_{L_1L_1}(f)G_{L_2L_2}(f)} \quad (7-1)$$

where  $G_{L_1L_2}(f)$  is the cross spectral density function between the lift forces at two spanwise locations, 1 and 2, and  $G_{L_1L_1}(f)$  and  $G_{L_2L_2}(f)$  are the power spectral density functions of the lift forces at positions 1 and 2, respectively. An analogous expression was used for calculating the coherence related to the moment. Further details of these calculations can be found in Appendix C.

Figure 7-4 shows the coherence of the lift forces for the Case 6 flows plotted versus a reduced frequency defined as:  $f\Delta y/U$  (where  $f$  is frequency in Hz,  $\Delta y$  is the spanwise separation, and  $U$  is the mean freestream velocity). Each plot corresponds to a different separation distance between pressure measurement locations. As the separation

distance increases, the coherence values fall for all reduced frequencies. For a given separation, the coherence values decrease exponentially with reduced frequency. The larger integral scale of the Case 6b flow results in coherence values larger than those of Case 6a over all reduced frequencies with a more gradual reduction with increasing spanwise separation. Coherence values for moments on a stationary cylinder in the Case 6 flows are shown in Figure 7-5. These plots show very similar trends to those observed for lift, but as with the correlation values discussed previously, the moment coherence is lower than that for lift.

Figure 7-6 and Figure 7-7 show the stationary model coherence functions for lift and moment, respectively, in the Case 12 flows. Increasing the turbulence intensity to 12% did not seem to affect the coherence values significantly. The values are very similar over the entire reduced velocity range suggesting that turbulence scale is a more important parameter for coherence than turbulence intensity. One notable difference does exist between Case 6b and Case 12b values. Case 12b values maintained a higher coherence for greater spanwise separation despite the fact that both incident flows had very similar integral scales. Turbulence intensity effects, therefore, should not be assumed insignificant.

Coherence values near zero frequency were less than unity. Even though the values near zero are quite high and decrease with increasing frequency, very low frequency values do not approach unity coherence. Similar coherence behavior was also reported in, for example, Larose & Mann (1998). A discussion of such behavior can be found in Kareem (1987).

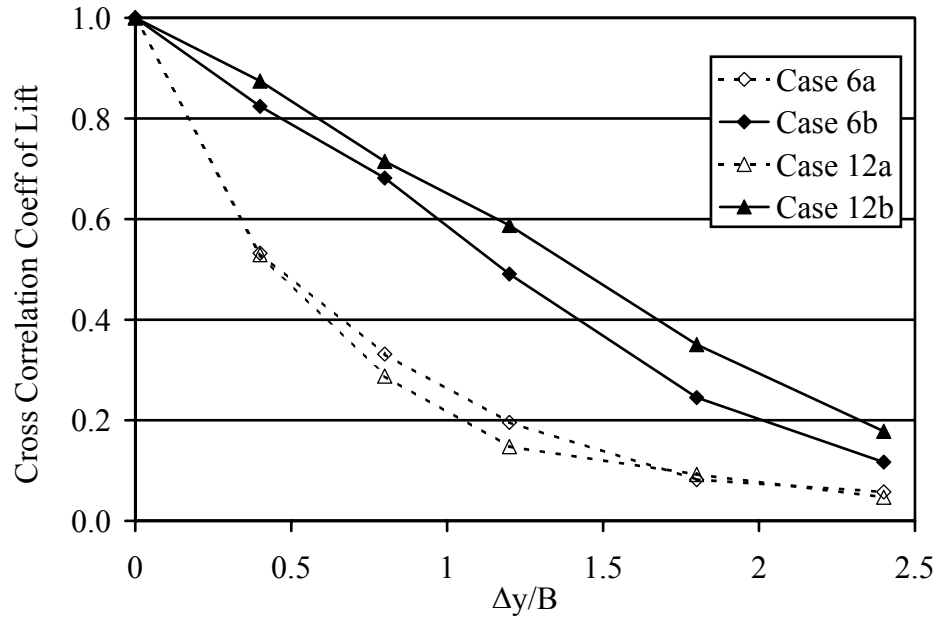


Figure 7-2 Maximum cross correlation coefficient values for lift on a stationary model.

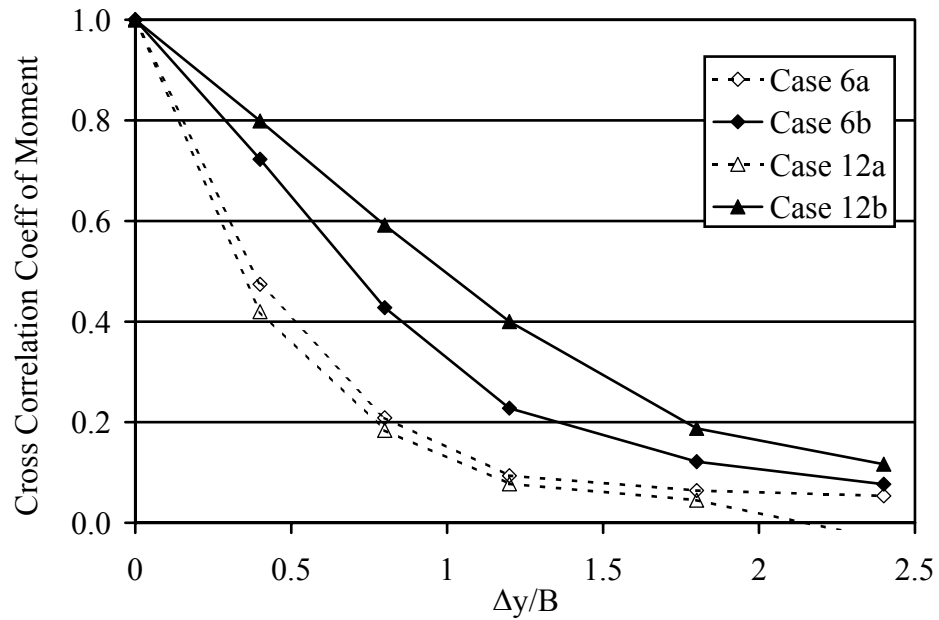


Figure 7-3 Maximum cross correlation coefficient values for moment on a stationary model.

Table 7-1 SPANWISE CORRELATION LENGTHS FOR WIND VELOCITY FLUCTUATIONS AND LIFT AND MOMENT ON THE STATIONARY MODEL

	$L_{ux}$	$L_{uy}$	$L_{wx}$	$L_{wy}$	$L_{Ly_s}$	$L_{My_s}$
Smooth	N/A	N/A	N/A	N/A	$3.59D$	$1.62D$
$I_u = 6\%$						
Case 6a	$1.81D$	$1.69D$	$0.86D$	$1.34D$	$4.70D$	$3.54D$
Case 6b	$4.9D$	$2.68D$	$2.56D$	$2.21D$	$10.15D$	$6.19D$
$I_u = 12\%$						
Case 12a	$1.34D$	$1.14D$	$0.61D$	$0.83D$	$4.32D$	$3.12D$
Case 12b	$4.89D$	$3.33D$	$2.66D$	$2.52D$	$12.54D$	$8.65D$

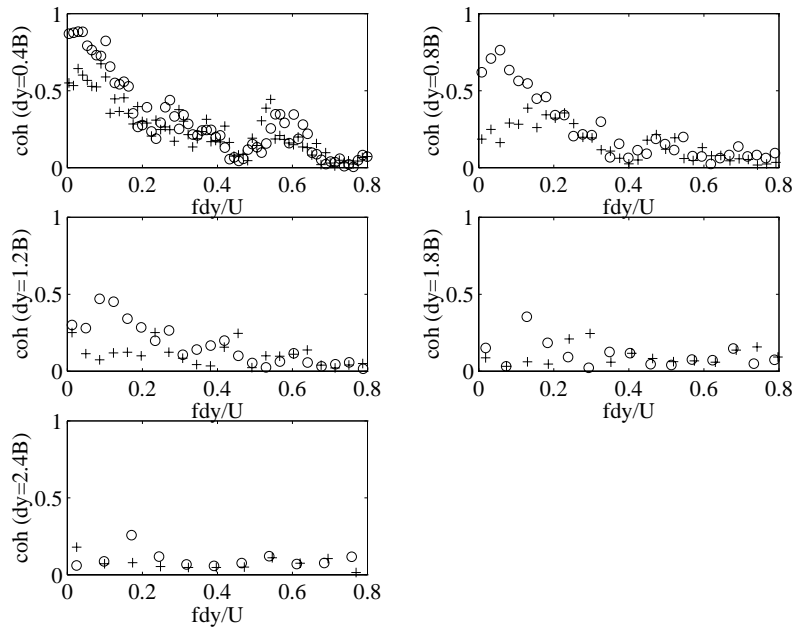


Figure 7-4 Coherence functions for lift on a stationary model in the Case 6 turbulent flows at several different spanwise separations ('+' Case 6a; 'o' Case 6b).

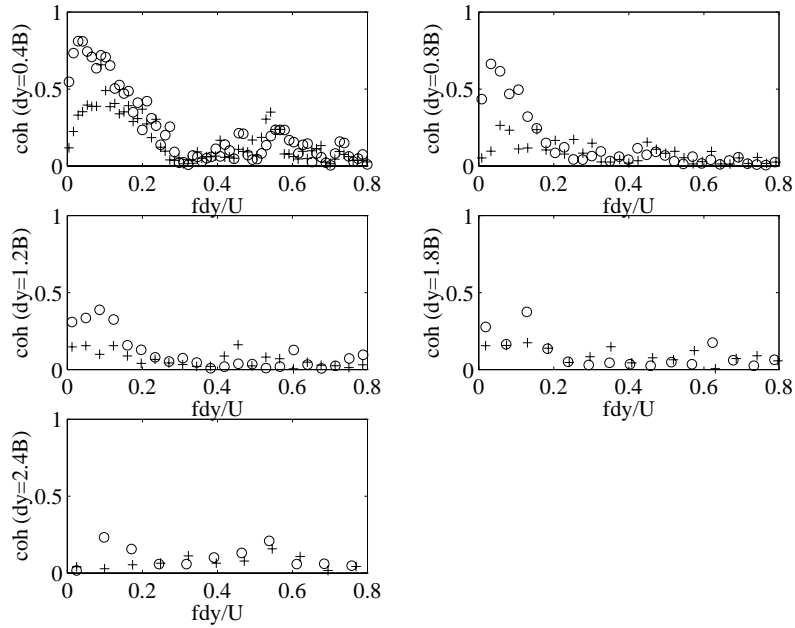


Figure 7-5 Coherence functions for moment on a stationary model in the Case 6 turbulent flows at several different spanwise separations ('+' Case 6a; 'o' Case 6b).

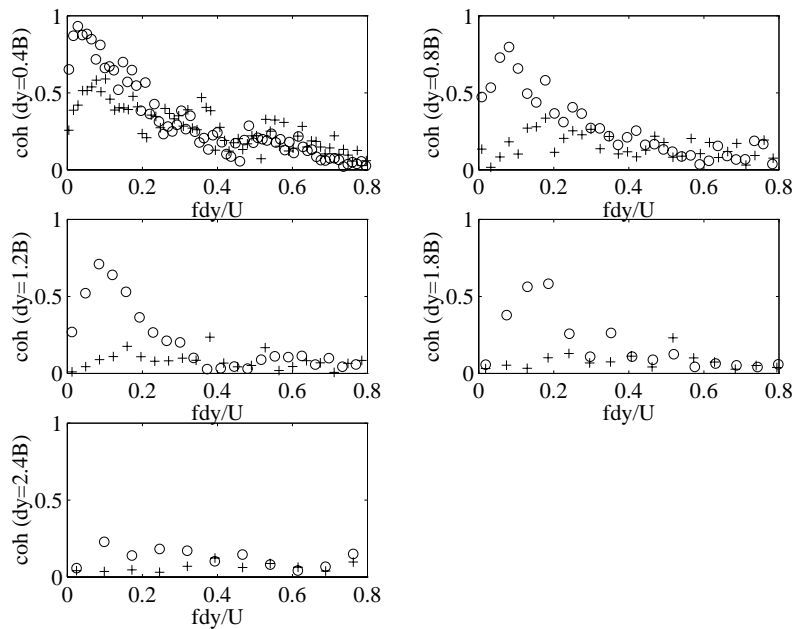


Figure 7-6 Coherence functions for lift on a stationary model in the Case 12 turbulent flows at several different spanwise separations ('+' Case 12a; 'o' Case 12b).

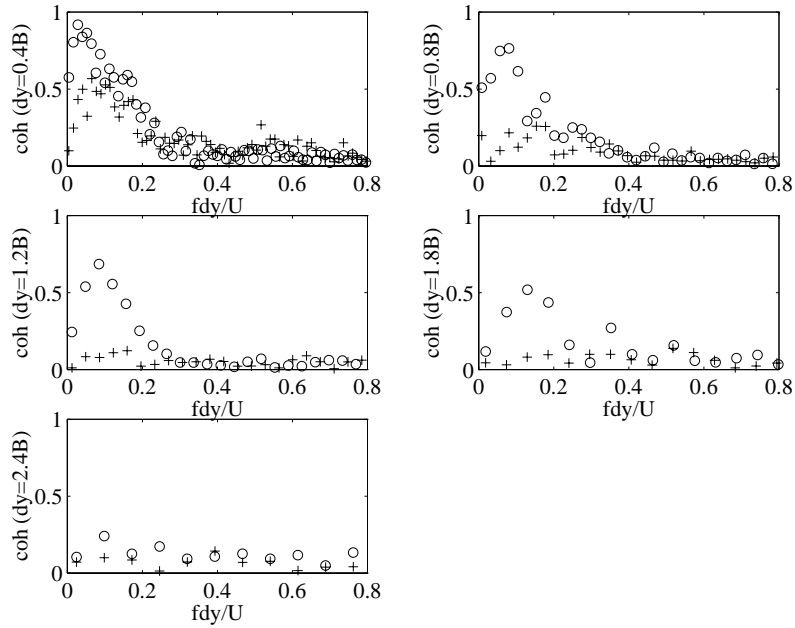


Figure 7-7 Coherence functions for moment on a stationary model in the Case 12 turbulent flows at several different spanwise separations ('+' Case 12a; 'o' Case 12b).

### 7.3 Streamwise Position Dependence of Spanwise Pressure Correlation—Stationary Model

To investigate the structure of the correlation values, cross correlation functions were computed between pressure signals at discrete streamwise locations. While section 7.2 presented the cross correlations between the integrated quantities of lift and moment, this section calculates the cross correlations between individual pressure signals as shown schematically in Figure 7-8. These correlations are presented in four figures (Figure 7-9 through Figure 7-12) each containing four plots, so each of the 16 streamwise positions (specific values of  $x/B$ ) has its own plot.

The pressure correlations in each flow case show an exponential decay with increasing spanwise separation. Positions from the leading edge to  $x/B \approx 0.6$  show the cases with larger turbulence scale having larger spanwise correlation. Beyond this point, however, this trend reverses, and the flows with larger integral scales have somewhat lower correlation values. Not all the pressure correlations, therefore, follow the same scale dependence as the lift and moment. Lift and moment behave as they do because the windward half of the model, where  $x/B \leq 0.6$ , experiences larger pressure magnitudes and is thus the greatest contributor to the integrated forces.

To quantify these trends better, exponential curves were fit to each of the pressure correlation curves. From these fits, spanwise correlation length scales were computed and are shown in Figure 7-13. In more concise form, this plot summarizes the results of the pressure correlation plots. For a given turbulence intensity, greater turbulence scale results in greater spanwise pressure correlation for streamwise positions less than  $0.6B$  and in slightly lower correlation for positions further downstream. Because of the small number of spanwise measurement locations, however, these spanwise scales are only rough estimates.

Two trends in Figure 7-13 are worthy of note. On the upstream half of the surface, spanwise correlation scale behavior of the “b” cases roughly consisted of a streamwise increase to a maximum and then a decrease. This is similar to the velocity correlation observations of Kiya & Sasaki (1983a) on a blunt, flat plate. They found that the spanwise correlation of the structures of the separated shear layer increased up to a maximum at reattachment. They did not measure too far downstream of reattachment, however. Figure 7-13 shows that the overall behavior of the spanwise scales in this

project were similar. In addition to this behavior on the upstream half of the model, the spanwise correlation scales increased near the trailing edge. This does not occur for blunt, flat plates where the body extends “infinitely” downstream. The shedding of vortices from the trailing edge may be exerting an organizing influence on the flow near the trailing edge thus increasing the spanwise correlation in that region.

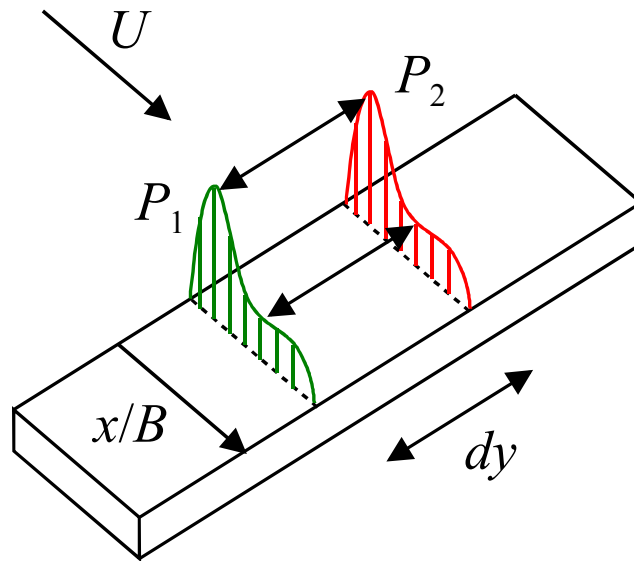


Figure 7-8 Cross correlations were calculated between individual pressure signals at each streamwise location for various spanwise separations as shown in the diagram above.

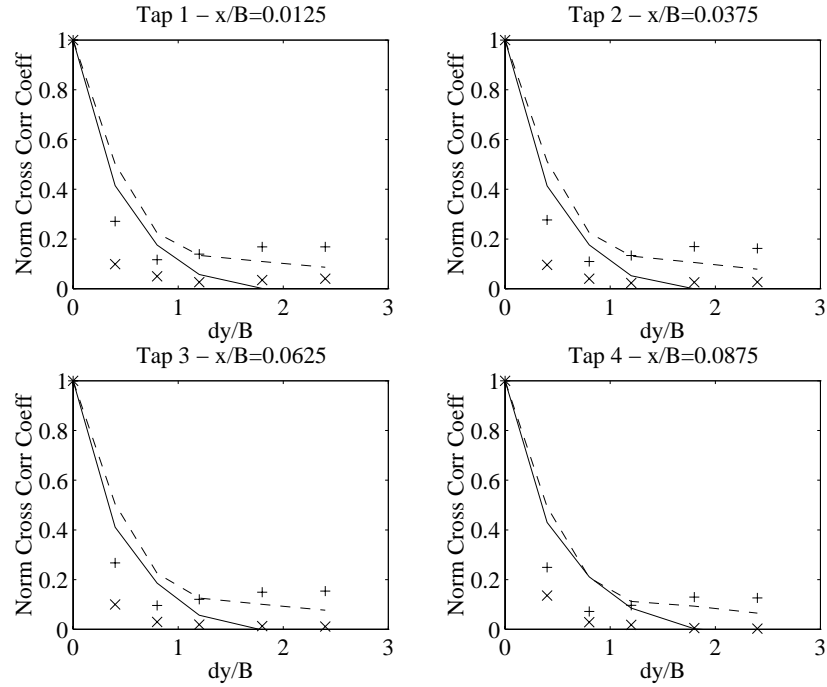


Figure 7-9 Pressure correlation functions for pressure taps 1-4 on a stationary model ('+' Case 6a; '- -' Case 6b; 'x' Case 12a; '—' Case 12b')

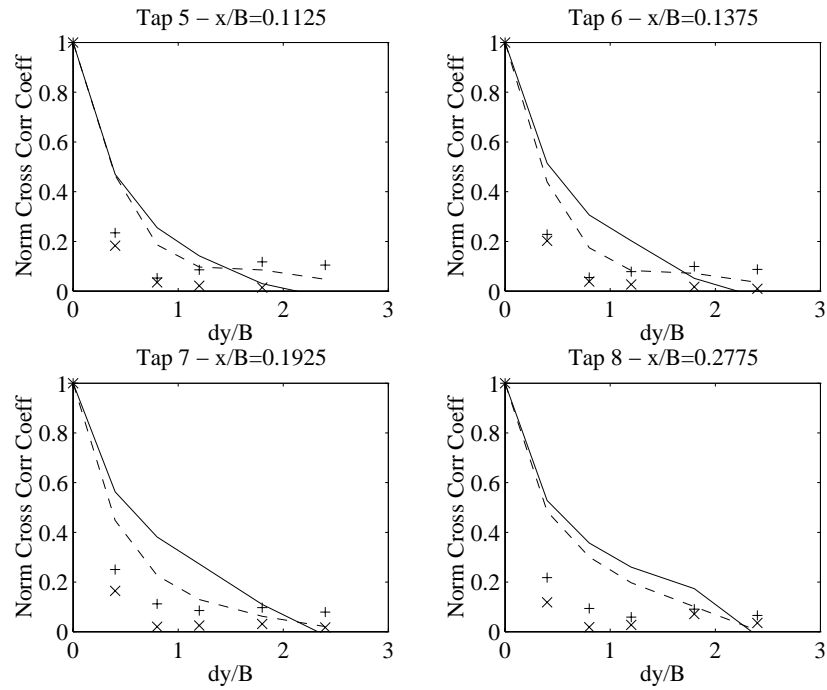


Figure 7-10 Pressure correlation functions for pressure taps 5-8 on a stationary model ('+' Case 6a; '- -' Case 6b; 'x' Case 12a; '—' Case 12b')

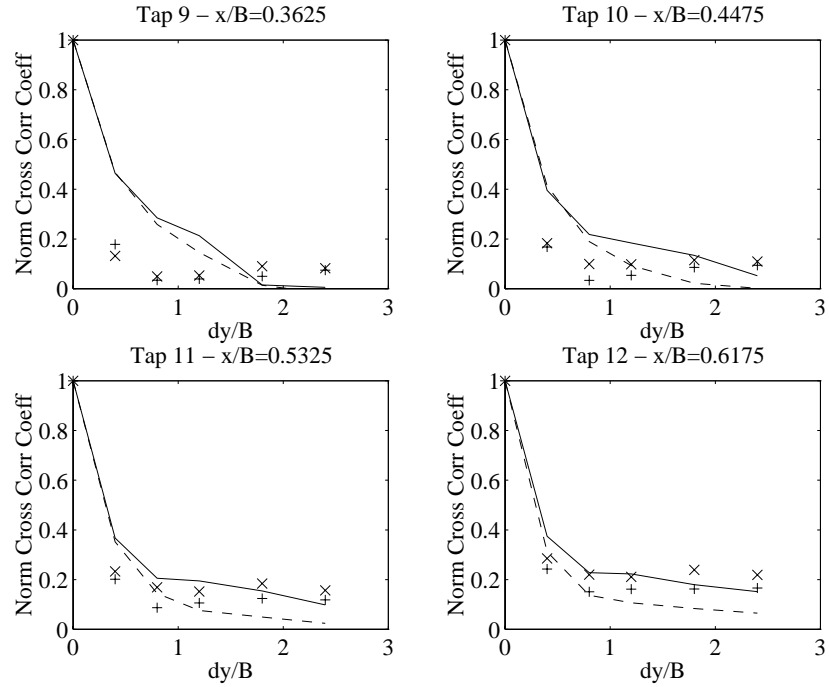


Figure 7-11 Pressure correlation functions for pressure taps 9-12 on a stationary model ('+' Case 6a; '-' Case 6b; 'x' Case 12a; '—' Case 12b')

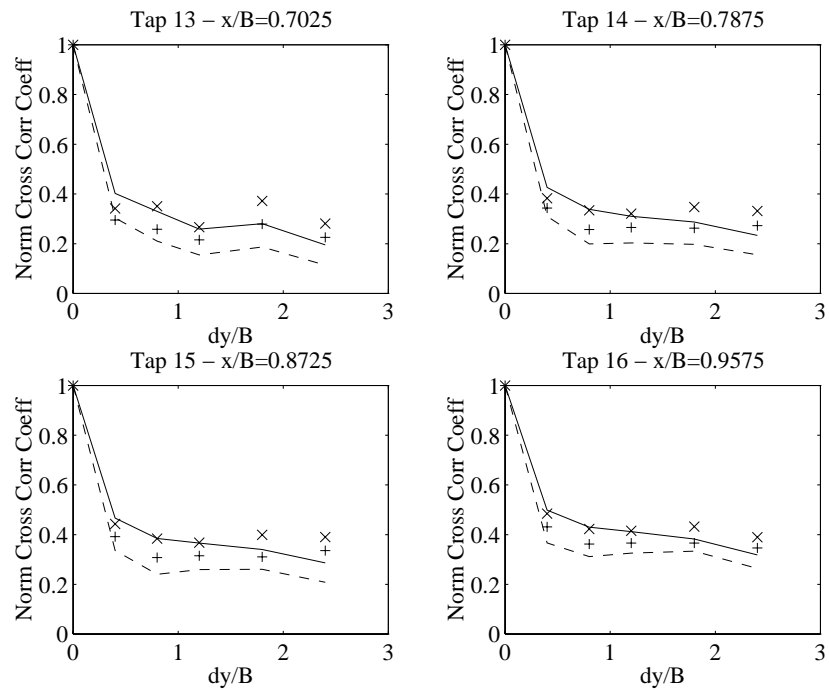


Figure 7-12 Pressure correlation functions for pressure taps 13-16 on a stationary model ('+' Case 6a; '-' Case 6b; 'x' Case 12a; '—' Case 12b')

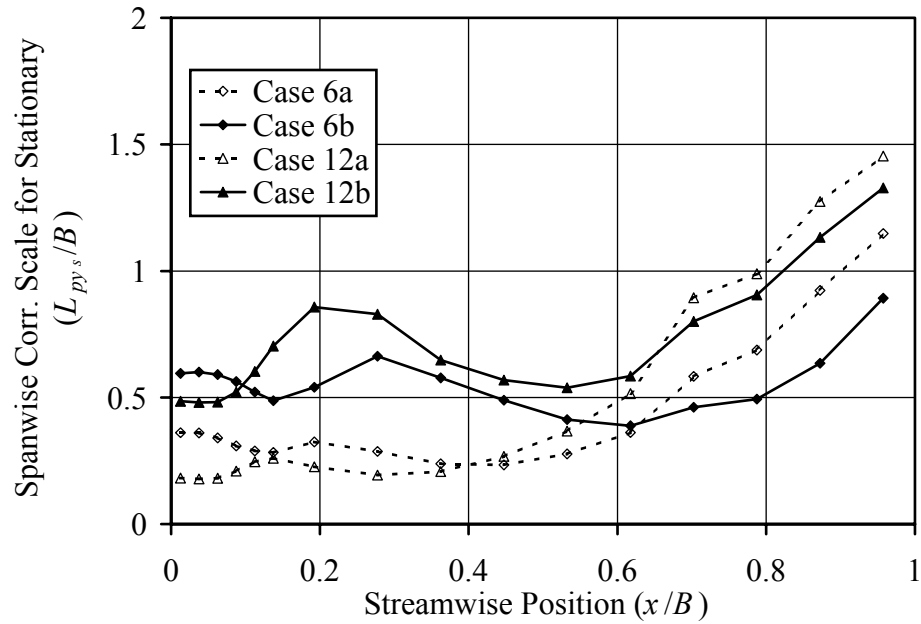


Figure 7-13 Spanwise correlation scales as a function of streamwise position for the stationary model in each of the four turbulent flows.

#### 7.4 Spanwise Correlation and Coherence of Forces—Oscillating Model

Like section 7.2, this section presents the spanwise correlation and coherence values computed from integrated lift and moment. This section, however, presents data measured while the model is oscillating at various reduced velocities. Because of the volume of data involved, only the data from three reduced velocities (3.1, 8, and 20) are presented here. These data sets sufficiently reveal the overall trends.

Figure 7-14 contains the cross correlation coefficients (at zero time lag) for the lift forces for  $U_r = 3.1$ . Two major differences between these values and those for a stationary model present themselves. The first is the much higher values for the oscillating model. Stationary model spanwise correlation scales were between  $0.3B$  and

$1.9B$  depending on the turbulence properties while oscillating model correlation scales were between  $5B$  and  $20B$  for turbulent flow and far greater for smooth flow. More details on these correlation scales will be discussed later in this section.

The second difference is the reversal of the trend with incident turbulence scale. While larger turbulence scales increase the spanwise correlation for the stationary cylinder, Figure 7-14 shows that the opposite is true for the oscillating cylinder at this reduced velocity. Both larger-scale “b” flow cases produced significantly lower spanwise lift correlation than the corresponding smaller-scale “a” cases. The effect of turbulence intensity was much more subtle—when comparing the correlations between flows having similar turbulence length scales, the flow with greater turbulence intensity had a slightly lower correlation value. The smooth flow correlation values also warrant mention due to the fact that they are higher than those of the turbulent flow cases—a behavior that is opposite the stationary model behavior. For the stationary model, the smooth flow correlation values were consistently lower than the turbulent flow values.

A dip in the correlation values near  $\Delta y/B = 0.8$  is also evident in Figure 7-14. This is likely due to experimental difficulties rather than flow physics. As described in chapter 3, the myriad of tubing lines within the model had to be rearranged for each spanwise separation setting. At times certain tubing lines would get pinched precluding data acquisition from that pressure tap. While every effort was made to minimize these problems, some impact on the results was unavoidable.

Figure 7-15 and Figure 7-16 show spanwise lift correlation values for reduced velocities of 8 and 20, respectively. The same trends with respect to turbulence intensity and scale hold for these curves as they did for those of  $U_r = 3.1$ . Although these trends

are the same, the overall values are different. To summarize the data in these last three figures and to track how the spanwise correlation depends on reduced velocity, Figure 7-17 shows the correlation length scale as a function of reduced velocity for each flow case. These curves suggest that maximum correlation scales occur between  $U_r = 3.1$  and  $U_r = 8$  followed by a gradual reduction as reduced velocity increases.

The next three plots, Figure 7-18 through Figure 7-20 include the moment cross correlation curves corresponding to the same three reduced velocities just considered for lift. Similar trends with respect to turbulence are evident comparing these curves to their lift correlation counterparts. However, lift correlation values have a slightly higher value than moment correlations for the reduced velocities of 8 and higher. Moment correlations have slightly higher values for the case of  $U_r = 3.1$ . Figure 7-21 shows a plot of the moment correlation length scales versus reduced velocity. Comparing these scales with the lift scales of Figure 7-17 illustrates the above-mentioned differences in values between lift and moment correlations.

The discussion in Chapter 8 will address these correlation values in greater depth. Specifically, the correlation of buffeting and self-excited components of the lift and moment will be considered.

Coherence functions were also calculated to examine these spanwise correlation issues in terms of frequency dependence as well. Figure 7-22 shows the coherence values for the Case 6 turbulent flows at  $U_r = 3.1$  for both the stationary and oscillating tests. Except for the coherence at the frequency of the model motion,  $f_m$ , the results from tests with and without motion are remarkably similar. At the model oscillation frequency, however, the oscillating-model coherence is very high, near unity. While the broad band

coherence decreases rapidly with separation distance, the coherence at  $f_m$  decreases only slightly and sustains extremely high values throughout the separation range considered.

Current bridge design practice highlights the importance of the comparison between the results for the stationary and oscillating tests. Since buffeting and self-excited forces are considered separately in the analytical estimates, they are measured separately as well. Buffeting force magnitudes and spanwise coherences are measured on stationary models and then employed in the overall dynamic analyses of the bridge decks. Results of these spanwise coherence experiments on *oscillating* models—the first of their kind to the author’s knowledge—support this practice at least in terms of the buffeting force coherence. Unfortunately, quantitative analysis of the *difference* in stationary and oscillating model coherence was not possible. The differences in the coherence values plotted here were within the random error of the calculations.

Figure 7-23 and Figure 7-24 show the coherence spectra for the  $U_r = 8$  and  $U_r = 20$  cases, respectively. Again, these functions are for the Case 6 turbulent flows and show that the results of stationary and oscillating model tests are very similar for the broadband coherence. Shifts in the locations of the near-unity peaks in the oscillating model coherence functions were caused by increases in the model oscillation frequency made to decrease  $U_r$ . The behavior of these peaks with respect to turbulence and reduced velocity will be discussed in subsequent paragraphs.

Lift coherence functions for the Case 12 turbulent flows at reduced velocities of 3.1, 8, and 12 are shown in Figure 7-25 through Figure 7-27, respectively. Like the Case 6 plots, the broadband coherence of the forces on the oscillating model were very similar to those on the stationary model—except for the peak at the model oscillation frequency.

Because the broadband coherence has already been described in this section and in section 7.2, the coherence peaks will now be the focus.

Moment coherence functions for reduced velocities of 3.1, 8, and 12 in Case 6 flows are presented in the three plots from Figure 7-28 through Figure 7-30. The Case 12 coherence functions for these same reduced velocities are shown in the three figures from Figure 7-31 through Figure 7-33. These values behave quite similarly to their lift coherence counterparts but with slightly lower magnitudes.

For  $U_r = 3.1$ , coherence values at the model oscillation frequency,  $f_m$ , are plotted versus separation in Figure 7-34 (similar plots of peak coherence values for  $U_r = 8$  and  $U_r = 20$  are shown in Figure 7-35 and Figure 7-36, respectively). With respect to turbulence, these coherence values show behavior similar to that of the correlation values. Smooth incident flow resulted in the highest lift coherence values, and turbulent flow produced forces with lower coherence. Larger scale turbulence caused larger decreases in the coherence values. These general statements are true of the spanwise correlation values discussed previously. The main difference for the coherence values is how much smaller the relative changes are in the different turbulent flows. For example, the lift correlation coefficient for  $\Delta y = 2.4B$  and  $U_r = 20$  (see Figure 7-16) dropped approximately 38% from smooth flow to Case 12b. The corresponding change in the coherence function at  $f_m$  was merely 5% (see Figure 7-36). Because the precision uncertainty in this range of coherence is about 3%, conclusive statements cannot be made concerning turbulence effects on these peak values. It would take a significantly longer model span to identify the separation lengths for which these coherence values would drop to insignificant levels.

Plots of the moment coherence values at the oscillation frequency are shown in three figures, Figure 7-37 for  $U_r = 3.1$ , Figure 7-38 for  $U_r = 8$ , and Figure 7-39 for  $U_r = 20$ . Comparing these moment results with their lift coherence counterparts reveals very similar values—again, with the subtle decreases with separation distance mentioned previously.

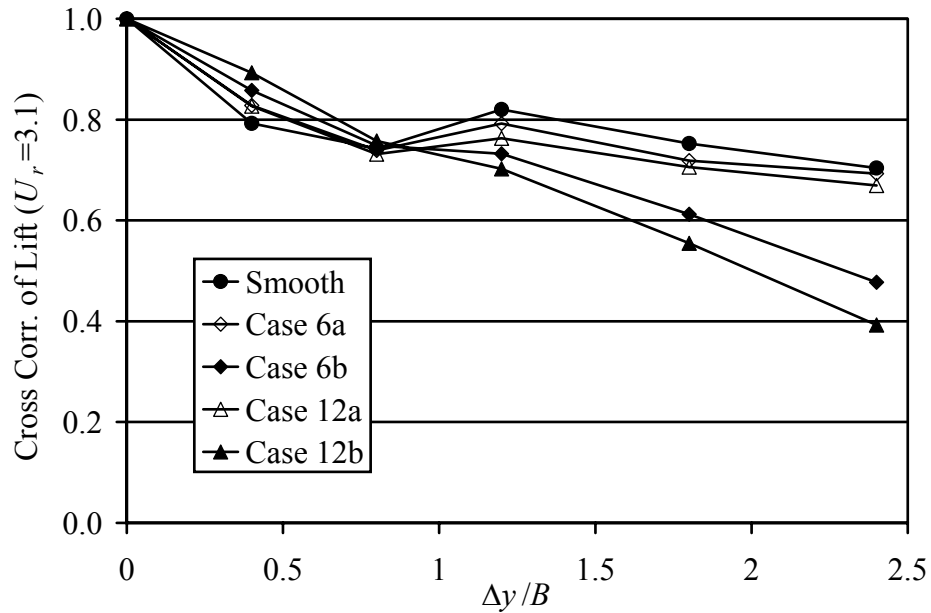


Figure 7-14 Cross correlation coefficient for lift for  $U_r=3.1$  in smooth and turbulent flows.

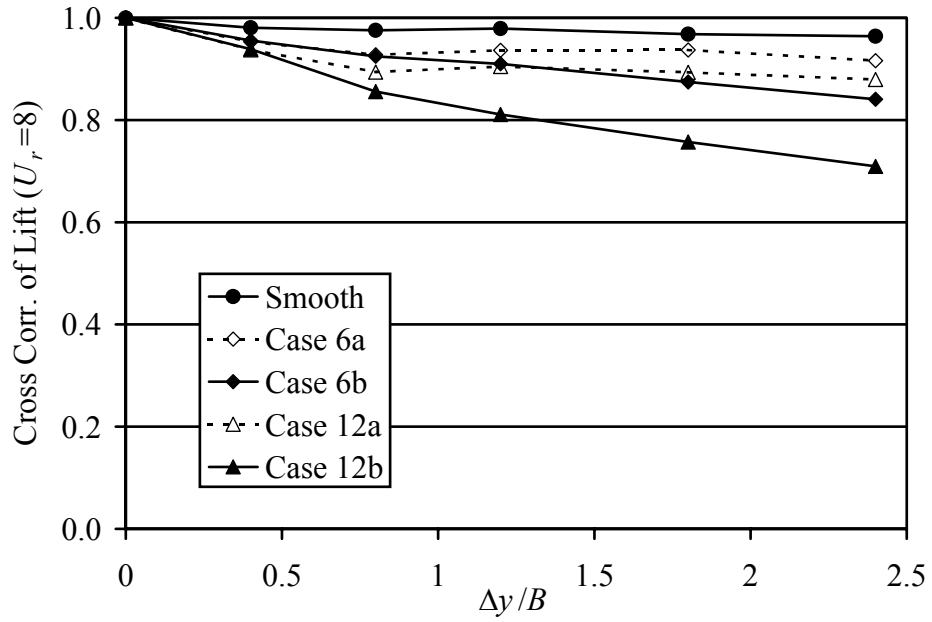


Figure 7-15 Cross correlation coefficient for lift for  $U_r=8$  in smooth and turbulent flows.

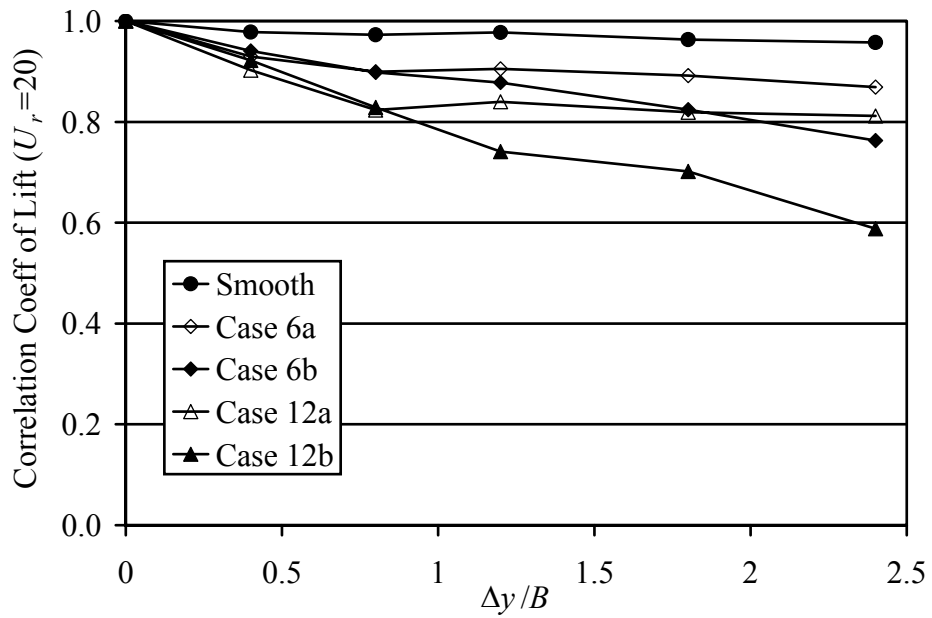


Figure 7-16 Cross correlation coefficient for lift for  $U_r=20$  in smooth and turbulent flows.

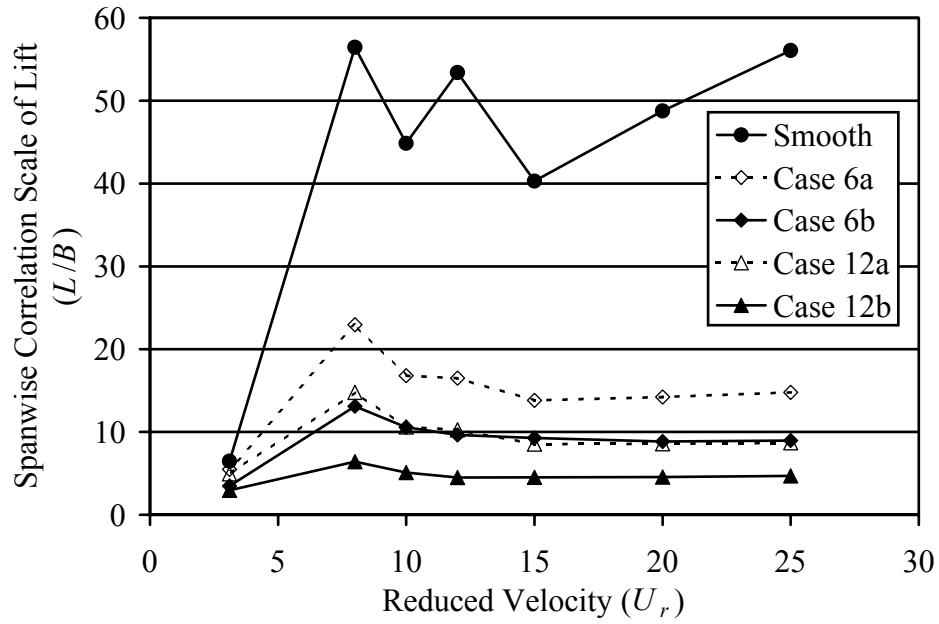


Figure 7-17 Spanwise lift correlation scale as a function of reduced velocity.

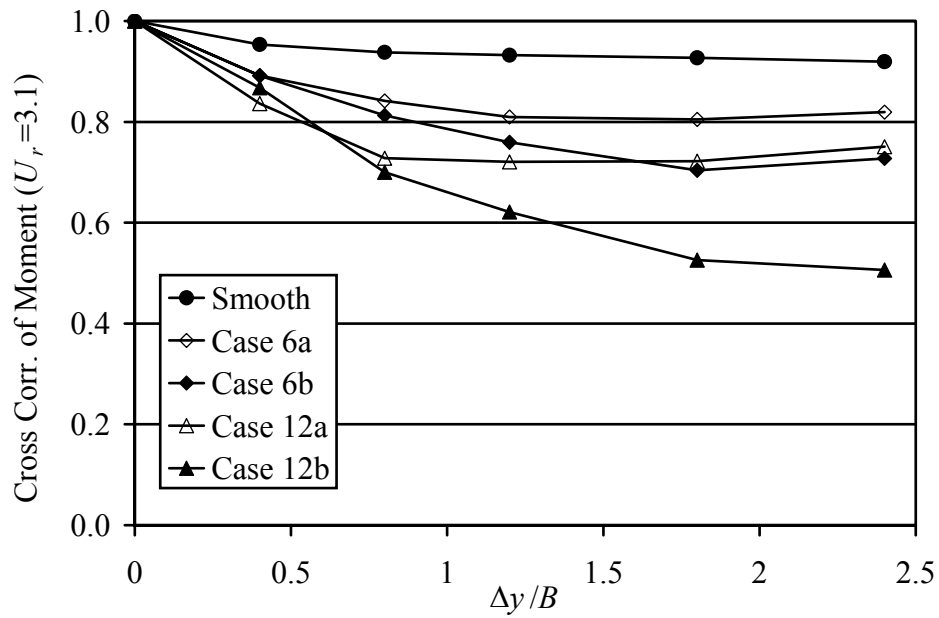


Figure 7-18 Cross correlation coefficient for moment for  $U_r=3.1$  in smooth and turbulent flows.

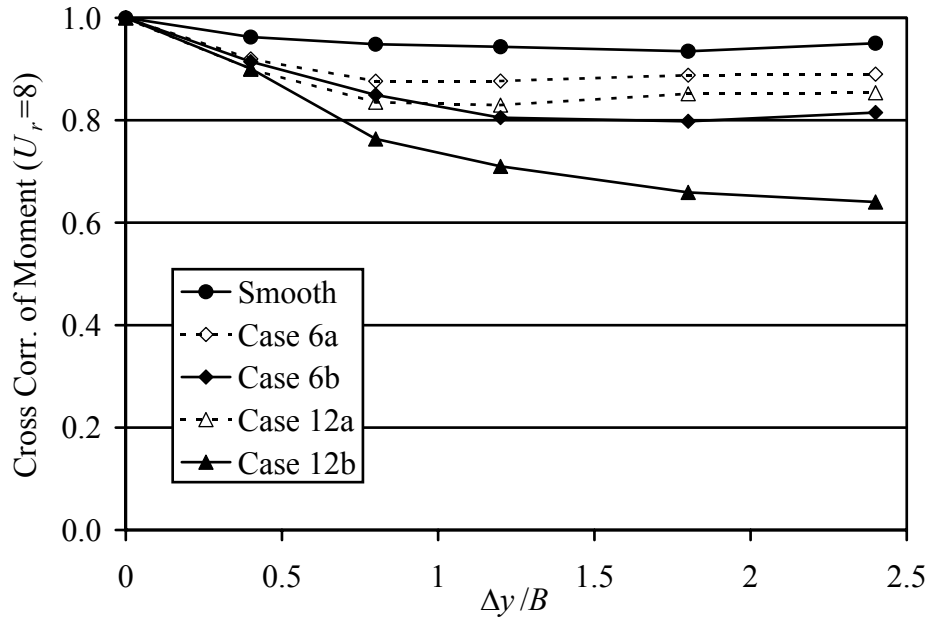


Figure 7-19 Cross correlation coefficient for moment for  $U_r=8$  in smooth and turbulent flows.

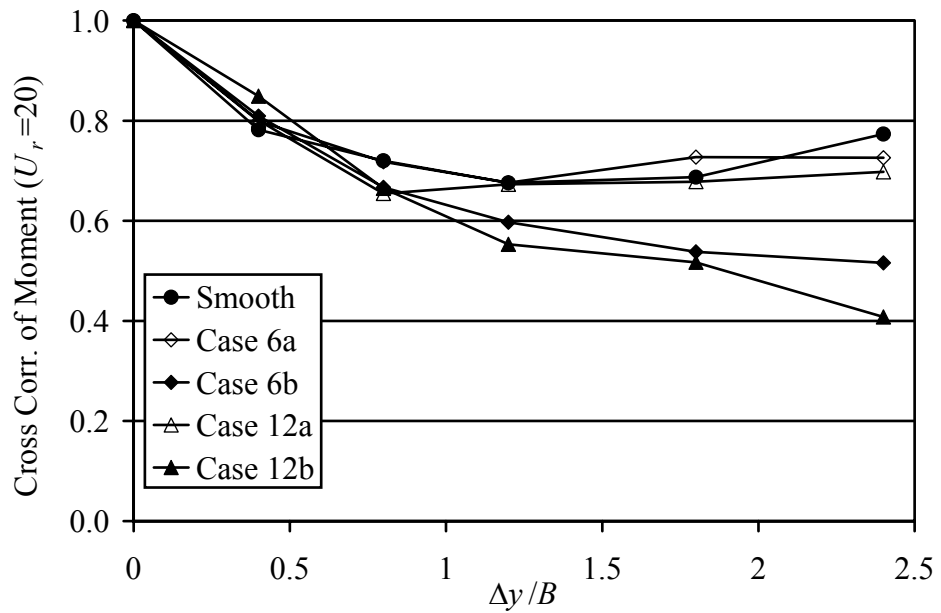


Figure 7-20 Cross correlation coefficient for moment for  $U_r=20$  in smooth and turbulent flows.

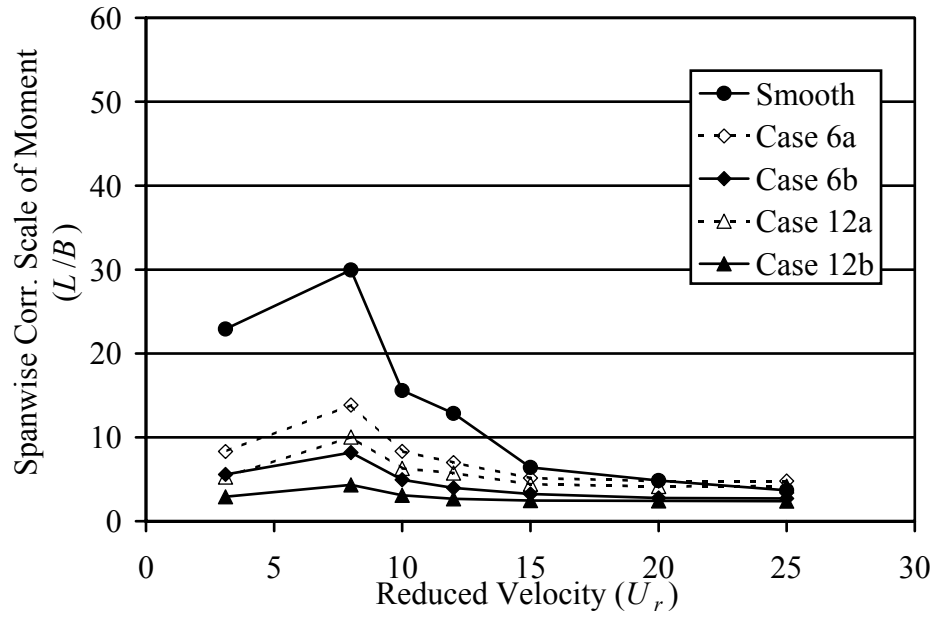


Figure 7-21 Spanwise moment correlation scale as a function of reduced velocity.

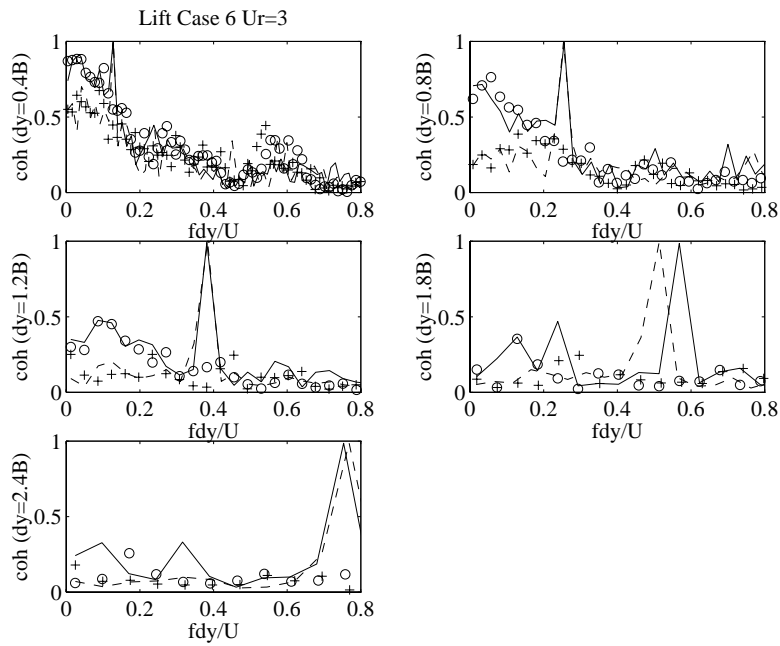


Figure 7-22 Coherence of lift at  $U_r=3.1$  in Case 6 flows for various spanwise separations ('+' Case 6a stationary; '- -' Case 6a oscillating; 'o' Case 6b stationary; '—' Case 6b oscillating).

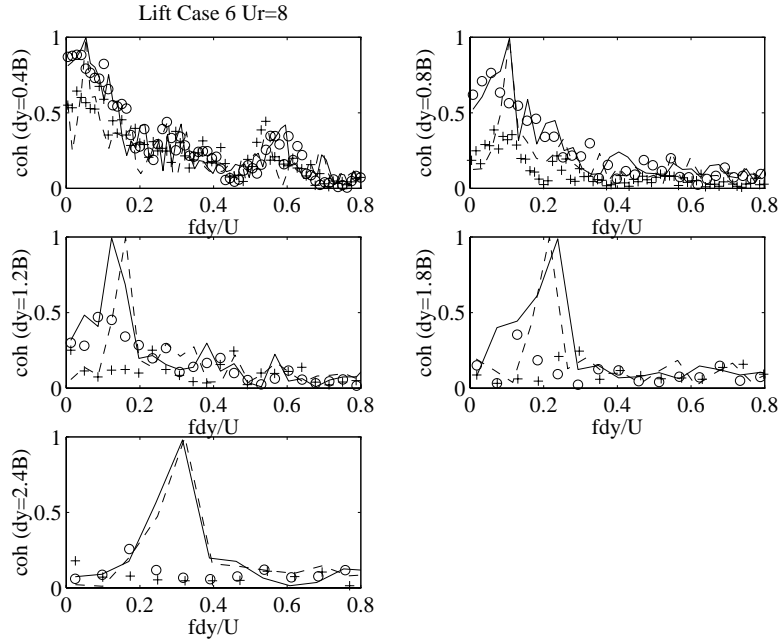


Figure 7-23 Coherence of lift at  $U_r=8$  in Case 6 flows for various spanwise separations ('+' Case 6a stationary; '- -' Case 6a oscillating; 'o' Case 6b stationary; '—' Case 6b oscillating).

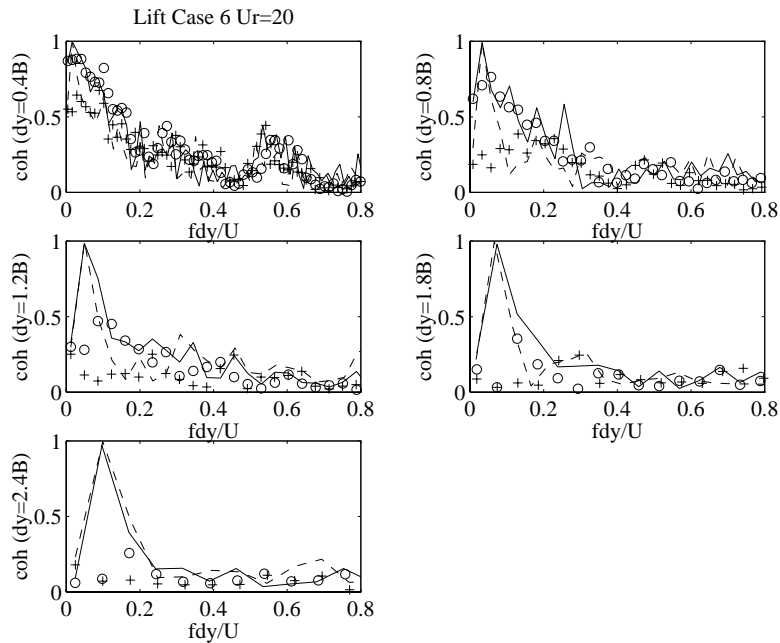


Figure 7-24 Coherence of lift at  $U_r=20$  in Case 6 flows for various spanwise separations ('+' Case 6a stationary; '- -' Case 6a oscillating; 'o' Case 6b stationary; '—' Case 6b oscillating).

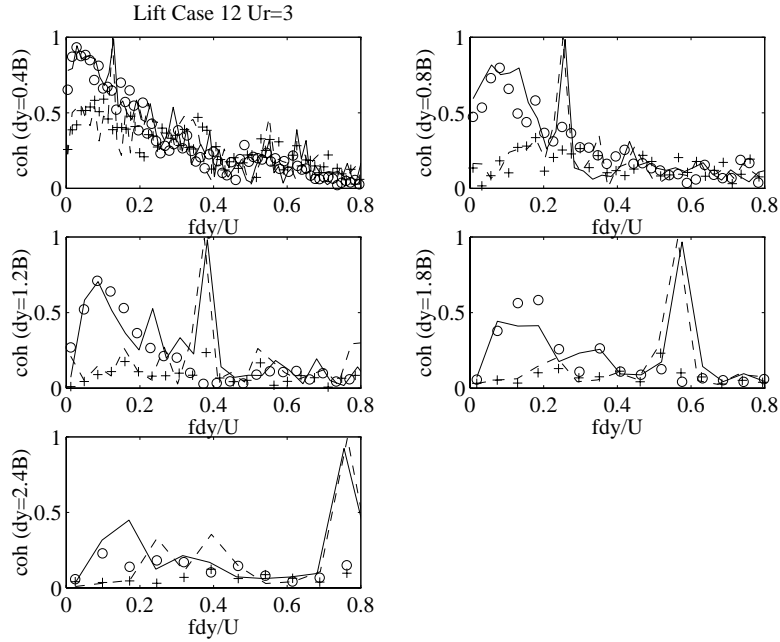


Figure 7-25 Coherence of lift at  $U_r=3.1$  in Case 12 flows for various spanwise separations ('+' Case 12a stationary; '- -' Case 12a oscillating; 'o' Case 12b stationary; '—' Case 12b oscillating).

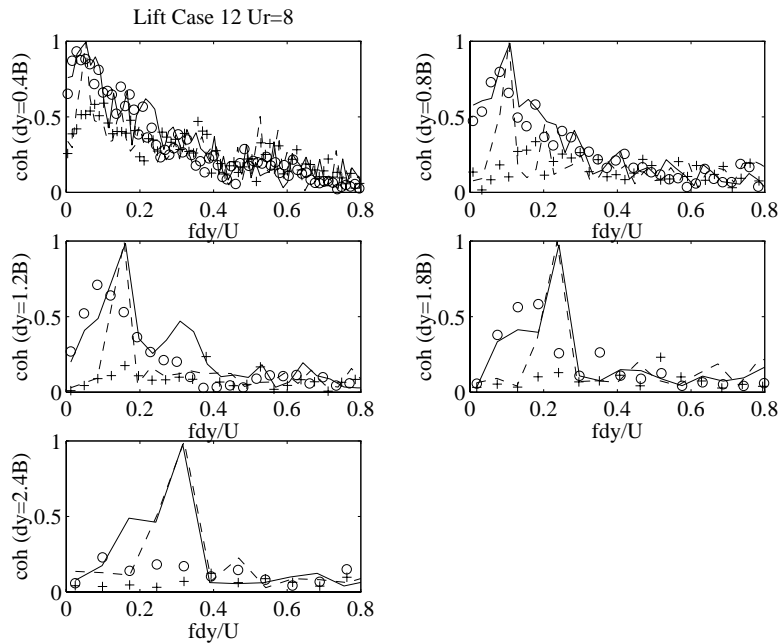


Figure 7-26 Coherence of lift at  $U_r=8$  in Case 12 flows for various spanwise separations ('+' Case 12a stationary; '- -' Case 12a oscillating; 'o' Case 12b stationary; '—' Case 12b oscillating).

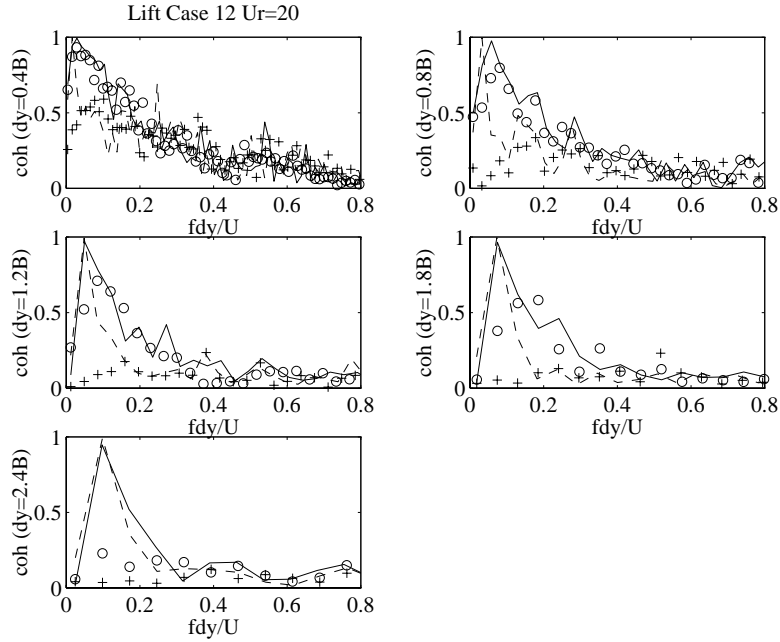


Figure 7-27 Coherence of lift at  $U_r=20$  in Case 12 flows for various spanwise separations ('+' Case 12a stationary; '-' Case 12a oscillating; 'o' Case 12b stationary; '—' Case 12b oscillating).

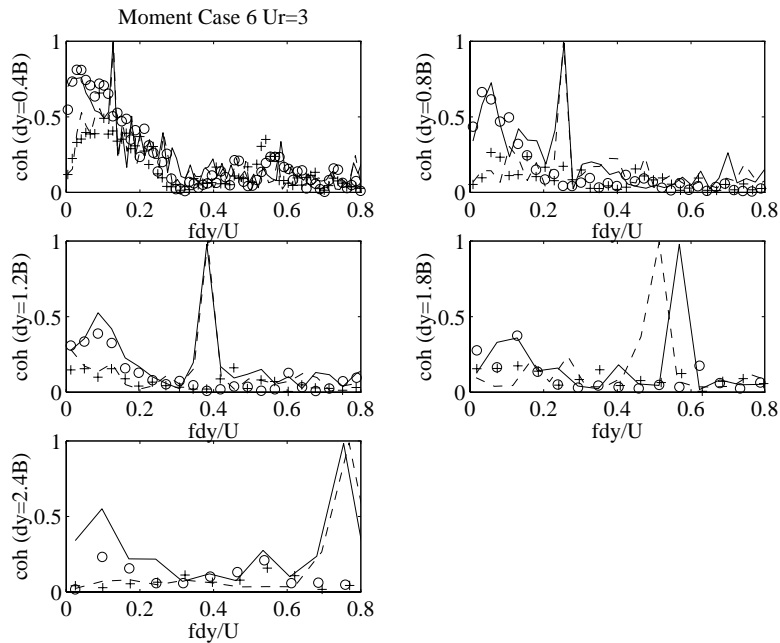


Figure 7-28 Coherence of moment at  $U_r=3.1$  in Case 6 flows for various spanwise separations ('+' Case 6a stationary; '-' Case 6a oscillating; 'o' Case 6b stationary; '—' Case 6b oscillating).

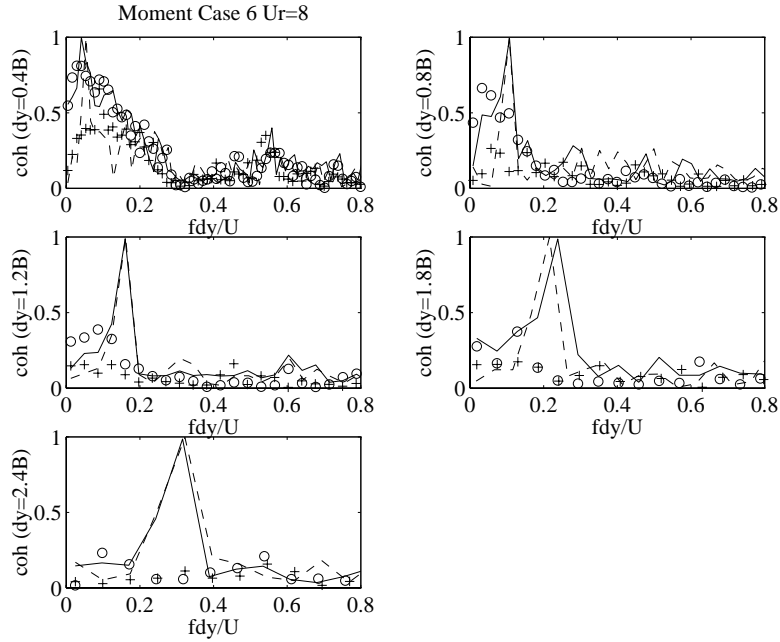


Figure 7-29 Coherence of moment at  $U_r=8$  in Case 6 flows for various spanwise separations ('+' Case 6a stationary; '-' Case 6a oscillating; 'o' Case 6b stationary; '—' Case 6b oscillating).

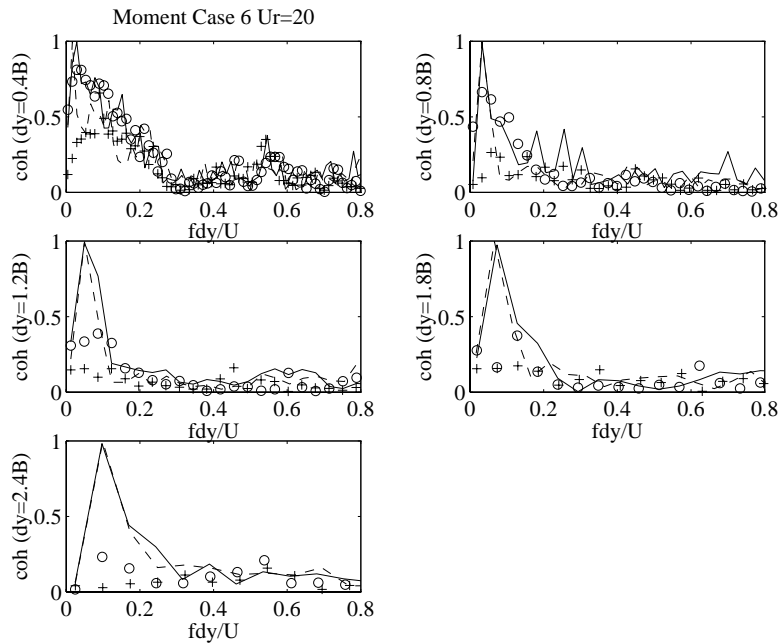


Figure 7-30 Coherence of moment at  $U_r=20$  in Case 6 flows for various spanwise separations ('+' Case 6a stationary; '-' Case 6a oscillating; 'o' Case 6b stationary; '—' Case 6b oscillating).

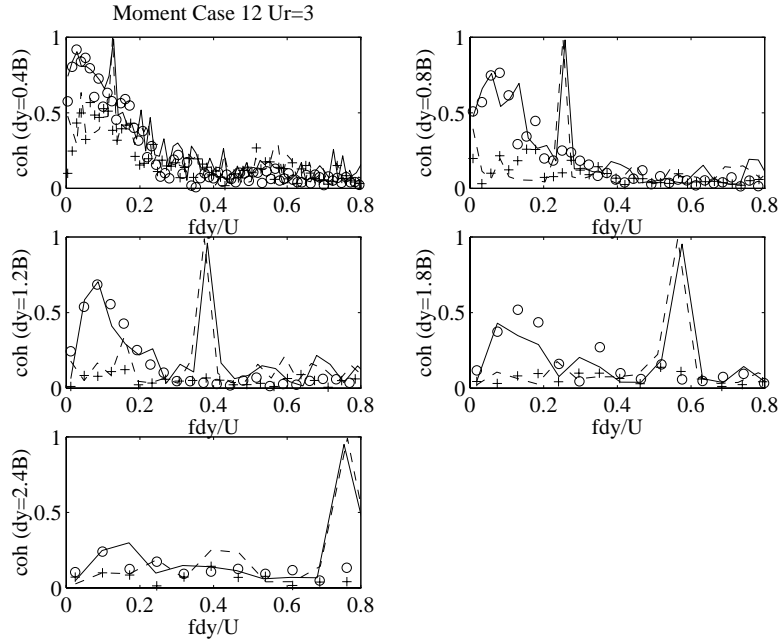


Figure 7-31 Coherence of moment at  $U_r=3.1$  in Case 12 flows for various spanwise separations ('+' Case 12a stationary; '-' Case 12a oscillating; 'o' Case 12b stationary; '—' Case 12b oscillating).

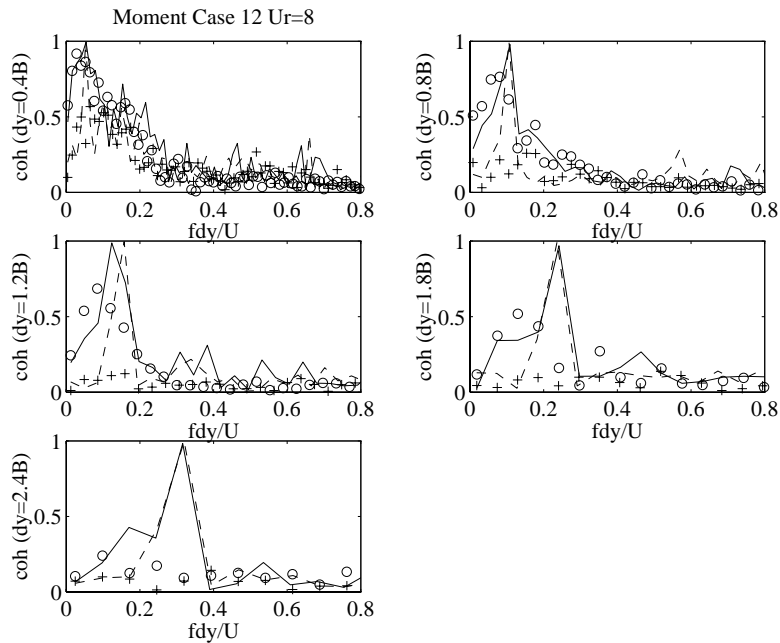


Figure 7-32 Coherence of moment at  $U_r=8$  in Case 12 flows for various spanwise separations ('+' Case 12a stationary; '-' Case 12a oscillating; 'o' Case 12b stationary; '—' Case 12b oscillating).

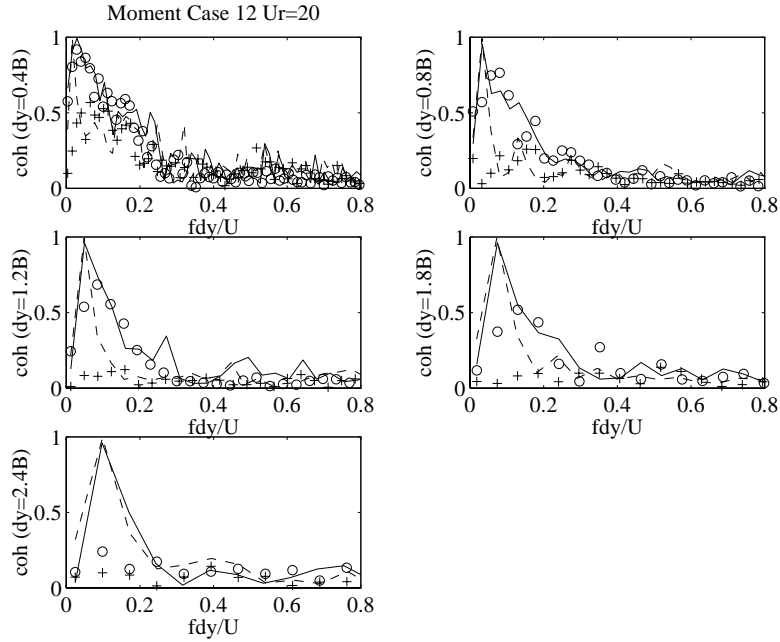


Figure 7-33 Coherence of moment at  $U_r=20$  in Case 12 flows for various spanwise separations ('+' Case 12a stationary; '- -' Case 12a oscillating; 'o' Case 12b stationary; '—' Case 12b oscillating).

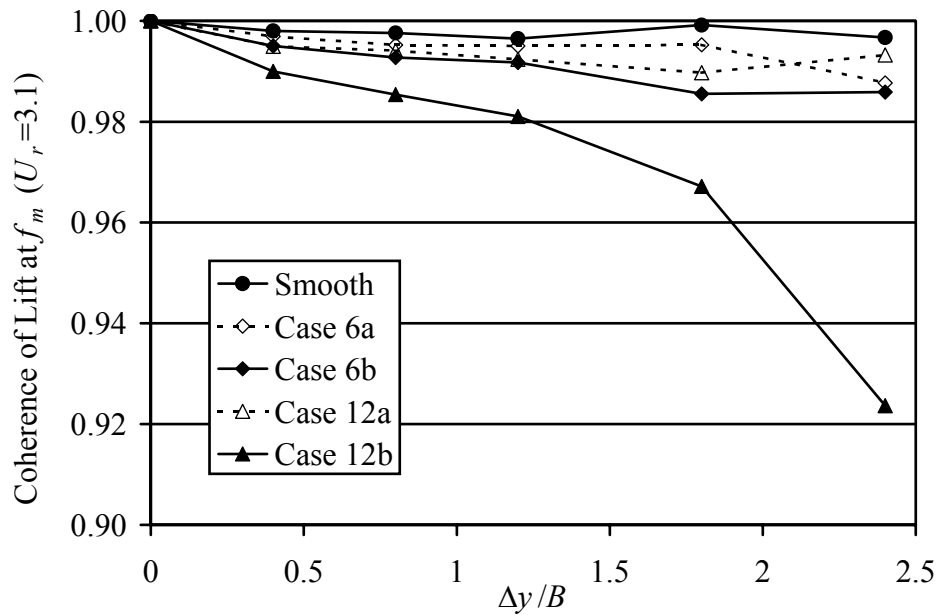


Figure 7-34 Coherence of lift at  $f_m$  for  $U_r=3.1$  in smooth and turbulent flows.

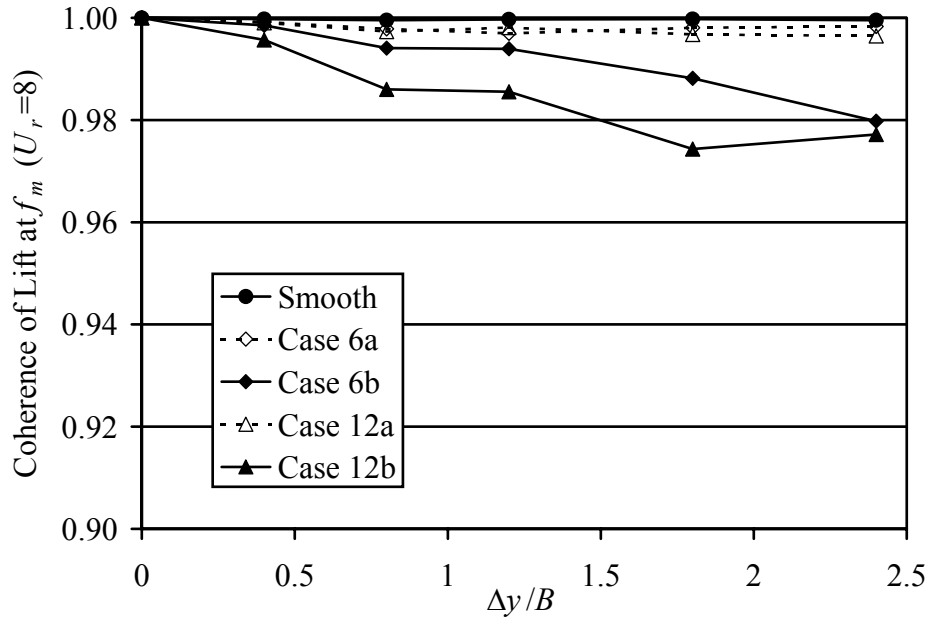


Figure 7-35 Coherence of lift at  $f_m$  for  $U_r=8$  in smooth and turbulent flows.

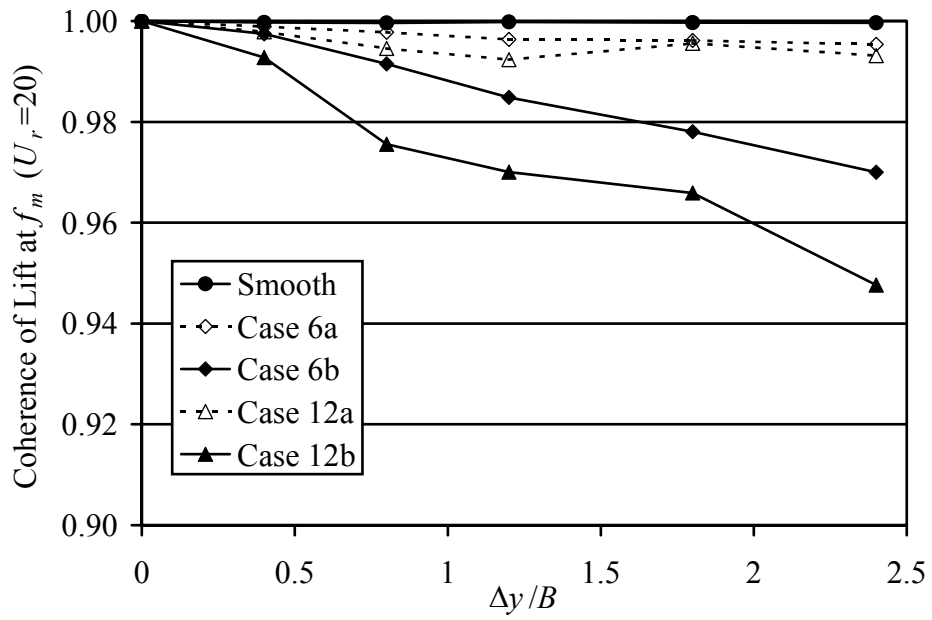


Figure 7-36 Coherence of lift at  $f_m$  for  $U_r=20$  in smooth and turbulent flows.

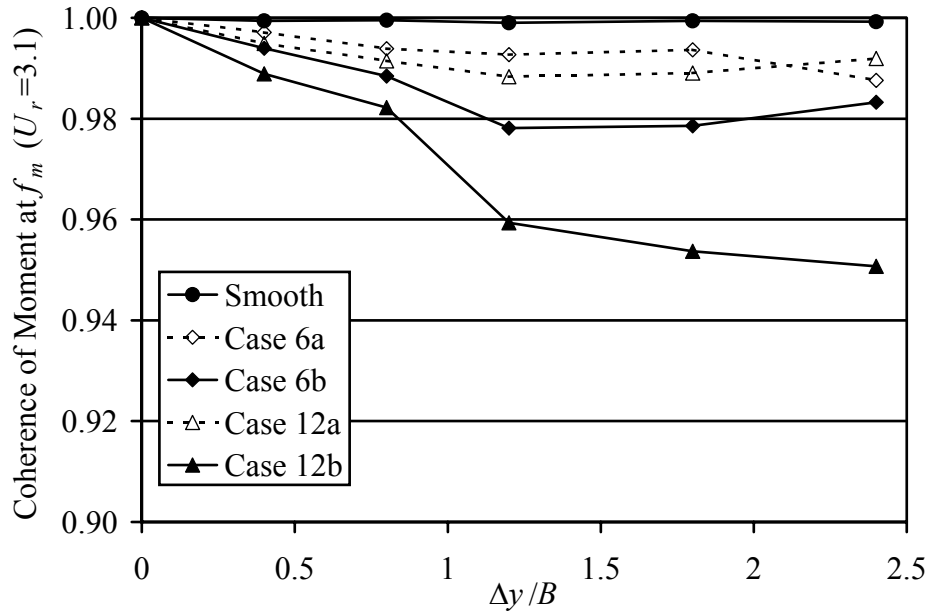


Figure 7-37 Coherence of moment at  $f_m$  for  $U_r=3.1$  in smooth and turbulent flows.

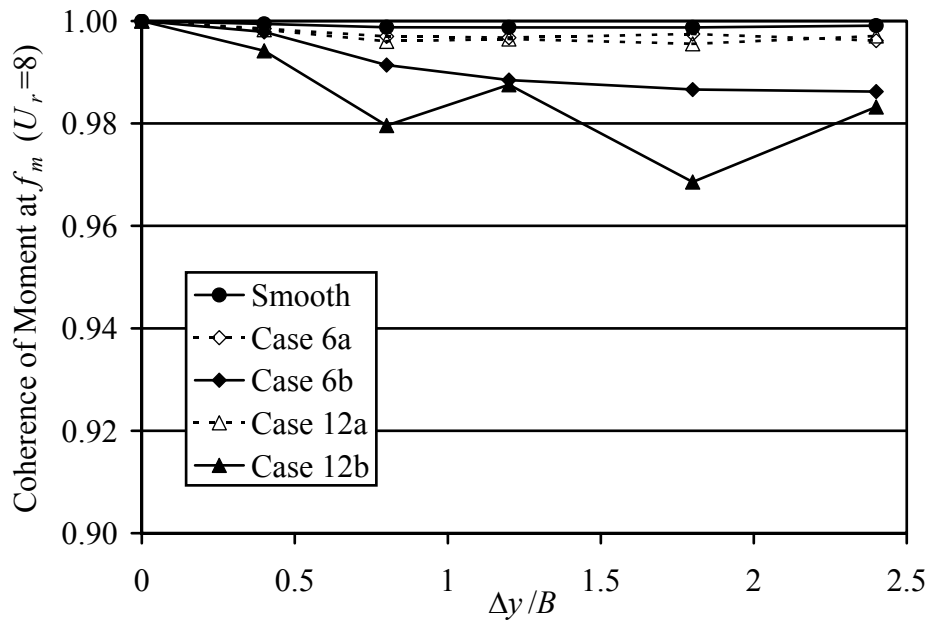


Figure 7-38 Coherence of moment at  $f_m$  for  $U_r=8$  in smooth and turbulent flows.

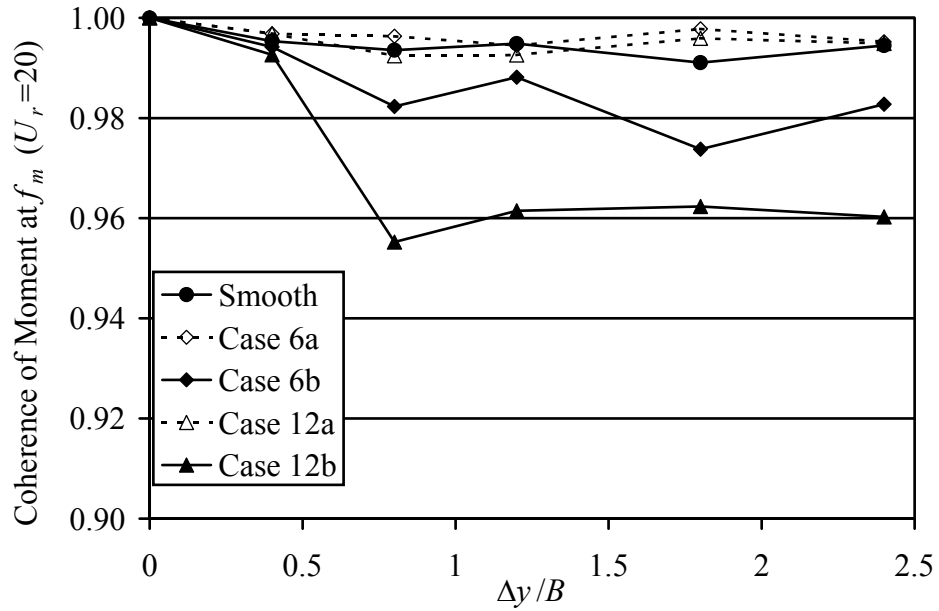


Figure 7-39 Coherence of moment at  $f_m$  for  $U_r=20$  in smooth and turbulent flows.

### 7.5 Streamwise Position Dependence of Spanwise Pressure Correlation—Oscillating Model

As in section 7.3 for stationary model tests, this section presents spanwise correlation calculations for discrete streamwise positions for oscillating model tests. The structure of the spanwise pressure correlations was thus examined rather than the correlation only of the integrated forces. Complete results will be presented for three of the reduced velocities tested—3.1, 8, and 20—as done in section 7.4 for the lift and moment correlation.

Spanwise pressure correlations are presented in groups of four figures. Each figure contains plots for four different streamwise locations. The group from Figure 7-40

through Figure 7-43 contains the normalized cross correlation coefficient values (at zero time lag) at each streamwise location in all the flows considered at  $U_r = 3.1$ . Values for smooth flow were always the highest among the five flow cases. For streamwise positions of  $x < 0.36B$ , correlation values are grouped generally according to turbulence intensity. Both Case 6 flows generated higher correlation values than both Case 12 flows without a significant effect of turbulence scale. Further downstream of  $x = 0.36B$ , however, a different trend is exhibited. Here the cases with the larger turbulence scales (the “b” cases) produced smaller correlation values. Both “b” cases had smaller correlation values than either “a” case.

These observations are illustrated clearly in the plot of the spanwise correlation scales as a function of streamwise position in Figure 7-44. Between the two regions of different behavior with respect to turbulence, near  $x = 0.36B$ , is a minimum in the correlation values. Upstream and downstream of this region correlation values are much higher.

The four figures from Figure 7-45 to Figure 7-48 show the spanwise pressure correlations for each streamwise position of the  $U_r = 8$  case. These correlation values also show a grouping according to turbulence intensity. The  $I_u = 12\%$  cases show lower values than the  $I_u = 6\%$  cases. Integral scale effects seemed to be greatest between  $0.1375B < x < 0.2775B$  for 6% turbulence intensity and  $0.0875B < x < 0.2775B$  for 12% turbulence intensity. An overall picture of these effects can be seen in Figure 7-49 where the spanwise correlation scales are plotted versus streamwise position. This plot

for  $U_r = 8$  does not show the same increase in correlation on the downstream half of the body that the  $U_r = 3.1$  case did.

Figure 7-50 through Figure 7-53 shows the spanwise pressure correlation values for  $U_r = 20$ . Comparing this case to lower reduced velocities, the correlation values are lower for a given separation. This trend agrees with that of the integrated lift and moment (in Figure 7-17 and Figure 7-21, respectively) where the spanwise correlation values decreased with increasing reduced velocity. The plots of spanwise pressure correlation scales in Figure 7-54 show, as with other reduced velocities, that greater turbulence intensity resulted in lower spanwise correlation. The decrease in correlation resulting from turbulence scale was less significant for this case than for lower reduced velocities.

An overall observation can be made for the plots of spanwise scale for each reduced velocity. Spanwise correlation scales presented here show an increase to a maximum when proceeding downstream from the leading edge. As discussed for the stationary model spanwise scales, this behavior is similar to that observed by Kiya & Sasaki (1983a) for spanwise correlation of velocity signals measured above a blunt, flat plate. They suggested that this might be due to a coalescence or amalgamation of vortices in the shear layer that no longer occurs after reattachment with the surface. The location of the maximum scales is located progressively further downstream for increasing reduced velocities. Downstream of this maximum the scales drop significantly. Interaction with the surface may add significant three-dimensional characteristics to these structures.

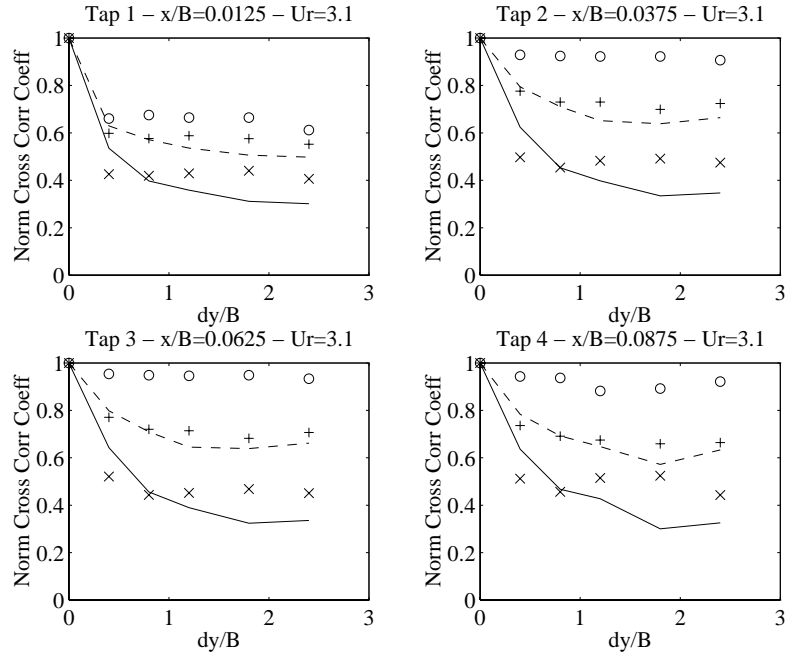


Figure 7-40 Pressure correlation functions for pressure taps 1-4 at  $U_r=3.1$  ('o' smooth flow; '+' Case 6a; '- -' Case 6b; 'x' Case 12a; '—' Case 12b')

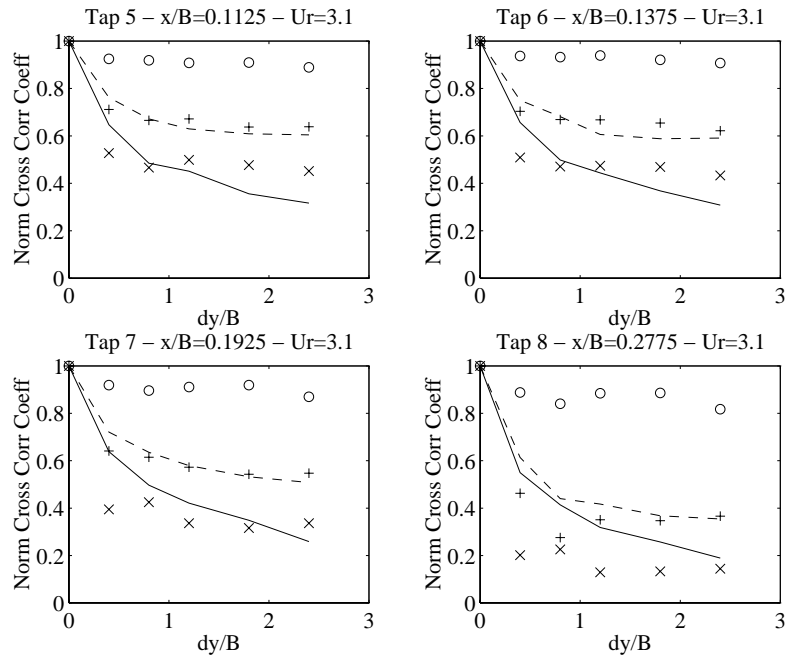


Figure 7-41 Pressure correlation functions for pressure taps 5-8 at  $U_r=3.1$  ('o' smooth flow; '+' Case 6a; '- -' Case 6b; 'x' Case 12a; '—' Case 12b')

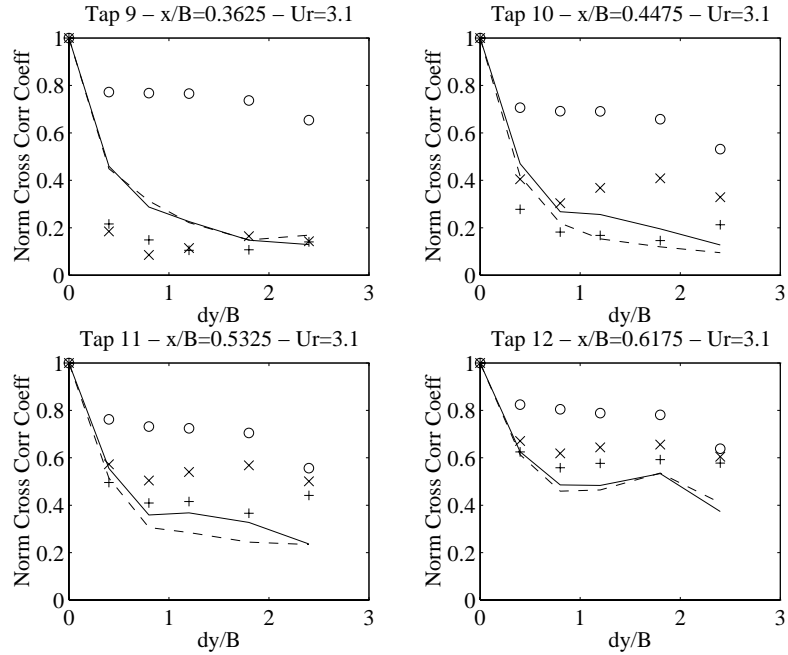


Figure 7-42 Pressure correlation functions for pressure taps 9-12 at  $U_r=3.1$  ('o' smooth flow; '+' Case 6a; '-' Case 6b; 'x' Case 12a; '—' Case 12b')

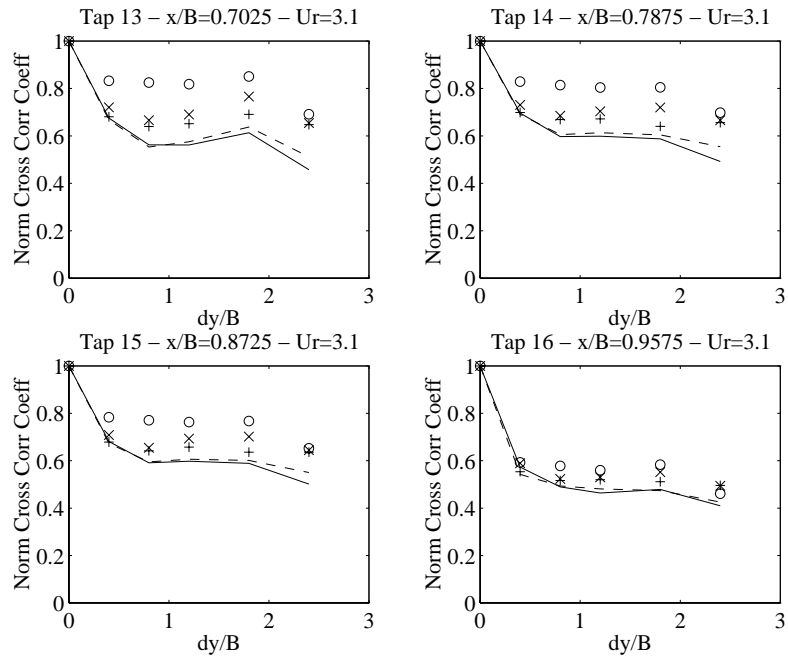


Figure 7-43 Pressure correlation functions for pressure taps 13-16 at  $U_r=3.1$  ('o' smooth flow; '+' Case 6a; '-' Case 6b; 'x' Case 12a; '—' Case 12b')

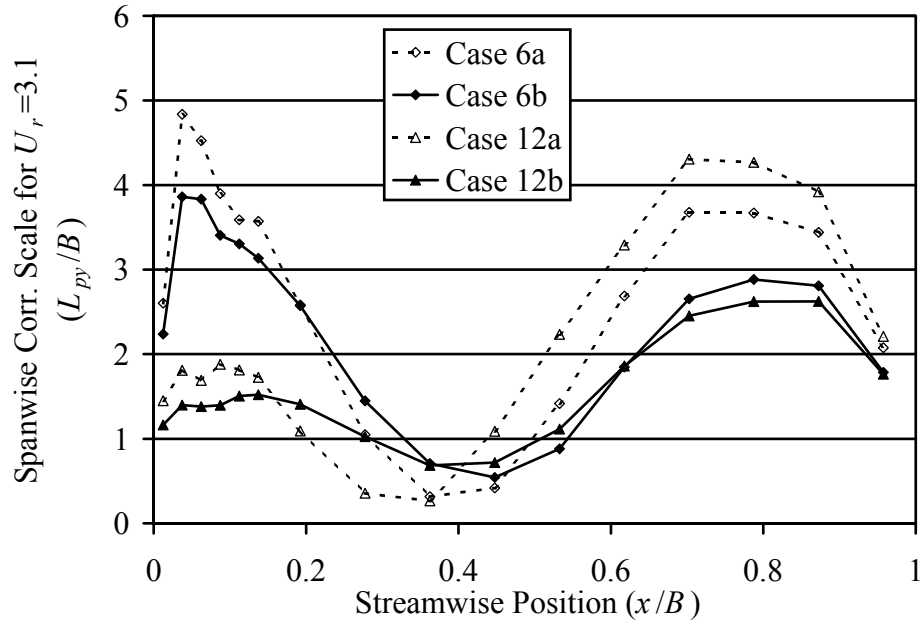


Figure 7-44 Spanwise pressure correlation scale,  $L_{py}$ , as a function of streamwise position for each turbulent flow case at  $U_r = 3.1$ .

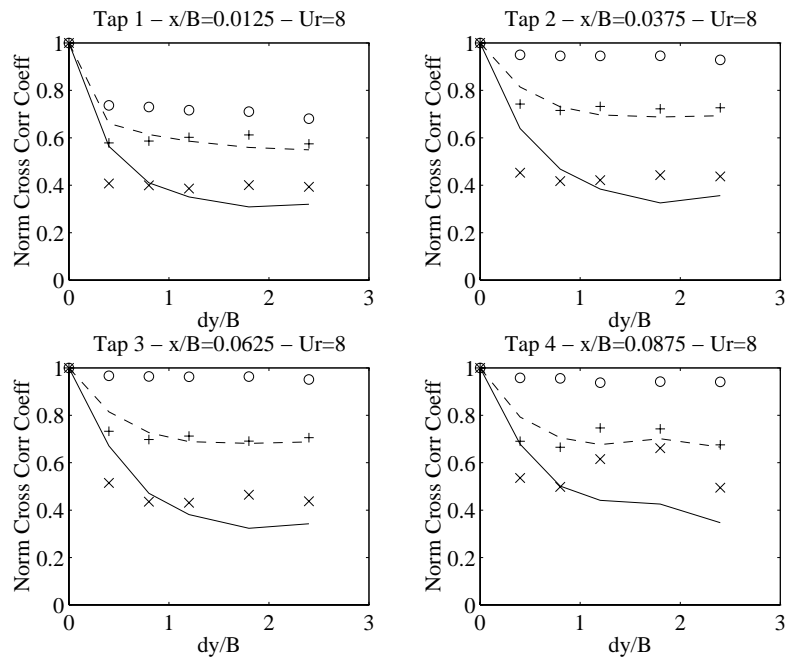


Figure 7-45 Pressure correlation functions for pressure taps 1-4 at  $U_r=8$  ('o' smooth flow; '+' Case 6a; '- -' Case 6b; 'x' Case 12a; '—' Case 12b)

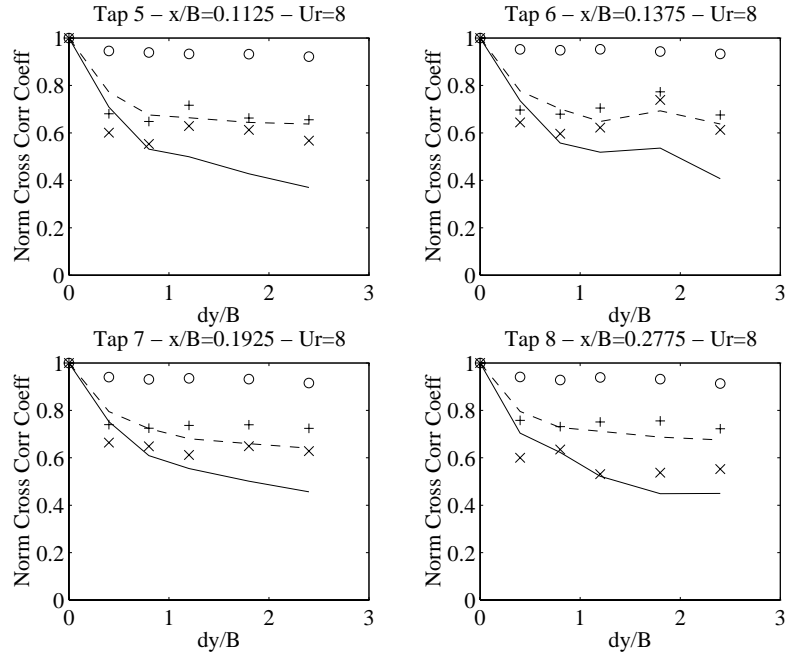


Figure 7-46 Pressure correlation functions for pressure taps 5-8 at  $U_r=8$  ('o' smooth flow; '+' Case 6a; '- -' Case 6b; 'x' Case 12a; '—' Case 12b')

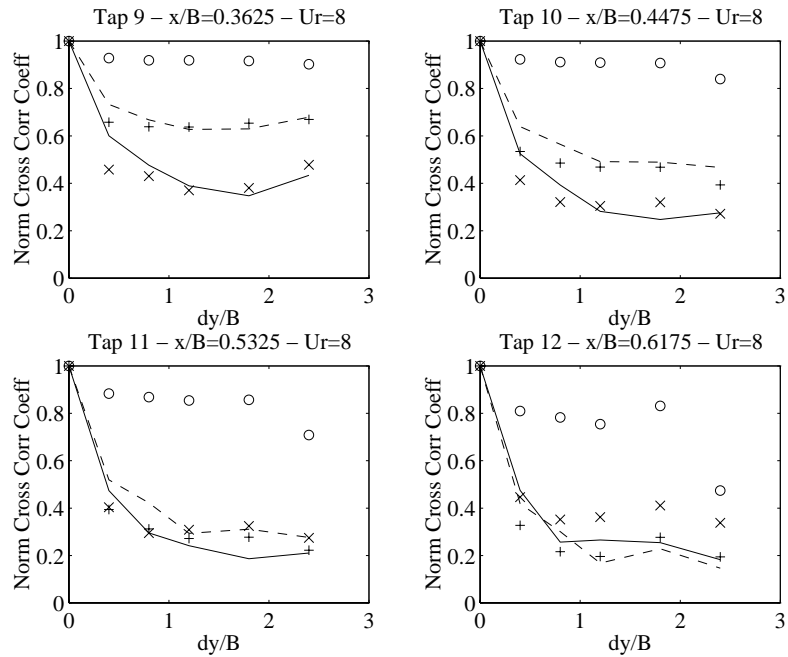


Figure 7-47 Pressure correlation functions for pressure taps 9-12 at  $U_r=8$  ('o' smooth flow; '+' Case 6a; '- -' Case 6b; 'x' Case 12a; '—' Case 12b')

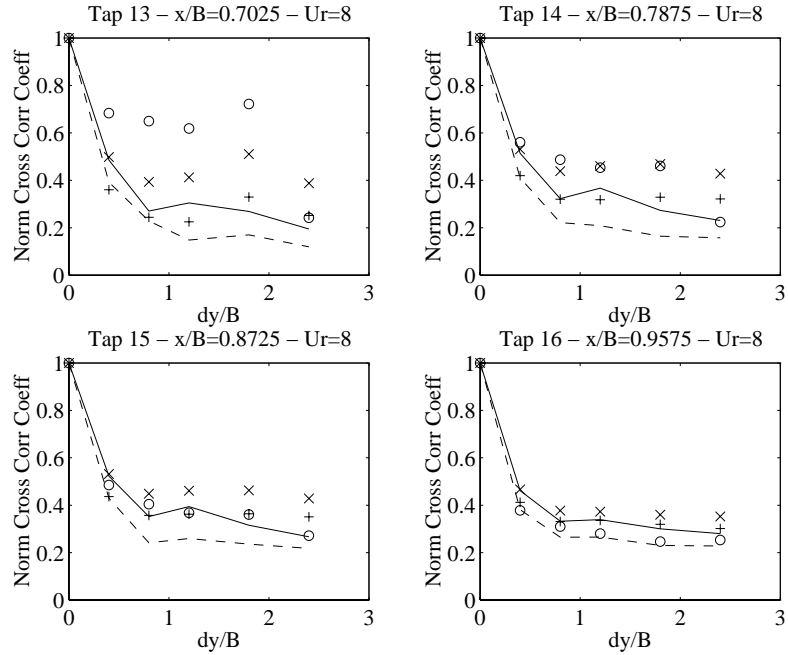


Figure 7-48 Pressure correlation functions for pressure taps 13-16 at  $U_r=8$  ('o' smooth flow; '+' Case 6a; '-' Case 6b; 'x' Case 12a; '—' Case 12b')

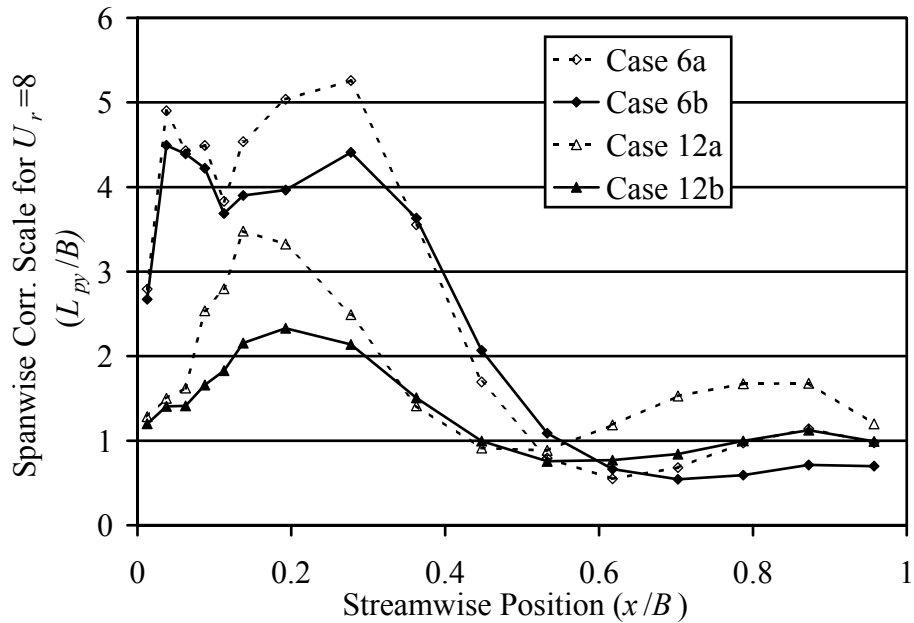


Figure 7-49 Spanwise pressure correlation scale,  $L_{py}$ , as a function of streamwise position for each turbulent flow case at  $U_r = 8$ .

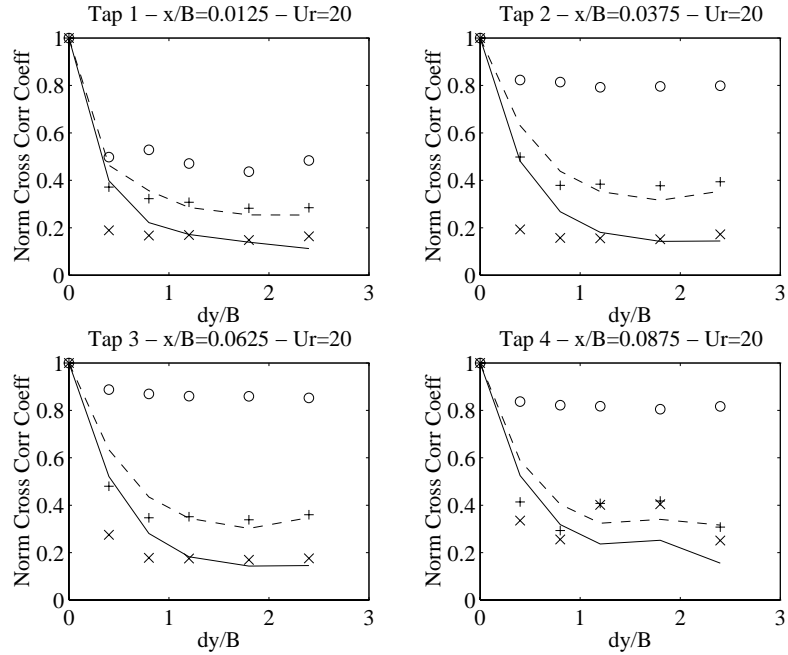


Figure 7-50 Pressure correlation functions for pressure taps 1-4 at  $U_r=20$  ('o' smooth flow; '+' Case 6a; '- -' Case 6b; 'x' Case 12a; '—' Case 12b')

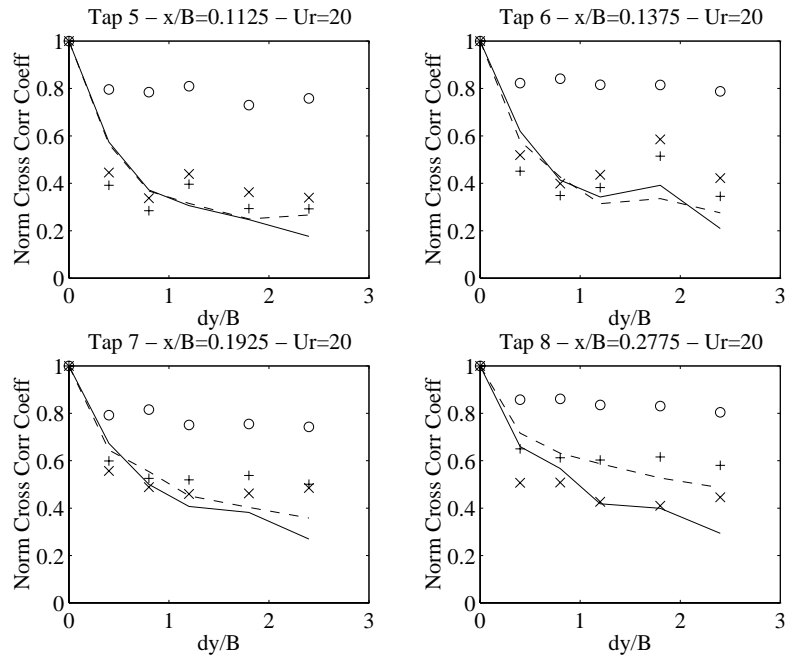


Figure 7-51 Pressure correlation functions for pressure taps 5-8 at  $U_r=20$  ('o' smooth flow; '+' Case 6a; '- -' Case 6b; 'x' Case 12a; '—' Case 12b')

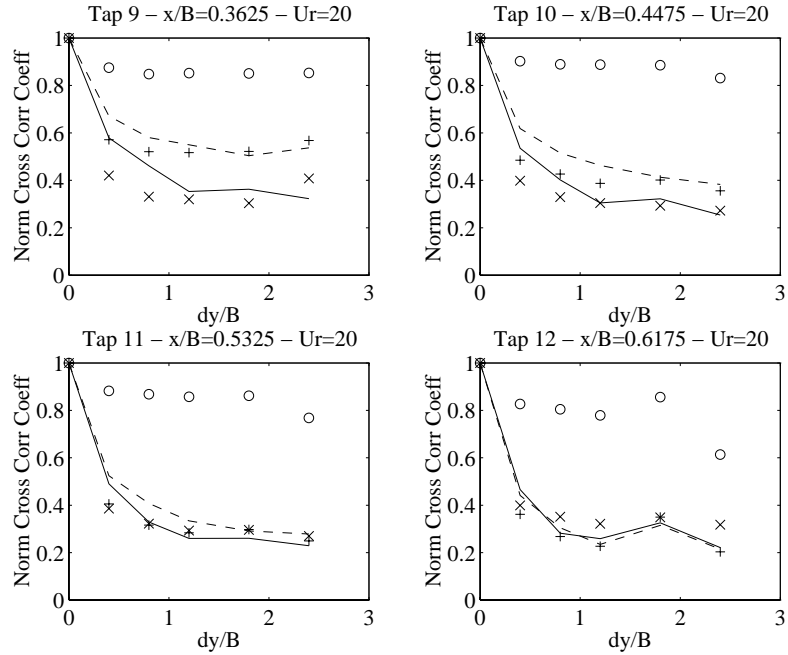


Figure 7-52 Pressure correlation functions for pressure taps 9-12 at  $U_r=20$  ('o' smooth flow; '+' Case 6a; '- -' Case 6b; 'x' Case 12a; '—' Case 12b')

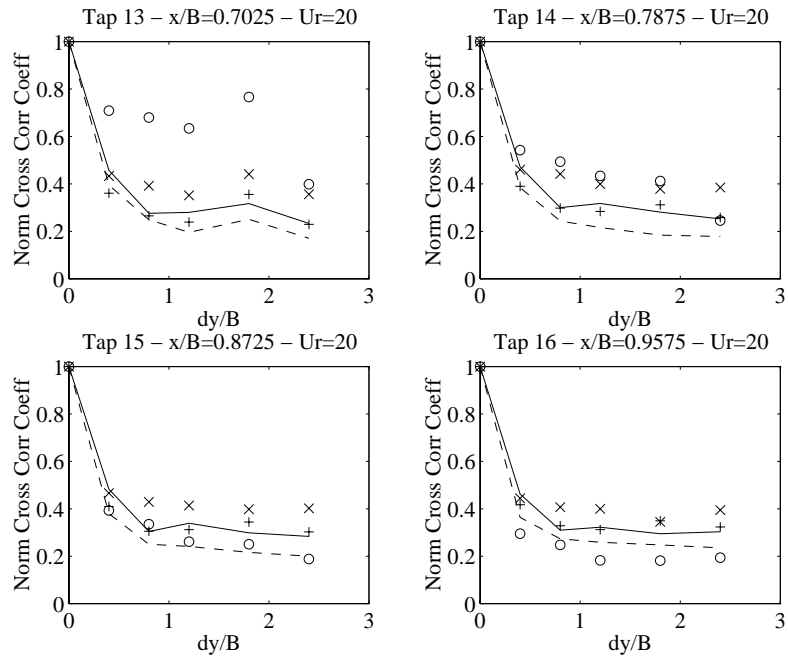


Figure 7-53 Pressure correlation functions for pressure taps 13-16 at  $U_r=20$  ('o' smooth flow; '+' Case 6a; '- -' Case 6b; 'x' Case 12a; '—' Case 12b')

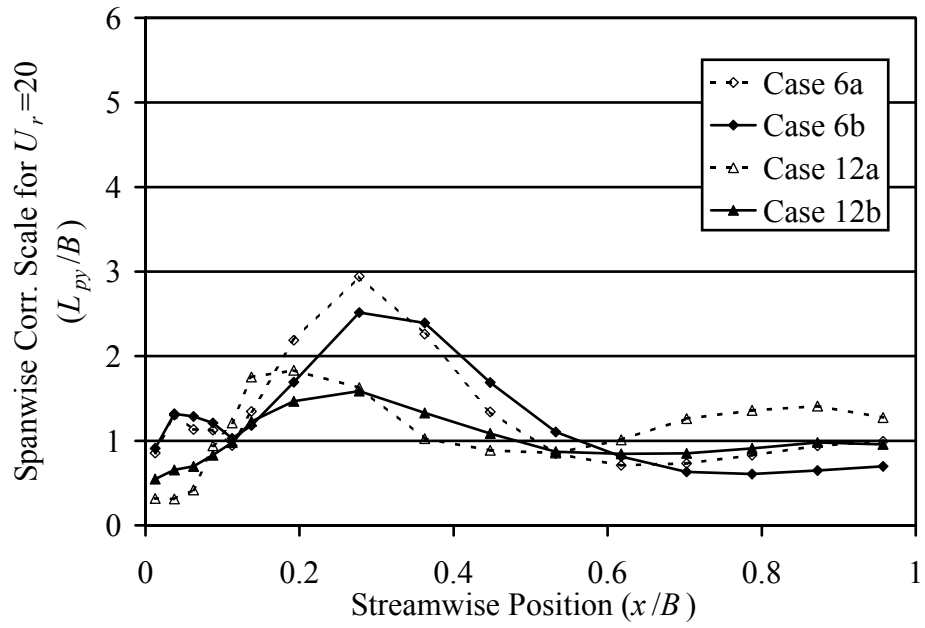


Figure 7-54 Spanwise pressure correlation scale,  $L_{py}$ , as a function of streamwise position for each turbulent flow case at  $U_r = 20$ .

## CHAPTER 8. DISCUSSION OF PRESSURE RESULTS

Results presented from the velocity and pressure measurements presented in Chapters 4 through 7 are discussed here. Sectional force results are examined first including discussions of both the pressure and phase behavior and the behavior of the integrated forces through the flutter derivatives. Spanwise behavior is then discussed followed by several comments regarding the application of these results to the analysis of long span bridges.

### 8.1 Discussion of Sectional Forces

Sectional forces discussed here include the measurements involving a single spanwise position. Turbulence modifications of pressure amplitudes and phases are examined first with some overall comments about potential physical mechanisms. This leads naturally into the discussion of how the pressure modifications relate to the behavior of the integrated lift and moment with respect to turbulence. The last sectional force topic discussed is the differences measured between buffeting forces on stationary and oscillating models.

### 8.1.1 Pressure Amplitude and Phase Behavior

The diagrams of the phase of the pressure signals at the body oscillation frequency (see chapter 6) show the presence of similar regions in each plot. Although these regions are not in the same place for each flow or for each reduced velocity, they are always present—for example, see the pressure phase distribution for  $U_r = 20$  in Figure 8-1. Figure 8-2 illustrates the arrangement of these regions schematically. Near the leading edge, phase is nearly constant. The downstream extent of this region is heavily dependent on the turbulence intensity. Immediately downstream of this constant phase region the phase increases rapidly. Phase values *increased* in this region for all cases tested. The boundary between this rapidly changing phase region and that of more slowly-varying phase is less distinct than that between the first two. In this region, the rate of phase increase levels off, and for many cases, the phase values begin to decrease. In some instances, these phase values become negative.

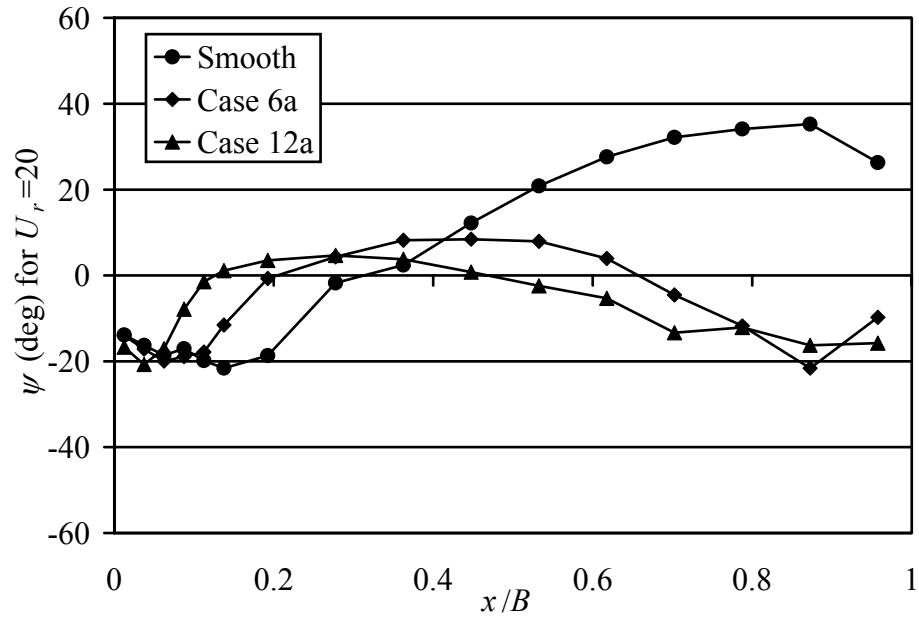


Figure 8-1 Pressure phase distributions for smooth flow and small-scale turbulent flows at a reduced velocity of 20.

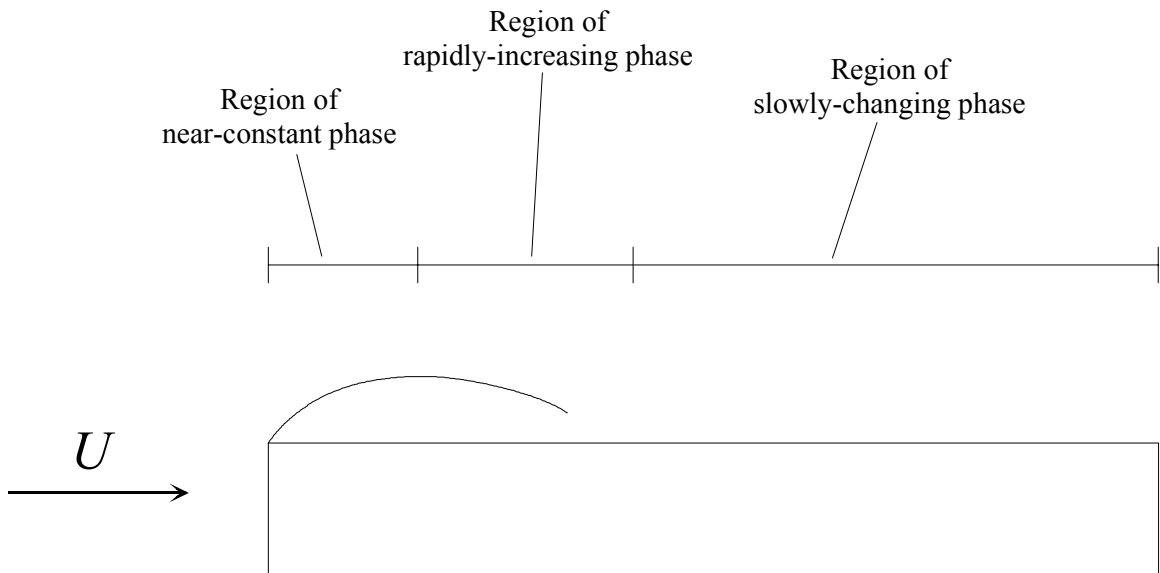


Figure 8-2 Schematic diagram labeling different regimes in the pressure phase diagrams. These regimes include regions of near-constant phase, rapidly-changing phase, and slowly-changing phase.

A number of researchers account for the phase change in the streamwise direction by attributing them to the convection of vortex-like structures shed from the leading edge shear layer (Matsumoto (1996), Kubo et al. (1992)). Such convection would be associated with a phase increase in the streamwise direction. While such an increase is evident in some regions of some phase distributions, it is not the only behavior exhibited.

To examine this issue, the two time scales used in the reduced velocity were considered. Reduced velocity defined as  $U_r = U/fB$  can be considered the ratio of two time scales. The first is the convection time,  $\tau_c = B/U$ . This is the time required for convection from the leading edge to the trailing edge. The second scale is the period of the body oscillation,  $\tau_\alpha = 1/f_\alpha$ . The reduced velocity in terms of these time scales is then  $U_r = \tau_\alpha/\tau_c$ , and since  $U_r$  is a primary parameter for unsteady aerodynamics both of these time scales play a role in the physical mechanisms.

These time scales can be roughly estimated from experimental results and physical considerations. Several researchers have made velocity measurements in and around the separated and reattaching shear layers about stationary rectangular cylinders. Vortex convection speeds found by these researchers range from  $0.5U$  to  $0.6U$  (Kiya & Sasaki, 1983; Cherry et al., 1984) where  $U$  is the mean flow velocity. The convection time scales could be estimated from these convection velocities as  $\tau_c = B/U_c$ . An estimate of the rate at which the body oscillation alters the pressures from the leading edge to the trailing edge can be obtained using the illustration of Figure 8-3. In half the period of oscillation the body moves from its maximum angle of attack to its minimum angle of attack. In approximately this much time, the reattachment line moves from one

extreme of its streamwise position to the other. The body motion time scale could then be estimated as  $\tau_\alpha = 1/2f_\alpha$ .

Phase values can be estimated from these time scales and compared with measured pressure phases. Such estimates have been plotted in Figure 8-4 for  $U_r = 20$ . This plot shows that the phase estimated from  $\tau_\alpha$  matches the changes in the “region of rapidly-increasing phase” much more closely than that estimated from  $\tau_c$ . Downstream, in the “region of slowly-changing phase” the phase estimated from the convection time scale,  $\tau_c$ , appears more appropriate. Figure 8-5 plots  $U_r = 3.1$  phase data with the same phase estimates. In this case, the phase estimates are much closer to each other, but the match with the rapidly-increasing phase region is poorer.

To fully understand the physics of the phase changes, velocity measurements must be made in the separated flow regions above oscillating models. However, even from these measurements of the unsteady pressures, it is evident that a time scale larger than that of the convection scale plays a role in the phase changes—particularly in the region where phase increases rapidly. As further evidence of the importance of this particular region, Figure 8-6 shows both the pressure amplitude and phase plotted together. This plot is typical of each case studied and shows that the maximum self-excited pressure amplitudes occur in or near this rapidly-increasing phase region. Whether the physical mechanism for these large amplitudes and fast phase changes are due to an expansion and contraction of the separation bubble or to slowly-convecting vortex structures, it is clear that this region is important to the unsteady pressure

generation. Subsequent sections of this chapter will discuss the impact of this region in more depth.

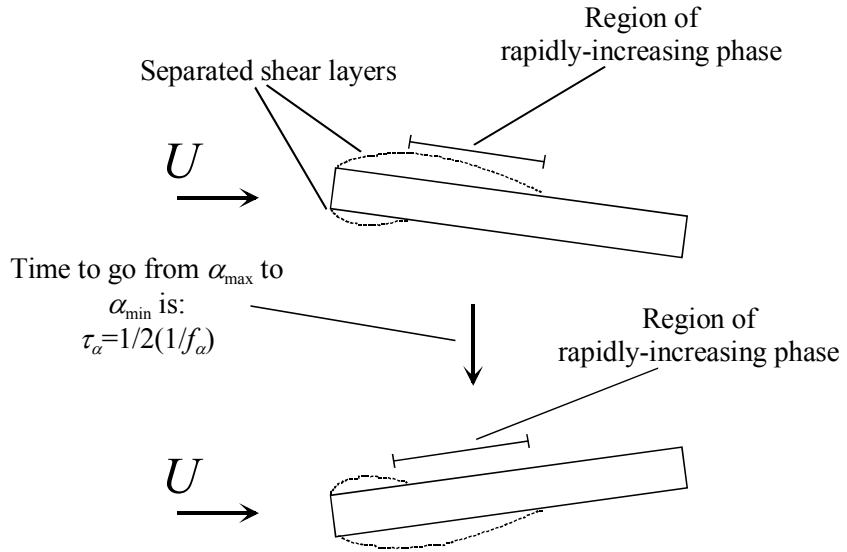


Figure 8-3 Schematic diagram illustrating the concept of the body motion time scale.

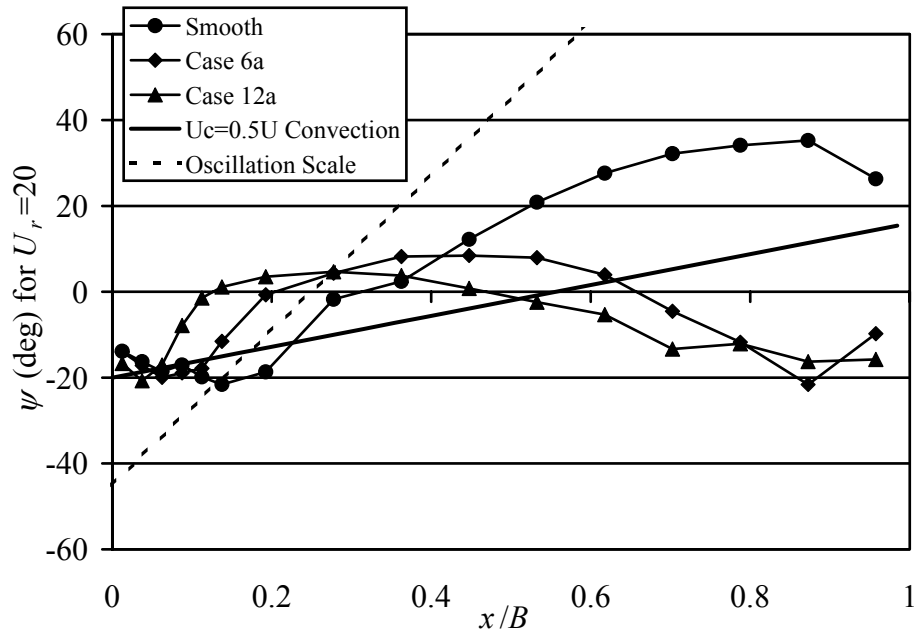


Figure 8-4 Pressure phase distributions for smooth and turbulent flows including phase estimated from both convection and oscillation frequency time scales ( $U_r = 20$ ).

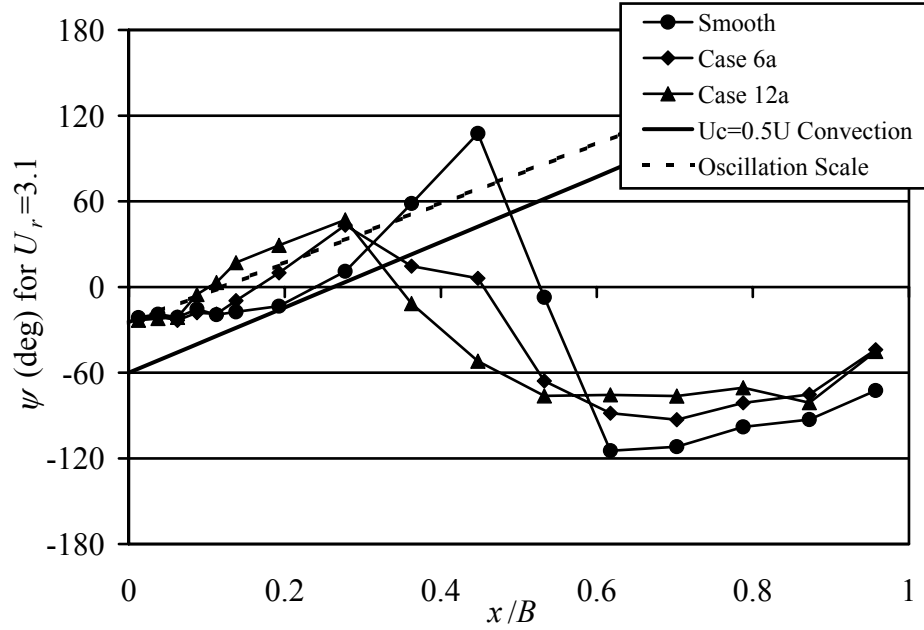


Figure 8-5 Pressure phase distributions for smooth turbulent flows including phase estimated from both convection and oscillation frequency time scales ( $U_r = 3.1$ ).

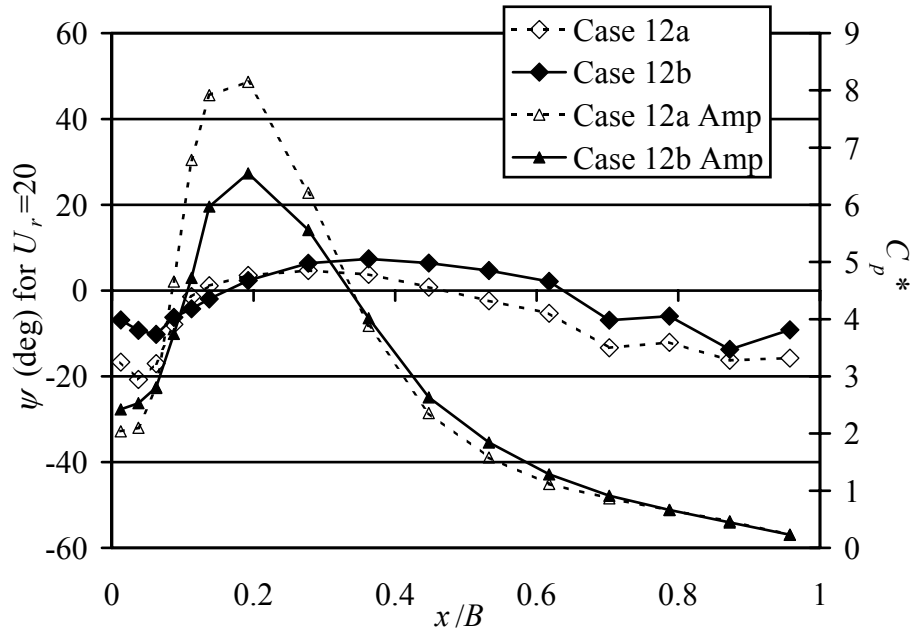


Figure 8-6 Pressure amplitude and phase distributions for the Case 12 flows at  $U_r = 20$ .

### 8.1.2 Flutter Derivatives

This section discusses the changes in the flutter derivatives and how these changes can be tracked as changes in the pressure distributions. More importantly, the effects of turbulence on the flutter derivatives will be illustrated through the turbulence-induced changes in the pressure distributions.

This discussion will start with  $A_2^*$  because its impact on aerodynamic stability is the most straightforward.  $A_2^*$  results for each incident flow are shown in Figure 8-7 along with the results of Matsumoto (1996) for bodies with different  $B/D$  ratios. One way to visualize how the pressure amplitude and phase distributions combine to set the flutter derivative values is to look at the integrands of the expressions used to calculate them (these expressions were derived in Chapter 2). The expression for  $A_2^*$  is:

$$A_2^* = \frac{1}{4k^2} \int_{-1}^1 x^* 2C_p^*(x^*) \sin \psi(x^*) dx^* \quad (8-1)$$

where  $x^* = x/b$  is the streamwise position (where  $x^* = 0$  corresponds here to midchord),  $b = B/2$ , and  $k = \omega_\alpha b/U$  is the reduced frequency. Equation (8-1) can be thought of as a measure of the centroid, with respect to midchord, of the distribution of  $C_p^*(x) \sin(\psi(x))$ .

Plotting this distribution in Figure 8-8 for various reduced velocities shows how the centroid of this distribution moves downstream of midchord as  $U_r$  increases. If the centroid is downstream of midchord, then  $A_2^*$  will have positive values. As discussed in the Introduction of Chapter 1, positive values for  $A_2^*$  correspond to unstable aerodynamic

influences. This can be thought of as a negative damping influence where the structural damping is effectively reduced or even eliminated.

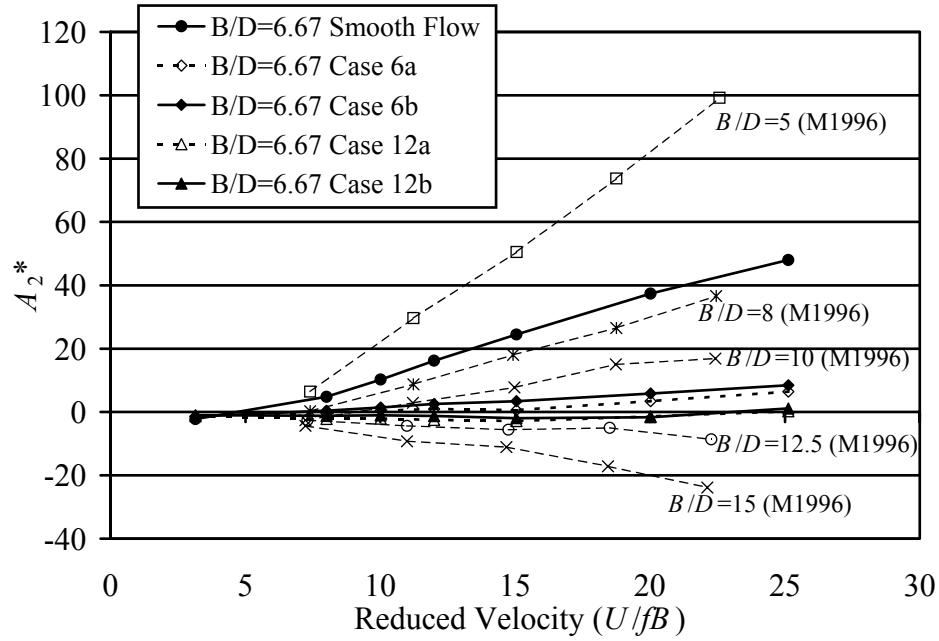


Figure 8-7  $A_2^*$  versus reduced velocity for smooth and turbulent flow cases from this study compared with smooth flow values for different  $B/D$  ratios (“M96” refers to Matsumoto, 1996).

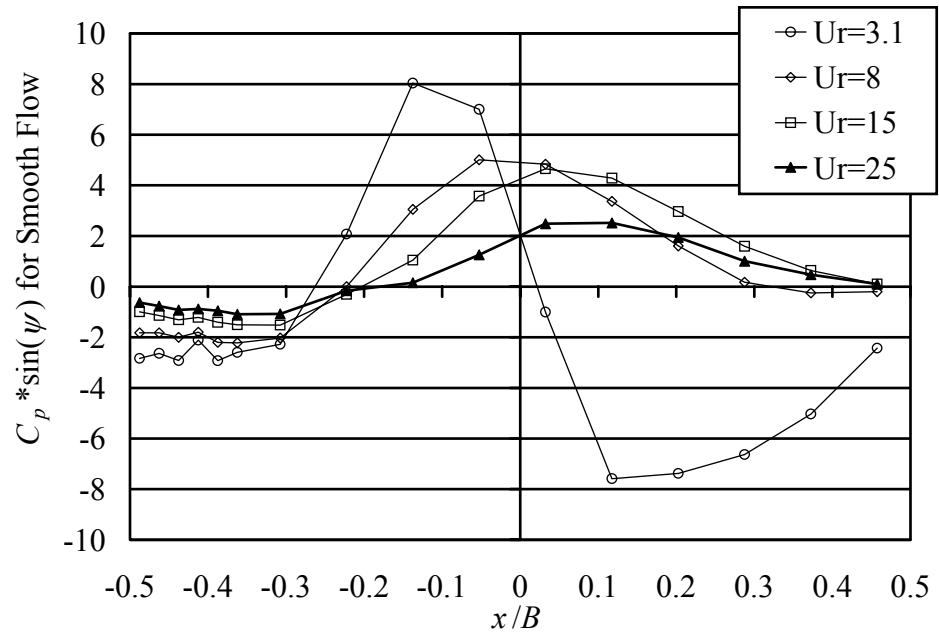


Figure 8-8  $C_p^*(x)\sin(\psi(x))$  plotted versus streamwise position for various reduced velocities in smooth flow.

The effect of turbulence on  $A_2^*$  can be illustrated similarly. Figure 8-9 shows  $C_p^*(x)\sin(\psi(x))$  plotted versus streamwise position for each flow case and a reduced velocity of 8. The centroid of  $C_p^*(x)\sin(\psi(x))$  shifts upstream with increasing turbulence intensity. This upstream shift of the centroid corresponds to shifts of both the amplitude distribution and the region of rapidly-increasing phase described earlier. The movement of the centroid toward the leading edge brought about significant decreases in  $A_2^*$  values. While smooth flow generated large positive values of  $A_2^*$ , flows with 6% turbulence intensity resulted in values  $\leq 10$ . Flows of 12% turbulence intensity resulted in negative  $A_2^*$  values for most of the  $U_r$  range considered.

This shifting of the pressure distributions with turbulence can be used to explain the behavior of the  $A_2^*$  curves with respect to turbulence intensity and scale. The plots of Figure 8-7 (originally presented in Chapter 6) show that  $A_2^*$  curves are grouped in pairs. Flows of similar turbulence intensity had similar values while turbulence scale played only a minor role. This fits the trend previously mentioned that turbulence intensity plays the greater role in shifting the pressure distributions toward the leading edge. Figure 8-9 shows that the upstream shift of  $C_p^*(x)\sin(\psi(x))$  is the major contributor to changes in  $A_2^*$ . This helps to illuminate the reason for the relative importance of intensity and scale for  $A_2^*$ .

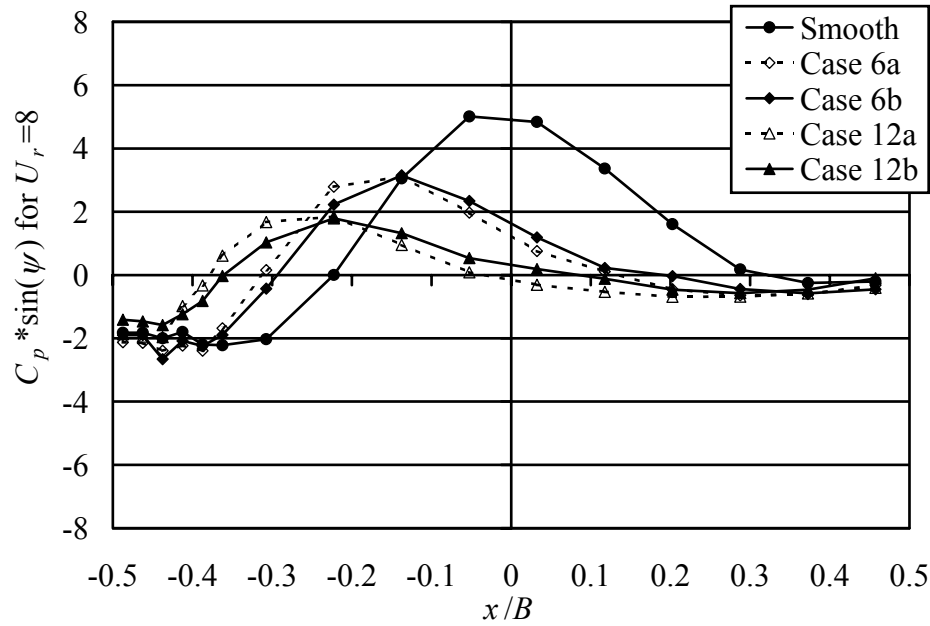


Figure 8-9  $C_p^*(x)\sin(\psi(x))$  plotted versus streamwise position for all flow cases at  $U_r = 8$ .

The stabilizing effect of free stream turbulence is not without similarity to the stabilizing trends seen as the aspect ratio of the cross section ( $B/D$ ) increases.

Matsumoto (1996) has studied the unsteady pressure distributions about a large number of rectangular cylinders in smooth flow. Comparing the pressure phase distributions of the current model (with  $B/D = 6.67$ ) in turbulent flow with that of Matsumoto's results for a longer model (with  $B/D = 12.5$ ) in smooth flow, one observes similarities. This comparison is shown in Figure 8-10. For  $I_u = 6\%$ , the model used in this study behaves similarly to that of a longer model in smooth flow. One can view this change as an "effective lengthening" of the body with free stream turbulence. This should not be taken as a fundamental understanding of the phenomenon but rather as another way to understand what is happening. This also emphasizes the fact that the  $A_2^*$  flutter derivative

is highly dependent on the aspect ratio of the cross section—illustrated in the data of Matsumoto (1996) shown in Figure 8-7.

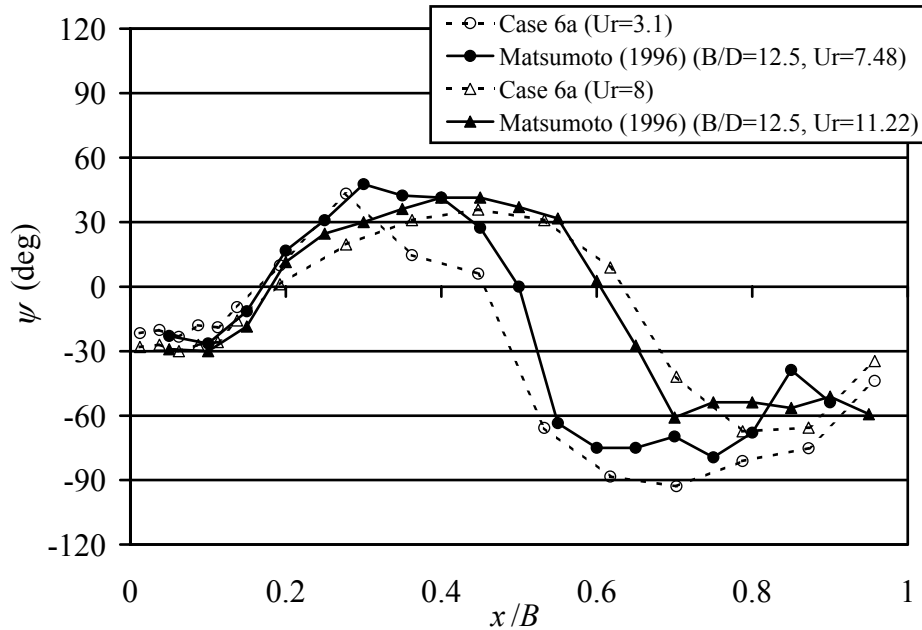


Figure 8-10 Comparison of pressure phase values in turbulent flow for the current model with  $B/D = 6.67$  with values in smooth flow for a model with a longer afterbody ( $B/D = 12.5$ ).

An examination of the effects of turbulence on  $A_3^*$  can also be done similarly to that done for  $A_2^*$ . The main component of the integrand for  $A_3^*$  is  $C_p^*(x)\cos(\psi(x))$ . This quantity is plotted in Figure 8-11 versus streamwise position for  $U_r = 20$ . As in the case of  $A_2^*$ , the integral is equivalent to the centroid, with respect to midchord, of the distribution of a function of the amplitude and phase—in this case, the distribution is  $C_p^*(x)\cos(\psi(x))$ . Because the cosine of the phase is involved rather than the sine, the character of the plot in Figure 8-11 is more like that of the amplitudes themselves. As the

peak amplitudes move closer to the leading edge—or, equivalently, as the centroid of the distribution moves further from midchord—the value of  $A_3^*$  increases.

Two comments can be made here regarding of turbulence effects. Increases in turbulence intensity moves the region of maximum pressure amplitudes nearer the leading edge. The increase in  $A_3^*$  resulting from this shift is evident in the results of Chapter 6. In addition, increases in turbulence scale decrease the pressure amplitudes without a significant streamwise shift in the distribution location. This amplitude decrease also decreases the  $A_3^*$  magnitude. In fact, the effect of scale for the cases considered was greater than that of turbulence intensity. A doubling of the turbulence intensity increased  $A_3^*$  by approximately 6% while nearly doubling the turbulence scale decreased  $A_3^*$  by nearly 20%.

Similar to the behavior of  $A_2^*$ , the turbulence-induced modifications to  $A_3^*$  produce values similar to smooth flow results for bodies with greater aspect ratio,  $B/D$ , such as the results of Matsumoto (1996).

Discussion of the aerodynamic coupling terms,  $H_2^*$  and  $H_3^*$  (presented in Chapter 6), can proceed similarly to that for  $A_2^*$  and  $A_3^*$  because of the similarity of their derivations. The integrands of the  $H_2^*$  and  $H_3^*$  expressions are the same as those for  $A_2^*$  and  $A_3^*$ , respectively, except for the factor of  $x^*$ , the moment arm (see Chapter 2 derivations). As a result, the anatomy of the magnitude of  $H_2^*$  can be examined using the  $C_p^*(x)\sin(\psi(x))$  plots of Figure 8-8 and Figure 8-9 as done for  $A_2^*$ . A corresponding study of  $H_3^*$  can be made using  $C_p^*(x)\cos(\psi(x))$  as done for  $A_3^*$ . In these cases, however, the

areas under  $C_p^*(x)\sin(\psi(x))$  and  $C_p^*(x)\cos(\psi(x))$  are the quantities of interest rather than their centroids with respect to midchord. In other words, the total lift is the concern rather than where it was generated.

In every case, incident turbulence reduced the self-excited pressure amplitudes. Increasing turbulence intensity reduced pressure amplitudes as did increasing turbulence scale. As a result, total self-excited lift decreased—which was reflected in the decreases in  $H_2^*$  and  $H_3^*$  with turbulence. Another reason for the magnitudes of  $H_2^*$  to drop so close to zero was that turbulence reduced the phase magnitudes as well. With  $H_2^*$  being proportional to  $\sin(\psi(x))$ , smaller phase values resulted in smaller magnitudes. In fact, the general form of  $C_p^*(x)\sin(\psi(x))$  in Figure 8-9 staying closer to zero as turbulence intensity increased was qualitatively similar to the behavior of the phase value,  $\psi(x)$ , itself (Chapter 6).

As was the case with  $A_3^*$ , the  $H_3^*$  magnitudes show more dependence on turbulence scale than the  $H_2^*$  magnitudes. The nature of the  $H_3^*$  dependence on  $\cos(\psi(x))$  means that  $H_3^*$  magnitudes will be more dependent on pressure amplitudes than on pressure phases. As a result, the trends of turbulence dependence of the magnitudes for  $H_3^*$  follow closely the trends of the pressure amplitudes. Increasing turbulence intensity decreases these amplitudes. Increasing turbulence scale for a given turbulence intensity showed a weaker effect but decreased the amplitudes slightly more.

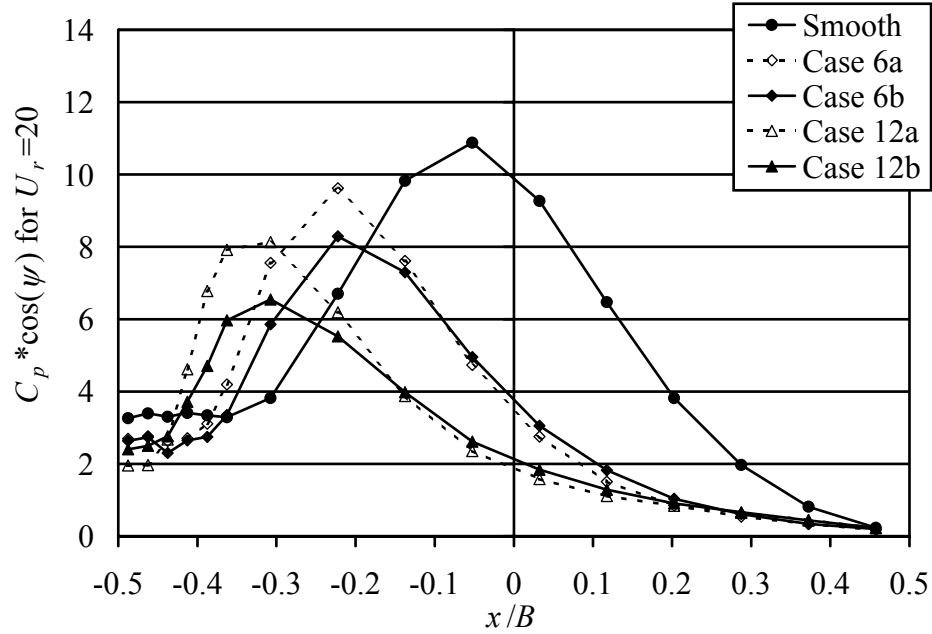


Figure 8-11  $C_p^*(x)\cos(\psi(x))$  plotted versus streamwise position for all flow cases at  $U_r = 20$ .

### 8.1.3 Buffeting Forces on Oscillating Models

Current long-span bridge analysis technique assume that the aerodynamic forces on a bridge deck can be separated into components representing self-excited and buffeting loads. To the author's knowledge, an experimental comparison of buffeting forces on stationary and oscillating bodies has not been done previously. The results of Chapter 6 show that buffeting loads on the oscillating model studied here are quite similar to the loads for the model when stationary. However, there were differences in these loads—oscillation increased the rms value of the broad band buffeting loads by 5% to 10%. These differences grew smaller for larger turbulence intensity and for larger turbulence scale. Although some of the oscillation-induced increases were evident

throughout the frequency range, the most significant increases were for frequencies greater than  $fD/U = 0.1$ . As expected, similar differences were evident in the aerodynamic admittance functions.

Studying the streamwise distribution of these differences showed that the majority of the added effect of the body oscillation occurred upstream of reattachment. This implies that bridge decks that experience less separation will show less difference between buffeting loads measured for stationary and oscillating conditions. Over the range of turbulence parameters measured here, trends with increasing turbulence intensity and increasing scale suggest that as these values increase to atmospheric levels this difference may decrease further. The differences quantified here warrant further study.

## 8.2 Discussion of Spanwise Behavior

Two issues concerning spanwise coherence are discussed here. First, the relationship between the results of stationary and oscillating model tests are compared, and a unique analysis technique is presented. Second, a few issues related the reduced velocity dependence of spanwise correlation are considered.

### 8.2.1 Comparison of Stationary and Oscillating Model Results

Spanwise coherence and correlation calculations were made from pressure measurements on both stationary and oscillating models. The results presented in Chapter 7, particularly the coherence results, suggest that perhaps the increase in spanwise

correlation going from stationary models to oscillating models may be due almost entirely to a single frequency. Broad band coherence levels for forces on stationary and oscillating were very similar. Only near the model oscillation frequency were the coherence values significantly different.

To examine this distinction, this discussion will calculate the correlation and coherence functions for distinct components of the signals measured on the oscillating model. Lift forces calculated at a given spanwise position will be separated as follows:

$$L_i(t) = L_{se_i}(t) + L_{b_i}(t) \quad (8-2)$$

where  $L_i$  is the total lift at spanwise position  $i$  ( $i = 1, 2$ ),  $L_{se_i}$  is the self excited lift force at position  $i$ , and  $L_{b_i}$  is the buffeting force at position  $i$ .  $L_{se}$  is the lift force component accounted for by the flutter derivatives and  $L_b$  is everything else—all of the broad band energy. As an example, Figure 8-12 shows each component of a lift signal a model oscillating at  $U_r = 20$  in Case 6a flow. A formulation analogous to that of equation (8-2) was used to define the corresponding components of the unsteady moment,  $M_i$ ,  $M_{se_i}$ , and  $M_{b_i}$ .

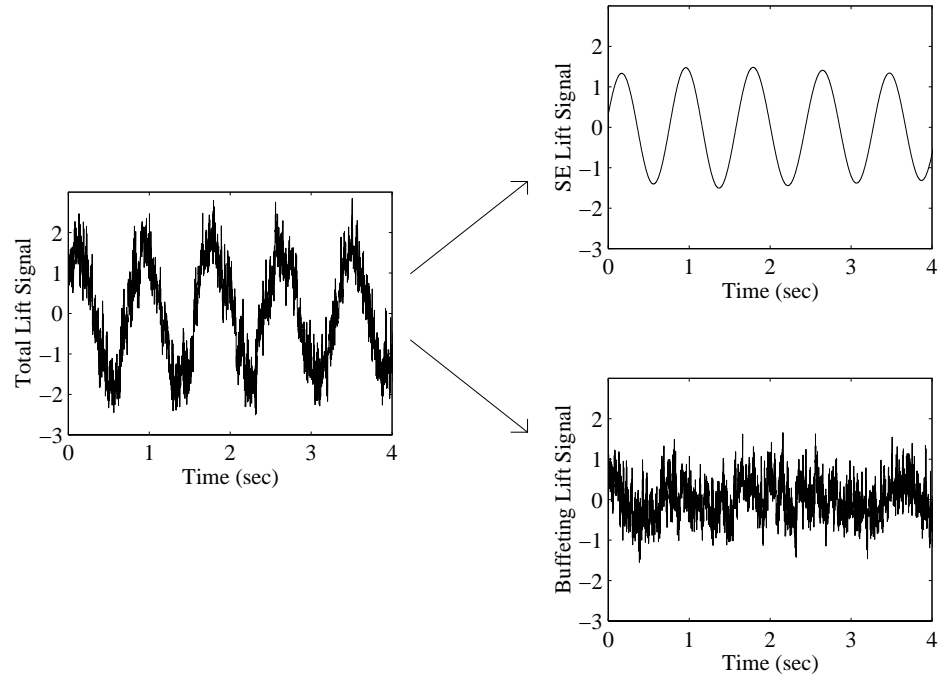


Figure 8-12 Plots of the total, self-excited, and buffeting components of lift for  $U_r = 20$  in Case 6a flow.

Appendix C describes the signal processing techniques used to split these signals into self-excited and broad band components. Correlation and coherence calculations were performed on each of these components separately. As an example, Figure 8-13 shows the cross correlation functions for the lift forces separated by  $\Delta y = 1.2B$  on the model oscillating at  $U_r = 20$  in Case 12b flow. The cross correlation function of the total lift force signals is shown on the left, and the correlation between each component,  $L_{se}(t)$  and  $L_b(t)$  is shown on the right. The self-excited components are for more highly correlated than the broad band buffeting components. The resulting correlation of the total force then is a correlation value between that of the self-excited forces and that of the buffeting forces.

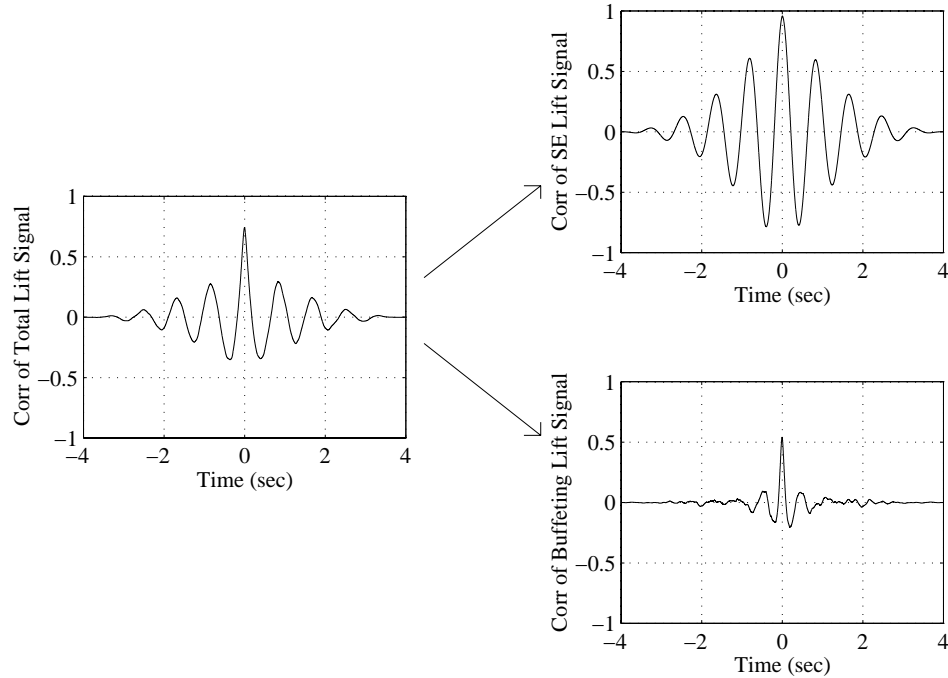


Figure 8-13 Cross correlation functions for the total, self-excited, and buffeting components of lift for  $U_r = 20$  in Case 12b flow at a separation of  $\Delta y = 1.2B$ .

The spanwise cross correlations presented in Chapter 7 were recalculated here to examine the behavior of the two components separately. Figure 8-14 through Figure 8-19 show the spanwise cross correlation coefficients (at  $\tau = 0$ ) for the buffeting components of the lift and moment signals compared with the correlation values computed for the stationary model. Figure 8-14 through Figure 8-16 present the correlations of  $L_b(t)$  for reduced velocities of 3.1, 8, and 20. Figure 8-17 through Figure 8-19 present  $M_b(t)$  correlation values for the same reduced velocities. The correlation values for  $L_b(t)$  and  $M_b(t)$  on the oscillating models were exceptionally close to those found for the stationary models. In some cases the oscillating model buffeting correlation was somewhat higher than that for the stationary model (for one example, see Figure 8-17).

Sources of such mismatches may include the effects of harmonics of the model oscillation frequency that were not removed in the splitting analysis, reduced velocity effects (discussed later in this chapter), or spurious correlation induced by non-aerodynamic effects (as discussed in Appendix A). The overall matches, however, are quite good suggesting that the correlation structure for the broad band buffeting components is essentially the same as that for the stationary cylinder.

Trends of the total signal correlation values on oscillating models (presented in Chapter 7) showed that increasing turbulence intensity and increasing turbulence scale decreased the spanwise correlation. The results of this splitting analysis have shown that, just like the behavior of the stationary cylinder buffeting forces, the correlation values between buffeting components acting on the oscillating cylinder increase with increasing turbulence scale. The next logical step was to examine the correlation between the self-excited components of the aerodynamic forces.

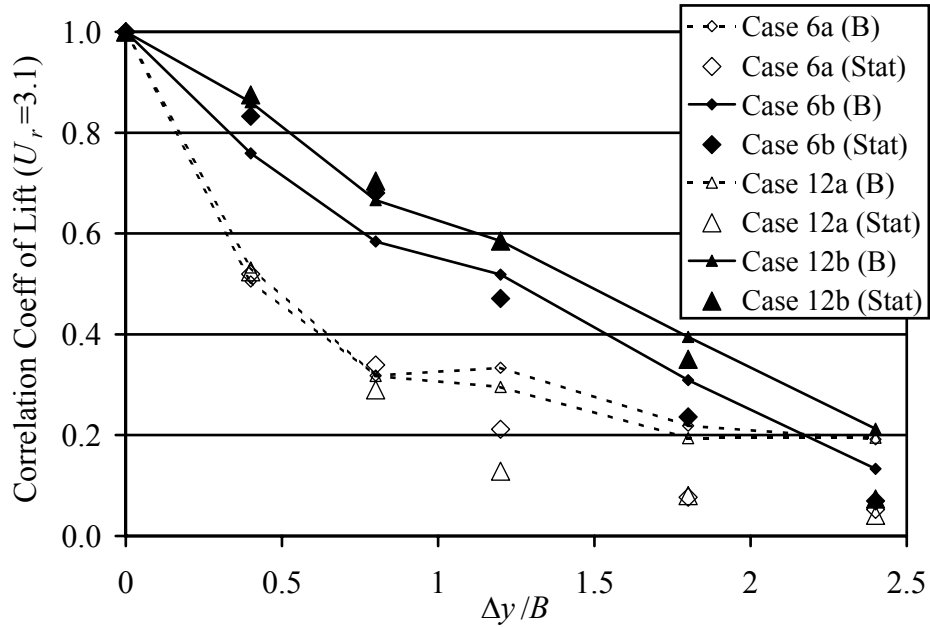


Figure 8-14 Cross correlation coefficients ( $\tau = 0$ ) of stationary model lift (Stat) and of the buffeting components (B) of lift with the model oscillating at  $U_r = 3.1$ .

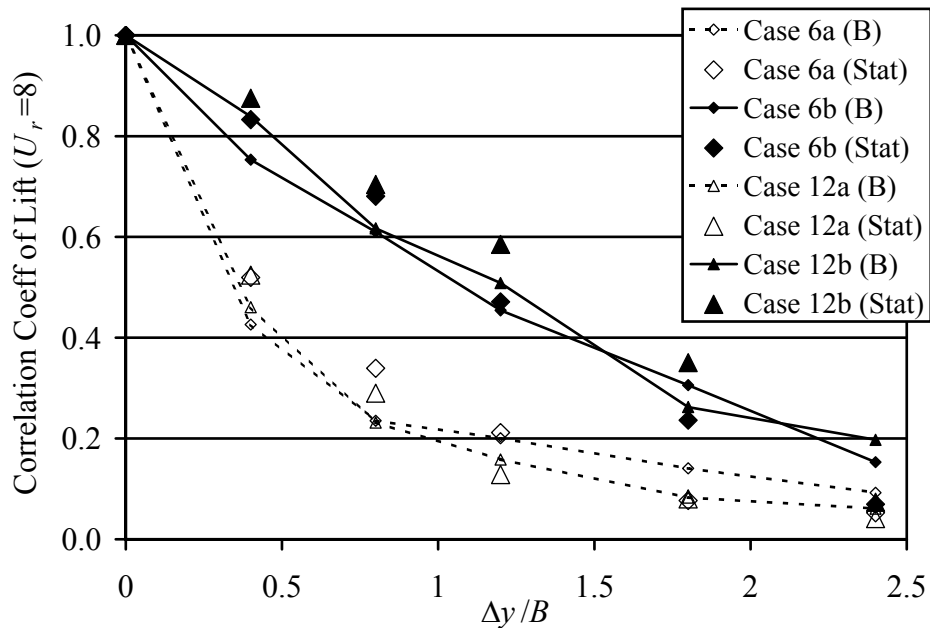


Figure 8-15 Cross correlation coefficients ( $\tau = 0$ ) of stationary model lift (Stat) and of the buffeting components (B) of lift with the model oscillating at  $U_r = 8$ .

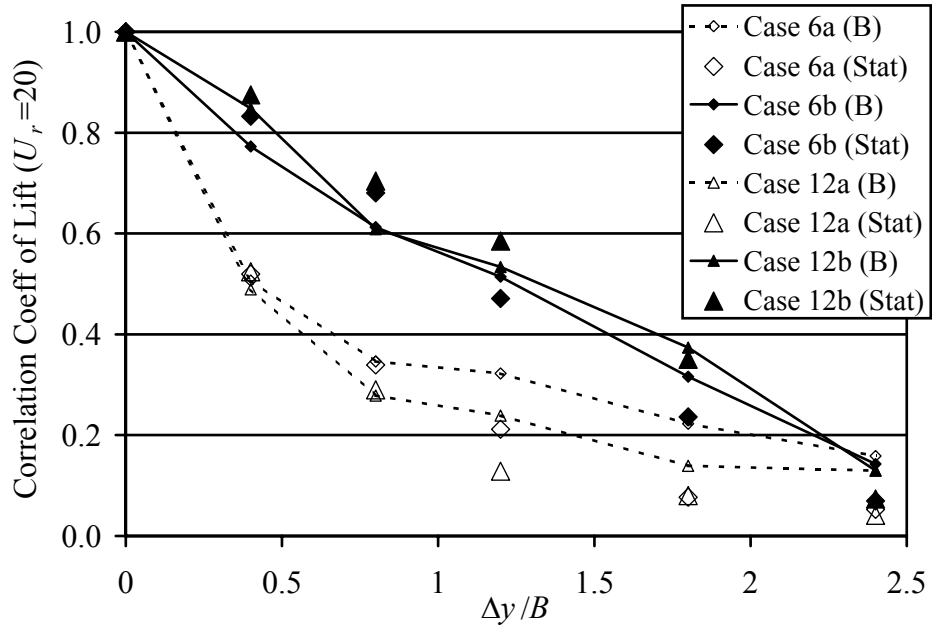


Figure 8-16 Cross correlation coefficients ( $\tau = 0$ ) of stationary model lift (Stat) and of the buffeting components (B) of lift with the model oscillating at  $U_r = 20$ .

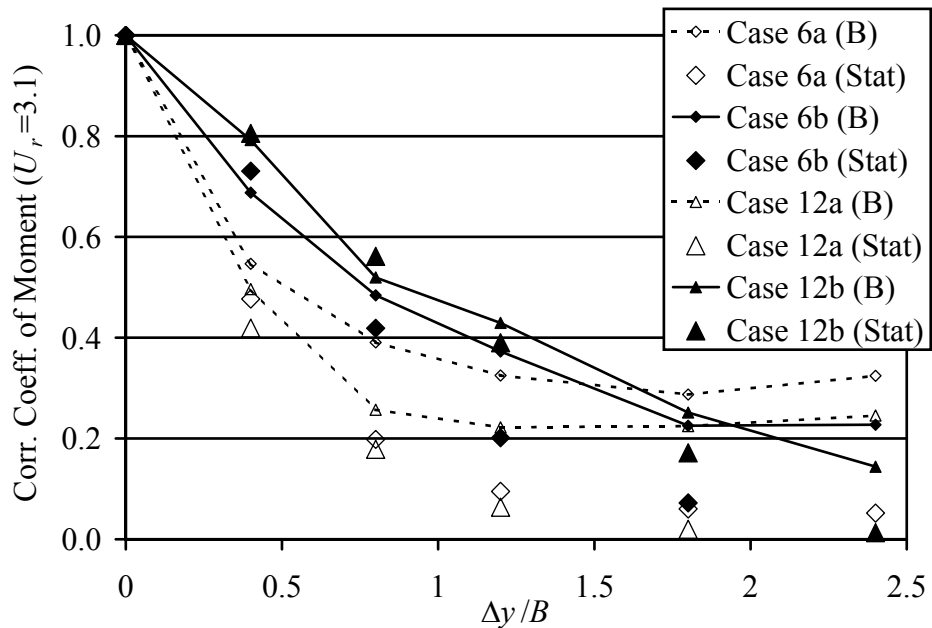


Figure 8-17 Cross correlation coefficients ( $\tau = 0$ ) of stationary model moment (Stat) and of the buffeting components (B) of moment with the model oscillating at  $U_r = 3.1$ .

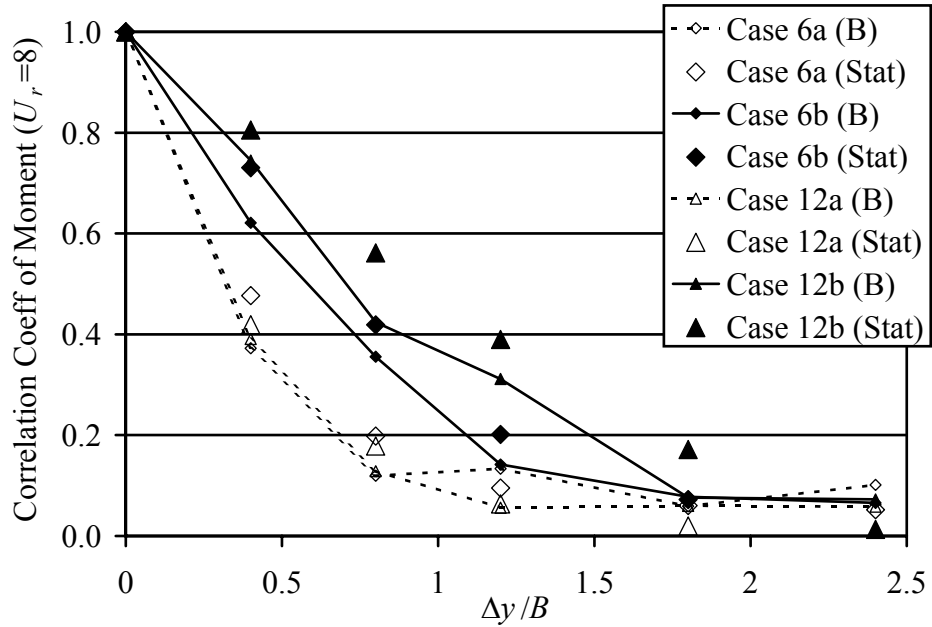


Figure 8-18 Cross correlation coefficients ( $\tau = 0$ ) of stationary model moment (Stat) and of the buffeting components (B) of moment with the model oscillating at  $U_r = 8$ .

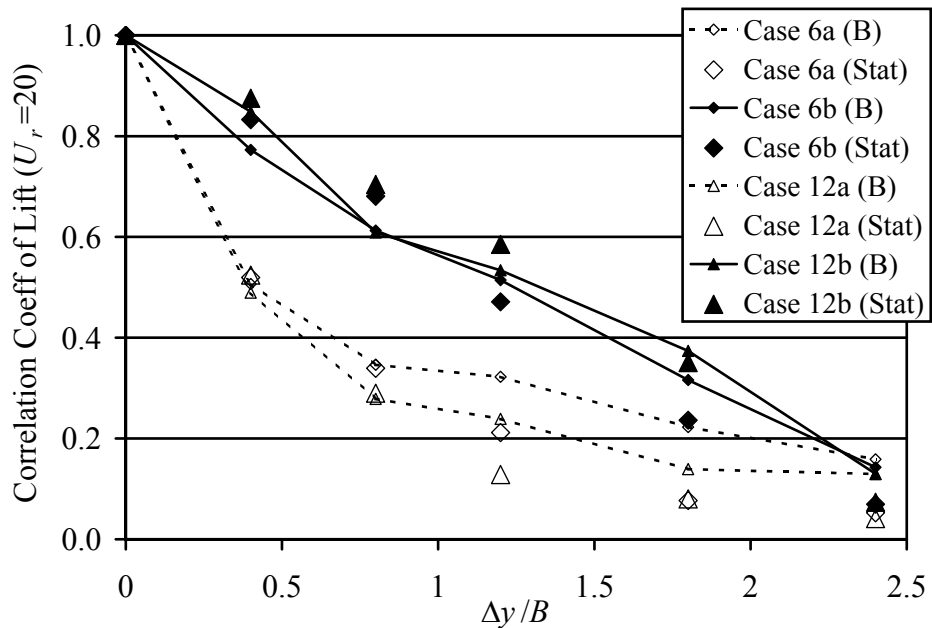


Figure 8-19 Cross correlation coefficients ( $\tau = 0$ ) of stationary model moment (Stat) and of the buffeting components (B) of moment with the model oscillating at  $U_r = 20$ .

Calculating cross correlation functions between the self-excited components of the lift and moment forces resulted in values above 0.96 for every incident flow, every reduced velocity, and nearly every separation. Only in two cases of  $\Delta y = 2.4B$  did the correlation value get below 0.96 to a value of 0.90. Figure 8-20 shows an example of the self-excited correlation values for  $U_r = 20$ . The general shape of this plot is typical of each case. Although the cases with larger turbulence scale showed a slightly lower correlation than those of smaller scale, the estimated 95% confidence intervals of  $\pm 0.03$  put all the values within the statistical spread of the others.

From these results it is clear that the self-excited forces are highly correlated in the spanwise direction. Experimental models with far greater aspect ratio (defined as span length,  $L$ , to deck width,  $B$ ) will be needed to identify how far such a high correlation can be sustained. The model studied here had an aspect ratio of only  $L/B = 4.2$ . Long span bridges, obviously, have much greater aspect ratios—for example, the ratio of the center span to the deck width of the Akashi-Kaikyo Bridge is 56. This correlation deserves further attention.

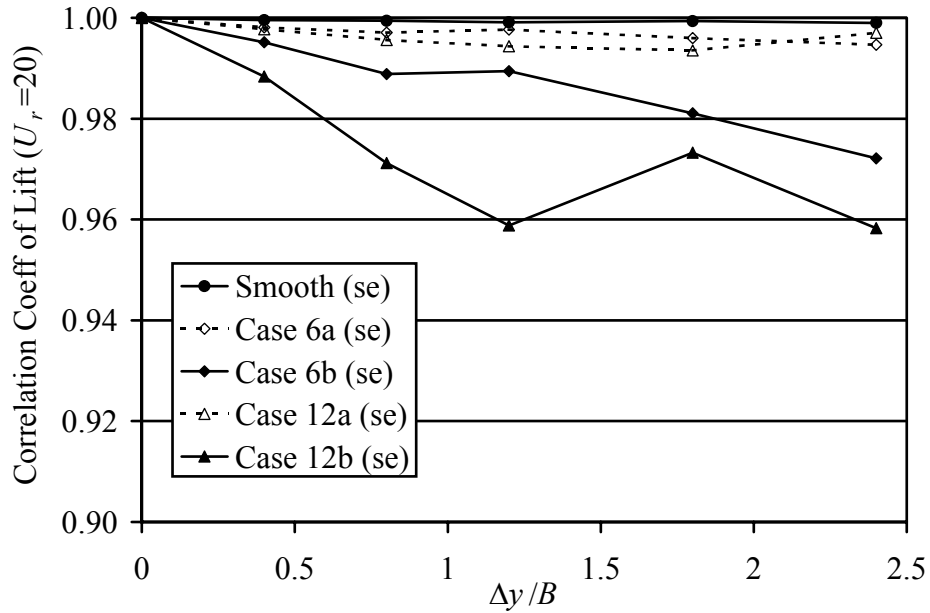


Figure 8-20 Cross correlation coefficients ( $\tau = 0$ ) of the self-excited components (se) of lift with the model oscillating at  $U_r = 20$ .

### 8.2.2 Comparison of Velocity and Pressure Correlation

An important factor in the prediction of the aerodynamic response of long-span bridges is the relation between the correlation of incident turbulent flow and the correlation of the resulting aerodynamic forces. Figure 8-21 presents a comparison of the spanwise correlation of the  $w$  component of velocity and the buffeting component of lift for  $U_r = 8$ . The vertical component of velocity was included in the comparison because its contribution to buffeting is far more significant than that of the longitudinal component. Two facts are obvious from the figure. Larger incident turbulence scales produce larger spanwise correlation of the lift, and the lift force has a significantly higher spanwise correlation than the turbulent flow. For Case 6a flow at a separation of

$\Delta y = 0.4B$ , the correlation value of the lift was 2.5 times that of the incident flow. The larger turbulence scale of the Case 6b flow resulted in greater lift correlation and a similar lift correlation to flow correlation ratio of 2.3. Figure 8-22 shows a comparison between flow and lift correlation values for Case 12 flows. For this greater turbulence intensity, the correlation of the buffeting component of lift was similar to that of Case 6. Again, the lift was correlated far better than the incident flow.

As discussed in section 8.2.1, the buffeting correlation values plotted in these two figures are very similar to those of the stationary model tests. Comparing the velocity correlation with the buffeting correlation for stationary tests or for other reduced velocities would show similar results. The important point here is that buffeting response predictions incorporating strip assumptions will be inadequate. The strip assumption assumes that the correlation of forces on the bridge deck are the same as the correlation of the incoming flow. As discussed in previous chapters, a number of researchers have recognized and reported the fact that aerodynamic forces are more highly correlated than incident turbulence on stationary bridge models (Larose et al., 1993; Sankaran & Jancauskas, 1993; Kimura et al., 1996; Larose & Mann, 1998). Results of this study support this observation even for the buffeting components of forces on oscillating bodies.

The spanwise correlation scale of the self-excited forces, however, was far larger than any velocity correlation scale. Only the body motion itself was correlated on the same order as the self-excited forces.

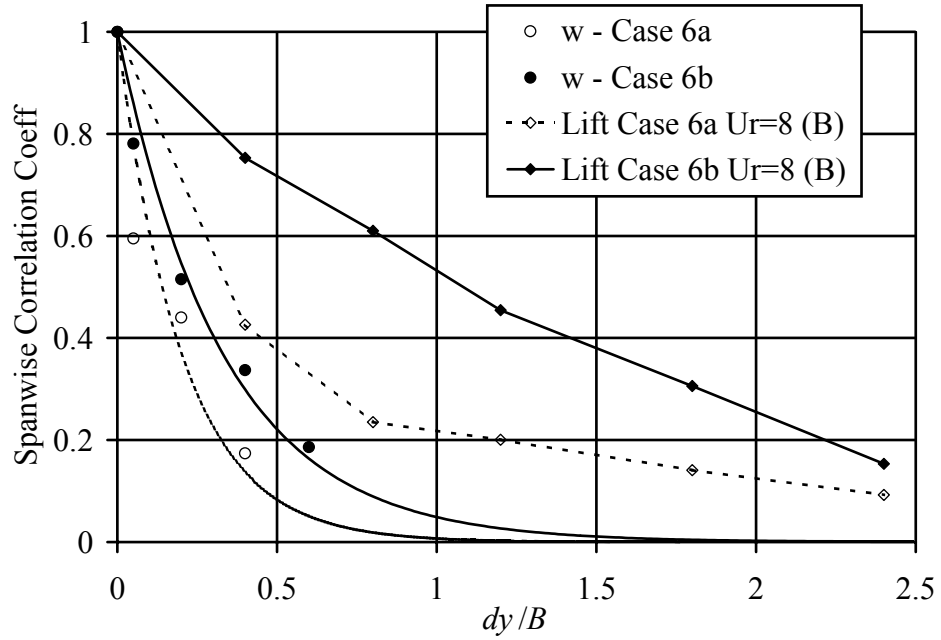


Figure 8-21 Spanwise correlation, in Case 6 flows, for both the  $w$  component of velocity and the buffeting component of lift for  $U_r = 8$ .

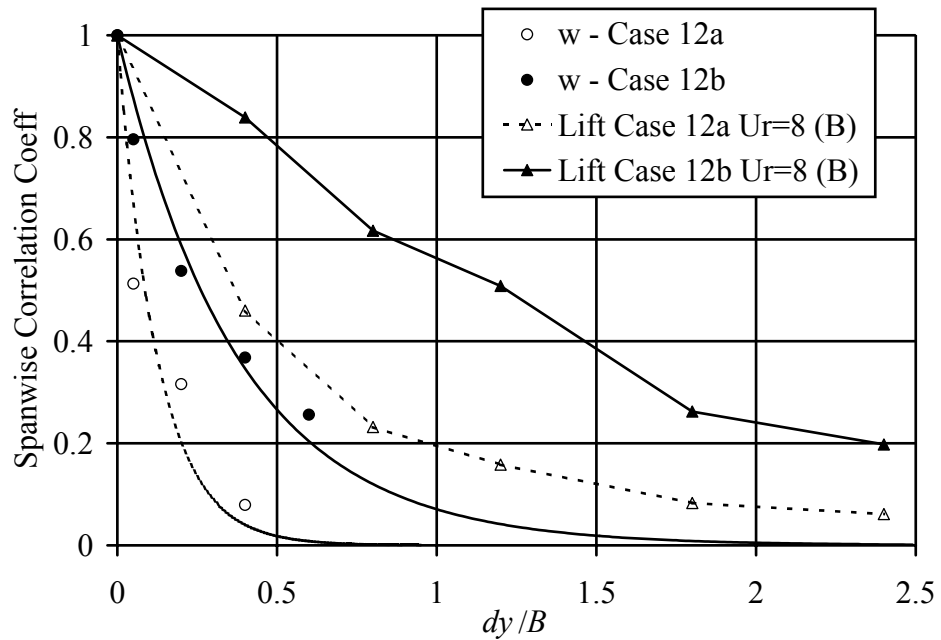


Figure 8-22 Spanwise correlation, in Case 12 flows, for both the  $w$  component of velocity and the buffeting component of lift for  $U_r = 8$ .

### 8.2.3 Reduced Velocity Dependence

In Chapter 7, the spanwise correlation values for the lift and moment were presented. When examining the spanwise correlation scales as a function of reduced velocity, it was observed that the maximum correlation scales occurred between  $U_r = 3.1$  and  $U_r = 8$ . Although the split analysis of the self-excited and buffeting forces presented in section 8.2.1 may suggest that the broad band buffeting correlation is the same as stationary model correlation and the self-excited forces are nearly perfectly correlated, this cannot explain the reduced velocity dependence. Potential physical explanations for this are discussed in this section.

A number of researchers investigating vortex-induced oscillations have found the spanwise correlation of both surface pressures and wake velocities to be dependent on the reduced velocity and the oscillation amplitude (for square section cylinders: Bearman & Obasaju, 1982; Wilkinson, 1981; for circular cylinders: Toebes, 1969). Spanwise correlation attains a maximum for reduced velocities for which the body experiences lock-in. “Lock-in” refers to that phenomenon where the vortex shedding frequency is “captured” by a mode of a structure which has a frequency close to that of the structure’s natural vortex shedding frequency. This natural shedding frequency is usually given in terms of the Strouhal number,  $St = fD/U$  (where  $f$  is the natural vortex shedding frequency,  $D$  is a characteristic dimension of the body, and  $U$  is the free stream velocity). This capturing means that for a range of  $U_r$  near  $1/St$  vortices are shed at the body’s oscillation frequency rather than at the frequency determined by the Strouhal number. Spanwise correlation of both pressure and wake velocity fluctuations reach

maximum values for  $U_r$  within the lock-in region. The magnitudes of these maximum values increase with greater oscillation amplitudes.

For the pitching rectangular cylinder in the experiment considered here, both  $U_r$  and oscillation amplitude must be considered with respect to the maxima in spanwise correlation. Normalized cross correlation coefficients for lift (for  $\tau = 0$ ) at a spanwise separation of  $1.2B$  are shown in Figure 8-23. The values for moment correlation at the same separation are shown in Figure 8-24. The reduced velocity dependence of the pitching oscillation amplitude (as shown in Chapter 3) is somewhat similar to that of spanwise correlation. Because of the dependence of spanwise correlation on oscillation amplitude, this may explain some of the change with reduced velocity. However, the decrease in the spanwise correlation of lift and moment for  $U_r = 3.1$  probably cannot be explained purely in terms of oscillation amplitude. Some discussion of the dynamics of the shear layer may be pertinent as well.

Discussing the spanwise correlation improvement on square section cylinders due to oscillation, Wilkinson (1981) pointed out that the nonlinear nature of the phenomenon is illustrated by the decrease for increasing frequency. Without some interaction with the shear layer, the added mass contribution to the dynamic pressure—which increases monotonically with frequency—would continue to increase the spanwise correlation as frequency increases. This does not happen. For reduced velocities less than that at the spanwise correlation peak (i.e. for frequencies greater than that at the spanwise correlation peak), the spanwise correlation decreases.

Some explanation of this decrease may be found by considering the shear layer behavior and the work of Sigurdson (1995) with *acoustically* excited shear layers.

Observations of the power spectral density plots of the pressure signals along the streamwise direction for both the stationary model tests and the oscillating model tests (in Chapter 6) reveal a low-frequency peak near 3.2-3.4 Hz. When scaled as  $F_{shed} D/U \approx 0.02$ , this frequency is comparable to that of the large-scale unsteadiness observed by Cherry et al. (1984) and Kiya & Sasaki (1983a). The reduced velocity of this unsteadiness is  $U_r = U/F_{shed} B \approx 6.7$  which is in the range for which the maximum spanwise correlation values occur for the current tests. Exciting the shear layer with forced oscillations near the reduced velocity of this large-scale shedding may cause behavior similar to that observed in vortex-induced vibration problems—that is, natural shedding mode of the structure is enhanced by the oscillation increasing the organization of the shedding and increasing the spanwise correlation.

Working with a flat-faced, circular cylinder aligned coaxially with the free stream, Sigurdson (1995) considered two instabilities relevant to the separated shear layer. The first was the Kelvin-Helmholtz instability, to which all free shear layers are subject, and the second was similar to Karman vortex shedding—having a lower frequency than the first. Exciting the shear layer near the frequency of the second instability caused increased the shear layer entrainment and caused reattachment to occur closer to the leading edge—phenomena also associated with the effects of free stream turbulence.

To find a scaling for the frequency of this instability, the hypothesis used was that the instability is “*like* Karman vortex shedding from a cylinder but the vortex interaction is with *image* vortices due to the wall rather than *actual* ones” (Sigurdson, 1995). Building on this concept, a scaling for the frequency was suggested similar to that

proposed by Roshko (1955) for vortex shedding from cylinders of different shapes.

Sigurdson's scaling is:  $F_{shed}h/U_s$  where  $F_{shed}$  is frequency (in Hz) of the shedding of vortices from the leading edge shear layer,  $h$  is height of the separation bubble, and  $U_s$  is the separation velocity. Similar to Roshko's scaling,  $h$  corresponds to half the distance between the vorticity of a shear layer and its counterpart of opposite sign. This scaling has a value near 0.08 for a surprisingly large number of different configurations including blunt flat plates, backward-facing steps, and the cylinders like those of Sigurdson's work.

It should be noted here that the instability studied by Sigurdson is of higher frequency than that of  $U_r \approx 6.7$  discussed for this project. To determine if perturbations at appropriate frequencies will enhance the entrainment and organization of this lower frequency shedding mode as for that of Sigurdson, of course, data from a greater number of reduced velocities near the range of  $4 < U_r < 8$  is necessary. Unfortunately, the design problems with the dynamics of the model's flexible couplings prohibited further study in this  $U_r$  range for this project.

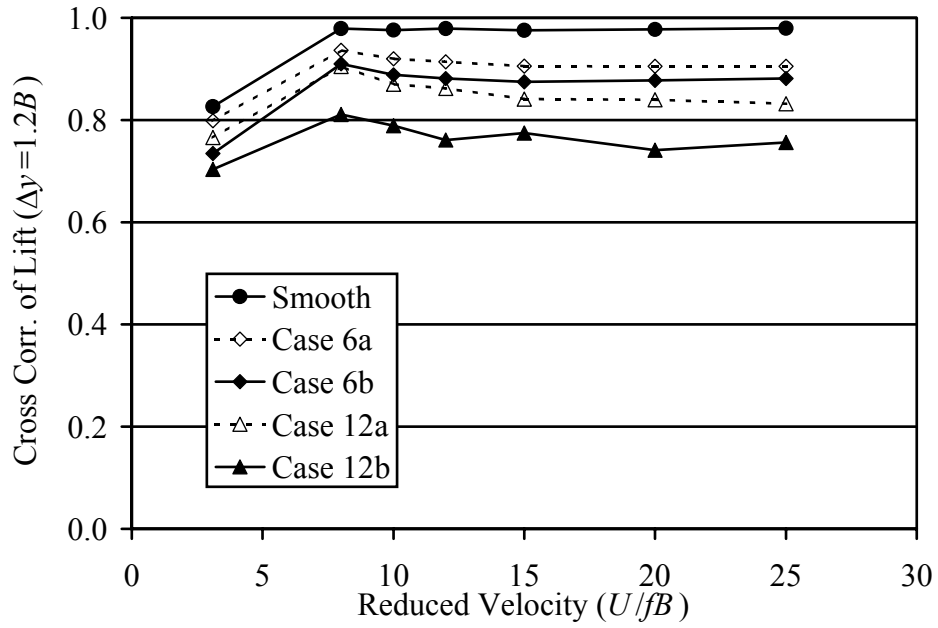


Figure 8-23 Normalized cross correlation coefficients for lift at a spanwise separation of  $\Delta y = 1.8B$ .

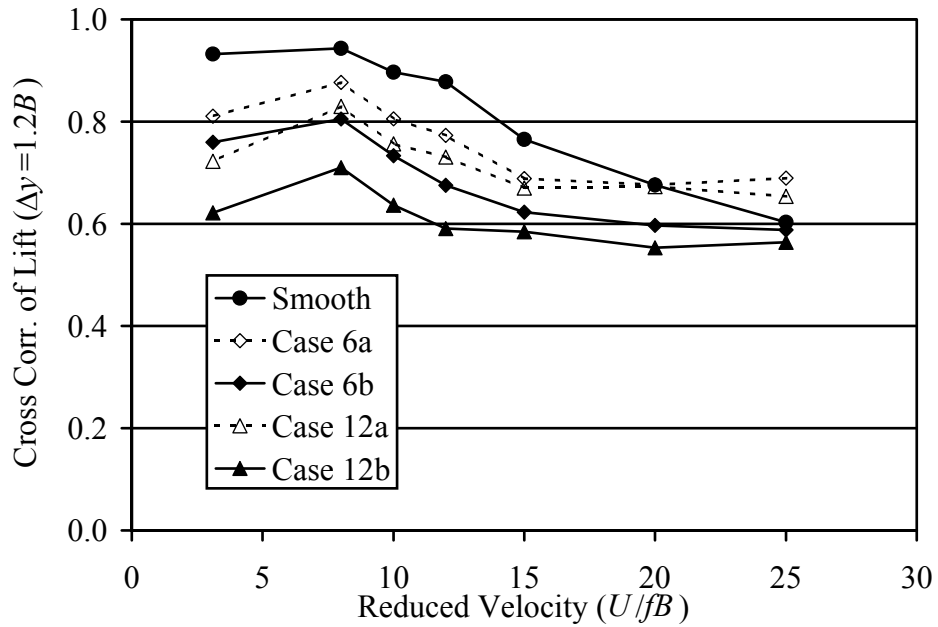


Figure 8-24 Normalized cross correlation coefficients for moment at a spanwise separation of  $\Delta y = 1.8B$ .

## CHAPTER 9. CONCLUSIONS AND RECOMMENDATIONS

A brief summary is provided here of the accomplishments and results of this research. After putting these results in the context of the current state of the art of long-span bridge aerodynamics, a few recommendations for further work on this topic are suggested.

### 9.1 Conclusions

A new test rig was designed and built for the experimental study of bridge aerodynamics using section models. The current research effort studied self-excited and buffeting forces on a model of rectangular cross section forced to oscillate in torsion. The apparatus was designed for future experiments as well. Its capabilities include combined pitching and plunging motion, amplitude variation, and mean angle of attack variation.

Grid generated turbulence was used to study the effects of both turbulence intensity and turbulence scale on aerodynamic forces. The results of this research have important ramifications for the current state of the art of aerodynamic analysis of long span bridges. By examining the unsteady pressure distributions over the bridge model rather than the flutter derivatives alone, a clearer understanding of how turbulence affects the unsteady forces was obtained. Both increasing turbulence intensity and increasing turbulence scale decreased the amplitudes of self-excited pressure fluctuations. The basic shape of the chordwise distributions of pressure amplitude—a single hump shape—

shifted upstream with increasing intensity of the free stream turbulence. This shift, however, was only slightly affected by the turbulence scale.

Phase values of the self-excited pressure (with respect to the body motion) was found to have several regimes in the streamwise direction. Near the leading edge, phase was nearly constant. Downstream of this region was a region where phase increased rapidly. Beyond this rapidly increasing phase zone was a region where the phase values leveled off and even decreased in some cases. While scale had little discernible effect on this phase value, turbulence intensity shifted the region of rapidly increasing phase toward the leading edge.

The stabilizing effects of turbulence observed in the flutter derivatives were related to these turbulence-induced shifts in the pressure amplitude and phase distributions. By tracking the integrands of expressions for lift and moment, specific changes in pressure amplitude and phase were linked to flutter derivative modifications. In addition, this upstream shifting in the unsteady pressure on the oscillating models was found to be similar to the behavior observed for pressure distributions over stationary models. This suggests that the vast amount of research done in bluff body aerodynamics on stationary bodies can aid in the understanding of oscillating body problems as well.

To the author's knowledge, prior to this study no experimental study had justified the conventional analysis technique in which the aerodynamic forces are separated into flutter and buffeting components. Pressure measurements made on oscillating models allowed an experimental assessment of this assumption. Overall, the assumption is quite close. Examination of the lift and moment spectra showed close agreement throughout the frequency range considered. Where the stationary and oscillating model spectra did

not agree, however, the oscillating model values were larger. This oscillation-induced increase in the broad band energy occurred mainly for frequencies above  $fD/U = 0.1$  although some differences were observed for lower frequencies as well.

Quantitative analysis of these differences showed that oscillating model buffeting forces could have rms values as much as 10% higher than their stationary model counterparts. This difference decreased for increased turbulence intensity and increased turbulence scale. For Case 12b, the flow with the highest intensity and scale considered, these differences were only around 2-3%. Observation of the streamwise distribution of such differences revealed that the location of oscillation-induced broad band increase was upstream of reattachment—for this case, this meant upstream of the location of the maximum rms pressure value. This implies that bodies which experience separation over smaller portions of their surface may exhibit less significant differences between stationary and oscillating model buffeting levels.

Through both coherence measurements and correlation calculations of self-excited force components, the self-excited forces were found to have near unity coherence over the entire spanwise separation range considered. The conventional assumption of self-excited forces being fully correlated in the spanwise direction was thus supported by the results of this study. Of course, this also means that the often-suggested hypothesis that a decrease in spanwise correlation of the self-excited forces causes the turbulence-induced increase in the critical flutter velocity was not supported by the current results. A conclusive investigation of self-excited force coherence would require much longer span lengths to observe whether appreciable changes occur for longer spanwise separations.

Coherence calculations also showed that the broad band coherence of the oscillating model matched that of the stationary model to within the uncertainty of the experiment. This supports current analytical practice as well. Extracting the buffeting components of the oscillating model forces for calculation of buffeting correlation on oscillating models also showed close matches between stationary and oscillating model results.

## 9.2 Recommendations for Future Work

Recommendations for future work include expanding the parameter ranges of the current project, considering additional techniques for studying the specific problem of the current project, and then improving the facilities and equipment.

An important parameter limit in this study was the maximum spanwise separation,  $\Delta y = 2.4B$ . The important finding of near unity correlation of the self-excited forces deserves study for larger separation values. Because the correlation and coherence values did not drop significantly from unity over the separations tested, conclusive estimates of spanwise correlation lengths scales were impossible. The hypothesis that the stabilizing effects of turbulence on three-dimensional structures is due, at least in part, to turbulence-induced drops in the spanwise correlation of the self-excited forces is an important concept in the current understanding of turbulence effects. The work of this study should be extended to determine whether this hypothesis holds.

Larger ranges of turbulence scales should also be tested. As discussed in Chapter 1, the effects of turbulence scales are not fully understood. While adding to the overall picture, the work of this study included only scale values less than  $1.0B$ . Future work

should include larger scales—most likely produced with active turbulence generation techniques—to identify whether the trends with scale observed in this project continue to increase or begin a return to behavior associated with smooth flow. As discussed previously, for some parameters such as mean pressure on stationary bodies, increasing turbulence scale beyond a certain point causes a reversal of trends back toward smooth flow results. This has been attributed to the fact that flows of very large integral scale behave more like flows with a slowly-varying mean velocity without the capability to alter the shear layer structure. Whether similar behavior exists for the self-excited forces studied here is an issue worthy of further study.

Additional information concerning the physical mechanisms of the observed turbulence effects would be gained doing velocity measurements in and around the separated shear layers. Hot wire anemometry or laser Doppler anemometry could be used to identify the structural changes the shear layer experiences with changes in turbulence characteristics. Specifically, the nature of the streamwise evolution of pressure phase could be studied with velocity measurements above the model surface.

Part of the purpose of this study was to establish a facility for testing section models of bridges in turbulent flows. With this accomplished, future work must include actual bridge deck shapes. These shapes should include generic and existing bridge deck shapes as well as sections for potential use in the super long span designs in development around the world. Future work with this facility should include tests both of turbulence effects and of the nonlinear effects (such as aerodynamic force dependence amplitude and mean angle of attack) which play an increasingly important role as bridge span

lengths increase. In addition to testing for various nonlinear effects, future testing should include the heaving degree of freedom as well as the torsional motion.

An additional consideration concerning testing of different bridge deck shapes is that of the mismatch measured here between stationary and oscillating body buffeting forces. This mismatch should be studied for actual bridge decks to determine the impact of any mismatch on engineering design. While the general trends of this work imply that more streamlined bodies and bodies experiencing more intense turbulence will have less significant mismatch, this issue warrants further attention.

## APPENDIX A. PRESSURE MEASUREMENT PROCEDURES

Calibration of the pressure measurement system included two phases, static and dynamic. A static calibration was performed for the pressure to voltage relations for each pressure transducer. Dynamic calibrations included estimating the dynamic pressure response of the tubing system, which connected the transducers to the pressure taps on the surface of the model, and estimating the acceleration response of the sensors and the tubing. The dynamic calibration efforts also covered several issues related to electrical noise effects on pressure correlation and coherence calculations. This appendix describes the transducers themselves, each of the calibration procedures in turn, and the techniques for identifying the actual pressure signals using these calibrations.

### A.1 Pressure Transducers

Two types of transducers were used in this study. Honeywell Microswitch sensors (model 163PC) with a range of 620 Pa were used with the Pitot-static probes, and SenSym transducers (model ASCX01DN) with a range of 6900 Pa were employed for use inside the model. Both types measure differential pressures, are temperature compensated, and have onboard voltage amplification. These transducers are piezoresistive devices—essentially strain gage sensors in which the strain gages are fabricated within silicon wafers using techniques common to the semiconductor industry (Honeywell, 1995; SenSym, 1996). The model ASCX01DN devices used have a range is

6900 Pa with a nominal sensitivity of 0.65 mv/Pa. Because the sensitivity is ratiometric to the supply voltage, it was increased to nominally 1.6 mv/Pa using a supply voltage of approximately 10.0 v.

To power the 64 pressure sensors used in this study, a separate power supply was constructed which provided voltage to each unit. Power regulation circuitry was then built for each transducer to ensure clean voltage supply—not affected by fluctuations due to other transducers. Each transducer was mounted on a small circuit board containing this regulation circuitry. All signal connections from these sensor-circuit units to the data acquisition system were shielded.

Pressure taps on the surface of the model were connected to the pressure sensors with Tygon tubing. To facilitate changing which taps were connected to sensors, each tap was fitted with a short stainless-steel tube to which the Tygon tubing was connected. Connecting the tubing to the transducer connectors required a special fitting made with a small stainless-steel tube and tubing of different diameters. All of these connectors are shown in Figure A-1 below. As discussed in Chapter 3, the large number of pressure tubes—a signal and a static line for each transducer made 128 tubes—inside the model made it difficult to avoid crimping the pressure lines when replacing the model's top surface. Rarely was the cover of the model closed without cutting off at least one or two pressure lines. The absence of the signals from these blocked lines was compensated for by either ignoring the entire distribution containing the bad signals or by interpolating between adjacent signals.

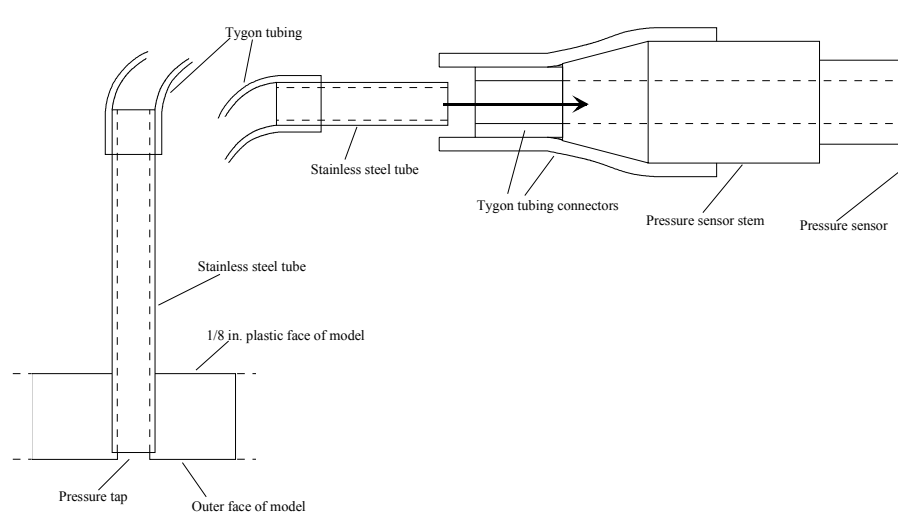


Figure A-1 Schematic diagram of the connectors used for connecting the plastic tubing to both the pressure taps on the surface of the model and the pressure transducers themselves.

## A.2 Static Pressure Calibration

Static calibration was conducted with the setup shown in Figure A-2 below. A plenum chamber was connected to a MityVac hand pump device. This provided a reference pressure that was connected to both a reference manometer and the model's pressure transducers. The reference manometer was a Betz Micromanometer Model 2500 (the specifications for this manometer are shown in the list of known bias and precision errors in the uncertainty calculations of Appendix D). The reference pressure for the calibration was delivered to each pressure transducer through the static pressure supply lines so that the sensors could be calibrated while the model was mounted in the wind tunnel. Power supply to each transducer and voltage acquisition from each transducer

was arranged exactly as in actual tests. The only difference between calibration and experiment was in how pressure would be generated.

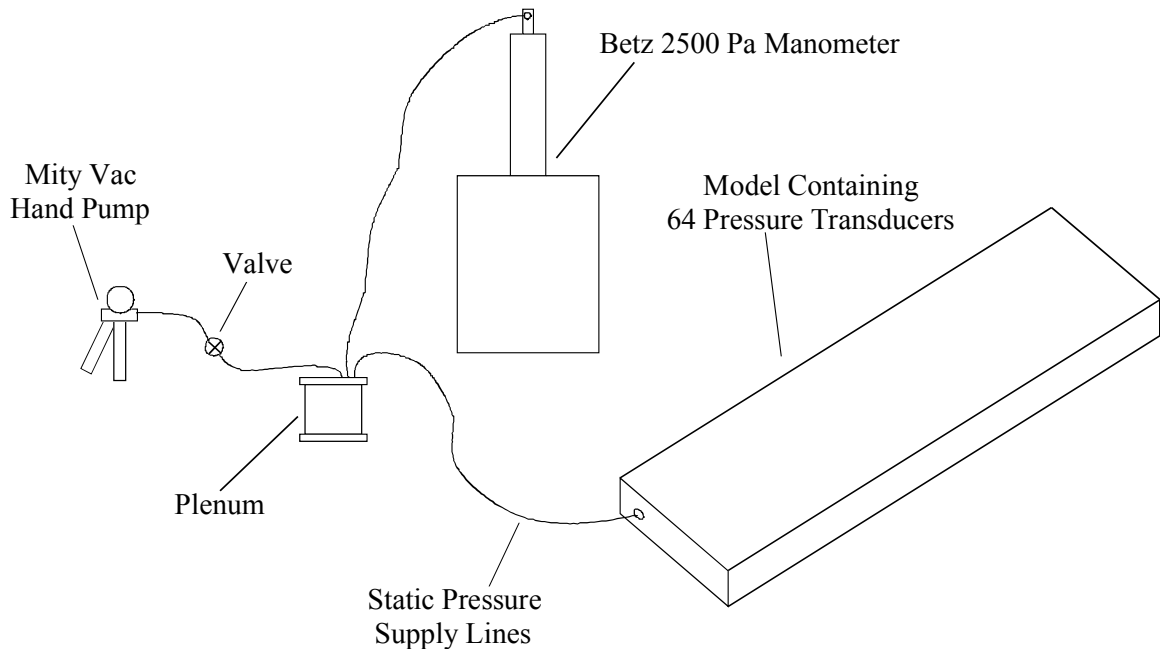


Figure A-2 Setup for static calibration of pressure transducers.

For each pressure set by the hand pump, the Betz manometer was read while the computer recorded transducer voltages for 32.8 seconds (16384 total samples at a sampling frequency of 500 Hz). The mean and rms values of transducer voltages were calculated from the measurements to obtain precision error estimates. The pressure range through which the transducers were tested covered 50% more than the estimated range to be experienced in actual tests. The largest possible negative peak pressures was estimated from the literature to be approximately  $8C_p$ , so testing up to  $11.6C_p$  was conducted. Figure A-3 shows a typical voltage versus pressure curve from this experiment. The entire pressure range was traversed several times with increasing pressure and decreasing

pressure to generate several points at each pressure value. The uncertainty analysis of this calibration process is described in Appendix D. A linear fit to these data rendered the function used to obtain pressures from the transducer voltages. Repetitions of these calibration experiments over a 10° F range of ambient temperature produced negligible changes in the slopes of these curves (less than 1%).

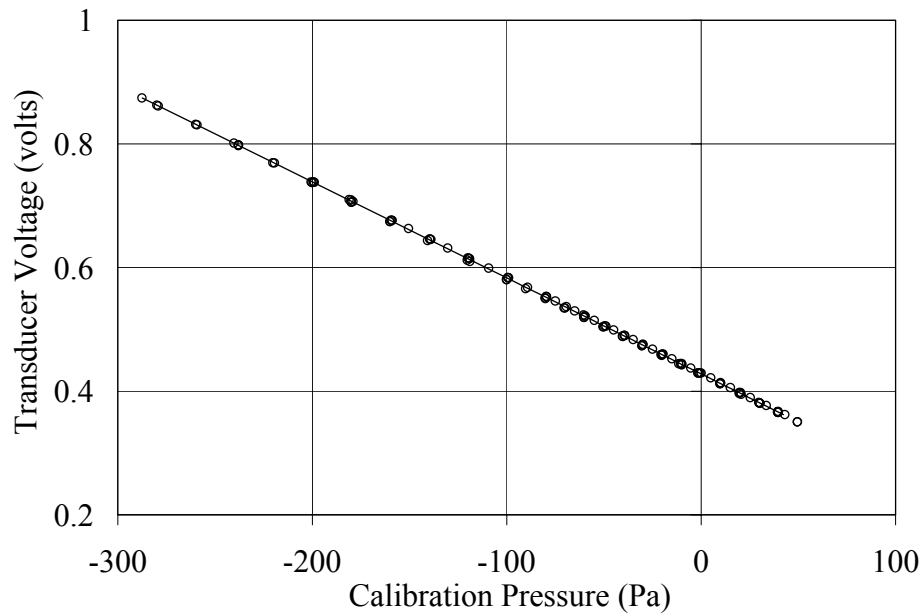


Figure A-3 Illustrative example of calibration data set for transducer voltage versus calibration pressure.

The piezoresistive design of the sensors gives them large dynamic ranges. The response time for a 0 Pa to full-scale pressure step change (given as 10% to 90% rise time) is specified as 100  $\mu$ s (SenSym, 1996). Since the dynamic range of the pressure fluctuations expected in this study was only around 500 Hz, a dynamic calibration was

assumed to be unnecessary. The frequency response of the sensor itself was assumed to be flat well beyond the range of the frequencies to be encountered.

### A.3 Dynamic Pressure Calibration

Dynamic calibration for this project involved two separate phenomena. The first dynamic calibration was performed to correct for the dynamic effects of the pressure tubing lines. The second calibration was an analytical study of how the air mass within a given pressure tube can induce pressure amplitudes and coherence with other pressure signals that have nothing to do with the aerodynamic problem being studied. Corrections for the dynamical response of the tubing was performed on all pressure signals, but the acceleration response analysis showed that no correction was necessary. Both studies are described in the following sections.

#### A.3.1 Pressure Tubing Dynamical Response

While dynamic calibrations were not necessary for the sensors themselves, the dynamic response of the tubing systems, which connect the pressure taps to the transducers, was examined. Because the characteristics of the pressures at the surface of the models are desired, the dynamic response added to the signals by the tubing must be eliminated. This requires two steps. The first is to quantify these effects, and the second is to mathematically remove the effects from the signals obtained by the computer.

To quantify the dynamic effects of the tubing, a calibration rig was constructed as shown in Figure A-4. This rig consists of a speaker with its electromagnetic “drive”

removed, an MB Dynamics Model PM 25 shaker, and a chamber with pressure ports. The shaker device drives the speaker from a signal input to the shaker's amplifier. A function generator supplied the input signals which consisted of series of swept sine wave functions. Swept sine waves were used rather than broadband signals because broadband signals failed to provide suitable coherence for the frequency response function. It is possible that this is due to the physics of the shaker-speaker system itself. The broadband excitation signals did not seem to be able to excite lower frequencies very well—particularly below 10 Hz.

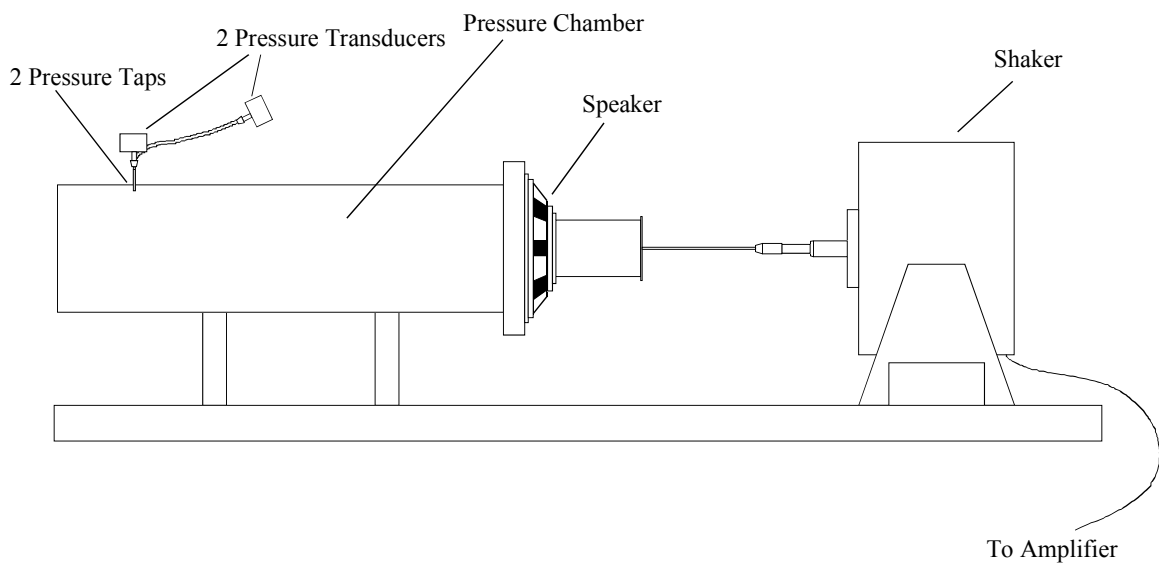


Figure A-4 Shaker and speaker equipment used for dynamic calibration of pressure system.

The swept-sine approach resulted in a frequency response function having good coherence only at the frequencies in the swept function. It was then necessary to run the swept-sine tests at multiple starting frequencies to fill in frequency bins. To generate the function in this form, a MATLAB code sorted through each frequency bin of each test's

results and extracted the frequency response function values only for frequencies with coherence greater than 0.999. The rest of the frequency bins were filled in by interpolation. Figure A-5 shows the completed frequency response function of the tubing used for every test in this project.

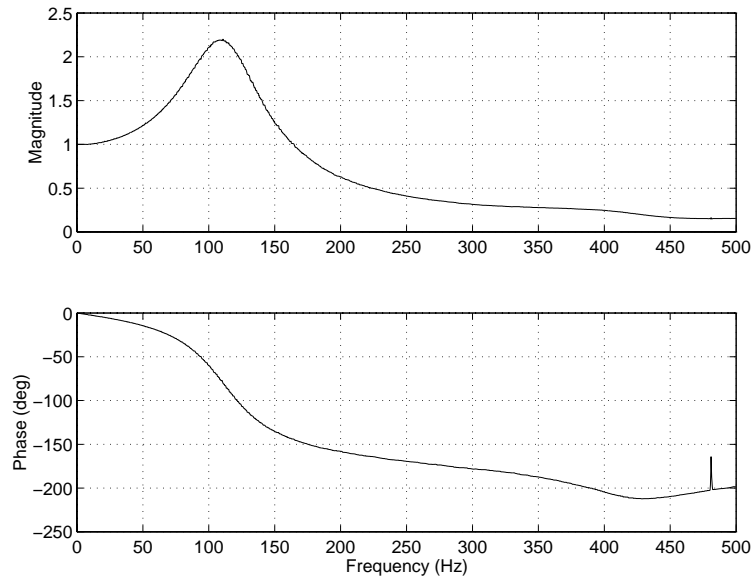


Figure A-5 Pressure tubing frequency response function,  $H_{tubing}(f)$ , as acquired with the swept-sine function approach.

Fast Fourier transform (FFT) techniques were used to remove the dynamic response of the pressure tubing from the pressure signals. This correction was performed up to a specified frequency,  $f_c$ , of 250 Hz. Above this frequency, the pressure signals neared the electrical noise level, and continuing to correct for pressure tubing effects above  $f_c$  would simply have amplified this ambient noise level. Such a correction required manipulation of the first and last  $N_c$  points of a given signal's discrete Fourier transform (where  $N_c = f_c/\Delta f$ ). Given the time series for a raw pressure signal,  $p_{raw}(t)$ ,

its Fourier transform,  $P_{raw}(f)$ , and the frequency response function of the tubing system,  $H_{tubing}(f)$ , the time series of the pressure signal corrected for the tubing was calculated as:

$$P(f_k) = \sum_{k=2}^{N_c+1} \frac{P_{raw}(f_k)}{H_{tubing}(f_k)} \quad (\text{A-1})$$

$$P(f_k) = \sum_{k=N-(N_c-1)}^N \frac{P_{raw}(f_k)}{H_{tubing}(f_k)} \quad (\text{A-2})$$

where  $f_k = (k-1)\Delta f$  is the frequency associated with  $k^{th}$  bin. For all the higher frequency components ( $f_k$  for  $k = N_c + 2$  through  $k = N - N_c$ ), no tubing correction was performed, i.e.  $P(f_k) = P_{raw}(f_k)$ . The time series of the corrected pressure signal,  $p(t)$ , was then obtained by performing an inverse fast Fourier transform (IFFT) on  $P_{raw}(f)$ .

### A.3.2 Acceleration Response of Air Mass in Tubing

When the model is in motion, both the air within the tubing system and the sensors themselves undergo acceleration. The voltage output of the pressure sensors includes components resulting from both of these sources. The response due to the former would not exist if the transducers were mounted flush with the model surface. Since flush mounting was not possible in this case, the magnitude of the response was investigated.

Other researchers have addressed this issue. Although no trustworthy experimental method of quantifying the acceleration effects exists, Obasaju (1977) and Bearman & Currie (1979) have derived an analytical correction for this acceleration response based on the model acceleration along the line connecting the model surface at

the pressure tap to the diaphragm of the pressure transducer. For an acceleration,  $\ddot{h}$ , in the direction of this line as shown in Figure A-6, these references give the induced pressure as:

$$p_a = -\rho\ddot{h}L \quad (\text{A-3})$$

where  $p_a$  is the pressure induced by the acceleration,  $h(t) = A\sin(\omega t)$  is the vertical motion of model (with dots signifying differentiation with respect to time),  $A$  and  $\omega$  are the amplitude and frequency of the motion, respectively.

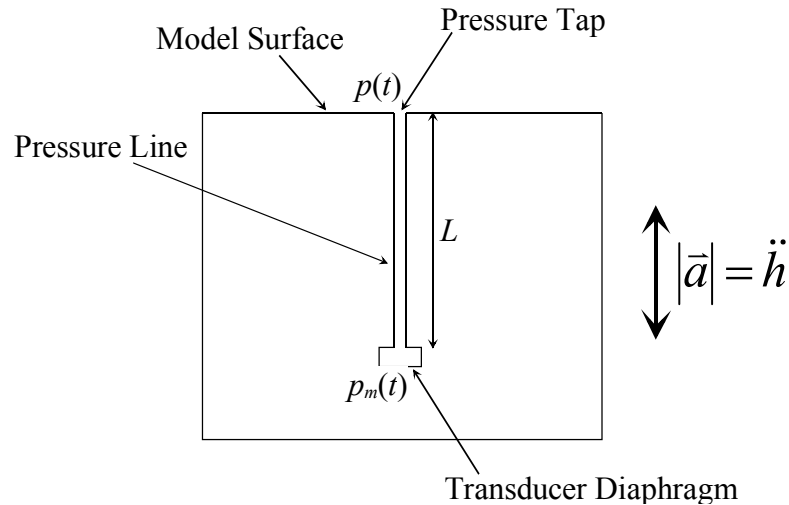


Figure A-6 Simplified sketch of a model with a pressure tap and transducer separated by a distance  $L$  and undergoing an acceleration  $\ddot{a}$ .

Rearranging equation (A-3) by substituting  $2\pi f$  for  $\omega$  and normalizing by the dynamic pressure to obtain a pressure coefficient yields the amplitude of the induced pressure coefficient:

$$C_{p_a}^* = 8\pi^2 AL \left( \frac{f}{U} \right)^2 \quad (\text{A-4})$$

This can be rearranged slightly to make it a function of reduced velocity as follows:

$$C_{p_a}^* = 8\pi^2 \frac{A}{B} \frac{L}{B} \left( \frac{fB}{U} \right)^2 = 8\pi^2 \frac{A}{B} \frac{L}{B} \left( \frac{1}{U_r} \right)^2 \quad (\text{A-5})$$

The equation relating the pressure at the model surface with that measured by the transducer is then:

$$C_p^* \sin(2\pi ft - \psi) + C_{p_a}^* \sin(2\pi ft) = C_{p_m}^* \sin(2\pi ft - \psi_m) \quad (\text{A-6})$$

where  $\psi$  is the corrected phase of the pressure fluctuations,  $\psi_m$  is the measured phase of the pressure fluctuations,  $C_p^*$  is the corrected amplitude of the pressure coefficient fluctuations,  $C_{p_m}^*$  is the measured amplitude of the pressure coefficient fluctuations, and  $C_{p_a}^*$  is the amplitude of the pressure fluctuation induced by the acceleration of the tubing.

Solving for the corrected values—the values corresponding to the pressure on the surface of the model—yields:

$$\psi = \tan^{-1} \left[ \frac{C_{p_m}^* \sin \psi_m}{C_{p_m}^* \cos \psi_m - C_{p_a}^*} \right] \quad (\text{A-7})$$

$$C_p^* = \sqrt{C_{p_m}^{*2} + C_{p_a}^{*2} - 2C_{p_m}^* C_{p_a}^* \cos \psi} \quad (\text{A-8})$$

The acceleration situation for the current work is more complex than that shown in Figure A-6. Figure A-7 shows the bridge model with an example pressure tap and transducer. Pitching motion will induce both vertical and horizontal acceleration—as shown with the vector  $\vec{a}$ —along the vector connecting the model surface to the transducer diaphragm.

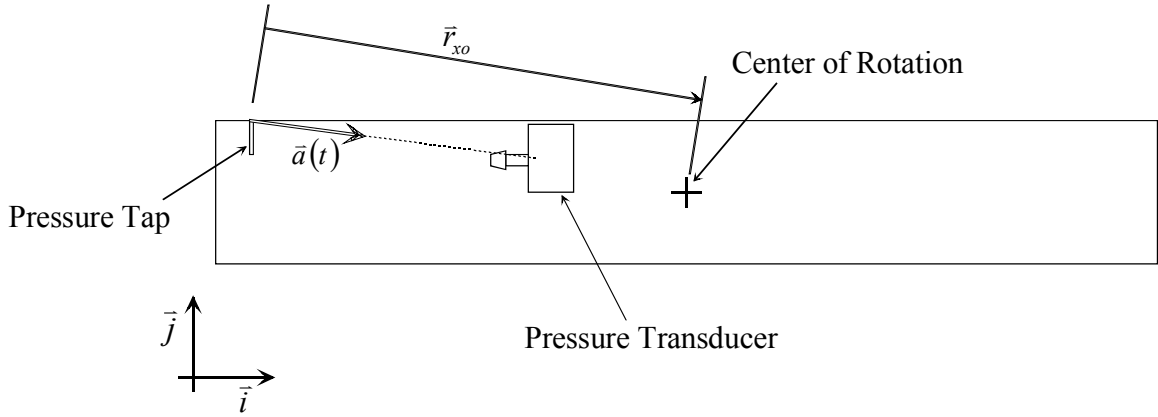


Figure A-7 Schematic diagram showing an example placement of a pressure tap and its corresponding transducer with an acceleration vector  $\bar{a}$  between them

For a pitching motion expressed as  $\alpha(t) = \alpha_0 \sin(\omega t)$ , the acceleration vector,  $\bar{a}$ , can be expressed as:

$$\bar{a}(t) = \ddot{\alpha}(t)\bar{k} \times \bar{r}_{xo} - (\dot{\alpha}(t))^2 \bar{r}_{xo} \quad (\text{A-9})$$

where  $\bar{r}_{xo}$  is vector connecting the pressure tap location to the center of rotation (it is approximated in this equation as being horizontal and as extending to the tap furthest from the center of rotation to give a worst-case estimate). Dividing equation (A-9) into components and dropping the  $(t)$  results in:

$$\bar{a} = (\ddot{\alpha}b \sin \alpha - (\dot{\alpha})^2 b \cos \alpha)\bar{i} + (\ddot{\alpha}b \cos \alpha + (\dot{\alpha})^2 b \sin \alpha)\bar{j} \quad (\text{A-10})$$

The dominant term of equation (A-10) is the third—a vertical acceleration. Each of the other terms is one or more orders of magnitude smaller. The third term was used as a test of the magnitude of the acceleration effect. It should be noted that this acceleration scenario is more complicated than that discussed by Bearman and Currie (1979) relating to Figure A-6. Instead of having all the systems' components—including pressure tubing and pressure transducers—experiencing the same acceleration, this scenario involves

accelerations that change with distance from the center of rotation. What this means is that the air inside the tubing is not experiencing a uniform acceleration but one that changes along the route from the tap to the transducer, i.e.  $\bar{a}(t)$  in equation (A-9) could have been written as a function of  $x$  as well. To estimate the maximum effects, this was ignored. This means that the estimate is based on the maximum acceleration that occurs at any point along the tube.

The maximum effect of acceleration was estimated as the maximum value of the third term of equation (A-10). With the maximum angular amplitude,  $2^\circ$ , the maximum oscillation frequency of 7.5 Hz, and a value for  $L$  corresponding to the vertical spacing between the model surface and the transducer diaphragm (0.5 in.), equation (A-4) yields a  $C_{p_a}^*$  value of 0.0069.

Using this  $C_{p_a}^*$  value and a sample data set at  $U_r = 3.1$ , comparison plots were generated using the correction equations (A-7) and (A-8). Figure A-8 shows a sample data set with uncorrected and corrected amplitudes, and Figure A-9 shows the uncorrected and corrected phases for the same data set. In each case, the differences are insignificant. Therefore, no pressure amplitude or phase data were corrected for these experiments.

Pressure signals induced as described above can also influence the experimental coherence values—i.e. two signals that are not correlated might show some correlation because all the pressure taps are being shaken in phase as an experiment is run. To investigate the extent of this influence, an analytical expression can be derived as follows.

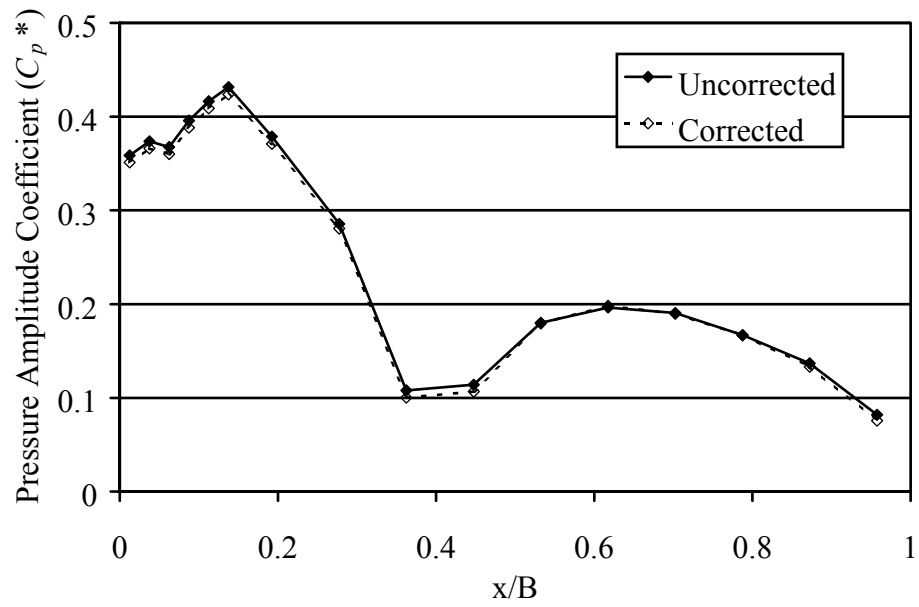


Figure A-8 Plot of pressure amplitude distributions as measured—uncorrected—and as corrected for model acceleration effects.

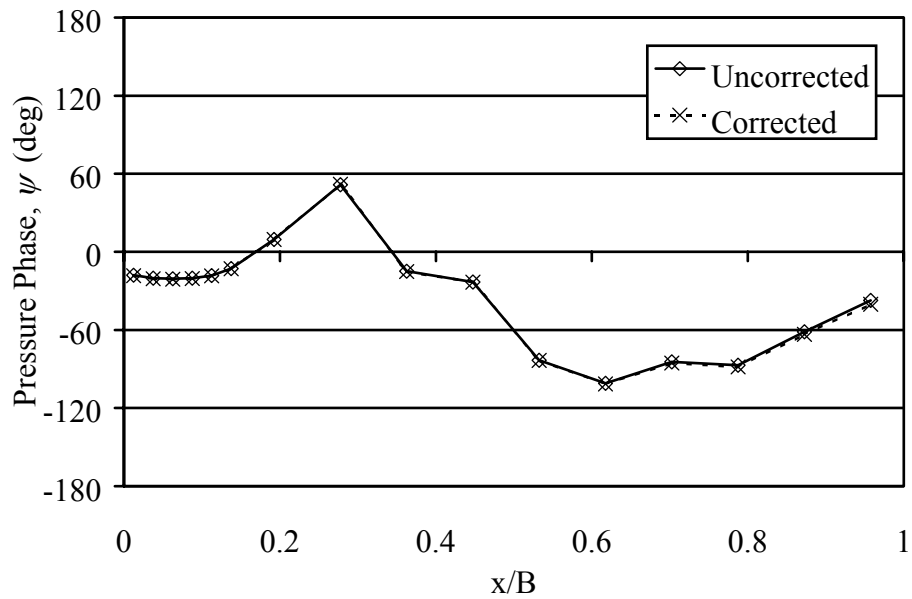


Figure A-9 Pressure phase distributions as measured—uncorrected—and as corrected for model acceleration effects.

Consider two pressure time series,  $p_1(t)$  and  $p_2(t)$ , that if measured perfectly at the surface of the model would be uncorrelated. Add to these signals components that are correlated with each other,  $c_1(t)$  and  $c_2(t)$ . These signals simulate what might be induced by the motion of the air in the tubing system. An experimental coherence calculation between these two signals would involve the coherence between  $e_1(t) = p_1(t) + c_1(t)$  and  $e_2(t) = p_2(t) + c_2(t)$ . This analytical derivation follows that in Bendat & Piersol (1986). Assuming that  $c_1(t)$  and  $c_2(t)$  are not correlated with  $p_1(t)$  or  $p_2(t)$ , then the cross spectra  $G_{p_1c_1} = G_{p_2c_2} = G_{p_1p_2} = 0$ . By definition the coherence function is calculated as:

$$\gamma^2(f) = \frac{|G_{e_1e_2}(f)|^2}{G_{e_1e_1}(f)G_{e_2e_2}(f)} \quad (\text{A-11})$$

By substituting  $G_{e_1e_1} = G_{p_1p_1} + G_{c_1c_1}$  and  $G_{e_2e_2} = G_{p_2p_2} + G_{c_2c_2}$ , it can be shown that:

$$\gamma^2(f) = \frac{|G_{p_1p_2}(f)|^2}{(G_{p_1p_1}(f) + G_{c_1c_1}(f))(G_{p_2p_2}(f) + G_{c_2c_2}(f))} \quad (\text{A-12})$$

Substituting with the ratios  $\alpha(f) = G_{p_1p_1}/G_{c_1c_1}$  and  $\beta(f) = G_{p_2p_2}/G_{c_2c_2}$ , equation (A-12)

becomes:

$$\gamma^2(f) = \frac{1}{1 + \alpha(f) + \beta(f) + \alpha(f)\beta(f)} \quad (\text{A-13})$$

For this project, where the pressure model is oscillated at a single frequency, it is helpful to consider the amplitudes of the signals at the driving frequency. Consider the case where the uncorrelated signals have the same amplitude,  $P$ , at a given frequency,  $f$ , and the correlated signals have the same amplitude,  $C$ . Equation (A-13) can then be rewritten as:

$$\gamma^2(f) = \frac{1}{\left(\left(\frac{P}{C}\right)^2 + 1\right)} \quad (\text{A-14})$$

This relationship is plotted in Figure A-10 where it can be seen that for all cases where the amplitude of the coherent signals is lower than that of the incoherent signals, the coherence is less than 0.2. The estimated value of the maximum induced pressure (from equation (A-4)) is  $0.0069q$ . The minimum pressure amplitude signal from oscillating model tests (reported in Chapter 6) can be computed from  $C_p^*$  values using its definition:  $p^*/q = \alpha_0 C_p^*$  (where  $p^*$  is the pressure amplitude and  $q$  is the dynamic pressure). The minimum value for  $p^*$  then is  $0.02q$ . The ratio  $C/P$  then is 0.3 which from Figure A-10 corresponds to a coherence value less than 0.1. Coherence values induced by the acceleration of the model were then considered negligible.

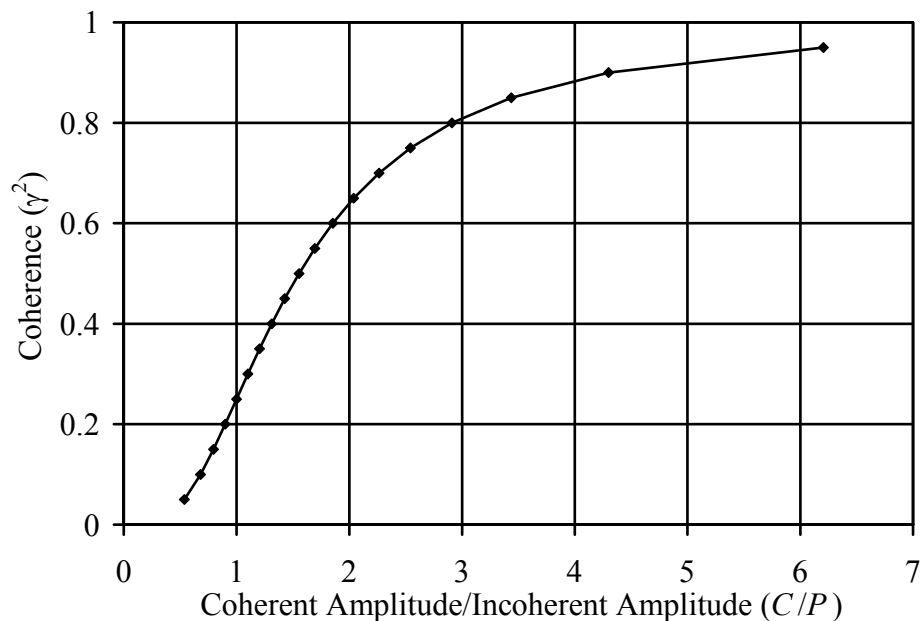


Figure A-10 Coherence at a given frequency as a function of the amplitude ratio of coherent to incoherent signals at that frequency.

### A.3.3 Electrical Noise Issues

Similar to the discussion of spurious correlation coming from tubing acceleration effects in section A.3.2, correlated electrical noise was also considered a source of correlation and coherence errors. Two types of tests were conducted to examine this issue. In both cases, time series data were collected from all of the pressure sensors—just as if it were a regular data acquisition run. The first type of test was run with the wind tunnel off, but all other support equipment on. This simulated the electrical noise conditions during a stationary model test. The second type of test was the same as the first except that the model oscillation motor was run over a range of speeds. Because motion of the model would generate both aerodynamic pressure and acceleration effects (like discussed in A.3.2), the oscillation mechanism was disconnected from the model during these tests. This test was to simulate electrical noise for an oscillating model test.

Correlation values were calculated among the time series just as they were for regular pressure tests. For the stationary model test simulation, all correlation values were well under 0.1. The oscillating model test simulation produced electrically induced correlation values dependent on the motor speed. As the motor speed increased, which for a real test would correspond to decreasing reduced velocity, the correlation values increased. While most of these correlation values were under 0.1, some combinations of transducers had correlation values as high as 0.3. The group of sensors with high correlation were all within the same SSH board. Several different grounding schemes were tested to eliminate this problem, but 0.3 was the minimum correlation achieved.

However, since these tests were artificial in that electrical noise signals were much smaller than actual pressure signals, simulated pressure signals were added to these

motor noise signals to simulate real conditions more appropriately. Simulated pressure signals were generated with the same rms and spectral distributions as smooth flow, stationary model pressure data. Smooth flow, stationary test data were chosen because they had the smallest rms values and would represent a worst case in terms of the influence of electrical noise. When the electrical noise time series described above was combined with the simulated pressure signals, correlation values dropped significantly. Those values below 0.1 dropped further, and all values above 0.1 dropped below 0.1. Electrical noise effects on correlation values were therefore considered negligible.

Coherence values were also tested just as the correlation values discussed above. Again, the coherence values were calculated from the electrical noise time series acquired with the wind tunnel off. The nature of the oscillating model coherence signals presented in Chapter 7 warranted a test of whether the extremely high coherence values were induced by non-aerodynamic sources. The coherence function had values similar to stationary model broad band values for all frequencies except the model oscillation frequency. Motor noise coherence values, however, showed no salient peaks at any model driving frequency. This was partially due to low electrical noise coherence and partly due to the frequency shift caused by the 4:1 gearhead used on the motor. A 4:1 speed ratio between the model oscillation frequency and the motor speed meant that the motor was never operating at the same frequency as the model oscillation. The highest peaks at any frequency were near 0.4. As before, these values dropped significantly when simulated pressure signals were added to the electrical noise time series. Coherence values were thus considered unaffected by electrical noise.

## APPENDIX B. VELOCITY MEASUREMENT PROCEDURES

Hot-wire anemometry and measurements of mean dynamic pressure were used to measure velocity. This appendix describes each type of sensor used and outlines the calibration procedure employed in each case.

### B.1 Description of Hardware

A Pitot-static probe mounted just upstream of the model was used to set the wind-tunnel velocity for each test. A differential pressure transducer measured the difference between the total and static ports on the probe to obtain the dynamic pressure. From the dynamic pressure, the mean velocity was calculated using Bernoulli's equation

( $U = \sqrt{2(p_{total} - p_{static})/\rho}$ ). This calculation also required the air density, which was obtained from the ideal gas relation ( $p = \rho RT$ ). Ambient temperature and pressure were measured with a thermometer and barometer mounted on the wall of the wind-tunnel laboratory.

All dynamic measurements of velocity were made using hot-film probes. Static calibration of these probes was accomplished using Pitot-static probes as the reference. TSI anemometry equipment included an IFA 100 Model 158 chassis with Model 150 anemometers and Model 157 signal conditioners. The signal conditioner was used to apply an offset and gain along with a third-order Sallen-Key type low-pass filter to the

signals. The offset and gain were used to optimize the voltage range of the signal with that of the analog to digital converter (ADC). The anemometer's internal test signal and front panel controls were used to tune the frequency response of the anemometer circuitry with the probes (according to procedures outlined in anemometer manual, TSI, 1992). This frequency response extended to approximately 3.5 kHz.

Probes with an X configuration were used to measure turbulence parameters in the absence of a bridge model. Because the heat transfer from a hot-wire/hot-film probe is dependent on the angle between the longitudinal axis of the wire and the flow direction, incoming flow velocities of various angles of attack can be identified. The X-probes used in this work—TSI 1241-20 film sensors—had two wires oriented at  $90^\circ$  to each other and  $45^\circ$  to the incoming flow. The voltages from the two wires uniquely identify two components of the incoming velocity vector.

## B.2 Description of Calibration and Measurement Procedures

The dedicated rig shown in Figure B-1 employs a 2D jet and a traverse for setting the velocity and angle of attack and measuring the resulting hot-film voltages. Jet velocity was measured with a small Pitot probe at the nozzle and controlled with a variable power supply connected to the fan. For velocities from 2.2 m/s to 11.5 m/s, voltages were measured for angles of attack from  $-30^\circ$  to  $+30^\circ$ . This velocity and angle ranges were chosen to be larger than what would be expected in actual tests.

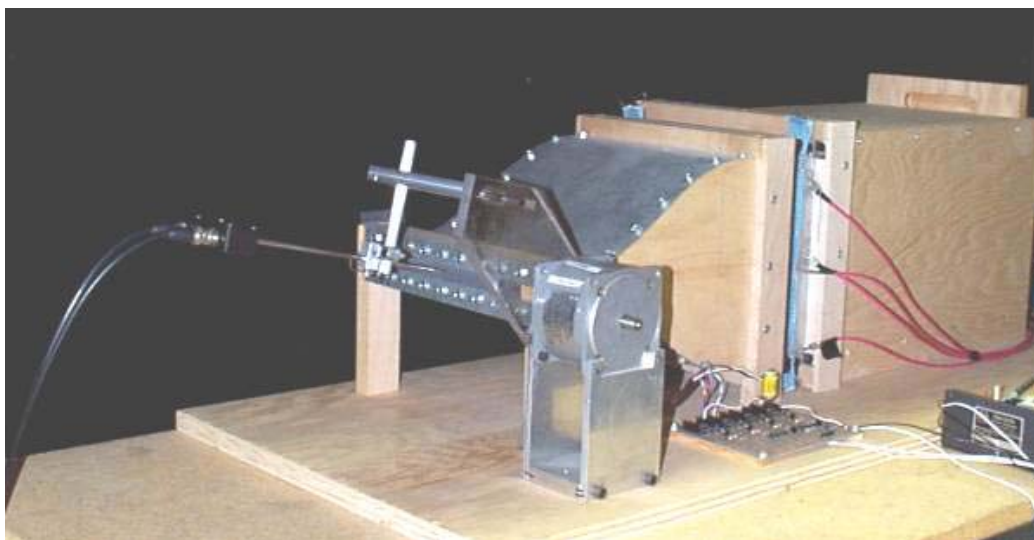


Figure B-1 The X-probe calibration rig used to step through different angles of attack for a range of velocities.

Each velocity-angle of attack pair resulted in a unique pair of voltages,  $E_1$  and  $E_2$ . From these data, a table for each component of velocity was constructed using a polynomial interpolation scheme as described in Lueptow, et al. (1988). The algorithm for this task was implemented using a slightly modified form of a FORTRAN code written by George Ross (1996). Figure B-2 and Figure B-3 show the example calibration tables in graphical form. Voltages obtained with X-probes were converted into two components of velocity using a bilinear interpolation scheme (Press et al., 1992) among the points in the tables. This calibration method requires little computational effort and is not compromised by assumptions made in traditional King's law approaches (e.g. interference from and heat conduction to the probe supports).

Running the voltage pairs obtained in the calibration experiments through the tables resulted in the  $u$  component of velocity matching to within 1% and the angle of attack matching to within  $0.3^\circ$ .

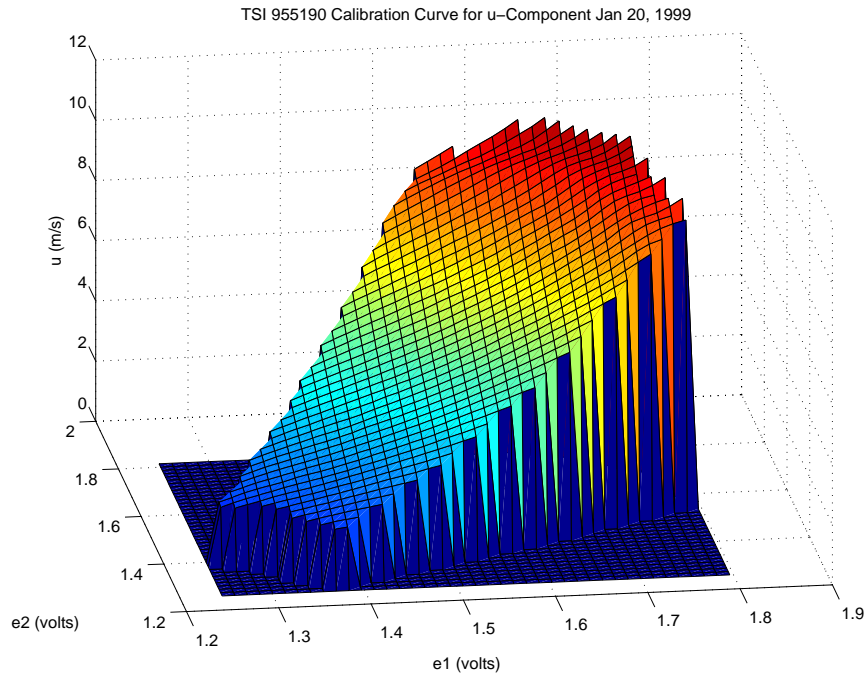


Figure B-2 X-wire calibration surface for the  $u$ -component of velocity as a function of  $E_1$  and  $E_2$ .

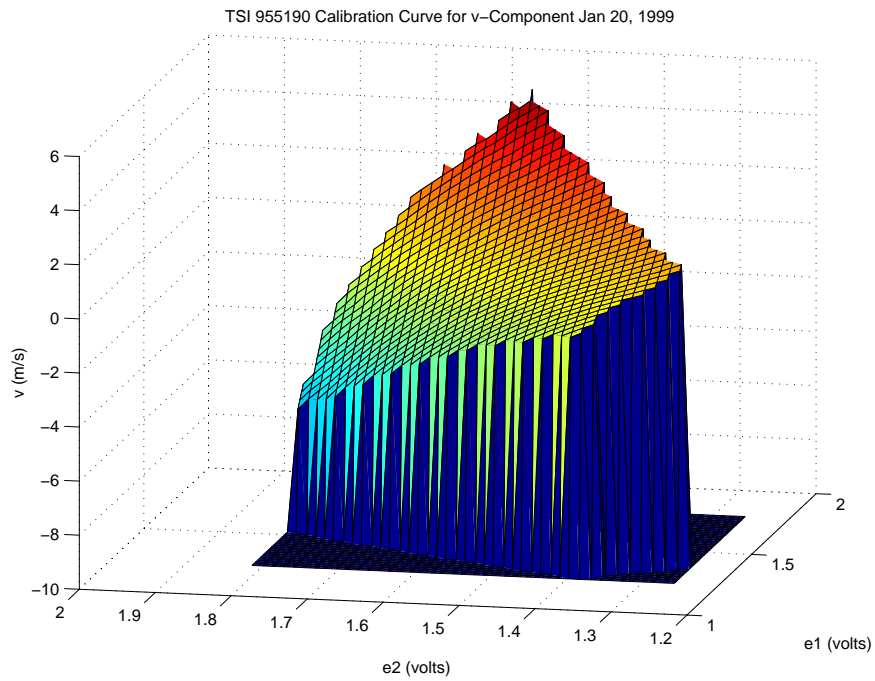


Figure B-3 X-wire calibration surface for the  $w$ -component of velocity as a function of voltages  $E_1$  and  $E_2$ .

## APPENDIX C. DIGITAL SIGNAL PROCESSING TECHNIQUES

This appendix summarizes all the major calculations involved in this study. This material is closely related to that of Appendix D on uncertainty analysis. That analysis of the uncertainty of the values resulting from these techniques will refer heavily to the descriptions found in this appendix. Each of the analysis techniques described here were implemented using MATLAB software from MathWorks or using LabVIEW software from National Instruments. LabVIEW was the data acquisition software used to acquire all the data. Implementing analysis techniques in LabVIEW allowed monitoring of data while tests were in progress.

### C.1 Statistical Estimates

A number of statistical estimates were made from velocity and pressure measurements. Mean and RMS values were calculated for velocities while mean, RMS, peak, and skewness values were calculated for pressure. Statistical values for pressures were all calculated within LabVIEW, the data acquisition software described in Chapter 3.

The mean value,  $\bar{x}$ , of the samples,  $x_i$ , of a random variable was calculated as:

$$\bar{x} = \frac{1}{N} \sum_{i=1}^N x_i \quad (\text{C-1})$$

RMS values were calculated as:

$$x_{RMS} = \left[ \frac{1}{N-1} \sum_{i=1}^N (x_i - \bar{x})^2 \right]^{1/2} \quad (C-2)$$

The skewness coefficient was calculated as:

$$S_k = \frac{1}{x_{RMS}^3} \left[ \frac{1}{N} \sum_{i=1}^N (x_i - \bar{x})^3 \right] \quad (C-3)$$

which is the skewness of  $x_i$  normalized by the third power of  $x_{RMS}$ .

The kurtosis coefficient was calculated as:

$$K_u = \frac{1}{x_{RMS}^4} \left[ \frac{1}{N} \sum_{i=1}^N (x_i - \bar{x})^4 \right] \quad (C-4)$$

which is the kurtosis of  $x_i$  normalized by the fourth power of  $x_{RMS}$ .

Negative peak values for pressures were also calculated. Each ensemble of pressure data was demeaned and searched for its minimum pressure value. The peak value reported for each pressure tap is the average of the peak values found over all the ensembles.

## C.2 Spectral Estimates

Spectral estimates were used to obtain two different quantities, power spectral density (PSD) functions of measured quantities and, from these, frequency-specific amplitudes. This section describes the calculations involved in both of these quantities.

When using an analog-to-digital converter (ADC) to obtain experimental data, one must ensure that no frequency components exist above the “Nyquist frequency,” i.e. half the sampling frequency,  $f_s$ . Components above this limit manifest themselves as energy at lower frequencies in the resulting digitized signal—this process is called

aliasing. Conventionally, anti-aliasing filters are employed to filter all signals above the Nyquist frequency before a signal is digitized. Such is the case for the velocity fluctuation measurements of this study. The anti-aliasing filters within the hot-film anemometer were used. For the pressure measurements of this study, the lengths of plastic tubing between the pressure taps and the transducers acted as an effective filter for the signals. The dynamic response of this tubing showed a roll-off for frequencies above 200 Hz—with a steeper decline occurring near 500 Hz (for more details, see the pressure calibration discussion of Appendix A). As a result, signals were sampled at 1000 Hz making the Nyquist frequency 500 Hz, and no further filtering was done. A more in-depth discussion of issues concerning aliasing and digital sampling can be found in Bendat & Piersol (1986).

Given an acquired time signal, the act of computing a power spectral density function from digital data is essentially that of organizing the power of a signal into “bins” associated with discrete frequencies. This organization can be nontrivial. To suppress the phenomenon called “leakage,” where power is from frequencies other than that of a particular bin is added to the power already associated with a bin, time series data were treated with a windowing function. This involved multiplying the time-domain signal by a particular window function (in this case, a Hanning window) and then adjusting the frequency-domain values by  $8/3$  to compensate for the window’s effects on the amplitudes. Again, further information can be found in Bendat & Piersol (1986).

Once the window was applied to the data, a fast Fourier transform (FFT) routine was employed. For a time series of discrete data points given by  $x_i$  (where  $x_i$  refers to values of a continuous function of time,  $x(t)$ , evaluated at discrete instants of time,  $t_i$ ),

the output from an FFT is a series of complex numbers represented here as  $X_k$ . The  $k$  here refers to the different discrete frequencies corresponding to the FFT values,  $X_k$ .

These discrete frequencies,  $f_k$ , are given as:

$$f_k = k \frac{f_s}{N} = \frac{k}{N\Delta t} \quad k = 0, 1, 2, \dots, N-1 \quad (\text{C-5})$$

where  $f_s$  is the digital sampling rate in Hz,  $N$  is the total number of points in the data set, and  $\Delta t$  is the sampling interval between digital samples (i.e.  $\Delta t = 1/f_s$ ).

The  $X_k$  values are assembled into a PSD function for  $x_i$  by the following equation:

$$G_{xx}(f_k) = \frac{8}{3} \frac{2\Delta t}{N} X_k^* X_k \quad k = 0, 1, 2, \dots, \frac{N}{2} \quad (\text{C-6})$$

where  $G_{xx}(f_k)$  is the PSD function evaluated at discrete frequencies,  $f_k$ , the  $8/3$  is the correction for the Hanning window, and the star denotes the complex conjugate of a complex number. The units of this PSD function are those of the original function squared multiplied by time. This can also be interpreted as [original units]<sup>2</sup> per Hz.

For this study, pressure signal amplitudes at specific frequencies were required. These amplitudes were calculated from the PSD functions by integrating about the peak value in the spectrum—i.e. integrating about the bin associated with the model oscillation frequency. The total amplitude was taken as the amount above the stationary cylinder spectrum at that frequency. Figure C-1 highlights the bins used in this integration—the bin containing the peak and the two adjacent bins. These three bins had to be included because the Hanning window applied to the time series effectively reduces the spectral

resolution. To obtain the full value of the peak, each bin was included as in the following equation for the pressure amplitude:

$$p^* = \sqrt{2} \sqrt{\left[ \sum_{k=k_{\max}-1}^{k=k_{\max}+1} G_{pp}(f_k) - G_{pp}^s(f_k) \right] df} \quad (C-7)$$

where  $p^*$  is the amplitude of the pressure fluctuation,  $G_{pp}$  and  $G_{pp}^s$  are the power spectral density functions of pressure signals from the oscillating model and the stationary model, respectively,  $df$  is the bandwidth of a single frequency bin (where  $df = f_s/N$ ), and  $k_{\max}$  is the index of the bin containing the maximum value. The integration of the spectra yields the variance of the signal at the desired frequency. Multiplying the square root of this variance by  $\sqrt{2}$  yields the amplitude. This integration is conducted offline using a MATLAB script.

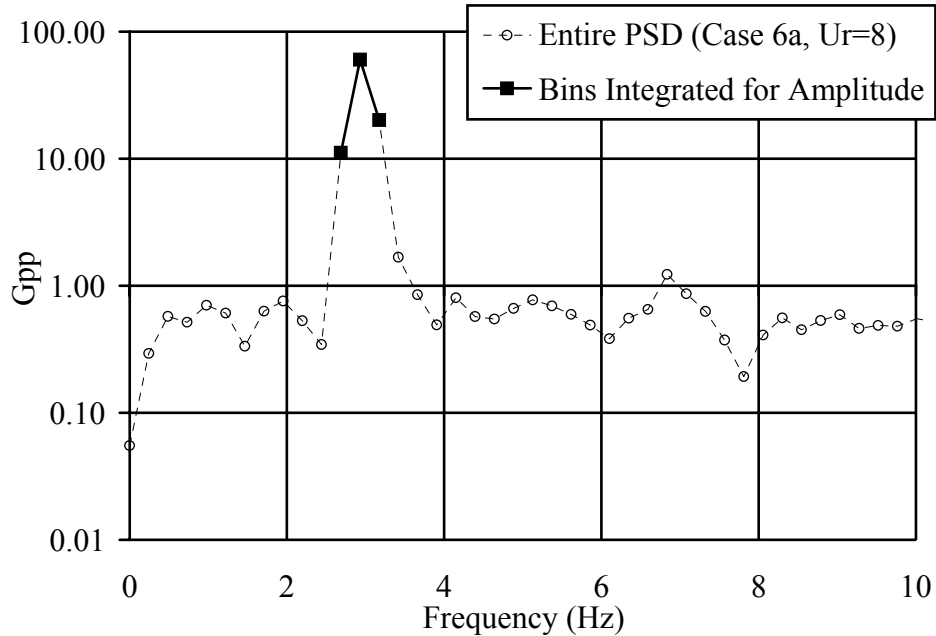


Figure C-1 Plot of a sample pressure PSD highlighting the bins integrated to calculate the signal's amplitude.

### C.3 Correlation Estimates

Correlations were used for several purposes. The first use was to identify autocorrelations and cross correlations of velocity fluctuations. These correlations were used to identify the largest scales of the incident turbulent flows used in these experiments. A second use was to identify the phases between unsteady pressures on the surface of the model and the motion of the model. A third use was to identify the spanwise correlations for lift, moment, and individual pressures.

In each of these cases, the basic calculation of the correlations is the same. What is different from one application to another is what is done with the correlation once calculated. This section will describe first the calculation of the correlations themselves and then the calculations relevant to each correlation application.

Given two time series (or just one if an autocorrelation is being calculated) of acquired discrete data,  $x_i$  and  $y_i$ , a cross correlation function was calculated using fast Fourier transforms. The procedure involved first adding  $N$  zeros to the data series (where  $N$  is the number of samples in the series) to avoid distortion due to the periodic assumption inherent in Fourier transforms. Without this measure the terms corresponding to a time delay of  $\tau$  will be influenced by correlation associate with both  $R_{xy}(\tau)$  and  $R_{xy}(T - \tau)$  where  $T$  is the total sample time of the data set (i.e.  $T = N\Delta t$ ). Further details concerning this effect and the derivation of the method of computing correlation functions using FFT's can be found in Bendat & Piersol (1986).

Fourier transforms are performed on these zero-padded data sets to obtain  $X_k$  and  $Y_k$ . The two-sided cross-spectral density function  $S_{xy}(f_k)$  is then calculated as follows:

$$S_{xy}(f_k) = \frac{\Delta t}{N} X_k^* Y_k \quad k = 0, 1, 2, \dots, 2N - 1 \quad (\text{C-8})$$

Taking advantage of the Fourier transform relationship between cross-spectral density functions and cross correlation functions, an inverse FFT is used as follows:

$$C_i = \frac{\Delta t}{x_{RMS} y_{RMS}} \text{IFFT}(S_{xy}(f_k)) \quad i = 0, 1, 2, \dots, 2N - 1 \quad (\text{C-9})$$

where “IFFT” denotes the performance of an inverse FFT and the RMS values of the two input signals are used to produce a cross correlation coefficient function having maximum and minimum values of 1 and  $-1$ , respectively. To obtain the final  $\rho_{xy}(\tau_i)$  values from the  $C_i$  coefficients, the following equations are used. The  $\rho_{xy}(\tau_i)$  values corresponding to positive lags are calculated as:

$$\rho_{xy}(\tau_m) = \frac{N}{(N-i)} C_i \quad \text{for } i = 0, 1, 2, \dots, (N-1); \quad m = 0, 1, \dots, (N-1) \quad (\text{C-10})$$

where  $\tau_m = m\Delta t$ . Values corresponding to negative lags are calculated as:

$$\rho_{xy}(\tau_m) = \frac{N}{(i-N)} C_i \quad \text{for } i = N+1, \dots, 2N-1; \quad m = -N+1, -N+2, \dots, -2, -1 \quad (\text{C-11})$$

where, again,  $\tau_m = m\Delta t$ . The value of  $\rho_{xy}$  corresponding to  $\tau_m = -N\Delta t$  needs no multiplying factor and is obtained directly from  $C_N$ .

An important application of cross correlations for this project was finding the phase lag of the pressure signals at each pressure tap with respect to the body motion. To illustrate this type of calculation, a typical angle-pressure signal pair is shown in Figure C-2. From the plot, one can see that at this particular location, the pressure signal leads the angular displacement of the model. The cross correlation function for these two

signals is shown in Figure C-3 where the peak value occurs at  $\tau = \tau_p$ . This time delay was converted to the associated phase according to the following expression:

$$\psi = 360 f_\alpha \tau_p \quad (\text{C-12})$$

where  $\psi$  is the phase (in degrees) between the pressure fluctuation and the angular displacement and  $f_\alpha$  is the frequency of the angular oscillation.

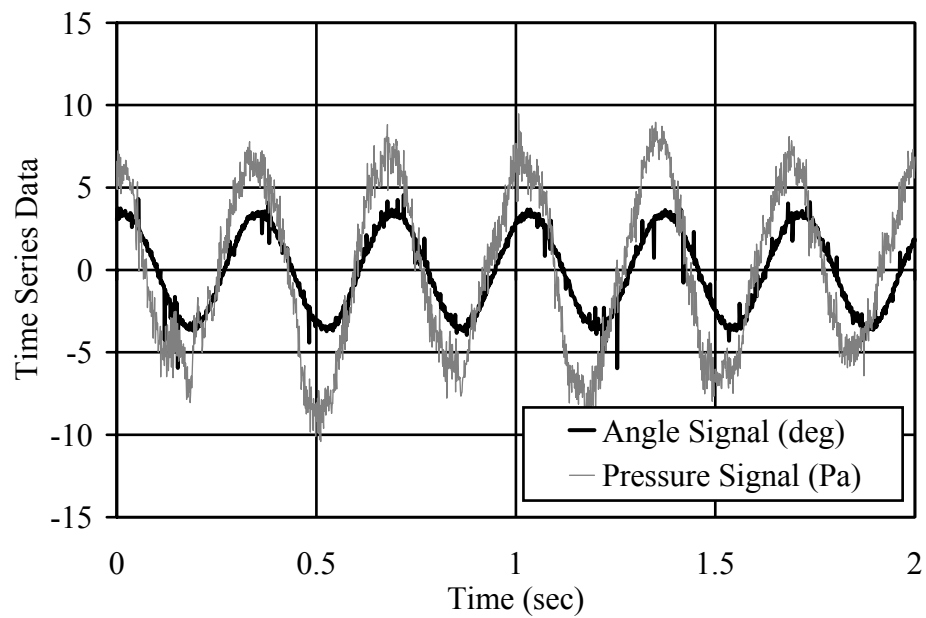


Figure C-2 Plot of an angle signal and pressure signal to illustrate the calculation of the phase from a cross correlation between them.

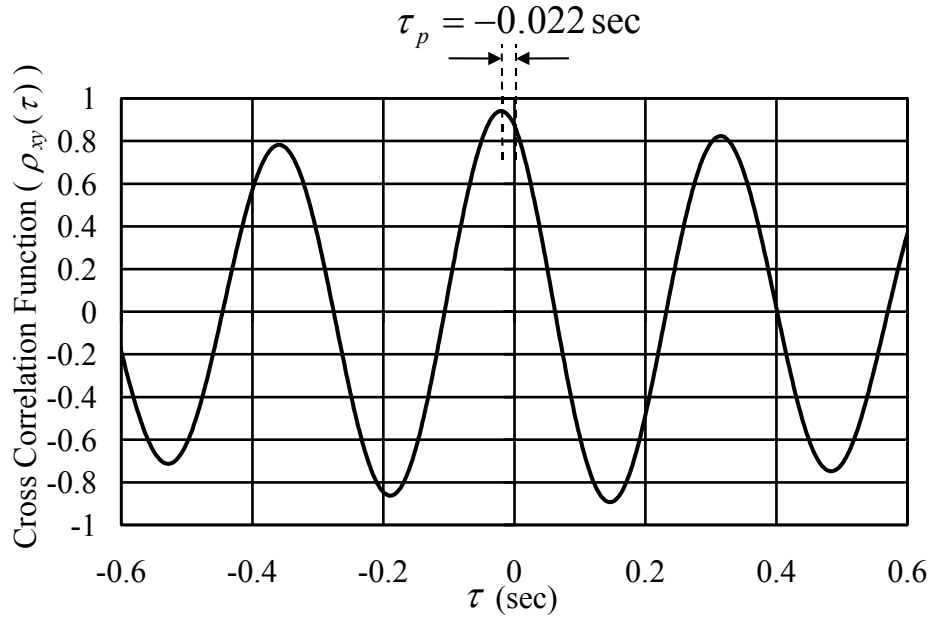


Figure C-3 Cross correlation function for the signals shown in Figure C-1 to illustrate the location of the peak and its associated time lag,  $\tau_p$ .

#### C.4 Coherence Estimates

Coherence calculations were used for investigating the frequency dependence of the spanwise lift and moment correlation. Coherence estimates were calculated using spectral methods. For two signals, say  $x(t)$  and  $y(t)$ , autospectra were calculated as in equation (C-6) of section C.2 while cross spectra, were calculated as follows:

$$G_{xy}(f_k) = \frac{8}{3} \frac{2\Delta t}{N} X_k^* Y_k \quad k = 0, 1, 2, \dots, \frac{N}{2} \quad (\text{C-13})$$

where all variables are described in section C.2.

Cross spectra and autospectra were ensemble averaged separately and then brought together to obtain coherence values according to the following definition:

$$287 \quad (\text{C-14})$$

$$\gamma_{xy}^2(f_k) = \frac{|G_{xy}(f_k)|^2}{G_{xx}(f_k)G_{yy}(f_k)} \quad k = 0, 1, 2, \dots, \frac{N}{2}$$

The results of this expression were used in two ways. For estimates of the coherence at specific frequency values—such as the coherence at the model driving frequency presented in Chapter 7—the values computed with equation (C-14) were used directly. However, due to the commonly “noisy” nature of coherence plots for broadband signals, coherence values were smoothed for those plots of the coherence function over a wide frequency range. This smoothing was a simple procedure. Groups of frequency bins were averaged into a single new bin. For example, three bins corresponding to frequency values of  $f_{k-1}, f_k, f_{k+1}$  were combined into a single bin corresponding to a frequency value of  $f_k$  and a coherence value of  $\frac{1}{3} \sum_{i=k-1}^{k+1} \gamma_{xy}^2(f_i)$ .

## APPENDIX D. UNCERTAINTY ANALYSIS

All measurements have some inherent degree of uncertainty. Calculations made from measurements have a degree of uncertainty as well. This appendix summarizes the analysis of this uncertainty for the measurements and calculations of this study of bridge aerodynamics.

Measurement uncertainties can be classified in two major groups—bias errors and precision errors. Bias errors remain constant for repeated tests at fixed conditions—they are a function of the device or the measurement procedure employed. Precision errors, also known as random errors, manifest themselves as the scatter in repeated measurements. Bias errors can be minimized by comparison with working standards while precision errors can be quantified statistically.

Because a PC-based data acquisition system was used, voltage measurements were by far the most common type of measurement performed. Uncertainty analysis of voltage measurements will be presented first. This will be followed by an example of calibration uncertainty analysis. Calibration can be defined as the process of exchanging the large bias error of a measurement device for the smaller bias error of a working standard and the precision errors of the calibration process. While pressure, velocity, and angular position each involved a calibration, only the uncertainty analysis for the pressure calibration is presented in depth here. Only the results from the velocity and position calibration uncertainty are presented. The final section of this appendix then

addresses the uncertainties of various derived quantities with special attention given to uncertainty analysis involving cross correlation calculations.

#### D.1 Voltage Measurement Uncertainty

As described in Chapter 3, the voltage measurement system consisted of two major components, a simultaneous sample and hold (SSH) board (SCXI-1140) and an analog to digital conversion (ADC) board (PCI-MIO-16XE-10). Specifications of accuracy of these devices was obtained from the documentation supplied by National Instruments—the PCI E Series User Manual and the SCXI-1140 User Manual. For the SSH board the following specifications are relevant for bias error estimates where  $B_{vi}$  corresponds to the  $i^{\text{th}}$  contribution to the voltage bias error:

$$B_{v1} = \text{Maximum gain error (for Gain=1.0)} = \pm 0.05\%$$

$$B_{v2} = \text{Thermal drift (for Gain=1.0)} = \pm 25 \text{ ppm}/^\circ\text{C}$$

For the ADC board, the following specifications were relevant to bias error analysis.

These specifications were supplied assuming that before each experiment, a calibration routine was run to set the board's ADC computations with an onboard reference.

$$B_{v3} = \text{Relative accuracy} = \pm 0.75 \text{ LSB}$$

$$B_{v4} = \text{Pre-gain offset error} = \pm 3 \mu\text{v}$$

$$B_{v5} = \text{Postgain offset error} = \pm 76 \mu\text{v}$$

$$B_{v6} = \text{Gain errors} = \pm 30.5 \text{ ppm of maximum reading}$$

$$B_{v7} = \text{Thermal drift} = \pm 120 \mu\text{v}/^\circ\text{C}$$

The following are precision errors associated with voltage measurement.  $P_{vi}$  corresponds to the  $i^{\text{th}}$  contribution to the voltage measurement precision error.

$$P_{v1} = \text{ADC resolution uncertainty} = \frac{1}{2} \frac{1.0\text{v}}{2^{16} \text{bits}} = 0.0076 \text{mv/bit}$$

$$P_{v2} = \text{Droop rate} = \pm 10 \text{mv/sec}$$

$$P_{v3} = \text{Ambient electrical noise} = 0.7 \text{mv (rms)}$$

where the droop rate is the amount of voltage drift that occurs while the SSH circuitry holds the voltage before the ADC digitizes the value. The maximum time for this to occur was calculated by the total number of channels multiplied by the interchannel acquisition rate of the ADC board (100kHz). This time was approximately 670 $\mu$ s. The ambient electrical noise was measured with all measurement equipment in place as in actual experiments but with the wind tunnel off.

The various contributions to voltage measurement uncertainty can be combined using the conventional square root of the sum of the squares (SRSS) method (as described, for example, in Figliola & Beasley, 1991) as follows:

$$B_v = \left[ \sum_i (B_{vi})^2 \right]^{1/2} = 1.5 \times 10^{-4} \text{v}$$

$$P_v = \left[ \sum_i (P_{vi})^2 \right]^{1/2} = 7.0 \times 10^{-4} \text{v}$$

where  $B_v$  and  $P_v$  are the total bias and total precision errors, respectively, for voltage measurements. These two can be combined for an estimate of the total voltage measurement uncertainty,  $u_v$ , as:

$$u_v = [B_v^2 + P_v^2]^{1/2} = 7.2 \times 10^{-4} \text{ v}$$

## D.2 Calibration Uncertainty

Calibration experiments were performed for pressure, velocity, and angular position measurements. As stated earlier, only the pressure calibration uncertainty analysis is presented here. Analysis for velocity and position are analogous. The voltage measurement uncertainty is used as part of the calibration uncertainty analysis for each type of measurement. These are combined to form a total bias error for the measurement of a given quantity. Total uncertainty in the measurement of these quantities then consisted of these bias errors along with the precision error associated with individual experiments.

The working standard used for all pressure calibration exercises was a Van Essen Instruments Betz 2500 Pa Manometer. To quantify the uncertainty in this working standard,  $U_{ws}(p)$ , its bias error and precision error are combined as follows:

$$U_{ws}(p) = [B_{ws}(p)^2 + P_{ws}(p)^2]^{1/2}$$

where  $U_{ws}(p)$  is the uncertainty in the working standard as a function of measured pressure,  $p$  (in Pa),  $B_{ws}(p)$  and  $P_{ws}(p)$  are the bias and precision errors, respectively, as a function of measured pressure. The calibration certificate from Van Essen Instruments

gives the bias error as:  $B_{ws}(p) = 0.3\text{Pa} + 2 \times 10^{-4} p$ . A safe maximum value of  $p$  for this project is 100 Pa, rendering a maximum value of  $B_{ws}$  of 0.32 Pa. The only precision error to be included in this estimate is that of the resolution uncertainty due to the manometer's scale, which is 0.15 Pa. These values result in a maximum value for  $U_{ws}$  of 0.35 Pa.

Quantifying the uncertainty in the calibration process consisted of finding the difference between values measured in the calibration experiment and values predicted by the calibration curve fit. The calibration curve fit took the form:

$$p_{\text{fit}} = C(v - v_0)$$

where  $p_{\text{fit}}$  is the pressure (in Pa),  $C$  is the calibration coefficient,  $v$  is the voltage measured from a pressure transducer, and  $v_0$  is the zero-pressure reference voltage. The difference in pressure values,  $E$ , between the curve fit and the working standard were calculated over the entire calibration pressure range according to the following relation:

$$E = p_{ws} - p_{\text{fit}} = p_{ws} - C(v - v_0) \quad (\text{D-1})$$

where  $p_{ws}$  is the pressure given by the working standard. As discussed in Appendix A, the pressure range was traversed several times during the calibration experiment, so a given pressure value was tested multiple times. As a result, an average value,  $\bar{E}$ , of the difference between the working standard and the curve fit was calculated for each pressure value. The calculated differences,  $\bar{E}$ , did not exhibit any obvious trends with respect to the magnitude of the pressure, so only a single value,  $\bar{E} = 0.2\text{ Pa}$ , was used for the entire range.  $\bar{E}$  was used as the contribution to bias error resulting from the calibration process.

The total bias error of the calibration process was then obtained by combining the working standard uncertainty with the bias in the calibration fit as follows:

$$B_{\text{cal}} = \left[ E^2 + U_{\text{ws}}^2 \right]^{1/2} = 0.40 \text{ Pa}$$

The uncertainty in the voltage measurement makes its contribution to the pressure measurement uncertainty here as an uncertainty in the estimate of  $E$ . The voltage uncertainty,  $u_v$ , was propagated essentially as a precision index through equation (D-1) by employing equation (D-3) of section D.3 as follows:

$$u_p = \left[ B_{\text{cal}}^2 + \left( \frac{\partial E}{\partial v} \frac{2u_v}{\sqrt{N_{\text{cal}}}} \right)^2 \right]^{1/2} = \left[ B_{\text{cal}}^2 + \left( C \frac{2u_v}{\sqrt{N_{\text{cal}}}} \right)^2 \right]^{1/2} = 0.40 \text{ Pa}$$

where  $N_{\text{cal}}$  is the number of data points acquired in the calibration experiment. The uncertainty value  $u_p$  was then “frozen” as the bias error of any pressure measurement. Subsequent pressure measurements used  $u_p$  along with precision errors estimated from the specific experiment.

Conducting similar calibration uncertainty analyses with the position and velocity measurements resulted in values of  $u_\alpha = 0.25^\circ$  for the angular position uncertainty and of  $u_u = 0.03 \text{ m/s}$  and  $u_w = 0.03 \text{ m/s}$  for the uncertainty of the  $u$  and  $w$  components of velocity, respectively.

### D.3 Uncertainty Propagation into Derived Quantities

A large number of derived quantities were calculated from the measured quantities of pressure, angular position, and velocity. In most cases, the largest

component of the uncertainty of a given quantity was its precision error. The precision error of measured quantities, whenever possible, was estimated from “end to end” calculations. This means that instead of propagating individual precision indices analytically through the various equations, the standard deviation of the *end* result of the actual experiments and calculations was calculated. This was the primary uncertainty calculation for most quantities presented.

For example, a large number of ensembles were averaged to compute the pressure amplitudes presented in Chapter 6. Rather than simply ensemble averaging the pressure amplitudes—which produces a mean and an accompanying precision index for the amplitude estimate—and then calculating a flutter derivative value from the mean amplitude, each amplitude ensemble was saved. A flutter derivative calculation was then made on each amplitude ensemble. This produced a large number of flutter derivative values from which uncertainty statistics could be calculated. Quantities for which precision errors were estimated in this way included pressure amplitudes, pressure phases, flutter derivatives, and turbulence length scales.

The physical setup of the pressure model allowed a large number of ensembles of some quantities from just one test. For example, because two spanwise positions of the model were instrumented on both the top and bottom surfaces, the pressure amplitude at a given streamwise position was measured at four locations for every test. This provided four ensembles of some quantities, such as pressure amplitude, for every actual data acquisition cycle. Ensemble averaging of quantities such as pressure amplitude, pressure phase, pressure spectra, and flutter derivatives took advantage of this multiple ensemble

aspect of the test setup. Obviously, this would not be warranted if the oscillation were not about a zero-mean angle of attack.

Precision indices were then calculated as follows. Any quantity, including a mean value or a variance value, computed from samples of a random variable will itself be a random variable. A mean value such as  $\bar{x}_{\text{exp}}$  computed from  $N$  independent observations of a random variable,  $x$ , has an associated “sampling distribution” (i.e. probability distribution function). A confidence interval for  $\bar{x}_{\text{exp}}$  can be expressed in terms of the estimated mean and variance:

$$\bar{x}_{\text{exp}} - \frac{\sigma_{\text{exp}} t_{n;\alpha/2}}{\sqrt{N}} \leq \bar{x} < \bar{x}_{\text{exp}} + \frac{\sigma_{\text{exp}} t_{n;\alpha/2}}{\sqrt{N}} \quad n = N - 1 \quad (\text{D-2})$$

where  $\sigma_{\text{exp}}$  is the standard deviation estimated from experimental data and  $t_{n;\alpha/2}$  is the Student  $t$  distribution with  $n$  degrees of freedom and probability value  $\alpha$ . The above expression is well known, and derivations of it can be found in Bendat & Piersol (1986) and in Ang & Tang (1975). Although it is derived assuming a Gaussian distribution for  $x$ , the central limit theorem allows its use for any distribution as  $N$  becomes large. Bendat & Piersol (1986) states that this assumption is “quite accurate in most cases” for  $N > 10$ . Uncertainty estimates calculated using this approach are not reported explicitly here—rather, 95% confidence intervals were presented along with the data in the previous chapters.

For those derived quantities where uncertainty was analyzed analytically, uncertainty was propagated to derived quantities through the conventional approach of Kline & McClintock (1953). The uncertainty,  $u_F$ , of a derived quantity,  $F$ , which is a

function of  $n$  independent variables,  $x_i$ , each having an uncertainty of  $u_i$ , can be written as:

$$u_F = \left[ \left( \frac{\partial F}{\partial x_1} u_1 \right)^2 + \left( \frac{\partial F}{\partial x_2} u_2 \right)^2 + \dots + \left( \frac{\partial F}{\partial x_n} u_n \right)^2 \right]^{1/2} \quad (\text{D-3})$$

One such analysis is presented here as an example. Uncertainty for other parameters was calculated similarly. The mean velocity measured with the Pitot static probe is calculated as:

$$U = \sqrt{2(p_{total} - p_{static})/\rho} \quad (\text{D-4})$$

where  $U$  is the mean velocity,  $\Delta p = p_{total} - p_{static}$  is the dynamic pressure (the difference between the total and static pressure measured across the ports of the Pitot static probe), and  $\rho$  is the air density. For the mean velocity uncertainty, equation (D-3) can then be written as:

$$u_U = \left[ \left( \frac{\partial U}{\partial \Delta p} u_{\Delta p} \right)^2 + \left( \frac{\partial U}{\partial \rho} u_{\rho} \right)^2 \right]^{1/2} \quad (\text{D-5})$$

where  $u_U$  is the uncertainty in the mean velocity,  $u_{\Delta p}$  is the uncertainty in the dynamic pressure, and  $u_{\rho}$  is the uncertainty in the air density. With the partial derivatives and the appropriate uncertainty values, this expression becomes:

$$u_U = \left[ \left( \frac{1}{\rho} \left( \frac{2\Delta p}{\rho} \right)^{-1/2} u_{\Delta p} \right)^2 + \left( \frac{\Delta p}{\rho^2} \left( \frac{2\Delta p}{\rho} \right)^{-1/2} u_{\rho} \right)^2 \right]^{1/2} = 0.009 \text{ m/s} \quad (\text{D-6})$$

A number of derived quantities, including turbulence intensity and rms pressure, involved rms values. Estimates for the precision errors in rms calculations for a given

random variable employed the following expression developed by Bendat & Piersol (1986):

$$\varepsilon[\sigma_x] \approx \frac{1}{\sqrt{2N}} \quad (\text{D-7})$$

where  $\varepsilon[\sigma_x]$  is the normalized random error in the rms estimate  $\sigma_x$  and  $N$  is the number of samples included in the estimate. Using this estimate, rms pressure uncertainty estimates were about 4.6%. This estimate propagated through the definition of turbulence intensity,  $I_u = u_{\text{rms}}/U$ , gave an uncertainty value for turbulence intensity of 0.04.

Two types of calculations required special uncertainty analysis attention. These included two different applications of cross correlation calculations. The uncertainty of both the cross correlation coefficients reported in Chapters 7 and 8 and the pressure phase estimates of Chapter 6 were analyzed using the derivations of Bendat & Piersol (1986). In each case, random errors are considered and bias errors are assumed negligible.

In this dissertation, correlation values between two signals,  $x(t)$  and  $y(t)$ , were most often presented as the zero time delay value of the cross correlation coefficient function,  $\rho_{xy}(\tau)$ , which is defined as:

$$\rho_{xy}(\tau) = \frac{R_{xy}(\tau)}{\sqrt{R_{xx}(0)R_{yy}(0)}} \quad (\text{D-8})$$

where  $R_{xy}(\tau)$  is the cross correlation function and  $R_{xx}(\tau)$  and  $R_{yy}(\tau)$  are autocorrelation functions. The uncertainty estimate of  $\rho_{xy}(0)$  employs the normalized uncertainty estimate for  $\hat{R}_{xy}(\tau)$ , the cross correlation estimate, given by Bendat & Piersol (1986) as:

$$\varepsilon[\hat{R}_{xy}(\tau)] \approx \frac{1}{\sqrt{2BT}} [1 + \rho_{xy}^{-2}(\tau)]^{1/2} \quad (D-9)$$

where  $B$  is the bandwidth of the signal in Hz (estimated here to be 100 Hz),  $T$  is the total record length of the measurement in seconds (which was 48 sec.). The uncertainty,  $u_{\hat{R}_{xy}}$ , in the cross correlation estimate is then given as:

$$u_{\hat{R}_{xy}} = \varepsilon[\hat{R}_{xy}(\tau)] \hat{R}_{xy}(\tau)$$

Incorporating this into an estimate of the uncertainty of the cross correlation coefficient,  $u_{\rho_{xy}}$ , requires use of the error propagation equation (D-3). After calculating the appropriate partial derivatives and rearranging, this results in:

$$u_{\rho_{xy}} = \rho_{xy}(0) \left[ \left( \varepsilon[\hat{R}_{xy}(0)] \right)^2 + \left( \varepsilon[\hat{R}_{xx}(0)] \right)^2 \right]^{1/2} \quad (D-10)$$

where, for the purpose of this uncertainty estimate,  $R_{xx}(0)$  has been assumed to be equal to  $R_{yy}(0)$ . Using equation (D-9) for  $\varepsilon[\hat{R}_{xy}(0)]$  and equation (D-7) for  $\varepsilon[\hat{R}_{xx}(0)]$ , because  $\sigma_x^2 = R_{xx}(0)$ , uncertainty values were calculated for various magnitudes of  $\rho_{xy}(0)$ .

Spanwise correlation plots in Chapter 7 include error bars computed as  $2u_{\rho_{xy}}$ .

Uncertainty in the pressure phase calculation also uses the  $\varepsilon[\hat{R}_{xy}(\tau)]$  estimate described above. Bendat & Piersol (1986) give the following expression for the random error associated with the time,  $\tau$ , associated with the peak in the cross correlation function:

$$\sigma_\tau = \frac{0.93}{\pi B} \left( \varepsilon[\hat{R}_{xy}(0)] \right)^{1/2} \quad (D-11)$$

where  $\sigma_\tau$  is the rms value associated with the precision error for  $\tau$ . Uncertainty bounds for  $\tau$  calculated as  $\pm 2\sigma_\tau$  were on the order of 0.001 sec.—the sampling rate of the data acquisition. As discussed in Appendix C, phase values were computed using the expression  $\psi = 360f_\alpha\tau$  where  $\psi$  is the pressure phase (in degrees) and  $f_\alpha$  is the model oscillation frequency. The phase uncertainty, therefore, was dependent on  $f_\alpha$ . For the  $U_r = 20$  tests (for which  $f_\alpha = 1.18\text{Hz}$ ), the phase uncertainty,  $u_\psi$ , was less than  $0.5^\circ$ . The largest uncertainty, however, was associated with the lowest reduced velocities. For the  $U_r = 3.1$  tests (for which  $f_\alpha = 7.5\text{Hz}$ ), the phase uncertainty was nearly  $3^\circ$ . In addition to this analysis, the phase uncertainty was considered by an “end to end” analysis as described earlier. The uncertainty bounds plotted in Chapter 6 are the result of the end to end analysis.

## REFERENCES

- Ang, A.H-S., Tang, W.H., *Probability Concepts in Engineering Planning and Design, Volume I-Basic Principles*, John Wiley & Sons, New York, 1975.
- Bartoli, G., Borri, C., Gusella, V., "Aeroelastic behavior of bridge decks: a sensitivity analysis of the turbulent nonlinear response." in *Wind Engineering, Papers for the 9<sup>th</sup> Int. Conf.* New Delhi: Wiley Eastern Limited, p. 851-862.
- Bearman, P.W., Currie, I.G., "Pressure-fluctuation measurements on an oscillating circular cylinder," *Journal of Fluid Mechanics*, v. 91, part 4 (1979) p. 661-677.
- Bearman, P.W., Morel, T., "Effect of Free Stream Turbulence on the Flow Around Bluff Bodies," *Prog. Aerospace Sci.*, v. 20 (1983) p. 97-123.
- Bearman, P.W., Obasaju, E.D., "An experimental study of pressure fluctuations on fixed and oscillating square-section cylinders." *Journal of Fluid Mechanics*, v. 119 (1982) p. 297-321.
- Beliveau, K.Y.R., Vaicaitis, R., Shinozuka, M., "Motion of suspension bridges subject to wind loads." *Journal of the Structural Mechanics Division, ASCE*, v. 103 (1977).
- Bendat, J.S., Piersol, A.G., *Random Data, Analysis and Measurement Procedures*, 2<sup>nd</sup> Ed., John Wiley & Sons, New York, 1986.
- Bietry, J., Delaunay, D., Conti, E., "Comparison of full-scale measurement and computation of wind effects on a cable-stayed bridge." *Journal of Wind Engineering and Industrial Aerodynamics*, v. 57, (1995) p. 225-235.
- Billah, K.Y.R., Shinozuka, M., "Random Vibrational Response and Stability Study of Long-Span Bridges." *Journal of Applied Mechanics, Trans. of the ASME*, v. 61, (1994) p. 302-308.
- Bisplinghoff, R.L., Ashley, H., Halfman, R.L., *Aeroelasticity*, Dover Publications, Inc., Mineola, NY, 1996.
- Bogunović Jakobsen, J., Hjorth-Hansen, E., "Determination of the aerodynamic derivatives by a system identification method." *Journal of Wind Engineering and Industrial Aerodynamics*, v. 57, (1995) p. 295-305.

Bucher, C.G., Lin, Y.K., "Stochastic Stability of Bridges Considering Coupled Modes." *Journal of Engineering Mechanics*, v. 114, n. 12 (1988) p. 2055-2071.

Castro, I.P., Haque, A., "The structure of a turbulent shear layer bounding a separation region." *Journal of Fluid Mechanics*, v. 179 (1987) p. 439-468.

Castro, I.P., Haque, A., "The structure of a shear layer bounding a separation region. Part 2. Effects of free-stream turbulence." *Journal of Fluid Mechanics*, v. 192 (1988) p. 577-595.

Chen, X., Matsumoto, M., Kareem, A., "Aerodynamic coupling effects on flutter and buffeting of bridges." *Journal of Engineering Mechanics*, v. 126, n. 1 (2000) p. 17-26.

Chen, X., Matsumoto, M., Kareem, A., "Time domain flutter and buffeting response analysis of bridges." *Journal of Engineering Mechanics*, v. 126, n. 1 (2000a) p. 7-16.

Cherry, N.J., "The effects of stream turbulence on a separated flow with reattachment." PhD thesis, Imperial College, University of London, 1982.

Cherry, N.J., Hillier, R. Latour, M.E.M.P., "Unsteady measurements in a separated and reattaching flow." *Journal of Fluid Mechanics*, v. 144 (1984) p. 13-46.

Counihan, J., "Adiabatic Atmospheric Boundary Layers: A Review and Analysis of Data From the Period 1880-1972." *Atmospheric Environment*, v. 9 (1975) p. 871-905.

Davenport, A.G., "Buffeting of a suspension bridge by storm winds." *Journal of Structural Engineering*, ASCE, v. 88, n. ST3 (1962).

Diana, G., Bruni, S., Cigada, A., Collina, A., "Turbulence effects on flutter velocity in long span suspension bridges." *Journal of Wind Engineering and Industrial Aerodynamics*, v. 48 (1993) p. 329-342.

Diana, G., Bruni, S., Collina, A., Zasso, A., "Aerodynamic challenges in super long span bridges design." in Larsen & Esdahl (eds.), *Bridge Aerodynamics, Proc. International Symp. On Advances in Bridge Aerodynamics*, Balkema, Rotterdam (1998).

Diana, G., Cheli, F., Zasso, A., Boccione, M., "Suspension bridge response to turbulent wind: Comparison of a new numerical simulation method results with full scale data." in Larsen et al. (Eds.), *Wind Engineering into the 21<sup>st</sup> Century, Proc. of 10<sup>th</sup> International Conference on Wind Engineering*, Balkema, Rotterdam (1999) p. 871-878.

Diana, G., Falco, M., Bruni, S., Cigada, A., Larose, G.L., Damsgaard, A., Collina, A., "Comparisons between wind tunnel tests on a full aeroelastic model of the proposed bridge over Stretto di Messina and numerical results." *Journal of Wind Engineering and Industrial Aerodynamics*, v. 54/55, (1995) p. 101-113.

Dowell, E.H. (Ed.), Crawley, E.F., Curtiss, H.C., Peters, D.A., Scanlan, R.H., Sisto, F., *A Modern Course in Aeroelasticity*, 3<sup>rd</sup> Ed., (Kluwer Academic Publishers, 1995).

Falco, M., Curami, A., Zasso, A., “Nonlinear effects in sectional model aeroelastic parameters identification.” *Journal of Wind Engineering and Industrial Aerodynamics*, v. 41-44 (1992) p. 1321-1332.

Figliola, R.S., Beasley, D.E., *Theory and Design for Mechanical Measurements*, John Wiley & Sons, Inc., New York, NY, 1991.

Fung, Y.C., *An Introduction to the Theory of Aeroelasticity*, Dover Publications, Inc., Mineola, NY, 1993.

Gartshore, I.S. *The effects of free stream turbulence on the drag of rectangular two-dimensional prisms*. Boundary Layer Wind Tunnel Laboratory 4-73, University of Western Ontario, 1973.

Hillier, R., Cherry, R.J., “The effect of stream turbulence on separation bubbles.” *Journal of Wind Engineering and Industrial Aerodynamics*, v. 8 (1981) p. 49-58.

Hinze, J.O., *Turbulence*, McGraw-Hill Book Company, New York, 1959.

Huston, D.R., *The Effects of Upstream Gusting on the Aeroelastic Behavior of Long Suspended-Span Bridges*, Princeton University Dissertation (1986).

Honeywell Pressure and Airflow Sensors, Catalog 15, MICRO SWITCH Division, Honeywell, Inc., Freeport, Illinois, 1995.

Irwin, H.P.A.H., Schuyler, G.D., “Experiments on a Full Aeroelastic Model of Lions’ Gate Bridge in Smooth and Turbulent Flow.” Report LTR-LA-206, National Aeronautical Establishment, National Research Council Canada (1977).

Jain, A., Jones, N.P., Scanlan, R.H., “Coupled flutter and buffeting analysis of long-span bridges.” *Journal of Structural Engineering*, ASCE, v. 122, n. 7 (1996) p. 716-725.

Jones, N.P., Scanlan, R.H., Sarkar, P.P., Singh, L., “The effect of section model details on aeroelastic parameters.” *Journal of Wind Engineering and Industrial Aerodynamics*, v. 54/55, (1995) p. 45-53.

Kareem, A., “Measurements of pressure and force fields on building models in simulated atmospheric flows.” *Journal of Wind Engineering and Industrial Aerodynamics*, v. 36 (1990) p. 589-599.

Kareem, A., “Wind effects on structures: a probabilistic viewpoint.” *Probabilistic Engineering Mechanics*, v. 2, n. 4 (1987) p. 166-200.

- Kareem, A., Cermak, J.E., "Wind-tunnel simulation of wind structure interactions." *ISA Transactions*, v. 18, n. 4 (1979) p. 23-41.
- Katsuchi, H., Jones, N.P., Scanlan, R.H., "Multimode coupled flutter and buffeting analysis of the Akashi-Kaikyo Bridge." *Journal of Structural Engineering*, ASCE, v. 125 (1999) p. 60-70.
- Kimbrell, J.T., *Kinematics Analysis and Synthesis*, McGraw-Hill, Inc., New York, 1991.
- Kimura, K., Fujino, Y., Nakato, S., Tamura, H., "Characteristics of the buffeting forces on flat cylinders." *Journal of Wind Engineering and Industrial Aerodynamics*, v. 69-71 (1997) p. 365-374.
- Kiya, M., Sasaki, K., "Free-stream turbulence effects on a separation bubble." *Journal of Wind Engineering and Industrial Aerodynamics* v. 14 (1983) p. 375-386.
- Kiya, M., Sasaki, K., "Structure of a turbulent separation bubble." *Journal of Fluid Mechanics*, v. 127 (1983a) p. 83-113.
- Kiya, M., Sasaki, K., "Structure of large-scale vortices and unsteady reverse flow in the reattaching zone of turbulent separation bubble." *Journal of Fluid Mechanics*, v. 154 (1985) p. 463-491.
- Kline, S.J., McClintock, F.A., "Describing uncertainties in single-sample experiments." *Mechanical Engineering*, v. 75, (1953) p. 3-8.
- Kubo, Y., Hirata, K., Mikawa, K., "Mechanism of aerodynamic vibrations of shallow bridge girder sections." *Journal of Wind Engineering and Industrial Aerodynamics*, v. 41-44 (1992) p. 1297-1308.
- Larose, G.L., Mann, J., "Gust loading on streamlined bridge decks." *Journal of Fluids and Structures*, v. 12 (1998) p. 511-536.
- Larose, G.L., Davenport, A.G., King, J.P.C., "On the Unsteady Aerodynamic Forces on a Bridge Deck in Turbulent Boundary Layer Flow." In Conference Proceedings of the 7<sup>th</sup> U.S. National Conference on Wind Engineering, UCLA (1993) p. 373-382.
- Larsen, A., Jacobsen, A.S., "Aerodynamic design of the Great Belt East Bridge," in Larsen, A. (ed.), *Aerodynamics of Large Bridges*, Balkema, Rotterdam (1992) p. 269-283.
- Larsen, A., Walther, J.H., "Aerodynamic analysis of bridge sections based on discrete vortex simulations." *Journal of Wind Engineering and Industrial Aerodynamics*, v. 67-68 (1997) p. 253-265.

- Lee, B., "The effect of turbulence on the surface pressure field of a square prism." *Journal of Fluid Mechanics*, v. 69 (1975) p. 263-282.
- Liepmann, H.W., "On the application of statistical concepts to the buffeting problem." *Journal of the Aeronautical Sciences*, v. 19 (1952) p. 793-800.
- Li, Q.C., "Measuring flutter derivatives for bridge sectional models in water channel." *Journal of Engineering Mechanics*, v. 121, n. 1 (1995) p. 90-101.
- Li, Q.C., Lin, Y.K., "New stochastic theory for bridge stability in turbulent flow II." *Journal of Engineering Mechanics*, ASCE, v. 121 (1995) p. 102-116.
- Li, Q.S., Melbourne, W.H., "An experimental investigation of the effects of free-stream turbulence on streamwise surface pressures in separated and reattaching flows." *Journal of Wind Engineering and Industrial Aerodynamics*, v. 54/55 (1995) p. 313-323.
- Lin, Y.K., "Motion of Suspension Bridges in Turbulent Winds." *Journal of the Engineering Mechanics Division*, ASCE, Vol. 105, No. EM6 (1979) p. 921-932.
- Lin, Y.K., Ariaratnam, S.T., "Stability of Bridge Motion in Turbulent Winds." *Journal of Structural Mechanics*, v. 8, n. 1 (1980) p. 1-15.
- Lin, Y.K., Li, Q.C., "New stochastic theory for bridge stability in turbulent flow." *Journal of Engineering Mechanics*, ASCE, v. 119 (1993).
- Lueptow, R.M., Breuer, K.S., Haritonidis, J.H., "Computer-aided calibration of X-probes using a look-up table." *Experiments in Fluids*, v. 6 (1988) p. 115-118.
- Matsumoto, M., "Aerodynamic Damping of Prisms." *Journal of Wind Engineering and Industrial Aerodynamics*, v. 59, n. 2-3 (1996) p. 159-175.
- Matsumoto, M., Shirato, H., Hirai, S., "Torsional Flutter Mechanism of 2-D H-Shaped Cylinders And Effect of Flow Turbulence." *Journal of Wind Engineering and Industrial Aerodynamics*, v. 41-44 (1992) p. 687-698.
- Matsumoto, M., Kobayashi, Y., Niihara, Y., Shirato, H., Hamasaki, H., "Flutter Mechanism and Its Stabilization of Bluff Bodies." *Wind Engineering, Papers for the 9<sup>th</sup> Int. Conf.* (1995) New Delhi: Wiley Eastern Limited.
- Melbourne, W.H., "Turbulence Effects on Maximum Surface Pressure – A Mechanism and Possibility of Reduction." *Wind Engineering, Proc. of Fifth International Conference*. Pergamon Press, 1979.
- Miyata, T., Yamaguchi, K., "Aerodynamics of wind effects on the Akashi Kaikyo Bridge." *Journal of Wind Engineering and Industrial Aerodynamics*, v. 48 (1993) p. 287-315.

Miyata, T., Tada, K., Sato, H., Katsuchi, H., Hikami, Y., "New findings of coupled flutter in full model wind tunnel tests on the Akashi Kaikyo Bridge." *Proceedings of Symposium on Cable-Stayed and Suspension Bridges*, Deauville, France, (1994) p. 163-170.

Murakami, S., Mochida, A., "Past, Present and Future of CWE: The View from 1999." In Larsen et al (eds.), *Wind Engineering into the 21<sup>st</sup> Century*, Proceedings of the Tenth International Conference on Wind Engineering, Balkema, Rotterdam (1999) p. 91-104.

Nakamura, Y., "Recent Research into Bluff-Body Flutter." *Journal of Wind Engineering*, Japan Association for Wind Engineering, n. 37, International Colloquium on Bluff Body Aerodynamics and Its Applications (1988) p. 1-10.

Nakamura, Y., "Bluff body aerodynamics and turbulence." *Journal of Wind Engineering and Industrial Aerodynamics*, v. 49 (1993) p. 65-78.

Nakamura, Y., Ohya, Y., "The effects of turbulence on the mean flow past two-dimensional rectangular cylinders." *Journal of Fluid Mechanics*, v. 149 (1984) p. 255-273.

Nakamura, Y., Ozono, S., "The effects of turbulence on a separated and reattaching flow." *Journal of Fluid Mechanics*, v. 178 (1987) p. 477-490.

National Instruments Corp., *SCXI-1140 User Manual*, Sept. 1994 Ed., National Instruments, Austin, Texas (1994).

National Instruments Corp., *PCI E Series User Manual*, July 1997 Ed., National Instruments, Austin, Texas (1997).

Obasaju, E.D., *Pressure fluctuations on stationary and oscillating square section cylinders*, Ph.D. Thesis, University of London, 1977.

Pandey, M.D., Ariaratnam, S.T., "Stability Analysis of Wind Induced Torsional Motion of Slender Bridges." *Structural Safety*, v. 20 (1998) p. 379-389.

Poulsen, N.K., Damsgaard, A., Reinhold, T.A., "Determination of Flutter Derivatives for the Great Belt Bridge." *Journal of Wind Engineering and Industrial Aerodynamics*, v. 41-44, (1992) p. 153-164.

Press, W.H., Teukolsky, S.A., Vetterling, W.T., Flannery, B.P., *Numerical Recipes in FORTRAN, The Art of Scientific Computing*, 2<sup>nd</sup> Ed. Cambridge University Press, New York, 1992.

Roshko, A., "On the Wake and Drag of Bluff Bodies." *Journal of the Aeronautical Sciences*, v. 22, n. 2 (1955) p. 124-132.

Ross, G. (1996) Personal communication.

- Saathoff, P.J., Melbourne, W.H., "The generation of peak pressures in separated/reattaching flows." *Journal of Wind Engineering and Industrial Aerodynamics*, v. 32, (1989) p. 121-134.
- Saathoff, P.J., Melbourne, W.H., "Effects of free-stream turbulence on surface pressure fluctuations in a separation bubble." *Journal of Fluid Mechanics*, v. 337 (1997) p. 1-24.
- Sabzevari, A., Scanlan, R.H., "Aerodynamic stability of suspension bridges." *Journal of the Engineering Mechanics Division*, ASCE, v. 94, n. 2 (1968) p. 489-519.
- Sankaran, R., Jancauskas, E.D., "Direct measurement of the aerodynamic admittance of two-dimensional rectangular cylinders in smooth and turbulent flows." *Journal of Wind Engineering and Industrial Aerodynamics*, v. 41-44 (1992) p. 601-611.
- Sankaran, R., Jancauskas, E.D., "Measurements of cross-correlation in separated flows around bluff cylinders." *Journal of Wind Engineering and Industrial Aerodynamics*, v. 49 (1993) p. 279-288.
- Sarkar, P.P., Jones, N.P., Scanlan, R.H., "A Comparative Study of the Aeroelastic Behavior of Three Flexible Bridges and a Thin Airfoil." Conference Proceedings, Vol. II, 7<sup>th</sup> U.S. National Conference on Wind Engineering, UCLA, 1993.
- Sarkar, P.P., Jones, N.P., Scanlan, R.H., "Identification of aeroelastic parameters of flexible bridges." *Journal of Engineering Mechanics*, ASCE, v. 120, n. 8 (1994) p. 1718-1742.
- Scanlan, R.H., "The action of flexible bridges under wind, I: flutter theory." *Journal of Sound and Vibration*, v. 60, n. 2, (1978a) p. 187-199.
- Scanlan, R.H., "The action of flexible bridges under wind, II: buffeting theory." *Journal of Sound and Vibration*, v. 60, n. 2, (1978b) p. 201-211.
- Scanlan, R.H., "Amplitude and Turbulence Effects on Bridge Flutter Derivatives." *Journal of Structural Engineering*, Vol. 123, No. 2, (1997) p. 232-236.
- Scanlan, R.H., "Interpreting Aeroelastic Models of Cable-Stayed Bridges." *Journal of Engineering Mechanics*, v. 113, n. 4, (1987) p. 555-575.
- Scanlan, R.H., "Problematics in Formulation of Wind-Force Models for Bridge Decks." *Journal of Engineering Mechanics*, v. 119, n. 7, (1993) p. 1353-1375.
- Scanlan, R.H., Béliveau, J., Budlong, K.S., "Indicial Aerodynamic Functions for Bridge Decks." *Journal of the Engineering Mechanics Division*, Proc. of the ASCE, v. 100, n. EM4 (1974) p. 657-672.

Scanlan, R.H., Jones, N.P., "Aeroelastic Analysis of Cable-Stayed Bridges." *Journal of Structural Engineering*, v. 116, n. 2, (1990) p. 279-297.

Scanlan, R.H., Stroh, S.L., Raggett, J.D., "Methods of wind response investigation employed for the Kap Shui Mun Bridge." *Journal of Wind Engineering and Industrial Aerodynamics*, v. 54/55, (1995) p. 1-11.

Scanlan, R.H., Tomko, J.J., "Airfoil and Bridge Deck Flutter Derivatives." *Journal of the Engineering Mechanics Division*, Proc. of the ASCE, v. 97, n. EM6, (1971) p. 1717-1737.

Scanlan, R.H., Wardlaw, R.L., "Aerodynamic Stability of Bridge Decks and Structural Members." In *Cable-Stayed Bridges*, A compilation of papers presented at Engineering Symposium Cable-Stayed Bridges, Pasco, Washington, 1977, Bridge Div., Office of Engineering, Federal Highway Administration, Washington, D.C. (1978) p. 169-202.

Sears, W.R., "Some Aspects of Non-Stationary Airfoil Theory and Its Practical Application." *Journal of the Aeronautical Sciences*, v. 8 (1941) p. 104-108.

SenSym Solid-State Pressure Sensors Handbook, v. 15. SenSym Inc., Milipitas, CA, 1996.

Shinozuka, M., Billah, K.Y., "Stability of long-span suspension bridges in turbulent flow." *Proc. Of 7<sup>th</sup> U.S. National Conference on Wind Engineering*, UCLA (1993).

Sigurdson, L.W., "The structure and control of a turbulent reattaching flow." *Journal of Fluid Mechanics*, v. 298 (1995) p. 139-165.

Simiu, E., Scanlan, R.H. *Wind Effects on Structures*, Third Ed., John Wiley & Sons, Inc., New York, 1996.

Stansby, P.K., "The effects of end plates on the base pressure coefficient of a circular cylinder." *Aeronautical Journal*, January, 1974, p. 36-37.

Steinman, D.B., "Suspension Bridges: The Aerodynamic Problem And Its Solution." *American Scientist*, July, (1954) p. 397-438,460.

Theodorsen, T., "General theory of aerodynamic stability and the mechanism of flutter." NACA Report 496, U.S. National Advisory Committee for Aeronautics, Langley, VA (1935).

Tieleman, H.W., Akins, R.E., "Effects of Incident Turbulence on Pressure Distributions on Rectangular Prisms." *Journal of Wind Engineering and Industrial Aerodynamics*, v. 36, (1990) p. 579-588.

Tieleman, H.W., "Myths in Wind Engineering." *Proceedings of the 80<sup>th</sup> Birthday Symposium in Honor of Professor Robert H. Scanlan*, The Johns Hopkins University (1994) p. 125-134.

Teunissen, H.W., "Characteristics of the Mean Wind and Turbulence in the Planetary Boundary Layer." UTIAS Review No. 32 (1970).

Toebes, G.H., "The Unsteady Flow and Wake Near an Oscillating Cylinder." *Journal of Basic Engineering*, ASME, Sept. (1969) p. 493-502.

Tsiatas, G., Gasparini, D.A., "Torsional response of long-span bridge in presence of turbulence." *Journal of Engineering Mechanics*, v. 113 (1987) p. 303-314.

Tsiatas, G., Sarkar, P.P., "Motion stability of long-span bridges under gusty winds." *Journal of Engineering Mechanics*, v. 114 (1988) p. 257-276.

TSI, Inc. *IFA 100 System Intelligent Flow Analyzer Instruction Manual*, TSI, Inc., St. Paul (1992).

Ukeguchi, M., Sakata, H., Nishitani, H., "An investigation of aeroelastic instability of suspension bridges." *Proceedings of the International Symposium on Suspension Bridges*, Research Laboratory for Civil Engineering, Lisbon, Portugal (1966).

Wilkinson, R.H., "Fluctuating pressures on an oscillating square prism." *Aeronautical Quarterly*, v. 32 (1981) p. 97-125.